DOI: 10.1007/s10297-006-0079-z
Originally published in J. Opt. Fiber. Commun. Rep. 4, 225–362 (2007)

Laser communication transmitter and receiver design

David O. Caplan

MIT Lincoln Laboratory, Lexington, Massachusetts

Abstract. Free-space laser communication systems have the potential to provide flexible, high-speed connectivity suitable for long-haul intersatellite and deep-space links. For these applications, power-efficient transmitter and receiver designs are essential for cost-effective implementation. State-of-the-art designs can leverage many of the recent advances in optical communication technologies that have led to global wide-band fiber-optic networks with multiple Tbit/s capacities. While spectral efficiency has long been a key design parameter in the telecommunications industry, the many THz of excess channel bandwidth in the optical regime can be used to improve receiver sensitivities where photon efficiency is a design driver. Furthermore, the combination of excess bandwidth and average-power-limited optical transmitters has led to a new paradigm in transmitter and receiver design that can extend optimized performance of a single receiver to accommodate multiple data rates.

This paper discusses state-of-the-art optical transmitter and receiver designs that are particularly well suited for average-power-limited photon-starved links where channel bandwidth is readily available. For comparison, relatively simple direct-detection systems used in short terrestrial or fiber optic links are discussed, but emphasis is placed on mature high-performance photon-efficient systems and commercially available technologies suitable for operation in space. The fundamental characteristics of optical sources, modulators, amplifiers, detectors, and associated noise sources are reviewed along with some of the unique properties that distinguish laser communication systems and components from their RF counterparts. Also addressed is the interplay between modulation format, transmitter waveform, and receiver design, as well as practical tradeoffs and implementation considerations that arise from using various technologies.

1. Introduction

Optical communications has provided unprecedented capacity in modern networks. The rapid growth of the Internet has led to investment in wide-band fiber-optic networks that now span the planet. The optical communications revolution has also led

to the development of new and enabling technologies that can be applied outside of conventional telecom applications. Free-space laser communications, also known as lasercom, is one area that can benefit from these recent advances. Free-space optical networks have the potential to surround the planet with flexible and agile wide-band lasercom that could extend to the moon, Mars, [1,2] and beyond—capable of bridging billion kilometer links at Megabit/sec (Mbps) data rates. Such capabilities require photon-efficient transmitters and receivers, the main thrust of this paper, which can extend unrepeatered links over ultra-long-haul distances exceeding the net fiber deployed on Earth today.

Free-space laser communication performance directly depends on the efficiency and sensitivity of optical transmitters and receivers. However, until recently, these factors were not the driving factors in the buildup of fiber-optic networks. But as the apparent demand for bandwidth has approached the limitations of deployed fiber-optic links, more sensitive receivers have become a means of improving network performance in terms of power and bandwidth efficiency. Consequently fiber- and free-space-based technology requirements have started to converge. High-sensitivity photon-efficient transmitter and receiver designs can reduce mid-span amplifier requirements, diminish nonlinear impairments, and extend link distances in fiber networks, but they are especially beneficial for free space optical (FSO) communication, since improvements in receiver sensitivity directly reduce transmitted power requirements which in turn, can lead to significant size, weight, power (SWAP) and cost reductions.

The availability of modular high-reliability high-performance commercial-off-the-shelf (COTS) technologies already developed for and widely used by the telecommunication industry is of great value to the development of future free-space laser communication systems [3]. Not only can the tremendous telecom investment in technology development be leveraged in many cases, but the field-proven heritage of such technologies can provide increased confidence in reliability and life-time estimates, as well as the component manufacturing process. This knowledge can be used to accelerate the process of integrating cutting-edge technologies into reliable designs, and reduce the expense of starting costly qualification programs from scratch. This is especially important in space-based systems, where repair is impractical, and both reliability and performance are critical design drivers. The value added from heritage telecom technologies which require Telcordia (formerly known as Bellcore) qualification, is of additional value since these standards (e.g., [4–9]) often test to mechanical and thermal levels that are similar to many of the environmental requirements for space-based platforms.

Free-space optical links have some notable advantages over both radio-frequency (RF) and fiber-optic links that allow greater flexibility in transmitter and receiver design and optimization. These include the absence of channel dispersion and nonlinearities, and virtually unlimited channel bandwidth, especially in space-based applications where atmospheric absorption is nonexistent. Such characteristics allow FSO transmitter (TX) and receiver (RX) designs to leverage the average-power-limited properties of optical transmitters to generate optimized signaling waveforms [10–15], which, when used in combination with photon-efficient modulation formats, can contribute substantially to overall link efficiency, η_{link}. A practical measure of η_{link} is energy required per bit-received, [J/bit].

1.1. *Background*

The theories that govern both RF and optical communications over a noisy channel are well established, dating back to 1949 to the work of Claude Shannon [16,17] in which he established the channel capacity theorem which states that error-free communications are possible up to rate C (bits/s) over a channel of bandwidth B (Hz) with a signal of average power, P (W) perturbed by additive white Gaussian noise (AWGN) of power spectral density of $N_0/2$ (W/Hz). The capacity of such a link is given in Eq. (1), which highlights the interplay between the three key system parameters: bandwidth, average signal power, and noise power spectral density [17–19]:

$$C = B\log_2(1+\mathrm{SNR}) = B\log_2\left(1+\frac{P}{N_0B}\right) = B\log_2\left(1+\frac{rE_b}{N_0}\right) \quad [\mathrm{bits/s}]. \tag{1}$$

The SNR is simply the ratio of the average signal power (P), to noise power, (N_0B). For a data rate R_b (bits/s), the average signal power is R_bE_b, where E_b is the energy-per-bit (J/bit). Substituting spectral efficiency $r = R_b/B$ [(bit/s)/Hz], we obtain the right-hand side of Eq. (1), where E_b/N_0 is the energy-per-bit to noise power spectral density ratio. For shot-noise-limited optical signals the E_b/N_0 term can be replaced by the average number of signal photons-per-bit (PPB) in most cases (see section 2.3) and corresponds to the SNR over the observation window, with the exception of coherent-homodyne RXs, where the quantum-limited SNR = PPB/2 [20]. The Shannon Limit shown in Fig. 1, achieved when $R_b = C$, is the optimum tradeoff between spectral-efficiency, r, and photon-efficiency. In the limiting case of optimum bandwidth expansion, with modulation and coding, Shannon-limited sensitivity of 0.7 PPB (or ~0.35 PPB for homodyne) corresponding to a –1.6-dB SNR can be achieved for the AWGN channel [17,18,21–23]. A detailed discussion of Shannon-limited capacities for optical communication systems is given in [23].

Also highlighted in Fig. 1 is uncoded performance at the 10^{-9} bit-error-rate (BER) and Shannon-limited capacities for on-off-keying (OOK), differential-phase-shift-keying (DPSK), and M-ary orthogonal-keying modulation formats such as M-ary pulse-position-modulation (M-PPM) and frequency-shift-keying (M-FSK) with hard-decision coding. DPSK has received significant interest from the FSO community and the telecom industry since it is both energy-efficient and spectrally-efficient. For a quantum-limited optically preamplified DPSK receiver with optimal coding, Shannon-limited performance approaches 3 PPB with ~0.5 bit/s/Hz efficiency. High-rate optically-preamplified receivers using 24.6% and 7% low-overhead forward error correction (FEC) with 0.8 and 0.935 bits/s/Hz efficiencies have demonstrated 7 and 9 PPB receiver sensitivities at 10 and 40 Gbit/s data rates, respectively [24,25].

While spectral-efficiency has long been a key design parameter in the telecom industry, in many optical communication links excess channel bandwidth is available, and can be used to improve performance where photon efficiency is the design driver. In such links, the available bandwidth can be used to improve receiver sensitivities by ~5 dB by using, for example, coded M-ary orthogonal modulation formats such as M-PPM. As shown in Fig. 1, the quantum-limited sensitivity (pre-amplified, direct detection) for uncoded 1024-PPM in which each symbol carries 10 bits of information, is ~6 dB-PPB (~4 PPB), with $100\times(M/\log_2 M)$ bandwidth expansion. With the addition of ~50% overhead (OH) hard-decision FEC, ~1.5 PPB sensitivity can be

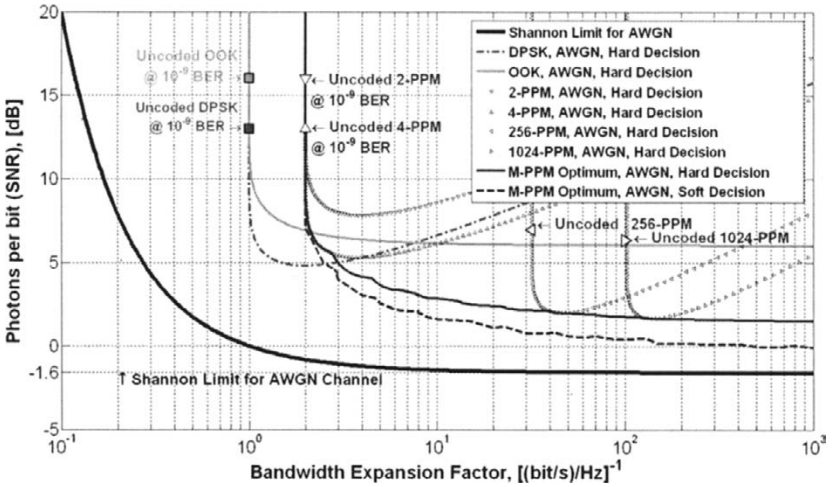

Fig. 1. The tradeoff between sensitivity (photon-efficiency) as measured in photons per bit, and bandwidth expansion (spectral-efficiency) for OOK, DPSK, and M-ary orthogonal, as well as the ultimate Shannon limit for AWGN systems [22]. Reprinted with permission of IEEE. (©2006 IEEE.)

achieved, and this can be extended to nearly 1 PPB by implementing optimal soft-decision decoding [22].

For the Poisson channel dominated by quantum noise, the Shannon-limited sensitivity per-photon can be made arbitrarily low, with a lower bound given by the ratio of thermal-noise-photon energy to signal-photon energy [26–28]:

$$\frac{B}{C_{\mathrm{ph\ Quantum-limit}}} = \frac{k_B T \ln(2)}{h\nu} \quad [\mathrm{photons/bit}], \tag{2}$$

where B is the receiver bandwidth in Hz, C_{ph} is the capacity in bits/sec per photon, k_B is Boltzmann's constant (1.38×10^{-23} J/K), h is Planck's constant (6.63×10^{-34} J s), and T is temperature in Kelvin (K). For the case of 1.5 μm signal photons at 300K, this yields a limit of 0.022 PPB (–16.6 dB SNR) or 46 bits/photon [27,28], which in principle, can be further improved by reducing the receiver temperature to 3K. Although this is not practically realizable, the promise of such capabilities has made the research and development of efficient wide-band photon-counting detector technologies an area of active research [1,2,29–32], especially since Gigabit-per-second (Gbps) class high-sensitivity communications employing super-conducting photon-counting detectors have recently been demonstrated [33–35].

A block diagram of the communication link is shown in Fig. 2, and the focus of this paper will be to optimize overall link performance (η_{link}) through the design of elements within the transmitter and receiver subsystems.

Functionally the free-space optical transmitter typically includes a laser source, a modulator that can impart a variety of modulation formats, a desired bit rate, coding, and a high power amplifier such as an Erbium-doped fiber amplifier (EDFA) with

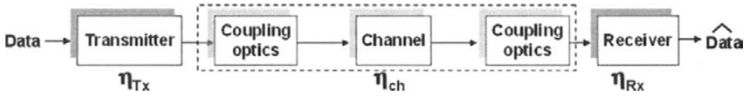

Fig. 2. Block diagram of the optical communications link, with the input being the data and the output being an estimate of the input data. Overall link performance $\eta_{\text{link}} = \eta_{\text{TX}}\eta_{\text{ch}}\eta_{\text{RX}}$.

an electrical to optical conversion efficiency which is often the dominant component of the net transmitter efficiency (η_{TX}). For transmission through the channel (η_{ch}), we can include transmitter optical (telescope) transmission efficiency (η_{TXOpt}), free space transmission efficiency (η_{space}), which is reduced by diffraction losses, atmospheric absorption, scattering, turbulence and scintillation, and interference from background radiance, e.g., loss and additive noise collectively ($1-\eta_{\text{atm}}$). Also included are pointing, acquisition and tracking efficiency (η_{PAT}), and lastly the receiver coupling efficiency (η_{RXOpt}). The net receiver efficiency (η_{RX}) includes the quantum-limited number of photons-per-bit to achieve the desired bit-error-rate (PPB_{QL}), associated implementation penalty (η_{QL}), and potential coding gain (G_{code}) from forward error correction (FEC). These terms are dependent on many factors such as the detection scheme, which may be direct, optically preamplified, homodyne or heterodyne detection, and the demodulation approach, which can be either incoherent or coherent and can occur in either the optical or electrical domain.

High-rate optical communication systems generally utilize PIN photodiodes which are commercially available with electrical bandwidths exceeding 50 GHz. Avalanche photodiodes are detectors with internal gain that can be used to improve RX sensitivity, although this generally comes at the expense of bandwidth and limited dynamic range of operation. A decoder circuit may be employed to process received FEC encoded data, and the final figure of merit is the BER, which is determined by comparing the input data (D) to the output estimate ($\hat{D}$). For systems which use FEC, the BER is often readily available and can be used as a feedback parameter to improve overall performance. Typically receiver sensitivities are measured in terms of the power received or the number of photons-per-bit required to achieve a particular BER, typically 10^{-9} (1 error per billion bits received), but the target can change depending on the application and system requirement.

Optical receiver sensitivities are ultimately limited by choice of modulation format, coding, and fundamental quantum fluctuations. This quantum noise is commonly referred to as "shot noise", which comes from the randomness in photon arrivals, and imposes theoretical limits on receiver performance. For high-rate high-sensitivity optical communication systems, optically preamplified receivers are the most practical, being widely used in the telecom industry and demonstrating the best performance at Gbit/s rates and beyond (see sections 4 and 5).

The theoretical (quantum limited) sensitivity is dependent on the modulation and receiver type and is often measured in terms of the number of PPB required to achieve a 10^{-9} BER. For optically-preamplified binary intensity modulation (IM) formats such as OOK and binary-PPM, the quantum limited sensitivity is ~40 photons-per-bit [20,36–39]. More complex orthogonal signaling formats such as M-PPM or M-FSK

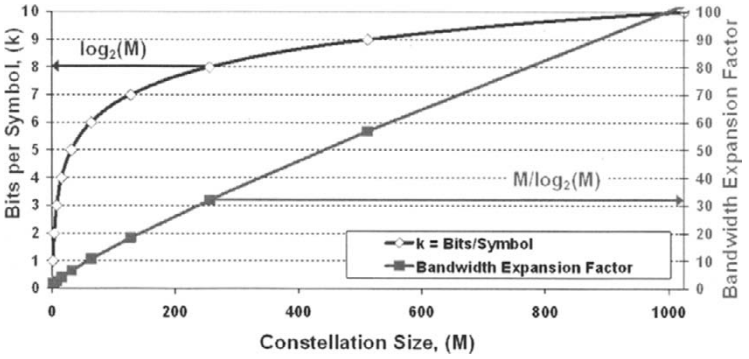

Fig. 3. Bits per symbol (left axis) and bandwidth expansion factor (right axis) for M-ary orthogonal signaling.

can be used to further improve the theoretical sensitivity at the expense of bandwidth, which degrades spectral efficiency by a factor of $(M/\log_2 M)$ as shown in Fig. 3.

For example 256-PPM improves receiver sensitivity by about a factor of 6, to ~6 PPB, but requires a factor of 32 expansion in bandwidth (see also Fig. 1). For high-rate bandwidth-limited applications, optically-preamplified Differential-Phase-Shift-Keying (DPSK) has demonstrated the best sensitivity, providing a ~3dB uncoded benefit over OOK and 2-PPM, corresponding to a theoretical sensitivity of ~20 PPB, although this comes at the expense of a more complicated receiver design.

Forward error correction coding is another powerful tool available to the system designer that is often a cost-effective means of improving receiver sensitivity [17,18,40]. FEC effectively operates by converting the BER of an input signal which contains redundant code bits to an improved output BER. As illustrated in Fig. 1, coding is needed in order to extend uncoded-quantum-limited performance to the ultimate Shannon-limited sensitivities. The use of FEC reduces spectral efficiency and increases TX and RX electronic complexity, requiring the additional encoding and decoding hardware, but can provide significant coding gain with relatively little overhead. For example, with commonly used enhanced Reed-Solomon 255/239 FEC coding, a ~6 dB sensitivity improvement is achieved by converting a $\sim 3 \times 10^{-3}$ input BER to a 10^{-9} output BER with only 7% overhead, i.e., additional bandwidth expansion relative to the rate. Given an optically preamplified DPSK receiver with near-quantum-limited performance this could improve sensitivities to ~6 PPB, within ~3 dB of the AWGN Shannon limit for DPSK. The benefits of such low-complexity FEC codes have been demonstrated at 10 [41] and 40 Gbps [25] data rates. They have also become commonly used in the telecom industry as a means of diminishing nonlinear impairments and increasing overall system throughput.

More powerful turbo codes with 100% overhead (rate $\frac{1}{2}$) have been developed that can closely approach Shannon-limited performance [42], however the complexity of implementing such serially concatenated codes has presently limited real-time application to low data rates <~50 Mbps [2,43–45]. But with less overhead (25%, rate 0.8) and complexity, block turbo codes have demonstrated ~10 dB coding gain at rates up

to 10 Gbps [24]. For the AWGN channel, with high-constellation orthogonal modulation formats such as M-PPM with optimal soft-decision decoding, ~1 photon/bit sensitivity can be achieved in principle [22].

1.2. Scope

This paper will expand upon the topics introduced above, providing an overview of state-of-the-art and future optical transmitter and receiver designs that are particularly well suited for FSO communication. For comparison, relatively simple direct detection systems used in short terrestrial or fiber optic links will be discussed, but emphasis will be placed on mature high-performance photon-efficient systems and technologies suitable for operation in deep space optical links.

While overall system level performance is dependent on many factors such as TX and RX aperture size, wavefront quality, and pointing acquisition and tracking (PAT) [3,46–48] this section will focus on practical design options for the TX and RX blocks of the communication link shown in Fig. 2. The remaining link elements—the coupling optics and channel considerations are discussed in detail in "Atmospheric channel effects on free-space laser communication", by Ricklin et al. (DOI 10.1007/s10297-005-0056-y) and "Free-space laser communication performance in the atmospheric channel", by Arun K. Majumdar (DOI 10.1007/s10297-005-0054-0) in this publication.

The fundamental characteristics of optical sources, modulators, amplifiers, detectors, and associated noise sources will be discussed along with some of the unique properties that distinguish laser communication systems and components from their RF counterparts. Practical tradeoffs and implementation issues that arise from using various technologies, and the interplay between modulation format, transmitter waveform, and receiver design and optimization will be presented.

This paper is intended to complement the rich subject of transmitter and receiver design, by highlighting practical design considerations and recent developments in the state-of-the-art high-performance FSO systems. While introductory and background material is included for clarity, the reader is directed towards the numerous papers, patents, and texts referenced at the end of this paper for a broader view of this subject.

1.3. Historical Perspective

There are many examples of free-space optical communications ranging from the use of mirrors and sunlight by the ancient Greeks, use of fire beacons by the Chinese (~800 BC) and later by Romans, and smoke signals by American Indians. Other notable examples include lighthouses, flags on sailing vessels, and Paul Revere's famous use of lanterns, "One if by land two if by sea" on April 18, 1775. Such early demonstrations of free-space optical communications were enabled by the use of widely available terahertz electromagnetic receivers, namely the human eye with its ability to detect the electromagnetic visible spectrum at wavelengths from about 400 to 750 nm. Alexander Graham Bell and Sumner Tainter demonstrated the first FSO telephone message using the patented "photophone" [49–53], illustrated Fig. 4. The photophone used sunlight as a source, modulated by reflecting off a vibrating mirror, and photoconductive selenium as the receiver on June 3, 1880.

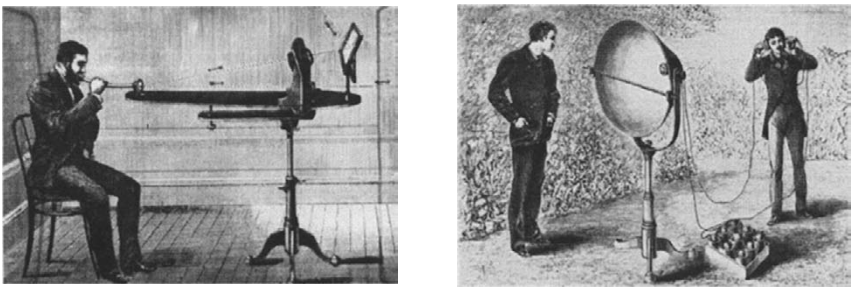

Fig. 4. (Left), The Bell photophone transmitter and (right) photophone receiver. *Rerinted with permission of Lucent Technologies, Inc./Bell Labs.*

However, despite these early advances, optical communications was soon overtaken by rapid development in wireline and wireless RF communications pioneered by the likes of Hertz [54], Bell[55], Edison [56], Marconi [57], Loomis [58], and Fessenden [59] in the late 1800s and early 1900s. During the following 100 years RF communications became a refined commodity with applications ranging from radio, television, cellular, and satellite communications. As the established means of wireless communications, the maturity and sophistication of existing RF capabilities make them worthy of comparison to up-and-coming FSO systems.

Present day FSO systems have significant potential to improve upon RF capabilities in areas where bandwidth or regulatory limitations exist, applications where security is important, and in ultra-long-haul space-based links where size, weight and power (SWAP) are at a premium and diffraction losses dominate. Since the invention of the laser in 1960, there have been significant developments in the critical technologies needed to tap the potential of photonic communications summarized in the list below.

Significant lasercom milestones

1960 Invention of the laser, [60–63]
1962 Invention of semiconductor diode laser, (GaAs) [64,65]
1964 Invention of fiber optical amplifier (Nd:glass 1μm) [66,67]
1970 First continuous-wave room-temperature semiconductor lasers [68]
1970 Development of low loss (<20 dB/km) glass fibers [69–74]
1980 First commercial optical fiber system at 45 Mb/s (AT&T)
1987 Development of Erbium-doped fiber laser amplifier EDFA (1.5μm) [75–77]
1988 First trans-Atlantic fiber cable (280 Mb/s, 1.3 μm) [78]
1989 First undersea tests of optically amplified (EDFA) fiber system
1992 First trans-Atlantic fiber cable using 1.5μm technology (560 Mb/s) [79]
1993 MCI purchases 500 EDFAs and begins installation in terrestrial network
1995 Bidirectional Ground-to-Orbit Lasercom Demonstration (GOLD), 1Mbps up- and down-link transmissions @ 0.514 and 0.830 μm on Engineering Test Satellite-VI (ETS-VI) in elliptical GEO transfer orbit [80–83]

1996 First trans-Atlantic fiber cable using EDFAs (5 Gb/s) [84]
1996 1 Tbit/s demonstrated over fiber [85–88]
2000 360 million km of fiber world wide [89]
2001 Capacity of commercial WDM systems exceeds 1.6 Tb/s [89]
2001 10 Tb/s demonstrated over fiber [90–94]
2001 Geosynchronous Lightweight Technology Experiment (GeoLITE) [95-97], successful demonstration of bidirectional laser communications between a satellite in geosynchronous orbit (GEO), ground, and aircraft
2001 Semiconductor Intersatellite Link Experiment (SILEX) [98–101], demonstrating bidirectional GEO-LEO and GEO-ground laser communications between the Advanced Relay Technology Mission Satellite (ARTEMIS) in GEO, with a 10mW (average) 2 Mbps (2-PPM) directly-driven semiconductor laser TX @ 0.8 μm and a 50 Mbps Si-APD based NRZ-OOK RX; the SPOT-4 imaging satellite in low earth orbit (LEO), and the optical ground station (OGS) [102,103].
2003 Mars Laser Communication Demonstration (MLCD) program initiated (targeting the ~300,000,000 km Mars to Earth link, ~1–30 Mbit/s) using 5W MOPA TX, coded M-PPM ($M = 16 - 64$) and photon-counting detectors @ 1.064 μm [1,2,104]. Critical technologies demonstrated but program cancelled in 2005.
2005 Successful bidirectional inter orbit lasercom link between Optical Inter-orbit Communications Engineering Test Satellite (OICETS) in LEO and ARTEMIS in GEO at 2 and 50 Mbps [105]

It is likely that within the next decade, we will see the first deployments of operational free-space laser communications systems with global and interplanetary reach.

2. General Wavelength Considerations

2.1. Carrier Characteristics

Electromagnetic (EM) waves can be described as an oscillating field with frequency, νs that travel at the speed of light, c. The inverse relationship between the EM carrier frequency (ν) and wavelength (λ) is

$$c = \lambda\nu \tag{3}$$

where the constant $c = 3.0 \times 10^8$ m/s is the speed of light in vacuum. Quantized energy is proportional to frequency, and is given by Planck's relation, which defines the energy-per-photon to be

$$E = h\nu = hc/\lambda \quad [\text{J}], \tag{4}$$

where $h = 6.63 \times 10^{-34}$ J s is Planck's constant. The illustration of the electromagnetic spectrum in Fig. 5 spans 15 orders of magnitude from kilometer long RF waves to picometer long gamma radiation and gives perspective into the broad range of wavelengths, frequencies, and photon-energies that can be used for communications.

As discussed in further detail in section 2.3, these basic EM properties profoundly impact the transmitter and receiver designs. For example, as we transition from using

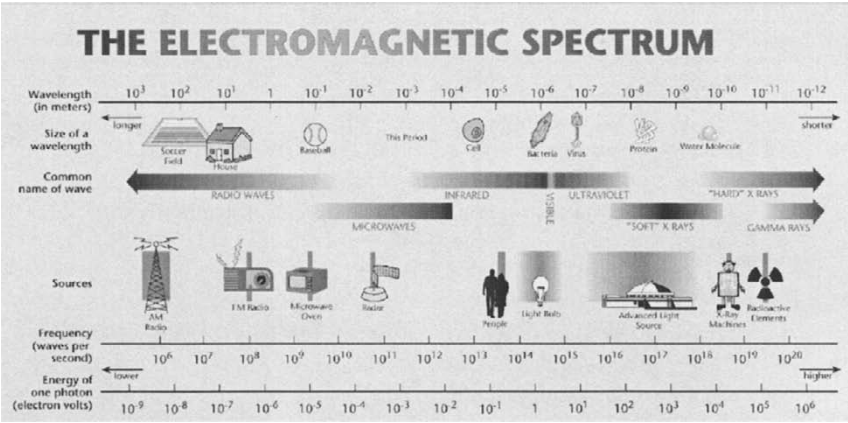

Fig. 5. The electromagnetic spectrum is shown in terms of wavelength along with corresponding frequency, and energy-per-photon. Conventional names of the spectral bands and example sources are also depicted. *Courtesy of the Advanced Light Source, Lawrence Berkeley National Laboratory.*

RF carriers towards higher frequency optical waves for communication, the carrier wavelength shortens. This directly impacts both transmit and receive antenna (aperture) size and diffraction, which is proportional to wavelength. The diffraction limited transmitter beam angle is approximately [47,106]

$$\theta = \lambda / D_{\mathrm{TX}} \quad [\mathrm{rad}], \tag{5}$$

where D_{TX} is the transmitter aperture diameter. Thus using shorter wavelengths allows for smaller divergence angles, or equivalently, better directivity for a given aperture size. Note that this also increases the precision required to hit the target receiver and therefore comes at the expense of increased difficulty in pointing, acquisition, and tracking. From Eq. (5), the far-field on-axis intensity ($\mathrm{W/m^2}$) can be estimated, and for a receiver with collection area (A_{RX}) the power delivered to the RX can be calculated. Diffraction losses reduce the free space transmission efficiency, η_{space}, defined as the ratio of on-axis received power and transmitted power, which in the far-field ($\lambda L \gg D_{\mathrm{TX}}^2$) is approximately given by [106],

$$\eta_{\mathrm{space}} \approx \frac{A_{\mathrm{RX}} A_{\mathrm{TX}}}{\lambda^2 L^2} = \left(\frac{\pi D_{\mathrm{RX}} D_{\mathrm{TX}}}{4 \lambda L} \right)^2 = 1 - \text{Diffraction Loss}, \tag{6}$$

and decreases with the square of the carrier wavelength (λ) and link distance (L).

Carrier frequency directly impacts the fractional bandwidth available for modulation, and therefore limits the maximum rate at which that information can be transmitted. For instance, if the modulation bandwidth is limited to 10% of the carrier frequency, this corresponds to 30 THz available bandwidth for a 1μm optical carrier versus 3 GHz bandwidth for a 1cm RF carrier. This highlights a key difference between high-rate RF and FSO communications, since RF systems need to be spectrally

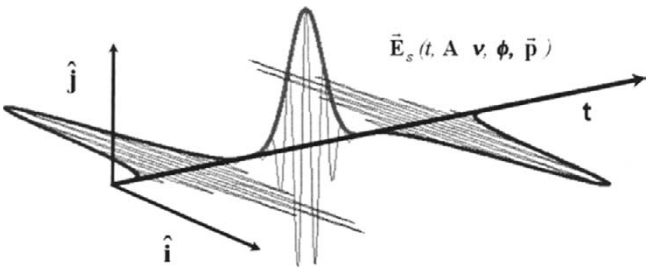

Fig. 6. A time varying electro-magnetic signal, $\vec{\mathbf{E}}_s(t, \boldsymbol{A}, \boldsymbol{\nu}, \boldsymbol{\phi}, \vec{\mathbf{p}})$, depicting the potential for amplitude, frequency, phase, and/or polarization modulation.

efficient in high-rate applications at the expense of energy or photon efficiency (see Fig. 1), whereas FSO systems can often use bandwidth as a flexible design parameter.

Channel properties also vary substantially with wavelength. Clouds, fog, rain, turbulence, scattering (e.g., Raleigh scattering $\propto 1/\lambda^4$), atmospheric absorption, etc. all have a strong wavelength dependence. Owing to the longer wavelength, RF communications are generally more robust in atmospheric channels where these factors are a limitation [107–109].

Lastly, photon energy is proportional to the quantum or shot noise in the transmitted signal, and therefore can impact the receiver sensitivity. As the photon energy (in Joules), increases, the number of photons per second decreases for a given power (in W, or J/s). This in turn increases the "graininess" or shot noise of the signal, which drives high-sensitivity optical receiver design as described further in section 2.3.

2.2. *Electromagnetic Signaling Options*

A general expression for a time varying electro-magnetic (EM) signal $\vec{\mathbf{E}}_s(t, \boldsymbol{A}, \boldsymbol{\nu}, \boldsymbol{\phi}, \vec{\mathbf{p}})$ is given in Eq. (7) and illustrated in Fig. 6 where variables $\boldsymbol{A}, \boldsymbol{\nu}, \boldsymbol{\phi}$, and $\vec{\mathbf{p}} = \mathbf{a}\hat{i} + \mathbf{b}\hat{j}$ represent the carrier amplitude, frequency, phase, and polarization field properties respectively, and can be time-dependent, e.g., $\boldsymbol{\phi} = \boldsymbol{\phi}(t)$:

$$\vec{\mathbf{E}}_s(t, \boldsymbol{A}, \boldsymbol{\nu}, \boldsymbol{\phi}, \vec{\mathbf{p}}) = A(t)\cos(2\pi\boldsymbol{\nu}t + \boldsymbol{\phi})\vec{\mathbf{p}} \quad [\mathrm{V/m}], \tag{7}$$

where $P(t) = |A(t)|^2/(2z_0)$ is the power in the field envelope in W, and z_o is the impedance of the medium, which is 300 Ω in free-space. Each of these basic field properties can be modulated either alone or in combination depending on the system needs. The additional dimensions can carry information, for use in multi-dimensional symbol constellations, or simply improve the modulation format.

For example, in narrowband intensity modulated optical systems where stimulated Brillouin scattering (SBS) nonlinearities are a limitation, carrier phase, polarization, and/or frequency can be modulated to expand the optical spectrum beyond the SBS bandwidth of ~50 MHz to mitigate this effect [110,111]. Even if unused, these parameters may need to be controlled, measured, or known at the receiver to achieve optimum performance. For instance, FSO receivers are often single polarization with

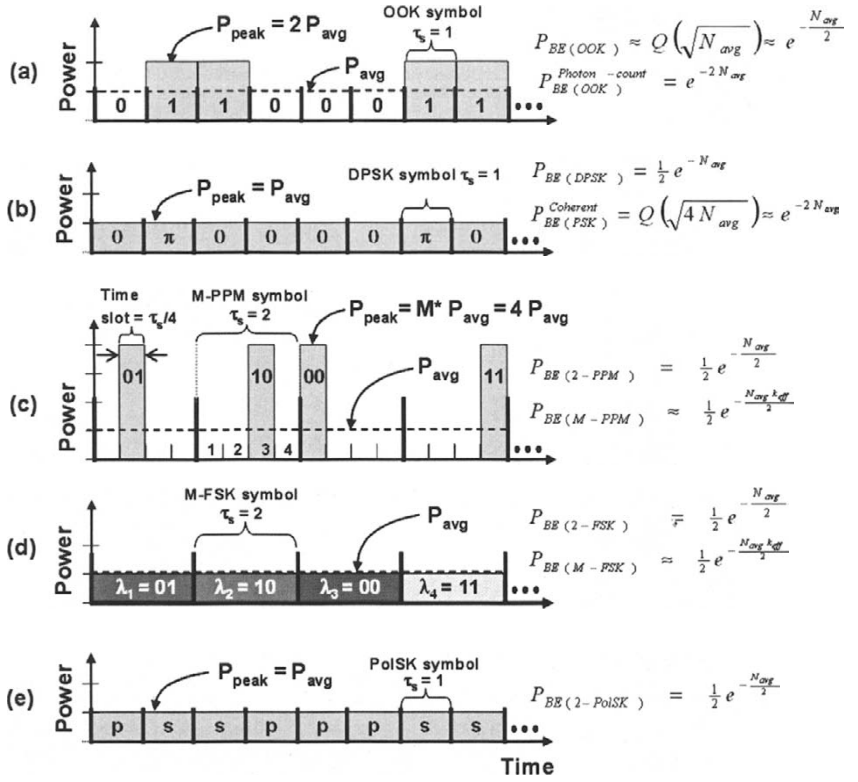

Fig. 7. Commonly used modulation formats (a) OOK, (b) DPSK, (c) 4-PPM, (d) 4-FSK, (e) PolSK with same data, data rate and average power. Also shown on the right-hand side is the approximate bit-error probably for the modulation formats (a)–(e) with ideal optically preamplified receivers [except for photon-counting OOK in (a) and coherent PSK in (b)].

tight spectral filtering to allow for efficient diplexing of transmit and receive signals [46], and/or to reduce detected noise. This requires proper alignment of transmit and receive wavelength and polarization, either by stable open loop control of both the TX and RX, tracking and compensation by the RX, feedback between the TX and RX, or a combination thereof.

2.2.1. Overview of FSO Modulation Formats and Sensitivities

While there are many modulation possibilities, the most common modulation formats considered for FSO links include on-off-keying (OOK), differential-phase-shift-keying (DPSK), phase-shift-keying (PSK), and orthogonal modulation formats such as M-ary pulse-position modulation (M-PPM) and frequency-shift-keying (M-FSK) illustrated in Fig. 7.

2.2.1.1. *On-Off-Keying (OOK)*

The predominant form of signaling used in optical communication systems today is on-off key (OOK) because the transmitter and receiver hardware are relatively simple and fiber optic networks generally operate at high signal-to-noise ratios with small dynamic range requirements and well controlled signal levels at the receivers. Also known as binary amplitude-shift-keying, OOK is a form of intensity modulation (IM) in which binary information is represented by the presence or absence optical signal energy within the symbol. At the receiver, the "1" or "0" logical decision is determined by the received symbol energy being above or below a predetermined threshold. The optimum threshold balances the probability of 0 and 1 errors, and is dependent on the received signal power and noise statistics, requiring adaptive thresholds for best performance over a fluctuating channel [20,39,112,113]. Regardless of the accuracy of optimum OOK threshold predictions based on theoretical calculations, the threshold and other operational parameters can be optimized with near-real-time BER feedback that is readily available with commercial FEC hardware [114,115]. Alternatively, modulation formats that inherently establish a threshold, such as antipodal or orthogonal signaling (e.g., PSK, DPSK, FSK, PPM) can be used to eliminate the need for adaptive thresholding.

For an ideal shot-noise-limited optically-preamplified receiver, the OOK error probability is approximately given by [18,20,23,37–39]

$$P_{\mathrm{BE(OOK)}} \approx Q\left(\sqrt{N_{\mathrm{avg}}}\right) \approx \frac{1}{2} e^{-N_{\mathrm{avg}}/2}, \tag{8}$$

where N_{avg} is the SNR, equal to the average number of photons-per bit (PPB) received, and the Q-function is

$$Q(z) = \frac{1}{\sqrt{2\pi}} \int_{z}^{\infty} e^{-x^2} dx = \frac{1}{2} \mathrm{Erfc}\left(\frac{z}{\sqrt{2}}\right) = \frac{1}{2}\left(1 - \mathrm{Erf}\left(\frac{z}{\sqrt{2}}\right)\right). \tag{9}$$

The Erf( ) and Erfc() functions are the error function and complementary error function, respectively [18, 20]. The 10^{-9} bit-error rate corresponds to 36 PPB, slightly lower than the right-hand approximation in Eq. (8) which results in ~40 PPB. When implemented with non-return-to-zero (NRZ) waveforms with an equal probability of 1's and 0's, the peak power is equal to twice the average. Pulsed return-to-zero or RZ waveforms can be used with all the modulation formats mentioned above, with the peak-to-average power ratio varying inversely with the duty-cycle.

Note that the analytical BER expressions in Eqs. (8)–(11) and (13)–(14) assume Gaussian noise statistics [18,39,116–118], which do not accurately reflect the Poisson noise statistics of the received input signal (see section 2.3.5), nor the statistics of the preamplified signal detected by the square-law photodetector. The statistics for a sinusoidal electric field with narrow-band additive white Gaussian noise after square-law detection for 0 and 1 signals are no longer Gaussian, they are Rayleigh and Rician, respectively [116,119,120]. However, detailed numerical evaluation of preamplified OOK performance assuming these distributions yields ~38 PPB at 10^{-9} BER [36, 38], compared to ~36 PPB with the Gaussian approximation. An additional correction includes the exact statistics based on the quantum-mechanical description of the

physical photon-detection process which are the degenerate Bose–Einstein probability distribution for 0's and the noncentral negative binomial distribution (NNB) also called the Laguerre distribution for 1's [47,121–126]. Nevertheless, the Gaussian approximation yields straightforward analytic BER expressions that provide a reasonable estimate of receiver sensitivity, with SNR estimates for a particular BER accurate to within ~1 dB relative to calculations based on with exact statistics [126,127].

2.2.1.2. Differential-Phase-Shift-Keying (DPSK)

Differentially encoded PSK [DPSK, see Fig. 7(b)] has received considerable attention by the FSO community and the telecom industry due to a ~3 dB sensitivity improvement over commonly used on-off-keying, and reduced peak power which mitigates nonlinear effects [24,25,41,128–133]. NRZ-DPSK can be implemented with a constant envelope, so that the peak power is equal to the average. Binary information is conveyed with two orthogonal symbols represented by the relative phase between two differentially encoded bits: a "0" represented by no-phase change and a "1" by a π phase difference, (or visa-vera). This phase modulation also tends to suppress the optical carrier, which can be advantageous in systems limited by slow optical nonlinearities such as SBS (see section 3.5.5). Typically, adjacent bits are differentially encoded with a time-separation τ_d of one symbol duration or a bit period, τ_{bit}, but this can generally be extended to an integer number n of symbol periods, i.e., $\tau_d = n\tau_{\text{bit}}$. This can provide some flexibility in implementing simplified multi-rate and multi-channel receivers (see, e.g., [134–136]), a subject discussed further in section 5.2.

DPSK's utility has been established with many long-haul fiber-optic experiments demonstrating multiple Tbit/s over ~10,000 km fiber spans with hundreds of WDM-DPSK channels (λs), e.g., [137–141]. Despite significant benefits, DPSK has not yet been widely deployed in operational systems, in part because the benefits of DPSK come at the cost of increased complexity over OOK, requiring a phase modulator and differential precoding in the transmitter, and an optical delay-line interferometer (DI) demodulator and balanced detection in the receiver in order to derive maximum benefit. The DPSK RX design is discussed further in section 5.2. Performance can also be degraded significantly by differential chirp [132,142]. However, DPSK is much easier to implement than coherent PSK, which requires a stable, narrow-linewidth local oscillator phase-locked to the received signal necessary to implement the homodyne receiver. In contrast, DPSK can be demodulated through a self-homodyne process of comparing the relative phase of the differentially encoded symbols. This eliminates the need for the LO and associated phase-locking challenges, and relaxes the need for narrow linewidth laser sources, since the self-homodyne process only requires phase-coherence for the time duration between the differentially encoded symbol. The theoretical error-rate for optically preamplified DPSK is

$$P_{\text{BE(DPSK)}} = \frac{1}{2} e^{-N_{\text{avg}}}, \tag{10}$$

corresponding to 20 PPB @ 10^{-9} BER [38]. The nearly 3 dB sensitivity benefit of DPSK over OOK can be viewed as a result of the differential encoding, which utilizes energy from the two symbols to determine the relative phase for one bit of information.

Optical differential quadrature phase shift keying (DQPK) [132,143–147] and duobinary modulation [148–152] are spectrally efficient modulation formats related

to DPSK that have recently been considered for use over long-haul fiber links, where dispersion is often a dominant limitation. However, dispersion and channel bandwidth are generally not limiting factors in free-space links, so the combination of reduced photon-efficiency and increased complexity make these modulation formats less attractive than DPSK for use in free-space applications.

2.2.1.3. Phase-Shift-Keying (PSK)

As noted above, coherent PSK has challenging LO and signal alignment requirements [20,153–155] needed to determine the absolute phase of the optical field. In addition, there are practical tradeoffs between PSK RX bandwidth and sensitivity, which are especially noticeable since, unlike preamplifier receivers, coherent receivers are not easily scaled to higher data rates via wavelength division multiplexing (WDM). For the additional complexity, coherent (binary) PSK provides among the best theoretical RX sensitivity, with

$$P_{\mathrm{BE(PSK)}} = Q\left(\sqrt{4N_{\mathrm{avg}}}\right) \approx e^{-2N_{\mathrm{avg}}}, \tag{11}$$

corresponding to 9 PPB RX sensitivity @ 10^{-9} BER [20,156]. But in practice the high-sensitivity potential of optical PSK has not been realized. As seen in Fig. 61, the best PSK demonstration reported uncoded sensitivity about 2.5 dB from theory at 4 Mbps [157]. In the Gbit/s regime the best PSK performance degraded to ~6 dB from theory at ~6 Gbps and ~9 dB from theory at ~8 Gbps [158], providing little benefit over optically preamplified DPSK, which is a WDM-scalable approach with numerous demonstrations of comparable or better performance in terms of sensitivity and data rate [24,25,41,128–130,133,159]. The nearly 4× sensitivity benefit PSK has over OOK is in part due to binary PSK being an antipodal format, in which a "0" is represented by signal field of −1 (π phase) and a "1" is represented by a 1 (phase of 0), so that 2-PSK has twice the signal-distance of OOK. The other 2× advantage can be viewed as a result the coherent detection process, which detects the peak power of the received optical carrier, that is twice the average power measured in intensity modulation formats.

2.2.1.4. M-ary Orthogonal Modulation

To improve receiver sensitivity, high-order M-ary orthogonal formats [18] such as M-PPM, M-FSK [160–162], and hybrid combinations can be used (see also section 5.3). While not spectrally efficient, these formats can significantly improve photon-efficiency. Two symbols m and n are considered orthogonal if

$$\int_0^{\tau_s} s_m(t)s_n(t)dt = \delta_{mn}, \tag{12}$$

where τ_s is the symbol period and δ_{mn} is the Kronecker delta function. The parameter M refers to the symbol alphabet or constellation size, with the information per symbol increasing as $k = \log_2(M)$ and bandwidth increasing with M. This results in a spectral efficiency [Bit/s/Hz] that varies as $\log_2(M)/M$ shown in Fig. 3, which clearly illustrates the trade between bandwidth (spectral efficiency) and SNR (photon

efficiency) noted by Shannon (see Fig. 1). For large M, ideal performance approaches Shannon-limited capacity [17,18,23]. Orthogonal modulation formats also establish their own threshold, with the optimum decision based on the largest sample within the symbol set. This enables the system to operate optimally over wide and rapid changes in signal level, without the need for adaptive thresholds that are necessary for OOK.

The bit-error rate for optically-preamplified binary-orthogonal modulation, e.g., 2-PPM is given by

$$P_{\mathrm{BE(2-ORTH)}} = \frac{1}{2} e^{-\frac{N_{\mathrm{avg}}}{2}}, \tag{13}$$

with sensitivity comparable to OOK and exactly twice that of DPSK, corresponding to 40 PPB at 10^{-9} BER. For M-ary orthogonal modulation, no simple closed form expression exists. An accurate but computationally challenging expression for the ideal optically preamplified symbol-error-rate is given by[163]

$$P_{\mathrm{SE(M-ORTH)}} = \int_0^\infty f_0(x_0) \left\{ 1 - \left[1 - \int_{x_0}^\infty f_1(x_1) dx_1 \right]^{M-1} \right\} dx_0, \tag{14}$$

where the Rician distribution [119]

$$f_j(x_j) = \frac{1}{N_{\mathrm{sp}}} e^{-\frac{x_j + N_{\mathrm{avg}j}}{N_{\mathrm{sp}}}} I_0 \left(2 \frac{\sqrt{N_{\mathrm{avg}j} x_j}}{N_{\mathrm{sp}}} \right), \tag{15}$$

is the probability density function for sample x_j, where x_1 represents a sample with both signal and noise, and x_0 represents the samples with noise only, and N_{sp} is the spontaneous emission factor related to the noise figure of the amplifier. For an ideal amplifier, $N_{\mathrm{sp}} = 1$. The function I_0 is the modified Bessel function of the first kind of zero order. Robinson, in [163] provides an excellent derivation of the optically-preamplified symbol-error rate in Eq. (14) along with simplified techniques for evaluating the expression.

For each symbol error, there is still a chance that some of the bits within the deocoded symbol are correct. Assuming that each symbol is transmitted with equal probability, the bit-error probability is

$$P_{\mathrm{BE(M-ORTH)}} = \left(\frac{M/2}{M-1} \right) P_{\mathrm{SE}} \quad \underset{M \to \mathrm{large}}{\Longrightarrow} \quad \frac{P_{\mathrm{SE(M-ORTH)}}}{2}. \tag{16}$$

Qualitatively, the M-ary orthogonal bit-error probability can be related to the binary BER expression in (13) by

$$P_{\mathrm{BE(M-ORTH)}} \approx \frac{1}{2} e^{-\frac{N_{\mathrm{avg}} k_{\mathrm{eff}}}{2}}, \tag{17}$$

where k_{eff} is related to the bits-per-symbol given in Eqs. (18)–(20):

$$k_{\mathrm{eff}} = k \left(1 - \frac{k-1}{k N_c} \right), \tag{18}$$

$$N_c = N_{\mathrm{avg}} \left(1.75 - \frac{1}{1 - e^{-T_k (N_{\mathrm{avg}} - 1)}} \right), \tag{19}$$

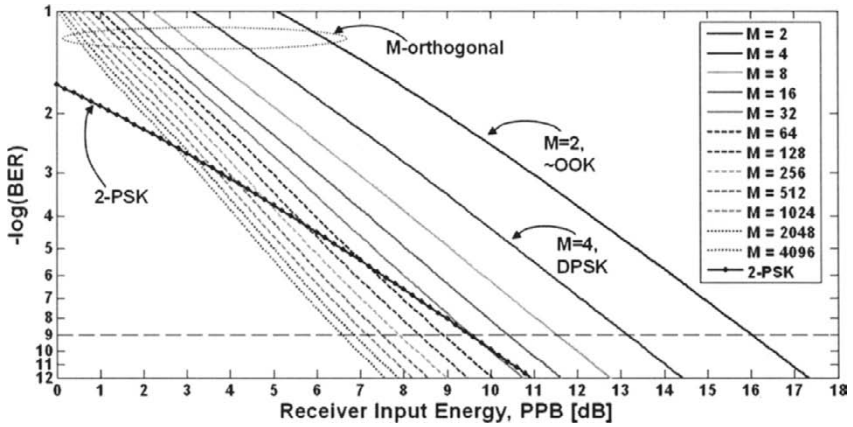

Fig. 8. BER curves for 2-PSK and optically preamplified M-ary orthogonal modulation.

$$T_k = 0.4\left(1 - \frac{4}{1 - e^{-(k-5)}}\right). \tag{20}$$

For small $M$and large received signal (N_s), $k_{\text{eff}} \to k$, yielding a receiver sensitivity of about 40 PPB/$\log_2 M$ or 40/k at 10^{-9} BER. This simple approximation overestimates the RX sensitivity by less than ~1.25 PPB, which for $M < 64$ at 10^{-9} BER is accurate to $\sim \frac{1}{2}$ dB with the accuracy improving at lower error rates. For increased accuracy without much computational complexity, Eq. (17) can be used to calculate M-ary othogonal BER performance with ~0.1 dB accuracy.

Bit-error rate curves as a function of photons/bit (in dB) are shown in Fig. 8 for ideal 2-PSK and optically premplified M-ary orthogonal modulation. Note that theoretical preamplified OOK and DPSK BER performance is similar to binary and 4-ary othogonal modulation, respectively. Without additional coding, 32-orthogonal modulation has comparable performance to ideal 2-PSK at 10^{-9} BER. At higher 10^{-3} BER, near the FEC threshold for enhanced 255/329 Reed-Solomon codes, 2-PSK RX sensitivity is as good as to 1024-orthogonal. Above 10^{-2} BER, ideal 2-PSK has a clear sensitivity advantage over preamplified M-ary orthogonal modulation. However in practice, at high rates above a Gbit/s (see Fig. 61), reported coherent-PSK [158,164–166] suffers ~5 dB greater implementation penalties than preamplified RXs [13,15,128–130,133,135,159], eliminating much of the theoretical benefit. While improved PSK designs may achieve the anticipated sensitivities, based on existing demonstrations, preamplified RX designs have exhibited superior sensitivity and data-rate, as well as WDM scalability [135,138,139,149,167].

2.2.1.5. M-ary Pulse-Position Modulation (M-PPM)

Pulse-Position Modulation (PPM) is a form of orthogonal signaling that uses the same transmitter and receiver hardware used for OOK. In M-PPM [2,15,26,43,168–171], k-bits of information are encoded by the position of an optical pulse within an M-slot symbol, (Fig. 7c). As a result, M-PPM waveforms have a low duty cycle, equal to $1/M$,

making it well suited for use with EDFA-based average-power-limited transmitters, but a poor choice for use with semiconductor-based peak-power-limited transmitters [172]. For M-PPM, the bandwidth expansion directly impacts the modulation bandwidth and associated transmit/receive electronic bandwidth

$$B_{\mathrm{E(M-PPM)}} = \frac{MR_{\mathrm{Data}}}{\log_2 M} = \frac{MR_{\mathrm{Data}}}{k} = S, \tag{21}$$

with associated symbol rate

$$R_{\mathrm{sym(M-PPM)}} = \frac{R_{\mathrm{Data}}}{\log_2 M} = \frac{S}{M}. \tag{22}$$

While electrical bandwidth limitations may limit the maximum slot-rate S for a single M-PPM channel, the high-speed 10 and 40 Gbps electronics developed for the telecom industry make it relatively easy to implement at reasonably high data-rates. For example, by transmitting 16-PPM at a slot-rate S = 10 Gslot/s, 2.5 Gbps can be delivered with symbol rate of 625 Msym/sec.

The low duty cycle of M-PPM waveforms can also lead to optical nonlinearities, which can limit the peak transmit power, a subject discussed further in section 3.5.5. On the receive side, M-PPM requires two clocks to be acquired, a symbol clock (R_{sym}) and slot clock at rate $S = MR_{\mathrm{sym}}$ [173]. Clock acquisition can be challenging for large M since received power at the clock frequencies varies as $\sim(1/M^2)$, which may require embedded synchronization bits within the data as M gets large [44].

M-PPM has several practical advantages over OOK and DPSK. As a result of the low duty cycle, PPM has less spectral content at low frequencies and consequently has a smaller fractional bandwidth than OOK and DPSK. Fractional bandwidth (B_f) is a factor used to classify signals as narrowband, wideband, or ultra-wideband and is often defined by the ratio of bandwidth at –10 dB points to center frequency [174] given by

$$B_f = \frac{\mathrm{BW_{10dB}}}{(f_h + f_l)/2} = \frac{2(f_h - f_l)}{(f_h + f_l)}, \tag{23}$$

where f_h and f_1 are the highest and lowest cutoff frequencies (at the –10 dB point) of the spectrum. For RF signals, $B_f > 20\%$ is considered ultra-wide band. However for optical communications signals, the spectrum of the RF drive spectrum typically has $B_f > \sim 200\%$ as shown in Fig. 9. For such broadband signals, a more relevant parameter is the high-low bandwidth ratio,

$$B_r = f_h/f_l. \tag{24}$$

For a pseudo-random bit sequence (PRBS) of 10 Gbps NRZ-OOK waveforms, B_r extends from a practical lower bound of ~10 kHz to ~10 GHz, or six decades. In contrast, the spectra for M-PPM waveforms operating at the same data rate span less than two decades, reducing B_r by over 4 orders of magnitude, despite having more high-frequency content (Fig. 9).

This relaxes the performance requirements on wide-band electronic amplifiers and drivers. In addition, since the longest string of consecutive 1's is two (from two adjacent PPM symbols), pattern-dependencies in transmit and receive hardware are reduced, making it easier to generate and receive high-quality waveforms. These benefits can also extend to the ultra-high-speed domain, where the reduced pattern dependence

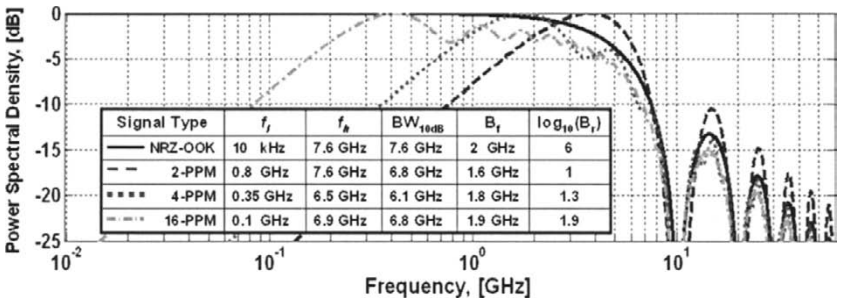

Fig. 9. Calculated spectra for square waveforms used in OOK and 2-PPM, 4-PPM, and 16-PPM modulation for with a fixed 100 psec pulse width [175]. The M-PPM waveforms have a smaller fractional-bandwidth (B_f) and a significantly smaller bandwidth ratio, ($B_r = f_h/f_l$) than OOK. For the OOK spectrum, f_l is set to 10 kHz, which is a common low-frequency specification for applicable broad-band electronics. Note that for a constant data rate, the M-PPM spectra are broadened by a factor of $M/\log_2(M)$, which increases $\mathrm{BW}_{10\mathrm{dB}}$ but does not impact B_r.

has improved the performance of all-optical demultiplexers [163,176]. M-PPM also benefits from the sequential nature of the symbol set, which enables a single-chain of drive electronics and associated filters to generate and receive the complete symbol set. This simplifies and improves decision process, since it is easier to make a fair comparison of the M-samples within a symbol to determine which is the largest.

2.2.1.6. *M-ary Frequency-Shift Keying (M-FSK)*

The FSK symbol set consists of M frequencies or wavelengths and like PPM, conveys $k = \log_2(M)$ bits of information per symbol (Fig. 7d). Since FSK transmits a different frequency for each symbol, modulation bandwidth and associated transmit/receive electronic bandwidth requirements are actually less than or equal to the data rate:

$$B_{\mathrm{E(M-FSK)}} = \frac{R_{\mathrm{Data}}}{\log_2 M} = R_{\mathrm{sym(M-FSK)}}. \tag{25}$$

The bandwidth expansion in M-FSK instead comes from the spread of M-frequencies used, which generally requires a parallel M-channel receiver design. This adds some complexity over the serially generated and received PPM waveforms mentioned above, since any imbalances in power or waveform fidelity in the M TX or RX parallel channels can degrade performance. As with DPSK, FSK waveforms can have a 100% duty cycle, making it well suited for use with average or peak power-limited transmitters. It can be implemented using a single frequency-modulated (FM) source with binary- [162,177–179] or M-ary modulation [160,180], or using external modulation and subcarrier multiplexing (SCM) [181,182]. These approaches generally require relatively tight wavelength spacing due to transmitter or receiver limitations [161]. However, with the use of independently-modulated wavelength-multiplexed-sources, or fast-tunable wideband DBR sources [180], arbitrarily wide wavelength spacing can be used. For parallel TX and RX designs, the duty-cycle per channel is

roughly $1/M$, assuming all symbols are equally likely, which leads to a similar reduction in the bandwidth-ratio and associated benefits that were described for M-PPM above.

2.2.1.7. *Polarization-Shift-Keying (PolSK)*

Binary-polarization-shift keying (2-PolSK) [183] can be used to extend the symbol set in the M-ary orthogonal formats described above by a bit (one bit per symbol), i.e., $M \rightarrow 2M$ and $k \rightarrow k + 1$, without increasing peak power or electrical bandwidth requirements per channel. The PolSK symbols encode binary information in two-orthogonal polarization bases, such as left and right-hand-circular polarizations or "s" and "p" linear polarizations, which can be implemented using combinations of phase modulator and parallel intensity modulators [184]. The performance of generalized M-PolSK has recently been evaluated for hybrid combinations with M-FSK [185] and multidifferential phase (DPSK) and amplitude modulation (ASK) [186,187]. However, for optimal sensitivity, an orthogonal M-ary signal set as defined in Eq. (12) is required. Like FSK and DPSK, PolSK is well suited for use with average or peak power limited transmitters, since it can operate with a 100% duty cycle. Further discussion of hybrid-modulation formats, performance, and implementation benefits is given in section 5.3.

2.3. *Comparison of RF and Optical Properties*

Until this point, the description of the EM field has been qualitative. However, there are many distinguishing characteristics between the RF carrier and the optical carrier that become apparent as the specific wavelengths are compared. A summary of values for a 1-cm microwave carrier and a 1-μm optical carrier at the same power level is shown in Table 1.

Table 1. Comparison of 1 cm RF and 1μm optical carrier characteristics.

	Microwave-RF	Optical	Units
λ	1.0×10^{-2}	1.0×10^{-6}	m
ν	3.0×10^{10}	3.0×10^{14}	Hz
$h\nu$	2.0×10^{-23}	2.0×10^{-19}	J
Power	1.0×10^{-9}	1.0×10^{-9}	W
r_{ph}	5.0×10^{13}	5.0×10^{9}	Photons/s
$r_{\mathrm{ph}} \times 10^{-9}$	5.0×10^{4}	5.0	Photons/ns
$r_{\mathrm{ph}} \times 10^{-10}$	5.0×10^{3}	0.5	Photons/100 ps

2.3.1. Diffraction

The factor of 10,000 between RF and optical wavelength leads to a substantial difference (10^8 or 80 dB) in free-space (vacuum) diffraction loss estimated in Eq. (6). Since diffraction loss increases with the square of the link distance-wavelength product, for equal TX and RX areas, the optical carrier can propagate a factor of 10,000 further before incurring the same loss, a primary reason for considering optical communications

for ultra-long-haul free-space communications. The optical signal is much is more directional and concentrated in the far field, delivering more signal to the target RX. But it does this at the expense of more challenging PAT, in contrast with RF systems which are more omni-directional.

The propagation losses in free-space grow as the square of the distance [see Eq. (6)] in contrast with fiber, in which the losses are exponential. The link loss for 12%, 100%, and 1000% free-space distance multipliers are 1, 6, and 20 dB, respectively. The channel loss for some potential planetary links, relative to an Earth to geosynchronous orbit link), are shown in Table 2 below. To highlight the difference between square-law diffraction and exponential losses, a link from Earth to Mars connected using low loss fiber with attenuation coefficient 0.2 dB/km would result in a loss of 80 million dB [104].

Table 2. Approximate maximum distance from Earth and relative diffraction loss for free-space propagation between the Earth and geosynchronous orbit, the Moon, Mars, Jupiter, and Saturn.

Orbit	Distance [km]	Relative Channel Loss [dB]
Geo	40,000	0
Moon	400,000	20
Mars	400,000,000	80
Jupiter	1,000,000,000	88
Saturn	1,600,000,000	92

Note that while pointing, acquisition, and tracking (PAT) is outside the scope of this paper, the TX and RX design can greatly facilitate PAT functionality. For example, prior to acquisition, the received SNR is generally poor due to low signal strength and since the benefits of filtering may need to be established. Such filtering may occur in several independent domains, e.g., spatial, temporal, spectral, and polarization; and acquisition or alignment in each may be necessary in order to acquire the link. Since the spatial acquisition generally poses the most fundamental challenge and time to acquire in FSO systems, streamlining acquisition or alignment in the other domains by providing fast clock recovery [188] recombined with stable TX polarization and wavelength that can be quickly aligned with the RX, can greatly expedite the overall acquisition process. PAT can also be simplified by increasing the number of RX spatial modes [1,2,47,189], by reducing tracking requirements and/or sensitivity to platform jitter, although this generally comes at the cost of increased RX noise.

2.3.2. Optical Detection

In contrast with RF electronics and detectors, which can directly detect the EM field and generally have bandwidths exceeding that of the carrier frequency, optical detectors are generally "square law detectors" with functional bandwidths that are a small fraction of the carrier frequency [190]. This means output is proportional to the square of the field, (proportional to the power intensity), with little direct dependence on optical phase, frequency, or polarization. Optical detectors can be extremely high speed, with bandwidths from DC to > 50 GHz. Because of optical detector bandwidth limitations, practical detectors have a response time which is generally much slower than the

~femtosecond (10^{-15}s) period of the optical field, so these detectors respond to the time average square of the field. The detectable low-frequency optical power is given by

$$P_s(t) = \frac{\left\langle \left| \vec{\mathbf{E}}_s(t) \right|^2 \right\rangle}{Z_0} = \left\langle \left| \frac{A(t)\cos(2\pi\nu t + \phi)\vec{\mathbf{p}}}{Z_0} \right|^2 \right\rangle$$
$$= \frac{|A(t)|^2 \left\langle \cos^2(2\pi\nu t + \phi)\vec{\mathbf{p}} \right\rangle}{Z_0^2} = \frac{|A(t)|^2}{2Z_0^2}, \quad [\mathrm{W/m^2}] \qquad (26)$$

where the time average of $\langle \cos^2() \rangle = \frac{1}{2}$. In high-speed designs, Z_0 is typically 50Ω in order to match RF waveguide impedance to minimize reflections.

In view of the intensity or power dependent response of optical detectors, the most commonly used optical modulation formats use intensity-modulated direct-detection (IM-DD) modulations. An example on-off-keying (OOK), in which the information is encoded by the presence (a logical "1") or absence (a logical "0") of the optical signal. In order to provide access to the phase, frequency or polarity of the electric field, more complex receivers which employ optical preprocessors are required. Preprocessors include wavelength dependent filters, interferometers, polarization beam splitters, and coherent measurements enable measurement of the electric field [153,157,160,161,179,191–195]. Further discussion of detector technologies, performance, and impact of noise sources is given in sections 2.3.5–2.3.7 and 4.

2.3.3. Technology Limitations

For some of the same reasons that fiber-optic communications presently dominates long-haul high-rate guided-wave applications, namely low channel losses and wide available bandwidth (with little or no regulatory limitations), FSO communications has a bright future. As summarized in Table 3 the technical advantages are considerable. For instance, there are roughly 4 orders of magnitude more bandwidth accessible via readily available WDM and ultra-wide-band, high-gain optical amplifiers. These optical technologies enable the trade of spectral-efficiency for improved photon-efficiency (as suggested in section 1.1), while maintaining the ability for scalable high-rate communications.

FSO terminals can also leverage robust wideband fiber-optic connectivity to permit modular construction [46] that is insensitive to electromagnetic interference (EMI).

On the other hand, RF technologies are generally more mature and have extensive ability to integrate. In terms of average TX power efficiency, RF transmitters have a ~3 to 6 dB advantage over amplifier-based optical transmitters, although this deficit is mitigated by the average-power-limited properties of optical amplifiers that enable the flexible use of variable-duty-cycle waveforms without reducing TX efficiency. Free-space RF communication is better suited for omnidirectional applications and provide improved reliability for links where clouds may be a limitation, However, for long-haul-high-rate free-space applications, especially space-based links, such benefits are overshadowed by the many advantages of optical technologies summarized above. Example link budgets in section 2.4, Table 4 based on fundamental carrier characteristics and in section 5.5, Table 15 based on currently available technologies illustrate these considerations.

Table 3. Comparison of RF and optical wavelength-dependent characteristics and technical limitations. *Note other optical bands are available, e.g., 0.85, 1 and 1.3 μm. The table includes references for efficient optical amplifiers at 1 μm [198, 204], which are generally ~1.5 to 2 times more power efficient than their 1.5 μm counterparts.

Parameter	RF	Optical
Wavelength (frequency)	~ 1 cm, (30 GHz)	1.5μm (200 THz)*,
RX noise limitation [dBm/Hz]	Thermal (KT = –174)	Shot ($h\nu$ = –159)
Bandwidth limitations	Government Regulated	Unregulated
	$\ll$ 30 GHz	$\ll$ 200 THz
State-of-the-art amplifiers		
Gain	10 dB	50 dB
Bandwidth	~ 50 GHz	~ 50 THz
NF	5 dB	3 dB
Transmitter Characteristics	Peak power limited	Average power limited
Integrability	Massive	Limited
Modulation Formats	Sophisticated	Basic
Efficiency (peak)	~ 50–80% [196]	~ 5–20% [172,197–200]
Efficiency (average)	~ 5%–46% [196,201–203]	~ 5–13% , 21% [172,197–200]
Waveguide Characteristics		
Type	Coax	Fiber
Bandwidth	~ 20 GHz	~ 50 THz
Loss	100 dB/km	0.2 dB/km
Free-space channel characteristics		
Diffraction Angle	10^{-2}/D	10^{-6}/D
Cloud penetration	Good	Poor

2.3.4. Average and Peak Power Limited Transmitters

RF transmitters are generally peak power limited, which means that there is an upper limit on the peak output power they can deliver (e.g., a maximum voltage). As a result, in order for RF systems to deliver maximum average power (the relevant metric for assessing communication performance), they need to operate with high ~100% duty cycles, which places limitations on the choice of modulation formats and waveforms. Furthermore, in order to maintain maximum transmitted power and operate at multiple rates, peak-power-limited systems need to alter the transmitted pulse width and shape so that the high duty cycle is preserved. In order to maintain optimum communication performance with this constraint, different receiver filters are necessary for each bit-rate, increasing RX complexity.

In contrast, optical transmitters are typically average power limited, which means that the average output power is independent of the transmitted waveform shape or duty-cycle. This provides significant advantages over peak-power limited RF systems, enabling optical communications systems to use aggressive pulse shaping techniques, and variable-duty-cycle modulation formats that can approach optimal performance

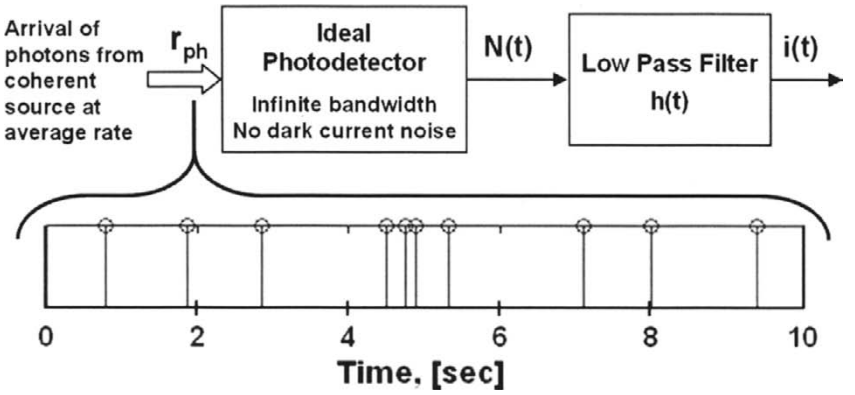

Fig. 10. Photodetection modeled as a fast noiseless ideal photon counting detector that generates a stream of detection events which form a discrete count $N(t)$ that is a function of the photon rate $r_{\rm ph}$, detection efficiency, and observation time-window described below. The detected impulse stream is then followed by an electrical filter with impulse response $h(t)$, that converts the detected events to a photocurrent.

over a wide range of rates while using simple high-sensitivity multi-rate receiver designs [10–15]. This subject is discussed further in sections 3 and 5.

2.3.5. Quantum Noise Limitations

When considering RF and optical quantum characteristics, the granularity of the photon flux is much more noticeable at optical frequencies, with rate corresponding to

$$R_{\rm ph} = P/(h\nu) \quad [\text{photons/s}], \tag{27}$$

where P is the optical power in W, and $h\nu$ is the photon energy in Joules. For a large number of photons per observation interval, the shot noise is relatively small relative to the average, and the photon flux appears continuous. However, for low photon flux, the shot noise or graininess in the interarrival times becomes apparent, as illustrated in Fig. 10. For the case of 1 nW of optical power and a 100-ps observation window in Table 1, on average, only $\frac{1}{2}$ a photon is detected, which means that statistically, no photons are detected in half the observations. Such quantum fluctuations in the detected photon counts, are fundamentally part of the optical signal, and therefore impose the ultimate limitation on optical receiver performance. This is in sharp contrast with RF receivers, which are typically dominated by thermal noise in the receiver. The impact of quantum and thermal noise on communication performance is discussed in further detail in references [20,121,127,190,205–207].

The statistics of photon arrivals for a coherent state, e.g., a laser source operating far above threshold, are Poisson [121,127] —with characteristics described in Eqs. (28)–(32) and illustrated in Fig. 11. The Poisson distribution in (28) gives the probability of detecting n photons in a time interval T given the average number of photon arrivals per interval is $< n >= N_{\rm avg}$:

$$P[n\,|N_{\text{avg}}] = \frac{(N_{\text{avg}})^n\, e^{-N_{\text{avg}}}}{n!} \underset{N\to\text{large}}{=} \frac{e^{-\frac{(n-N_{\text{avg}})^2}{2N_{\text{avg}}}}}{\sqrt{2\pi N_{\text{avg}}}}. \tag{28}$$

The right-hand expression in Eq. (28) is a discrete Gaussian approximation of the Poisson distribution which is accurate for large N_{avg}. As shown in Eq. (29), N_{avg} can be interpreted as the product of the rate of detected photons r_{ph} over observation interval T,

$$N_{\text{avg}} = r_{\text{ph}}T = \frac{\eta P}{h\nu}T = \eta\text{PPB}, \tag{29}$$

where η is detection efficiency, P is incident optical power, $h\nu$ is energy-per-photon, and PPB is the incident number of photons/bit when $T$is the bit period. For a Poisson distribution, the mean number of photon arrivals during the observation window, m, is equal to the variance, σ^2, as shown in Eqs. (30) and (31), which can be derived by twice differentiating the Taylor expansion of e^N [208].

$$m = \langle n\rangle = \sum_0^\infty nP[n\,|N_{\text{avg}}] = \sum_0^\infty \frac{n\,(N_{\text{avg}})^n\, e^{-N_{\text{avg}}}}{(n)!} = N_{\text{avg}}, \tag{30}$$

$$\sigma_{\text{sh}}^2 = \left\langle (n-\langle n\rangle)^2\right\rangle = \sum_0^\infty n^2 \frac{(N_{\text{avg}})^n\, e^{-N_{\text{avg}}}}{n!} - N_{\text{avg}}^2 = N_{\text{avg}}. \tag{31}$$

Accordingly, the SNR (in terms of received electrical power, proportional to detected photocurrent squared), given by[1]

$$\text{SNR} \equiv \frac{\langle n\rangle^2}{\langle \Delta n^2\rangle} = \frac{m^2}{\sigma_{\text{sh}}^2} = N_{\text{avg}} = \eta\text{PPB} \tag{32}$$

is also equal to the mean number of photons received. For the case where the observation interval is one bit duration, N_{avg} is equal to the number of photons/bit. As the mean number increases, the Poisson distribution becomes more symmetric and converges towards a Gaussian, also with equal mean and variance. While not noise free, the statistics of laser light are relatively quiet when compared to single-mode thermal light sources that follow Bose-Einstein statistics [121] shown also in Fig. 11.

From Eq. (32), the SNR for a shot-noise-limited signal can be interpreted as having a signal with N_{avg} photons accompanied by 1 noise photon with energy $h\nu$ Joules, or equivalently with a noise power spectral density:

$$N_{\text{shot}}(\nu) = h\nu \quad [\text{W/Hz}], \tag{33}$$

the shot noise power in 1 Hz of observed bandwidth. For an observation bandwidth of B Hz, the total shot noise power is

$$P_{\text{shot}}(\nu) = h\nu B \quad [\text{W}]. \tag{34}$$

For an ideal noiseless photodetector, the continuous-time photocurrent $i(t)$ generated by detecting a discrete photon stream is described by a random process with mean (signal) and variance (noise):

[1] Note that the SNR can alternatively be defined in terms of received electrical current or voltage rather than power. This alternative definition, commonly used in photon counting applications, yields $\text{SNR}_v \equiv \text{Mean}/\sqrt{\text{Variance}} = \sqrt{N_{\text{avg}}}$.

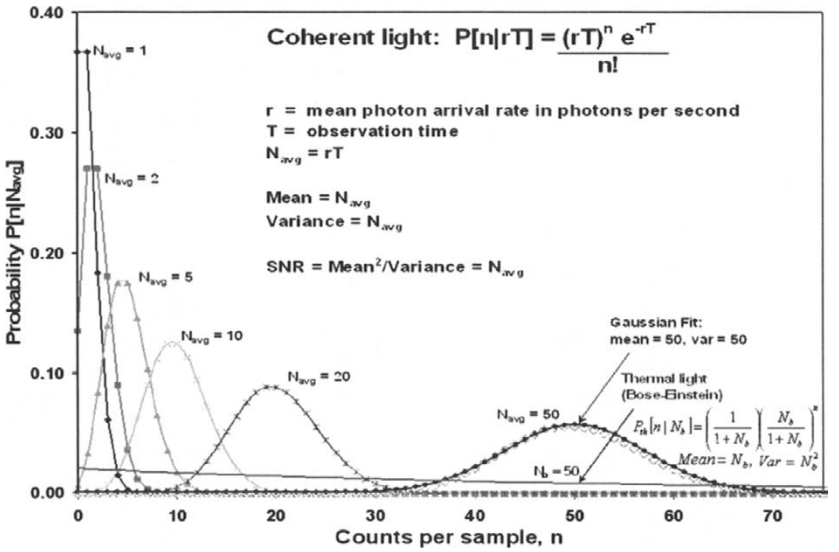

Fig. 11. The discrete Poisson probability distribution function (PDF) gives the probability of detecting n photons given a photon rate $R_{\rm ph}$ and observation window T, or equivalently the average number of photons in the interval $N = R_{\rm ph}T$, shown for $N_{\rm avg} = 1, 2, 5, 10, 20$, and 50. Also shown are a Bose-Einstein PDF (representing the statistics of thermal light in a single mode) with a mean of 50, and Gaussian PDF with mean and variance of 50 ($m = \sigma^2 = 50$).

$$i_{\rm avg}(t) = \langle i(t) \rangle = \frac{\eta q}{h\nu} \int_{-\infty}^{\infty} P(t)h(t-\tau)d\tau \quad [\text{amp}], \tag{35}$$

$$\sigma_{\rm sh}^2(t) = \left\langle (i(t) - i_{\rm avg})^2 \right\rangle = \frac{\eta q^2}{h\nu} \int_{-\infty}^{\infty} P(t)h^2(t-\tau)d\tau \quad [\text{amp}^2], \tag{36}$$

where $h(t)$ is the impulse response of the filtered photocurrent with integrated area normalized to a unit charge [20,127,208]. For example, given a photodetector with a simple exponential electrical impulse response,

$$h(t) = \frac{qe^{-t/\tau}}{\tau} u(t) \longleftrightarrow H(f) = \frac{q}{1 + j2\pi f\tau}, \tag{37}$$

where τ is the filter time constant and $u(t)$ is the unit step function, then with constant incident optical power P,

$$i_{\rm avg} = \frac{\eta q}{h\nu} P = r_{\rm ph} q \quad \text{and} \quad \sigma_{\rm sh}^2 = \frac{\eta q}{h\nu} P \left(\frac{q}{2\tau} \right) = 2q i_{\rm avg} B_e. \tag{38}$$

The far right-hand term in Eq. (38) is the well known general expression for the shot noise power (in units of amps^2) associated with the average photocurrent, where B_e is the noise equivalent power bandwidth of the electrical response over which the noise is observed, i.e.,

$$B_e = \int_0^\infty \left(|H(f)|^2 / H_{\max}\right) df. \tag{39}$$

For the case of the exponential filter in Eq. (37), $B = 1/(4\tau)$. We can solve for the quantum-limited SNR for direct detection by substituting Eq. (38) into Eq. (32), yielding

$$\mathrm{SNR_{DD}} = \frac{m^2}{\sigma_{\mathrm{sh}}^2} = \frac{\eta P}{2h\nu B_e} = \frac{r_{\mathrm{ph}}}{2B_e} = r_{\mathrm{ph}}\tau_{\mathrm{eff}} = N_{\mathrm{eff}}, \tag{40}$$

where τ_{eff} is the effective integration time of the electronic response, equal to 2τ in the example above. Note the similarities with the expressions for photon count in Eqs. (32) and (29) above. As with photon-counting, the direct-detected photocurrent SNR is proportional to the average number of photons N_{eff} received per effective observation interval. For communications, this is often the number of received photons-per-bit, which is reduced by any losses preceding detection. Examples of the impact of discrete photon arrivals and the resulting shot noise generated in the received photocurrent as a function of RX bandwidth are given in Fig. 12.

In practice, it is challenging to achieve quantum-limited performance due to the presence of other noise sources such as thermal noise (section 2.3.7) and dark current, effects that were neglected in the analysis above. Techniques of overcoming these limitations are discussed in sections 4 and 5.

2.3.6. Quantum-limited Direct Detection (DD)

One of the simplest optical receivers is an On-off-keyed (OOK), direct detection receiver. With knowledge of the photon statistics, the impact of shot noise on optical communication performance can be readily observed and quantified for the ideal intensity-modulation TX and direct-detection (IM/DD) photon-counting RX shown in Fig. 13. On-off-intensity-modulated-photons from the transmitter representing a logical "1" and no-photons (e.g., perfect modulation extinction) representing a logical "0" are received by a noiseless photon-counting receiver, (i.e., a Geiger Mode photon counting detector with no dark counts, after pulsing [30–32,209,210] background noise, or other parasitics such as timing jitter and inter-symbol-interference (ISI)).

Without background noise, the optimum decision rule is: if no photons are detected, assume that data $D =$ "0" was sent; and if photons were detected ($\hat{D}$= "1"), assume that $D =$ "1" was sent. For these rules, bit errors only occur if a photon is not detected, e.g., $\hat{D} =$ "0" when $D =$ "1" was sent, which is an "erasure" error. The photon-counting OOK probability of bit error is given by

$$\begin{aligned} P_{\mathrm{BE(OOK)}} &= P[D=0]P[\hat{D}=1|D=0] + P[D=1]P[\hat{D}=0|D=1] \\ &= \frac{1}{2}P[n=0|N] = \frac{1}{2}e^{-r_{\mathrm{ph}}T} = \frac{1}{2}e^{-2N_{\mathrm{avg}}}, \end{aligned} \tag{41}$$

where the number of photons during the observation interval (N) when a "1" is received is twice the average number received ($N = 2N_{\mathrm{avg}}$), which is true for equal probabilities of transmitting "0" or "1" data. From Eq. (41), the 10^{-9} BER is achieved for $N_{\mathrm{avg}} = 10$ photons/bit and corresponds to the "quantum limit" for the ideal IM-DD photon counting OOK, since the only limiting noise source is signal shot noise.

A similar analysis can be performed for ideal photon counting binary PPM, in which each symbol is determined by the location of the optical pulse, with "0" corresponding to photons detected in the first half of the symbol and "1" from the second

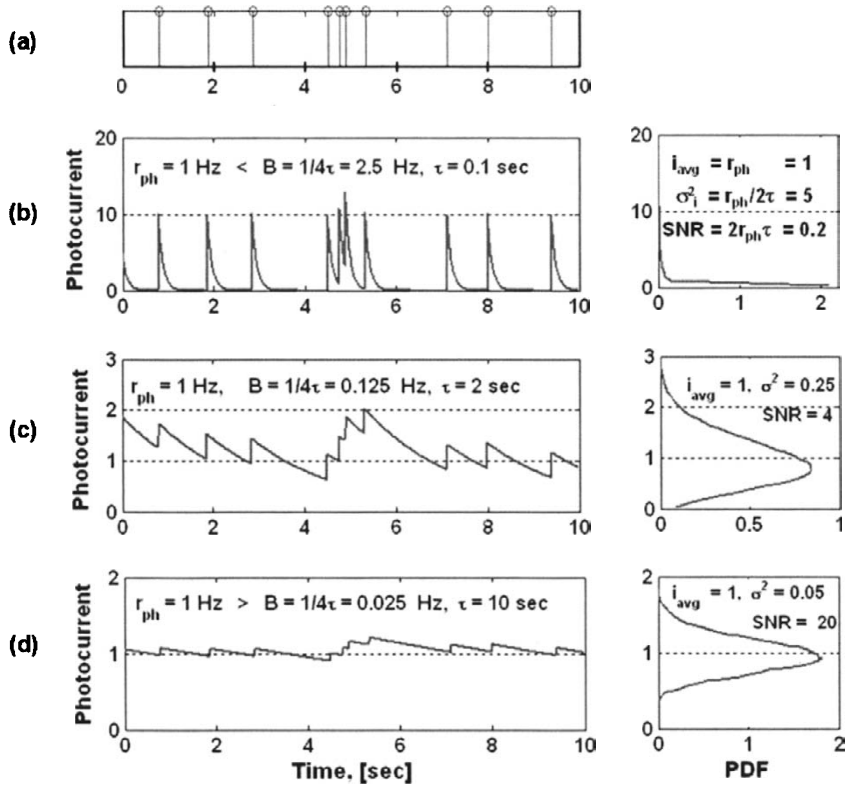

Fig. 12. Photocurrent and shot noise. The granularity of a stream of photons and the resulting variance in the signal is shown as a function of the effective receiver filter bandwidth B_e, where $B_e = 1/4\tau$ for the low-pass filter described in Eq. (37). (a) A discreate Poisson impulse stream of photons with arrival rate $r_{\rm ph} = 1$ photon/s. (b)–(d) left show the continuous-time photocurrent as filter bandwidth B_e is reduced two orders of magnitude from 25 to 0.025 Hz, and (b)–(d) right show the corresponding probability distribution functions (PDFs) of the received photocurrent for each filter bandwidth. The SNR improves as the bandwidth decreases or equivalently as the filter integration time increases. But even with significant filtering in which multiple photons are detected within the filter time constant, the (shot) noise added by the random arrival of discrete photons is apparent. Note that for simplicity, the units of photocurrent have been normalized per unit charge.

half. Bit errors in this ideal photon-counting system only occur when no photons are received. In this case, a "coin flip" is used to decide (arbitrarily) which slot is the winner (since both slots are identically zero in the ideal noiseless case) [163,211]. The coin flip gives the correct answer $\frac{1}{2}$ the time, yielding

$$P_{\rm BE(2-PPM)} = \frac{1}{2}e^{-r_{\rm ph}T/2} = \frac{1}{2}e^{-N_{\rm avg}}. \tag{42}$$

This is similar to the OOK result but note the factor of $\frac{1}{2}$ in the exponent that comes from the fact that the number of photons during any observation interval (either

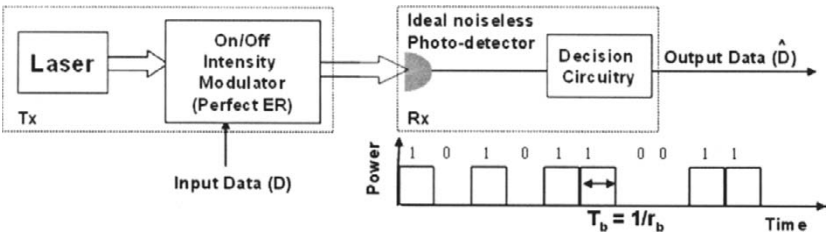

Fig. 13. Ideal photon-counting OOK TX and RX.

"0" or "1") is the same and equal to the average number received ($N = N_{\text{avg}}$). Thus, the quantum-limited photon counting sensitivity for 2-PPM is N_{avg}= 20 photons/bit at 10^{-9} BER.

Extending the binary case to M-ary PPM, in which each symbol is divided into M positions (slots) and carries $\log_2(M)$ bits per symbol, the probability of error within a symbol is

$$P_{\text{SE(M-PPM)}} = \left(\tfrac{M-1}{M}\right) e^{-N_{\text{avg}}}, \tag{43}$$

where the coefficient term is the (uniform) probability of symbol error when no photons are received [211], and the exponential term is the probability of detecting no photons.

Substituting Eq. (16) into Eq. (43) and accounting for the number of bits per symbol, yields the general expression for ideal photon-counting M-PPM:

$$P_{\text{BE(M-PPM)}} = \frac{1}{2} e^{-N_{\text{avg}} \log_2 M} = \frac{1}{2} e^{-N_{\text{avg}} k}. \tag{44}$$

As M increases, the PPB required to achieve a particular BER is reduced by $\log_2 M$, the number of bits per symbol, which can extend to arbitrarily low values in theory without additional coding. However, as noted by Yamamoto and Haus [27,28], a practical theoretical limit of ~0.02 PPB would ultimately be imposed by the ratio of photon to thermal noise energy. In practice, photon-counting receivers are not ideal, having parasitic effects such as dark counts, after pulsing, timing jitter, and limited bandwidth [1,2,30–32,209,210], which impose additional constraints on performance. Furthermore, background noise and transmitter imperfections can further degrade receiver performance [21,212].

To illustrate this point, given a TX with imperfect modulation extinction (ER = power off/power on), the probability of bit-error P_{BE} for the OOK photon-counting expression in Eq. (41) becomes

$$\begin{aligned} P_{\text{BE(OOK,ER)}} &= P[\hat{D} = 0 | D = 1] + P[\hat{D} = 1 | D = 0] \\ &= \frac{1}{2} P[n = 0 | N] + \frac{1}{2} P[n > 0 | N \cdot \text{ER}] \\ &= \frac{1}{2} P[n = 0 | N] + \frac{1}{2} \left(1\text{-}P[n = 0 | N \cdot \text{ER}]\right) \\ &= \frac{1}{2} \left(e^{-(2N_{\text{avg}} - N_{\text{avg}}\text{ER})} + 1 - e^{-N_{\text{avg}}\text{ER}} \right). \end{aligned} \tag{45}$$

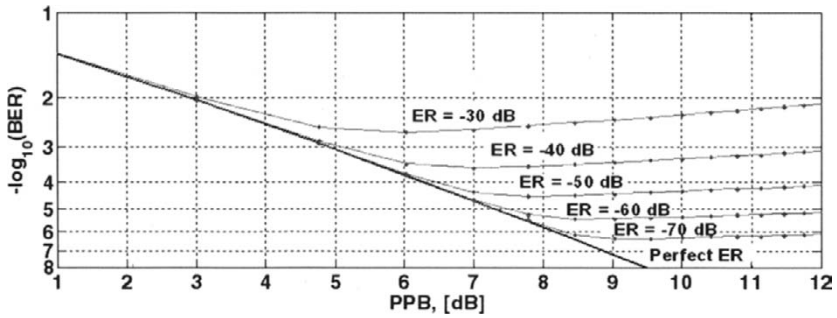

Fig. 14. Photon-counting OOK BER curves for varying TX extinction ratio (ER).

The $(1-e^{-N_{\text{avg}}\text{ER}})$ term is the modulator seepage penalty due to the N_{avg}ER (signal-dependent) background noise photons that arrive during the "0s". As shown in Fig. 14, the background noise resulting from the imperfect ER imposes an error floor that is a few times higher than the ER, (i.e., a 10^{-3}ER $\Rightarrow\sim 2\times 10^{-3}$ error floor). The error rate continues to worsen as the signal is increased since the optimum threshold is a function of the signal dependent "0" noise, not zero as assumed in Eq. (45). This illustrates a potential limitation of photon-counting using this approach in the presence of background noise, and the need for powerful FEC[42,213] that can generate error-free performance with input error-rates of $\sim 10^{-2}$[33,214] to overcome such limitations:

$$P_{\text{BE(2-PPM)}} = \frac{1}{2}e^{-\frac{N_{\text{avg}}^2}{4N_b}}, \quad (N_{\text{avg}} \ll N_b). \tag{46}$$

Binary PPM is similarly impacted by the presence of background-noise photons, although an adaptable decision can be easily implemented by comparing the first-half and second-half of the symbol. For the case where the background N_b is much larger than the signal, the BER expression becomes [212].

For average power limited transmitters, extending the modulation format to M-PPM is a technique for overcoming background noise (improving SNR) without increasing the average power. As shown in Fig. 15, both OOK and 8-PPM waveforms have the same average power, the peak of the OOK waveform is $\frac{1}{2}$ the background, whereas the peak of the 8-PPM waveform is twice the background, making it easier to distinguish (improving the SNR over the observation window), while conveying more information (3-bits per symbol), at 1.5 times the bit-rate. A more detailed discussion of M-PPM and other orthogonal formats is given in section 5.3.

2.3.7. Thermal Noise

There are two fundamental noise limitations in RF communications systems. One is thermal noise in the receiver, which is due to the temperature-dependent random-thermal-motion of charge carriers in resistive elements. This is often referred to as

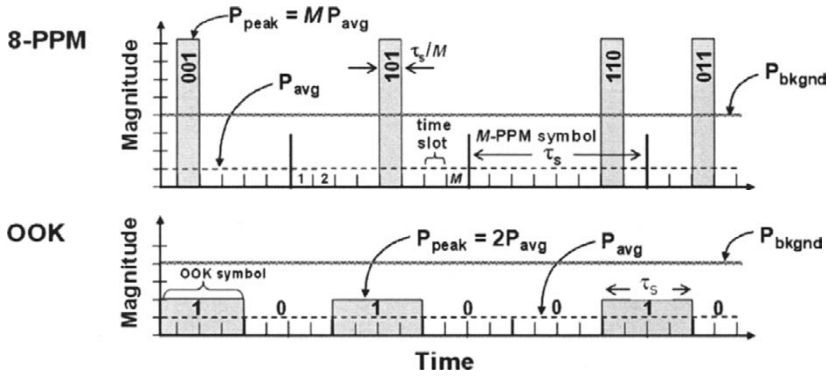

Fig. 15. On-off-keyed (OOK) and 8-ary Pulse Position Modulation (8-PPM) waveforms are shown for the same average power (P_{avg}) and background noise level. For a given average power, the peak power of the M-PPM waveform increases with m, improving the ability to distinguish the signal from the noise.

Johnson-Nyquist noise after Johnson [215], who first measured thermal noise in conductors, and Nyquist [216], who derived a theoretical expression to fit Johnson's measurements in 1928. The available thermal noise power spectral density delivered to a matched load can be described by [216,217]

$$N_{\text{th}}(\nu, T) = \frac{h\nu}{e^{h\nu/k_B T} - 1} \quad \underset{\nu<100\text{GHz}}{\longrightarrow} \quad \approx k_B T \quad [\text{W/Hz}], \tag{47}$$

where k_B is Boltzmann's constant (1.38×10^{-23} J/K), T is temperature of the resister in Kelvin, and the approximation $k_B T = -174$ dBm/Hz at room temperature. Note that in contrast with shot noise, thermal noise is dependent on temperature, and for practical bandwidths ($<\sim$100 GHz), is independent of signal power or wavelength. (See [20,156,218] for additional detail.)

The second noise source is received thermal blackbody background radiation, which is also described by Eq. (47) for a single mode and polarization, where T in this case is the average temperature within the field-of-view of the receiver. This shared expression for the two thermal noise sources arises from the fact that the resistive thermal noise can be viewed as the blackbody radiation emitted into a single mode. The contributions from these two thermal noise sources can be combined in a single effective temperature

$$T_{\text{eff}} = T_{\text{RX}} + T_{bb}. \tag{48}$$

The general expression for noise density that incorporates both thermal and shot noise is given by [217]

$$N(\nu, T_{\text{eff}}) = N_{\text{th}}(\nu, T_{\text{eff}}) + N_{shot}(\nu) = \frac{h\nu}{e^{h\nu/k_B T_{\text{eff}}} - 1} + h\nu \quad [\text{W/Hz}], \tag{49}$$

which is plotted in Fig. 16 for a receiver operating at four effective temperatures, 6000K (sun) [47,219], 290K (room temperature), 77K (liquid Nitrogen), and 2K (liquid Helium).

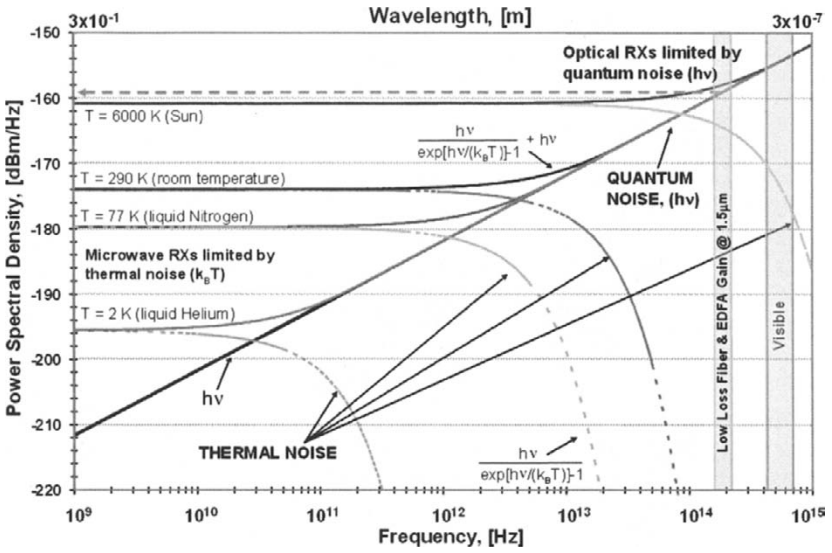

Fig. 16. The fundamental limits of receiver noise density at various temperatures. At high frequencies (e.g., optical), quantum noise (shot noise) dominates. At low frequencies, (e.g., RF or lower), temperature dependent thermal noise dominates. *Adapted from S.B. Alexander* [20].

Note that at 1.5 μm wavelengths, the shot noise dominated noise density, N_{shot}, is –159 dBm/Hz, 15 dB larger than the thermal noise component at room temperature.

Expanding on an example by Alexander [20], consider the fundamental noise limitations of a 30-GHz (λ=1 cm) microwave and a 300- THz (λ=1 μm) optical receiver, both with 1 GHz bandwidth operating at operating in room temperature (290K), looking into deep space with a conservative estimate of background temperature of 70K [220]. Thermal noise dominates the RF receiver with a noise power of

$$P_{\text{th}} = k_B T_{\text{eff}} B = (1.38 \times 10^{-23})(360)(1 \times 10^9) = 5 \times 10^{-12}\ \text{W} = -113\ \text{dBW}, \tag{50}$$

whereas quantum noise dominates the optical receiver with a noise power of

$$P_{\text{shot}} = h\nu B = (6.63 \times 10^{-34})(3 \times 10^{14})(1 \times 10^9) = 2 \times 10^{-10}\ \text{W} = -97\ \text{dBW}. \tag{51}$$

Thus the RF receiver limited by thermal noise can be be 40 times (16 dB) more sensitive than the shot-noise limited optical receiver, and this advantage can potentially be increased to 200× and ~2000× by lowering the effective temperature of the RF receiver to 77K (using LN_2) or ~8K, respectively. Note that in order to achieve the full limits of RX cooling, it must be looking directly into deep space (without channel loss), where the blackbody contribution to the effective background temperature is ~4K [220,221]. It is important to take into account such factors when making comparisons between RF and optical link designs, especially when nearly ideal superconducting photon-counting detectors [33,34,210,222] are considered.

This illustration highlights some additional benefits of free-space optical receivers over RF receivers—they can be much less sensitive to background noise, potentially allowing for a wider range of use. By using, for example, a super-cooled optical receiver including a narrow-band optical filter, thermal noise can be virtually eliminated from the receiver, since the incoming blackbody radiation at optical frequencies is significantly lower than that of shot noise for practical operational temperatures (i.e., $T_{bb} < 300\text{K}$). Even when pointing directly at the sun, where $T_{bb} = \sim 6000\text{K}$ (assuming the telescope doesn't melt), the blackbody noise is still $\sim$10 dB lower than the shot noise (at 1 μm)[2] for a single-mode receiver (single spatial-temporal and polarization mode), degrading a shot-noise limited signal by only $\sim$0.5 dB (see [47,223] for detailed analysis of background radiation and its impact on free-space optical links). On the other hand, for an RF receiver, this would degrade performance in excess of 13 dB. This illustrates potential benefits of using true single-mode optical receivers. While coupling into a single spatial mode can be more challenging, the reduced background due to strong spatial-filtering and available low-loss matched spectral filters can enable operation that is insensitive to background noise levels.

2.4. *Example Sensitivities and Link Budget*

Based on the fundamental noise limitations described above, Table 4 shows a rudimentary link budget comparing Optical and RF free-space performance over a 40,000 km link (e.g., distance to geosynchronous orbit) with the same transmit power-aperture product.

Table 4. Comparison of simplified FSO and RF link budgets based on fundamental noise-limited receiver sensitivities for a common 1-GHz RX bandwidth (at room temperature), 0.3-m TX antenna diameter and a 1.5-m RX antenna diameter, and 40,000 km link distance (Earth to GEO). *Adapted from S. Alexander*[20].

Item	$\lambda = 1 \times 10^{-6}$ m	$\lambda = 3 \times 10^{-2}$ m	Units
Transmitter			
1) Avg. TX Power	0	0	dBW
2) TX Losses	–2	0	dB
Channel			
3) Space Diffraction Loss	–41	–131	dB
Receiver			
4) RX Loss	–2	0	dB
Power at Comm. Detector	–57	–131	dBW
RX Sensitivity at 1 Gbps	–97	–114	dBW
Link Margin	50	–17	dB

Given these constraints, and some practical implementation considerations, the overall optical link has a 67-dB advantage, largely attributed to the optical carrier

[2] Note, at 1 μm, the kT approximation no longer holds, and blackbody radiation needs to be calculated with the exact expression on the left-hand side of Eq. (47).

size, and corresponding spectral, temporal, and spatial advantages. Furthermore, the 1000× bandwidth advantage of FSO systems, which can be used to scale data rates or improve RX sensitivity [22], is not accounted for in the basic accounting in Table 4. A more detailed link analysis which incorporates realizable modulation and coding performance suggested in Fig. 1 is given in section 5.5.

It's important to note that some of the RF deficit can be improved by increasing the RF aperture, which is practically easier due to reduced wavefront quality requirements. Also, RF systems usually have better transmitter efficiencies, providing another ~3–7 dB benefit, but ~60 dB is still an enormous shortfall to overcome. For instance, if both TX and RX aperture diameters were increased by a factor of ten, this would improve the RF link by 40 dB, still leaving a factor of 100 (20 dB) deficit. Thus, the net power efficiency advantage combined with the fundamental ability to efficiently scale to higher data rates, make free-space laser communications a promising technology for future long-haul communication links.

3. Transmitter Technologies

Factors that impact optical communication transmitter performance include the following: modulation bandwidth and extinction ratio, waveform generation and fidelity (control of shape and parasitic chirp), average and peak output power, output polarization state, wavelength, spatial profile and perhaps most important, wall-plug (electrical-to-optical conversion) efficiency (Joules required per photon transmitted). In contrast with transmitters for fiber-optic networks, in which the average and peak power that can be delivered over the fiber channel are generally limited by channel nonlinearities, the FSO link has no such constraint. While there are power limitations within the FSO transmitter, they are several orders of magnitude higher than those used in fiber networks.

Present lasercom transmitter designs incorporating high-power optical amplifiers, can reliably output in excess of 10W average and ~1 kW peak power in a single spatial mode with little waveform distortion or power loss due to nonlinear spectral broadening [21,198] with potential to increase to 100 kW levels [224]. The lack of dispersion over the FSO channel allows for more flexibility in wavelength selection and greatly reduced need for spectral efficiency. There are ~10 THz of optical bandwidth in 1.5 μm Erbium band [92,93,126], and other bands are available for the FSO link such as 0.5 and 0.8 μm [81–83,98–101,225], 0.98 nm [226], 1.06 μm [1,2,223,227–230], 1.3 and 10.6 μm [223]. While still subjected to practical availability and reliability constraints, the FSO transmitter and receiver designer has considerable leeway in optimizing the overall link efficiency,

$$\eta_{\text{link}} = \eta_{\text{TX}}\eta_{\text{ch}}\eta_{\text{RX}} \quad [\text{J/bit}], \tag{52}$$

the Joules-transmitted per bit-received. Here, η_{TX} is the transmitter (electrical to optical) efficiency [J/photon], η_{ch} is the net channel loss, and η_{RX} is the net receiver efficiency [photons/bit]. While the TX contribution η_{TX} is accounted for explicitly in the efficiency with which it can generate the photons, the TX indirectly influences channel loss, which is wavelength dependent, and receiver sensitivity, which is dependent upon modulation format and TX waveform fidelity.

3.1. *Direct Modulation and Semiconductor Laser Sources*

Present-day semiconductor lasers are robust, compact, efficient sources of coherent light. For Telcordia-qualified laser diodes [4,5], the mean-time-to-failure (MTTF) can exceed 100 years ($\sim 1 \times 10^6$ h) [231]. A practical feature of semiconductor lasers is that the output power can be directly modulated, at speeds approaching the relaxation oscillation frequency [232,233], f_{RO}, which is given by

$$f_{\mathrm{RO}} = \frac{1}{2\pi}\sqrt{\frac{\frac{c}{n}\frac{dg}{dN}S}{\tau_{\mathrm{ph}}}}, \tag{53}$$

where c/n is the velocity of light in the semiconductor material, dg/dN is the differential gain, S is the photon density in the cavity, and τ_{ph} is the photon lifetime. At output power levels of 10–25 mW, f_{RO} can exceed $\sim$10 GHz, which is particularly useful for subcarrier-multiplexing many narrow-band MHz class analog signals onto a single laser source, a capability that is commonly used by the cable television (CATV) industry [234,235]. However, for wide-band digital applications, direct modulation rates are practically limited to lower values, e.g., a few GHz, by parasitic capacitance in drive electronics or chirp-induced penalties [236].

As discussed in section 1, one of the simplest forms of digital modulation is on-off-keying (OOK), in which the logical information is imparted on the optical carrier by switching the light on and off. While direct modulation is an easy means of applying the intensity modulation suitable for OOK, there is a residual wavelength (or frequency) modulation or chirp ($d\phi/dt$) due to fast current density fluctuations and a slower temperature dependence of the refractive index in the active layer which causes a shift in the laser wavelength [233,237]. In fact, the fast change in laser frequency can be used for directly generating FM waveforms [160,162,177,178,180,238]. For the case of large frequency deviations, the residual IM due to current changes may need to be compensated. This can be achieved via dynamic compensation in the time domain [239] or relatively static gain/wavelength flattening in the frequency domain.

Chirp is often defined in terms of the α-parameter [240], which is the ratio of amplitude modulation to phase modulation, where

$$\alpha = \frac{d\phi}{dt}\left(\frac{1}{\frac{1}{E}\frac{dE}{dt}}\right) = \frac{d\phi}{dt}\left(\frac{1}{\frac{1}{2I}\frac{dI}{dt}}\right), \tag{54}$$

and I, E and ϕ, are instantaneous intensity, field amplitude and phase.

The chirped-output waveforms from a direct-drive laser have a broadened spectrum, that can be much larger than the modulating signal spectrum, i.e., the waveforms are not transform limited[3] (see, e.g., [236]). An example of a chirped waveform is shown in the spectrogram in Fig. 17.

The spectrogram is measured using a time-resolved technique [241–244] with time and frequency resolution of 100psec and 5 GHz, respectively. A direct-drive $\sim$75 mA current pulse causes a $\sim$20 GHz frequency shift in the laser center frequency, yielding a fast wavelength tuning response $d\lambda/di_{\mathrm{ac}} = -280$ MHz/mA. In addition, transient

[3] The transform limit (or Fourier limit), can be described as the minimum pulse duration which is possible for a given optical spectrum of a pulse. A transform-limited pulse has no chirp, a minimum time-bandwidth product, and a spectrum that is the Fouier-Transform of the pulse envelope.

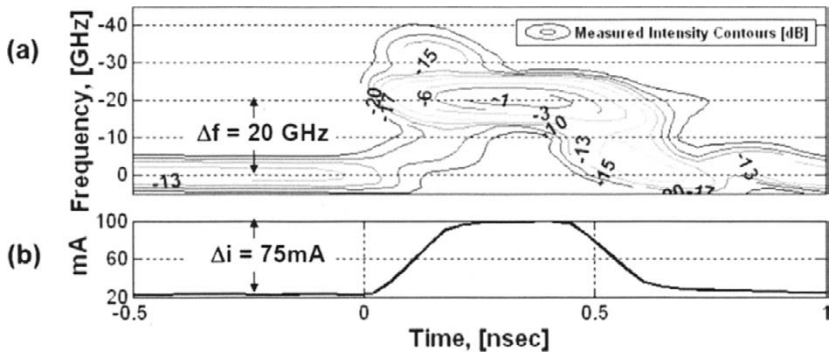

Fig. 17. (a) Measured time-frequency spectrogram (top view) of a directly-driven DFB laser biased at 25 mA, about 5 mA above the ~20 mA threshold current. Contours represent lines of constant power in dB, with the peak normalized to 0 dB. Due to the low bias current, the laser is operating near threshold, yielding relatively good ~13 dB ER (b) Measured input drive-current, with ~400 ps pulse width and ~75 mA peak current change. During fast current transitions, spectral components are generated that far exceed the transform-limited waveform spectrum, especially at the leading edge—which produces the characteristic '*h*' pattern above. This effect grows along with timing jitter on the leading edge as the laser bias approaches the laser threshold.

spectral generation, especially during the leading edge in semiconductor lasers biased near threshold, can be very wide band, exceeding 100 GHz. This leads to increased dispersion penalties in fiber-optic links and can limit receiver sensitivity in nearly-quantum-limited free-space links [245,246]. Furthermore, since chirp is a function of modulation depth, communication links which employ direct modulation need to balance conflicting extinction ratio and dispersion penalties.

In fiber-optic links, such considerations practically limit the extinction ratio (ER) to ~10 dB, which in turn can degrade RX sensitivity with ~3 dB penalties in preamplified RXs [see Eq. (64) in section 3.5.2], and limit modulation rates to less than 2.5 Gbps [233,247]. Since transmitter cost is generally a bigger concern than performance in telecom applications, directly-modulated lasers have widely been used for lower-rate (<~2.5 Gbps) links. But in FSO links, receiver sensitivity is often a design driver, and due to the limitations noted, conventional direct modulation is generally not considered the preferred approach. Channel capacity and bit-error-rate (BER) performance are degraded significantly by poor ER and chirp-induced spectral broadening, which increases the mismatch penalty between the TX signal and RX filter, a subject discussed in more detail in section 5.1.

3.1.1. Spectral Shaping

Direct-drive laser chirp and extinction ratio characteristics can be modified via subsequent optical filtering, a process that converts the frequency-shifted laser output to intensity modulated waveforms. When followed by an average power limited amplifier, this combination can be used as a power efficient source of high-fidelity transmit waveforms [10] despite the loss of the filter (see section 3.5.5). Reduced chirp and

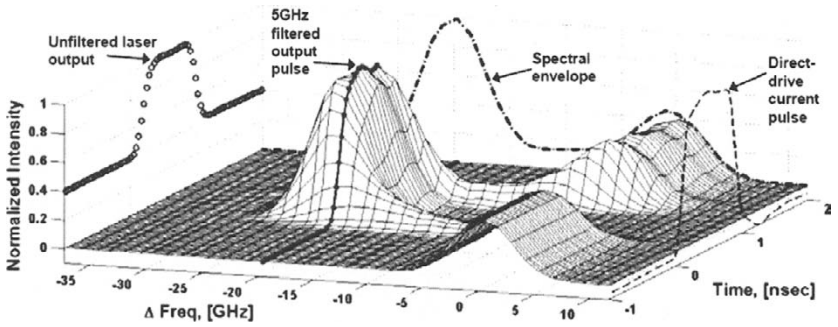

Fig. 18. Measured time-frequency spectrogram (oblique view) of a directly-driven DFB laser biased at 75 mA, with a ~20 mA threshold current. Time and frequency resolution are approximately 100 ps and 5 GHz, respectively. The response to a 1-ns, ~75-mA current pulse starting at time=0, increases output power by 2.4 times (~4 dB) and shifts the laser center frequency by 20 GHz.

improved ~13 to 14 dB ER have been demonstrated using this approach [244,248]. More recently, direct-drive chirp-managed lasers (CMLs) [249], which incorporate periodic filters into the laser package, have demonstrated impressive 10 Gbps long-haul fiber-communication performance without dispersion compensation [250,251]. Due to the complex interaction of pulse shape, dispersion, nonlinearities, and power launched over the fiber channel, these demonstrations showed better overall link performance with poor ~8 dB ER. However, these results are contrary to the impact of ER over the FSO channel, where good ER, generally > 30 dB is necessary to avoid performance penalties, especially in low-duty-cycle applications.

With narrower optical filtering, however, these approaches show promise for achieving low-chirp high-ER performance with compact power-efficient direct drive lasers, especially when used in conjunction with a subsequent TX amplifier (a subject discussed further in section 3.5.5). As shown in the spectrogram in Fig. 18, the (unfiltered) ~1 ns laser output has a ~4 dB ER and a ~20 GHz of spectrum. After narrow-band optical filtering, the ER is improved to ~30 dB and the spectrum is reduced to ~5GHz. As the external optical filter spectrum approaches the match to the desired signaling waveform, nearly transform-limited waveforms can be generated.

Another limitation with direct-drive laser modulation arises due to the non-uniform FM response that results from competing thermal and carrier modulation effects [238,241,252–256] that can lead to waveform distortion and pattern dependent errors. This can be compensated by pre-equalization of the modulation signal with a passive network in some cases [160,177,238]. However, this solution reduces the FM response and consequently leads to increased drive requirements. Another means of mitigating these effects is to limit the low-frequency drive content through pattern coding/scrambling [160,162,248], which can be achieved by driving the laser with low-duty-cycle waveforms such M-ary PPM or FSK modulation formats (see Fig 9). In addition, for low-duty-cycle waveforms, directly-modulated DFB lasers can be used in cascade with an external modulator and/or narrow-band optical filters to achieve

time/frequency windowed direct modulation. This can be a power-efficient technique to obtain high modulation extinction, while maintaining stable wavelength and near-chirp-free waveforms during transmission, a subject discussed further in section 3.5.2.

3.2. Semiconductor Laser Structures

There are several semiconductor laser design structures that are commonly available today. Fabry-Perot lasers have the simplest structure, but usually output multiple longitudinal (frequency) lasing modes, and therefore, are not well suited as signal sources for high-performance FSO links. But they are well suited as pump laser sources for commonly used Erbium-doped fiber amplifiers (EDFAs), Ytterbium-doped fiber amplifiers (YDFAs) and codoped Er:Yb EYDFAs. Here the increased spectral bandwidth is not a liability owing to broad absorption bands in the gain media [126] and since the effective reduction in spectral density lowers the risk of SBS penalties [110,111]. In order to provide some spectral selectivity and stability, Fabry-Perot-based pump lasers are often used in conjunction with narrow-band reflectors that are part of the laser cavity, or external stabilization filters such fiber-Bragg-grating (FBG) reflectors [257–259] to provide feedback that efficiently lock the center of the lasing spectrum (composed of 5 to 10 frequency modes) to that of the FBG.

Semiconductor lasers with integrated distributed Bragg reflectors (DBR) have been used to provide agile, tunable, single lasing modes in simultaneous time-division-multiplexed and frequency-division-multiplexed (TDM/FDM) digital communications [180,260]. In such lasers, great care needs to be taken in the control of the drive current and chip temperature in order to provide accurate and stable wavelength control to prevent mode-hopping. The use of such tunable sources is gaining traction in the telecom industry for flexible reconfigurable WDM networks, and especially since a single widely tunable laser could be used as a spare for any other channel.

For stable single-frequency operation, distributed-feedback (DFB) lasers are most commonly used throughout the telecom industry. A representative COTS DFB laser is shown in Fig. 19. The DFB laser has an index grating written into the gain medium which allows for only one lasing frequency mode within the gain-bandwidth of the laser. This typically provides a side-mode-suppression ratio (SMSR) exceeding ~45 dB, which precludes mode-hopping to other Fabry-Perot resonances. The DFB laser linewidth ($\Delta\nu$) is a function of output power and can be influenced by external reflections [233,261–263]. Typically $\Delta\nu <\sim 1$ MHz for well-isolated 20 mW DFB lasers, making them well suited for DPSK communication rates exceeding ~1 Gbps (see section 5.2), since coherence length penalties are incurred as the laser linewidth exceeds ~1% of the bit rate[4] [264].

[4] Linewidth penalties for DPSK are negligible when the interference between the differential bits is complete. This occurs when the coherence time of the signal is sufficiently long, i.e., $\tau_c \gg \tau_d$, where the laser coherence time $\tau_c = 1/\Delta\nu$, and τ_d, is the time delay between the differentially encoded bits. This ensures that coherent interference is achieved over the entire bit duration. Typically, DPSK data are encoded using adjacent bits, so that $\tau_d = \tau_b$, the bit period, with bit rate $R = 1/\tau_b$. However, DPSK data can be differentially encoded with a multiple-bit delay, e.g., $\tau_d = m\tau_b$, where m is a positive integer. For this general case linewidth penalties are avoided when $R \gg m\Delta\nu$, and thus, multi-bit differential-encoding imposes stricter linewidth requirements.

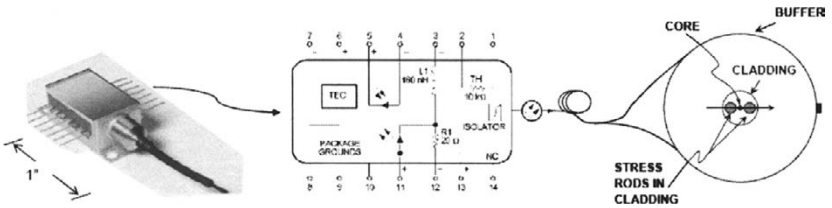

Fig. 19. Typical semiconductor DFB lasers come packaged in a 14-pin butterfly package with built-in thermo-electric cooler (TEC) and thermister for temperature control, and an internal optical isolator for increased stability. Since most external modulators require a polarized input, DFBs often come with polarization maintaining (PM) output fiber. In applications where tight wavelength stability is required, an internal etalon and monitor diode can be included within the package to provide an independent measure of wavelength that can provide sub-GHz wavelength stability when combined with external feedback [265].

3.3. Laser Wavelength Control

For optimum communication performance, narrow optical receiver filters that are well matched to the transmit signal spectrum are used (see section 5), requiring precise wavelength alignment of TX signal and RX filters. This can achieved via RX tracking of the incoming signal, but this approach is not always desirable from the system perspective. For instance, providing open-loop TX and RX control speeds acquisition and enables an FSO system to coast through fades, without having to re-acquire wavelength. In WDM applications, tight control of TX wavelength is valuable for both FSO and fiber-optic links, allowing for closer channel spacing, which improves spectral efficiency and overall link capacity. Precise open-loop control of the transmitter signal wavelength can provide additional benefits in WDM-DPSK links by facilitating acquisition and enabling cost-effective multi-channel DPSK receiver designs [266] as discussed further in section 5.2.

The steady-state laser wavelength is dependent on the optical path length within the laser cavity, which is a function of both laser temperature and average drive current. At 1.55 μm, these relations are given by

$$\frac{d\lambda}{dT} \approx 0.1\frac{\text{nm}}{^\circ\text{C}} = 12.5\frac{\text{GHz}}{^\circ\text{C}}, \tag{55}$$

$$\frac{d\lambda}{di_{\text{dc}}} \approx 0.004\frac{\text{nm}}{\text{mA}} = 0.5\frac{\text{GHz}}{\text{mA}}. \tag{56}$$

For a $\pm 10^\circ$C range with 10-bit control (corresponding to $\pm 0.01^\circ$C precision), the typical DFB laser can be temperature tuned over a range of $\pm$1nm ($\pm$125 GHz at 1.55μm) with $\pm$125 MHz resolution. Similar resolution can be obtained with current control better than $\pm$0.25 mA as shown in Fig. 20. Note that the wavelength dependence on drive current is complex (see, e.g., [233,238,253,256]), having fast components dependent on current density and slower components that are a function of carrier and thermal diffusion resulting from current transients.

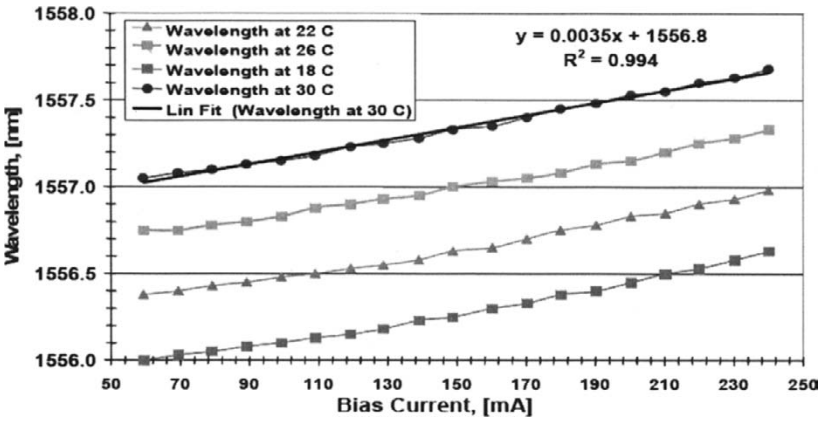

Fig. 20. Steady-state DFB laser wavelength measurements as a function of drive current for various temperature settings. The linear fits to the data yield a current dependence of $d\lambda/di_{\mathrm{dc}}$= 0.0035 nm/mA or ~440 MHz/mA and a temperature dependence of 0.14 m/°C. Note that this value is of larger magnitude and opposite sign of the fast wavelength dependence on current $d\lambda/di_{\mathrm{ac}} = -280$ MHz/mA observed in Figs. 17 and 18.

Over the long term, Telcordia-qualified COTS continuous-wave (CW) DFB lasers have demonstrated sub-GHz wavelength stability and repeatability over years of operation in the field. Precise temperature and current control combined with occasional feedback to correct for potential long term drifts in laser wavelength tuning characteristics $s\lambda(i,T)$, could enable ~100 MHz class wavelength tuning over the ~25+ year life of the laser. Such characteristics are useful since they allow for the option of open-loop TX wavelength alignment to RX filters, a capability which is particularly desirable for FSO links, especially those employing RX interferometers (e.g., DPSK—see section 5.2), where the need for spectral acquisition and tracking can significantly increase overall acquisition times.

The cost of DFB laser wavelength tunability includes two digital-to-analog converters (DACs) for adjustable current and temperature control, a feedback mechanism (e.g., a wave meter) to correct for long-term drifts, and the electrical power needed to drive the TECs to maintain a stable temperature. However, most applications require some degree of laser wavelength control, especially those employing DWDM, so some form of fixed current and temperature control is implemented anyway. The only additional cost for tunability becomes the additional DACs and the feedback mechanism. In addition to using calibrated current and temperature to control DFB laser wavelength, integrated etalon-based wavelength monitors are commercially available with Telcordia qualification [5], providing compact, reliable, locally-resident sub-GHz resolution feedback that can be used to align the laser wavelength over a 20+ year lifetime [231,265]. In some cases, the feedback information on laser wavelength (and power) can be remotely located, for instance at the receive terminal, and periodically be communicated back to the laser control via low-bandwidth back channel [266–268] (see section 5.2.2).

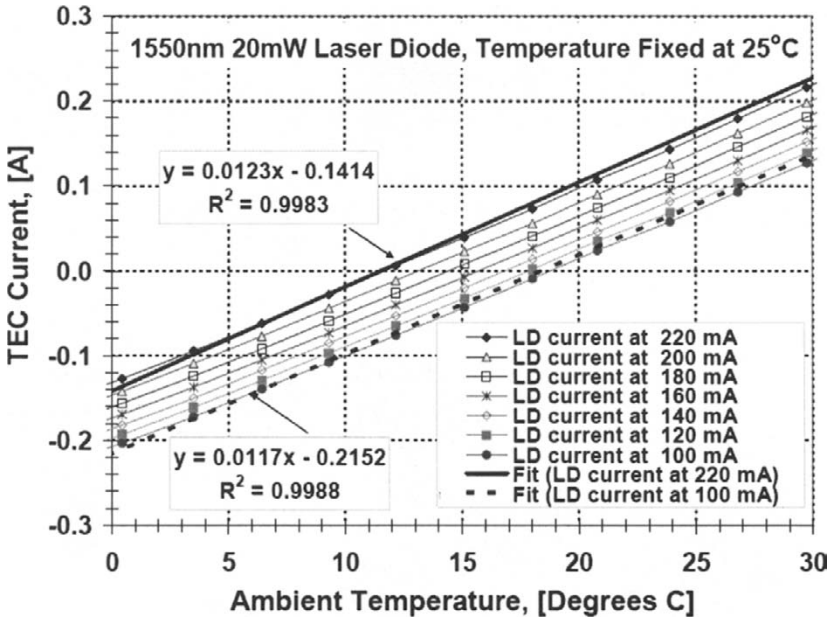

Fig. 21. TEC current versus ambient temperature for several drive currents while the laser is fixed at 25°C. The measured linear fits over the ±15°C range correspond to a TEC current slope $\frac{di_{\mathrm{TEC}}}{dT} \approx 12$ mA/°C and $\frac{di_{\mathrm{TEC}}}{di_{\mathrm{LD}}} \approx 0.4$ mA/mA. The 'zero-TEC-current' temperature is about 15°C.

As shown Fig. 21, The TEC power can be minimized if the laser is selected to output the desired wavelength near the 'zero-TEC-current' point, which is ~15°C in this case. The TEC current required to change the laser temperature, or equivalently, compensate for fluctuations in the ambient, is ~12 mA/°C. Over a range of drive currents, at 15°C ± 5°C ambient temperature, the TEC current is bounded by about 100 mA, which for a 3-V power supply limits the power requirement to < 300 mW. If power is not a driver in the design, TECs can be used to stabilize to temperature differentials up to ~40°C, although this may consume several watts of power. Note that the zero-TEC-current ambient temperature is about 10°C below the set point for the laser in Fig. 21, due to self heating from the laser drive current. This differential is typically in the range of 5°C to 10°C, dependent on the optical-electrical conversion efficiency of the laser.

3.4. Cavity-Dumped and Q-Switched Lasers

Cavity-dumped and Q-switched laser sources are capable of efficiently generating extremely high peak-power levels (e.g., tens of MW), and are especially useful for generating periodic pulse streams, used in Laser Radar (LADAR) and Laser Imaging Detection and Ranging (LIDAR) applications [269–273]. However, they are not partic-

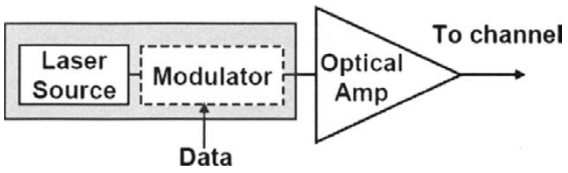

Fig. 22. Master oscillator power amplifier (MOPA) transmitter, consisting of a modulated laser source followed by a power amplifier. For high-rate applications, the MOPA is often uses a CW laser source and external modulation.

ularly well suited for high-sensitivity laser communications due to limited bandwidth and modulation options , difficulty in pulse shaping for optimized receiver sensitivity, and timing jitter [227], all of which tend to degrade communications performance. For these reasons, the MOPA transmitter discussed in the next sSection is most commonly used for high-rate-high-sensitivity communications applications.

3.5. Master Oscillator Power Amplifier (MOPA)

The Master Oscillator Power Amplifier (MOPA) transmitter shown in Fig. 22 is a flexible and scalable approach, compatible with both TDM and WDM communications at Mbit/s rates to tens of Gbit/s and beyond.

The MOPA design can be modular, allowing for a more flexible choice of waveforms, and independent design and optimization of the laser, modulator, and power amplifier. The design is commonly used for high rate optical communications in the telecom industry and is well suited for free-space lasercom platforms, where high-fidelity waveforms are required.

3.5.1. Modulation

As discussed in detail in section 3.1, direct-modulation of laser current can be used as a relatively simple method of generating a modulated optical signal at low rates. In order to transmit at high rates (e.g., 10 or 40 Gbps) or use more sophisticated modulation formats with carefully tailored pulse shapes (e.g., M-PPM, RZ-DPSK, etc.), external modulators that can generate nearly transform-limited chirp-free waveforms are generally used. Two kinds of modulators are commonly used for high-rate intensity modulation: Mach-Zehnder modulators (MZMs), which are interferometric based devices; and semiconductor-based electro-absorption modulators (EAMs) (see, e.g., [274–277]). EAMs are compact, offer ease of integration with other elements such as lasers and semiconductor optical amplifiers (SOAs), and can be cost-effective for wide-band intensity modulation transmitters. While EAMs are usually very wide band, they can introduce parasitic chirp, and often have high-loss (5–10 dB) and poor extinction at practical drive voltages. Therefore EAMs are generally not the first choice for use in high-sensitivity FSO applications.

MZMs on the other hand, are extremely versatile wide-band devices, able to modulate both intensity and phase at rates exceeding 40 Gbps. They also can be used to

generate a controlled amount of chirp depending upon the MZM design [240], which can be used to pre-compensate for the effects of dispersion [278–280]. In addition, MZMs can be used to make high-rate high-fidelity pulse-carved return-to-zero (RZ) waveforms that facilitate optimized (nearly matched) receiver design (see section 5) commonly used in series with data-modulating MZMs. For these reasons, MZMs are commonly used in high-performance fiber-optic and FSO links.

3.5.2. Mach-Zehnder Modulator (MZM)

The Mach-Zehnder interferometer structure (Fig. 23) named after its two inventors[5] [281,282] is commonly used in many optical devices including modulators, DPSK receivers, and wavelength interleavers. Active MZMs are most often fabricated in lithium niobate ($LiNO_3$) waveguides (see, e.g., [283–290]). To improve fabrication yields, they are typically constructed from y-junction couplers so that there is usually only single input (E_{in1}) and output ports (E_{out1})—with the secondary input and output ports being unguided waste ports. MZMs are also fabricated in semiconductor materials such as GaAs [143], InP [291,292], Si [293,294], and optical polymers [295]. For ultra-fast applications, nonlinear interferometric switches constructed from fibers, semiconductor optical amplifiers, and other nonlinear materials [296–302], have demonstrated 100 GHz class all-optical logic, wavelength conversion, and clock-recovery. Non-interferometric switching has also been demonstrated using self-phase modulation (SPM) and four-wave-mixing (FWM) [303–305] nonlinear processes.

The basic MZM geometry is shown in Fig. 23, composed of two directional couplers (ideally 50/50), the first splitting an incident electric field (e.g., E_{in1}) into two equal top and bottom propagating waves.

The two fields are then recombined in the second 50/50 splitter after experiencing controlled phase delays ϕ_{top} and ϕ_{bottom}. The two outputs (Eout_1 and Eout_2) are determined by the coherent addition (interference) of top and bottom fields incident on BS_2. The interference is a function of their amplitudes and relative phase ($\Delta\phi = \phi_{\text{top}} - \phi_{\text{bottom}}$). Chirp-free intensity modulation is achieved for balanced field amplitudes when the MZM operates in push-pull mode, with ϕ_{top} and ϕ_{bottom} having equal magnitude and opposite sign [240], which removes all residual phase modulation.

The MZM time-domain field impulse responses are given in Eqs. (57) and (58) for the two MZM outputs,

$$\begin{aligned} E\text{out}_1(t) &= \sqrt{R_1R_2}\delta(t+\tau/2) + \sqrt{T_1T_2}\delta(t-\tau/2) \\ &= \frac{1}{2}\left[\delta(t+\tau/2) + \delta(t-\tau/2)\right]_{\text{ideal}}, \end{aligned} \tag{57}$$

$$\begin{aligned} E\text{out}_2(t) &= \sqrt{R_1T_2}\delta(t+\tau/2) - \sqrt{T_1R_2}\delta(t-\tau/2) \\ &= \frac{1}{2}\left[\delta(t+\tau/2) - \delta(t-\tau/2)\right]_{\text{ideal}}, \end{aligned} \tag{58}$$

where factors of constant phase have been dropped, and the ideal impulse responses occur when BS_1 and BS_2 are 50/50 splitters, i.e., $R_1R_2 = T_1T_2 = 1/4$ and $R_1T_2 = T_1R_2 = 1/4$. These correspond to the sum and difference of two delta functions

[5] L. Mach and L. Zehnder independently invented in 1891/1892 what has become known as the Mach–Zehnder interferometer which could monitor changes in refractive index, and hence density, in compressible gas flows

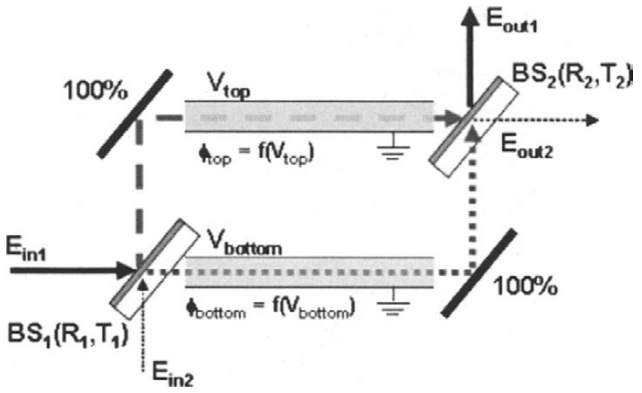

Fig. 23. The basic structure for a Mach-Zehnder modulator consists of two beam splitters $BS_{1,2}$ with intensity reflection and transmission coefficients $R_{1,2}$ and $T_{1,2}$, respectively. Ideally, the $BS_{1,2}$ are 50/50 splitters, i.e., $R_{1,2} = T_{1,2}$= 50%. The phase difference between the two arms: $\Delta\phi = \phi_{\text{top}} - \phi_{\text{bottom}}$, determines the output splitting ratio based on the constructive or destructive interference of the top and bottom arms at BS_2. For electro-optic MZMs, the phase change is proportional to the applied drive voltages V_{top} and V_{bottom}.

separated by time difference τ. In the frequency domain, the Mach-Zehnder outputs are periodic sinusoids given in Eqs. (59) and (60):

$$E\text{out}_1(f) = \left(\sqrt{R_1R_2}e^{j\pi f\tau} + \sqrt{T_1T_2}e^{-j\pi f\tau}\right) = \cos(\pi f\tau)_{\text{ideal}}, \quad (59)$$

$$E\text{out}_2(f) = \left(\sqrt{R_1T_2}e^{j\pi f\tau} - \sqrt{T_1R_2}e^{-j\pi f\tau}\right) = \sin(\pi f\tau)_{\text{ideal}}. \quad (60)$$

The sinusoidal MZM field and intensity transfer functions for $E\text{out}_1$(f) and $I\text{out}_1(f) = |E\text{out}_1(f)|^2$ are shown in Fig. 24, and highlight many attractive features. The voltage required to generate the π phase shift is referred to as the switching voltage, V_π, and corresponds to the voltage required to go from an intensity transmission peak to a null. By biasing the modulator at the 50% transmission point (referred to as the quadrature point), the MZM can generate intensity modulation (IM) waveforms when driven with a differential voltage $\Delta V = \pm V_\pi/2$, as illustrated for the superimposed OOK and PPM drive waveforms.

While it is not a requirement to operate the modulator from transmission null all the way to the peak as shown, doing so maximizes the optical transmission and reduces the impact of waveform distortion such as transient ringing on the input electrical signal. This is due to the nonlinear $\cos^2()$ transmission characteristics which tend to compress fluctuations at the transmission peak and null, and steepen transitions in between.

MZMs can also be used for digital phase modulation. By driving the MZM around the transmission null, the sign of the electric field output transitions from positive to negative, which corresponds to an abrupt π phase change suitable for generating DPSK and DQPSK waveforms. These digital characteristics offer advantages over

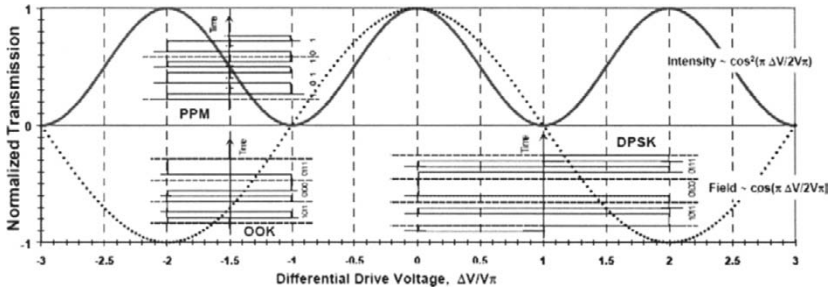

Fig. 24. MZM transfer function for the cos() arm versus differential drive voltage normalized to $V\pi$, the switching voltage. Superimposed are digital modulation drive waveforms (drive voltage versus time) for OOK, PPM, and DPSK formats, which are achieved by simply varying the drive bias position and amplitude.

linear phase modulation in which energy is transmitted during the phase transition (as the modulator slews between 0 and πp, which degrades the SNR. In order to extract maximum phase-modulated output power, the MZM is biased at a transmission null and is driven between two successive transmission peaks, requiring a drive voltage of $\pm V_\pi$, twice that of IM, corresponding to four times the drive power. As in the IM case, digital phase modulation can be achieved using a small drive voltage around the null to conserve power, at the expense of increased insertion loss and waveform fidelity that is sensitive to the input drive waveform. Furthermore, for non-ideal MZMs, this can also lead to increased chirp penalties for differential phase-modulation formats.

3.5.2.1. MZM Phase Elements

The time delay τ in Eqs. (57)–(60), has components of distinct origin

$$\tau = \tau_{\text{static}} + \tau_{\text{random}} + \tau_{\text{drive}}, \tag{61}$$

which map to optical phase, $\phi(\lambda)$ given by

$$\phi(\lambda) = \phi_{\text{static}} + \phi_{\text{random}} + \phi_{\text{drive}} = \tau\left(\frac{2\pi c}{\lambda n}\right) \quad \text{[radians]}. \tag{62}$$

The static delay, ϕ_{static}, corresponds to a fixed difference between the two arms due to manufacturing, and is typically many optical periods and much larger than the other components. Thus, τ_{static} determines the interferometer periodicity commonly referred to as the free-spectral range (FSR), where

$$\text{FSR} = 1/\tau_{\text{static}}. \tag{63}$$

Modulation bandwidth is limited to a small fraction of the FSR, and therefore the design target for τ_{static} is typically near zero, which enables a wide range of operation. For example, if $\tau_{\text{static}} \ll 8$ ps, the modulation bandwidth is $>\sim$125 GHz, or 1nm at

1550nm wavelengths. Note that this time is long relative to the optical period, corresponding to many hundreds of cycles of the ~5 fs carrier. For a modulator to operate simultaneously over the entire EDFA C-band (i.e., 1535–1565nm), $\tau_{\text{static}} \ll 0.2$ ps, which can be achieved in practice with precision manufacturing. This is important for wide-band WDM applications in which a single modulator may be used to modulate and/or shape (pulse carve) many channels (see, e.g., [93,138]).

3.5.2.2. MZM Bias Control

The MZM random phase term, ϕ_{random}, represents a slow drift ($>\sim$1 s to $>$ 1 day time-constant depending on the mechanism) in the relative phase between the two modulator arms. This is a well studied phenomenon that can be attributed to mechanisms such as thermal gradients [306] and charge buildup [307]. Consequently, closed-loop drive bias control is generally required to maintain the proper bias position while compensating for modulator drift [180,308]. Advances in MZM designs have significantly reduced the amount and rate of drift [309–313], but even small drifts can degrade extinction ratio which is important for low-duty-cycle applications [2,11,15,21,314] and lead to deleterious chirp in DPSK applications [132,142]. As long as the drift rate remains slower that the closed-loop control bandwidth, and is contained (within a few π), the random phase can be compensated indefinitely with closed-loop control (see, e.g., [315–317]) which applies a voltage typically up to a few V_π to counter the drift over a range of several interferometer fringes. If the random-phase drift continues to move in one direction beyond the range of the control loop, a reset is required, in which the control loop jumps back to the center of its operating range and re-optimizes the bias position. Such resets can be completed within ~1 ms, depending on the speed of the control system, during which the modulator is uncontrolled. With present modulator designs, such resets are becoming less frequent, and as long as the average reset rate is $>$ 1 hour this corresponds to better than 99.9999% availability. Present modulator designs have estimated reset-free operation times exceeding 20 years [311,313,318]. Further, since such resets can be anticipated as the bias slowly approaches a rail, steps can be taken to mitigate the effects of infrequent reset outages.

3.5.2.3. Extinction Ratio (ER)

Modulator extinction ratio (ER), defined as the power off-to-on ratio, impacts communication performance in many ways. It determines the initial distance between logical '0' and '1' power levels in OOK modulation and leads to multiple interferometric cross talk [319], which adversely impacts both TDM [320] and WDM systems. Incomplete ER can significantly degrade the sensitivity in optically preamplified links [15,20,314,321,322]. For ideal optically preamplified OOK, a slight modification of the upper-bound estimate for the SNR penalty given in [20], yields

$$\Delta\gamma = \frac{1 - 2\text{ER}}{1 + 2\text{ER} + 2\sqrt{\text{ER}}}\left(1 + \frac{2}{3}\sqrt{\text{ER}}\right), \tag{64}$$

which is accurate to about $\pm$ 0.2 dB for all SNR levels. This corresponds to a ~0.7 dB penalty for a 20-dB ER (i.e., ER = 0.01) and ~2.8 dB for a 10-dB ER. In addition, poor ER limits the dynamic range of data-rates for variable duty-cycle multi-rate optical communications and transmitter power efficiency low-duty-cycle modulation formats

such as M-PPM [1,10,11,15,21,22,198,214,314], due to "power robbing" from the signal at the transmitter output, (discussed further below and in section 3.5.3). Such low-duty-cycle modulation formats are particularly attractive for use in high-sensitivity FSO applications.

In order to have complete extinction, the fields interfering at BS_2 must have equal amplitudes, same polarization and π phase difference. For this reason, MZMs with high extinction typically have polarizing elements which force the interfering waves to be co-polarized. For non-ideal interferometer splitting ratios, the ER is given by

$$\mathrm{ER} = \left(\frac{\rho - 1}{2(\rho + 1)}\right)^2, \tag{65}$$

where $\rho = R_1R_2/(T_1T_2)$ for $E\mathrm{out}_1$ and $\rho = R_1T_2/(T_1R_2)$ for $E\mathrm{out}_2$ in Eqs. (57)–(60). For perfect extinction ρ = 1. A 20-dB ER results from ρ = 2/3, which can be achieved with BS_1 = 50/50 and BS_2 = 60/40 coupling ratios. For BS_2 = 47/53, a 30-dB ER can be achieved.

Since common telecom specifications for ER requirements are only ~13 dB, there are few vendors that market good-ER (ER < –30 dB) MZMs, despite the fact that such devices should be relatively easy to produce given the relations above. Nevertheless, commercially-available MZMs typically have ER better than –20 dB (at frequency), and MZMs with internal high-extinction polarizers have demonstrated modulation ER < –45 dB individually and ER < –60 dB in cascaded operation [15]. By actively balancing the input powers to the MZM output coupler, a commercial MZM was configured with ER = ~–70 dB using a single modulator [323]. Note that for ultra-wideband applications (e.g., >~30 nm), modulation bandwidth and ER may also be limited by coupler/waveguide wavelength dependence.

For low-duty-cycle waveforms, windowed direct modulation may be used as a power efficient technique for achieving high modulation extinction, while maintaining stable wavelength and chirp-free waveforms during transmission as illustrated in Fig. 25. In this manner, the power required for driving the laser and external modulator can potentially be reduced by a factor approaching the duty cycle. Such windowing could be performed in both the frequency-domain via narrow-band optical filtering and the time-domain, which could, for example, leverage a single pulse-carving modulator to efficiently time-window many WDM channels simultaneously.

3.5.2.4. Extinction Ratio Characterization and Optimization

While measurement of modulator ER is relatively straightforward for CW signals, measurement of ER for high-frequency waveforms can be challenging. Owing to the frequency dependence of transmitter components, the ER can vary as a function of the bit-rate and data pattern, so CW measurements of ER are often insufficient to accurately characterize the performance of wide-band modulators. Consequently, high-speed detection equipment is generally required to directly measure the ER for wide-band waveforms using time-domain techniqus [324,325]. But these methods can have limited accuracy and range of measurement, typically <~20 dB, or impose symmetry requirements on the waveforms being measured. Therefore they are not well suited for measuring RZ, low-duty-cycle or high extinction ratio waveforms.

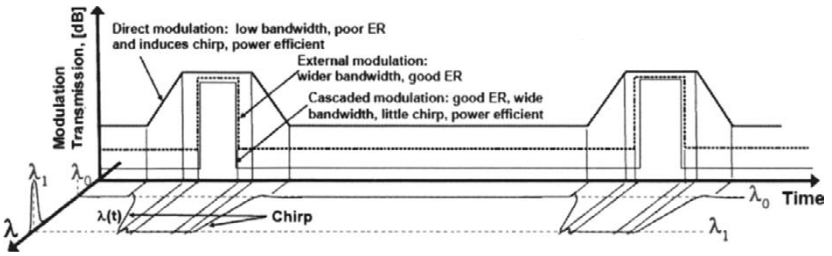

Fig. 25. Illustration of cascaded direct and external modulation waveforms showing both intensity and wavelength changes in time. The external modulator can improve extinction, waveform and spectral fidelity via a windowing function, but this need not be square as depicted. Other functions such as a variety of Gaussian-like RZ waveforms (discussed at the end of section 3.5.2) can be efficiently implemented without transmitter power penalty as long as it is followed by an APL amplifier. In a similar manner, spectral filtering can be used to improve ER, spectral fidelity, and reduce power requirements, by, for example, using a passive narrow band filter to pass the desired signal λ_1 and reject the unwanted λ_2.

However, with knowledge of the duty cycle[6] (DC), e.g., the ratio of *ones* to *zeros* transmitted, and the ability to accurately measure the average power ($\bar{P}$) and peak power ($P_{\rm pk}$), modulator ER performance can be characterized with the use of Eq. (66) [11,314]:

$$\mathrm{ER} = \frac{\bar{P}/P_{\rm pk} - \mathrm{DC}}{1 - \mathrm{DC}} \underset{\lim \mathrm{DC}\to 0}{\Rightarrow} \frac{\bar{P}}{P_{\rm pk}}. \tag{66}$$

For average-power-limited measurements, such as of a saturated MOPA TX output, the peak power is proportional to the average power and grows as the duty-cycle is reduced, as long as ER $\ll$ DC. This follows by solving Eq. (66) for $P_{\rm pk}$ which yields

$$P_{\rm pk} = \frac{\bar{P}}{\mathrm{DC} + \mathrm{ER}(1 - \mathrm{DC})} \underset{\lim \mathrm{DC}\to 0}{\Rightarrow} \frac{\bar{P}}{\mathrm{ER}}. \tag{67}$$

A plot of $P_{\rm pk}$ versus duty cycle for various ER is shown in Fig. 26. As the duty cycle approaches the ER, the peak power is reduced by half as the denominator in Eq. (67) approaches 2. For very low duty cycles, (i.e., DC $\ll$ ER) the normalized peak output power assymtotically approaches the ER. By fitting normalized peak power measurements to the calculated curves, the ER can be determined.

For peak-power-limited measurements, such as for the modulator output, the peak power is fixed and equal to the average power for a 100% duty cycle. In this case,

$$\mathrm{ER} = \frac{\bar{P}_{\rm norm} - \mathrm{DC}}{1 - \mathrm{DC}} \underset{\lim \mathrm{DC}\to 0}{\Rightarrow} \bar{P}_{\rm norm}, \tag{68}$$

where $\bar{P}_{\rm norm} = \bar{P}(\mathrm{DC})/\bar{P}(\mathrm{DC}) = 100\%$), and the measurement of ER can be achieved entirely with CW measurements as DC gets small relative to ER, without

[6] The duty cycle of a periodic or re-occurring intensity waveform, $s_I(t)$ is the percentage of '*on*' time during the period T, i.e., DC= $\frac{1}{T}\int_0^T (s_I(t)/\max[s_I(t)])dt$.

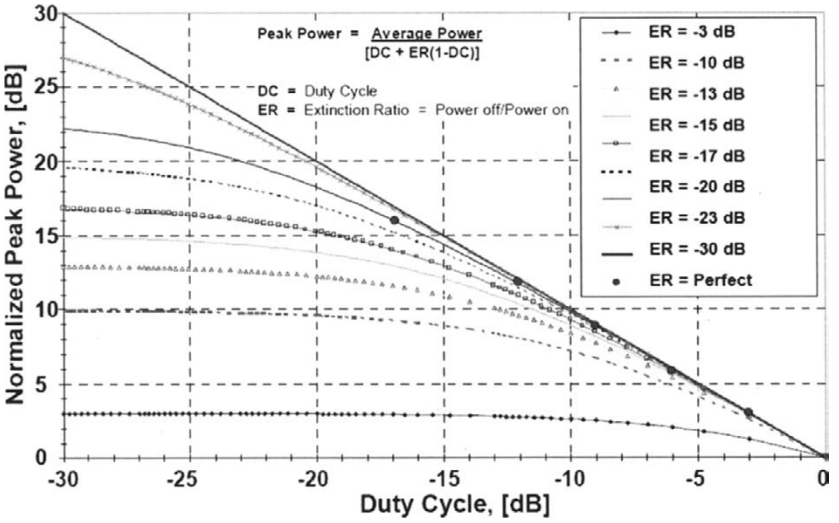

Fig. 26. Peak output power for an average power limited transmitter versus duty cycle for several values of modulator extinction [314]. Reprinted with permission. (©2000 IEEE.)

the need for high-speed measurement capabilities. Both the peak and average-power-limited measurement approaches described above have been used to characterize modulator ER with good agreement, accurately characterizing modulators with extinction > 60 dB [15,214].

Modulator control and ER optimization is often accomplished by minimizing the power-off transmission directly after the modulator [308,326]. However, for low duty-cycle or variable-rate average-power limited (APL) systems [11], another potentially more sensitive method of minimizing the ER is to maximize P_{pk} given in Eq. (67) at the output of the MOPA TX, since this value becomes increasingly sensitive to ER as the duty-cycle is reduced [314]. The peak power is maximized when the ER is minimized, and this effect is exaggerated significantly at low duty-cycles, by an amount that is approximately inversely proportional to the duty-cycle. Thus, this approach serves to optimize ER performance by maximizing the peak signal power delivered from the TX.

3.5.2.5. MZM Drive Power and Chirp Considerations

As shown in Table 5, typical values of V_π range from 3 to 5 V. Since operating power is often a primary consideration in many FSO applications, lower drive voltage ($V_\pi < 2$ V) is desirable and provides compatibility with COTS high-frequency low-voltage drive electronics. For a given electro-optic coefficient, V_π can be lowered by maximizing device interaction length (d), or increasing electric field (E) across the waveguide. Since $E = V/d$, decreasing d allows the voltage to be lowered while maintaining the same electric field. Both of these approaches tend to increase insertion loss and capacitance, which in turn reduces device bandwidth. Traveling wave designs can be

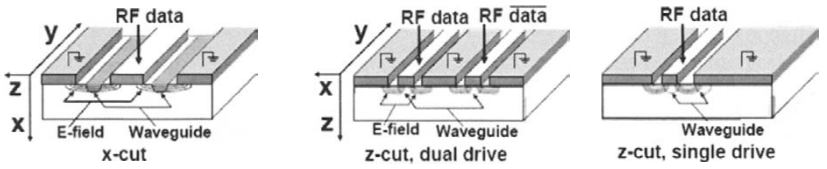

Fig. 27. Common $LiNb0_3$ modulator electrode configuration and crystal orientation with electric-field lines: (left) x-cut, (center) dual-drive z-cut, (right) single-drive z-cut.

used to mitigate the bandwidth issue [327–329], but RF-optical velocity matching constraints make it challenging to obtain a uniform response over the wide fractional bandwidth (e.g., 40 KHz to 40 GHz—6 orders of magnitude) desired in broad-band digital applications. This results in a frequency dependent $V_\pi(f)$, which can lead to pattern dependence in the transmitted waveforms.

There are two crystal orientations commonly used to make MZMs in $LiNbO_3$, x-cut and z-cut [283,330], shown in Fig. 27. X-cut designs have a single electrical modulation drive input that is split within the modulator to provide the push-pull action required for switching. If designed properly, the drive voltages arrive on each arm of the interferometer simultaneously and impart the same phase shift (for all frequencies of interest), resulting in chirp-free modulation. However, since there is only a single electrical input, there is no means of compensating with the drive waveform if there are fabrication errors.

Z-cut modulators come in dual- and single-drive configurations. Dual-drive z-cut MZMs can be used to adjust chirp by controlling the instantaneous imbalance of the input drive voltages (V_{top} and V_{bottom}). The resulting chirp parameter defined in Eq. (3) is given by [278]

$$\alpha = \frac{V_{\text{top}} + V_{\text{bottom}}}{V_{\text{top}} - V_{\text{bottom}}}. \tag{69}$$

The ability to adjust the chirp can be used, for example, to compensate for modulator fabrication errors or optimize transmission through a dispersive and nonlinear fiber-optic link [278–280,331,332], dynamically if necessary.

For the same V_π, dual-drive z-cut modulators require half the drive power of x-cut modulators, since each of the two drivers needs only $V_\pi/2$, which corresponds to a net power of $V_\pi^2/(2R_\Omega)$ for the z-cut, versus $V_\pi^2/2$ for the x-cut, where R_Ω is the modulator impedance. The dual-drive design also distributes the power load over a larger area, reducing the heat density which can be advantageous in the carefully controlled thermal environment of space-based platforms.

For single-drive z-cut MZMs, (Fig. 27-right), the electric field is stronger in the optical waveguide centered under the RF data electrode, with only $\sim$15% of the field driving the secondary waveguide. This fixed asymmetry leads to a phase-imbalance and residual chirp, with $\alpha = -0.7$. A summary of the above characteristics and representative (minimum) drive powers is given in Table 5.

Table 5. Summary of $LiNbO_3$ modulator drive and chirp characteristics for common crystal orientations and drive configurations.

	x-cut	z-cut single-drive	z-cut dual-drive
Typical V_π	5 V	4 V	4 V
Drive Power R_Ω = 50 ohms	V_π^2/R_Ω = 0.5 W	V_π^2/R_Ω =0.32W	$V_\pi^2/(2R_\Omega)$ = 0.16W
Chirp (α)	~0 (fixed by design)	–0.7 (fixed by design)	$-\infty < \alpha < \infty$ (in principle) $-2 < \alpha < 2$ (used in practice)
Layout size	smaller	smaller	larger
Heat density	higher	higher	lower

3.5.2.6. Pulsed Waveform Generation

Pulse carving using a MZM is a subject that has been discussed extensively in the literature [10,13,14,25,41,132,138,140,141,159,333–336] as a means of generating high-fidelity waveforms that are well suited for long-haul high-rate fiber and free-space optical links. Sinusoidal-drive techniques have also been used for ultra-high-speed serial-parallel conversion in optical time-division multiplexed (OTDM) systems [337] and photonic analog-to-digital converters [338]. Pulse carving reduces the influence of imperfections in the drive electronics, such as transient ringing, pattern dependence and inadequate bandwidth, on waveform quality. Broad-band high-fidelity electronics are not essential, since a variety of shaped-RZ waveforms with desirable characteristics can be generated by simple narrow-band sinusoidal waveforms with appropriate bias and drive amplitude and frequency [132,336]. Of particular interest are Gaussian-like waveforms that can be generated in this manner that can facilitate robust nearly-matched optical communication performance [13,14] a subject discussed further in section 5. A general expression for the MZM-pulse-carved power is given by

$$P(t) \propto |E(t)|^2 = \cos^2\left(\frac{V_a}{V_\pi}\frac{\pi}{2}\sin(2\pi f t) + \frac{\pi}{2}\frac{V_b}{V_\pi}\right), \tag{70}$$

where V_π is the switching voltage, V_a and f are the sinusoidal drive amplitude and frequency, respectively, and V_b is the bias voltage, which centers the drive input at locations summarized in Table 6. Note that the static and random phase offsets of Eq. (11) are not shown explicitly in Eq. (19) since it is assumed that these offsets are compensated for by bias-control.

Table 6. Summary of MZM bias points and corresponding bias voltages.

Bias Point	V_b/V_π	
Peak	m,	$[m \in \text{even}]$
Quadrature	$\frac{1}{2}m$,	$[m \in \text{odd}]$
Offset	$m \pm 1/4$,	$[m \in \text{odd}]$
Null	m,	$[m \in \text{odd}]$

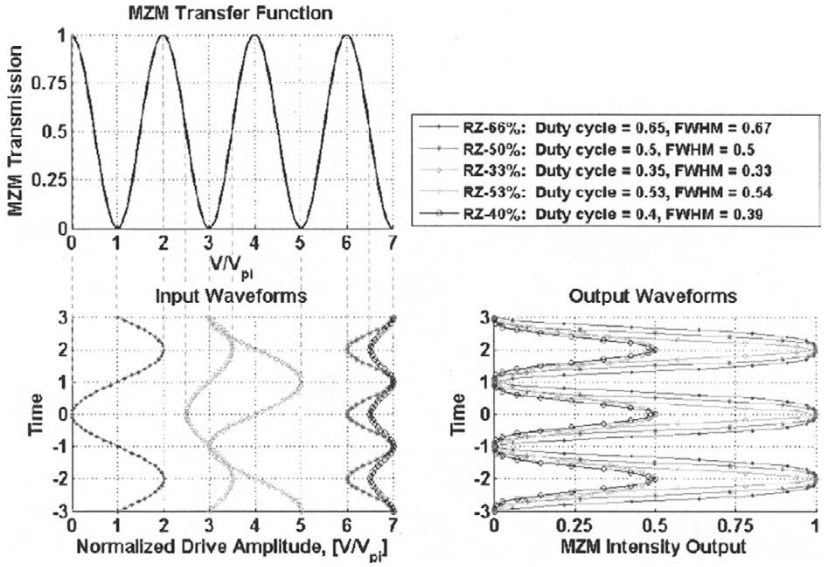

Fig. 28. Pulse carving waveform generation: (top) MZM Transfer Function, (bottom left) sinusoidal input waveforms, and (bottom right) output waveforms for RZ-66% (CSRZ) in red, RZ-50% in pink stars, RZ-33% (~Gaussian) in green diamonds, RZ-53% (Raised Cosine) in light blue triangles, and RZ-40% (~Gaussian) in blue circles, respectively. Note the differences in drive amplitude, frequency, and bias position.

Depending on the drive amplitude and bias position, pulsed-waveforms of duty-cycles ranging from 33% to 66% can be generated as shown in Figs. 28 and 29. A summary of waveform spectral and temporal characteristics and drive sensitivities are given in the pulse carving trade space matrix of Table 7.

The RZ-33% (Gaussian), RZ-66% (carrier-suppressed), and RZ-53% (raised cosine) waveforms are biased at either a transmission peak or null, and output a pulse stream at twice the drive frequency. However, when used with DPSK or DQPSK modulation, these waveforms require accurate drive amplitude or phase balance across the two arms of the MZM in order to avoid significant chirp-induced penalties [132,142].

In contrast, the 50%-RZ is attractive for use with DPSK for several reasons. The drive voltage is reduced by a factor of two, which widens the availability of driver amplifiers and reduces the power requirements. Also, the sensitivity to drive amplitude (V_a) and bias position (V_b) is reduced, making it easier to achieve stable bias control and long-term waveform fidelity, as well as diminished chirp penalty [132,142], since the MZM carver does not traverse the transmission null, the point at which the output phase is inverted. These characteristics in turn, make it easier to generate desired transmitter waveforms and optimize receiver sensitivity [133].

A representative pulse-carving MOPA TX is shown in Fig. 30. The data source can include an FEC encoder, which outputs the encoded data and corresponding channel clock at a rate equal to the data clock plus the coding overhead. The data formatter is

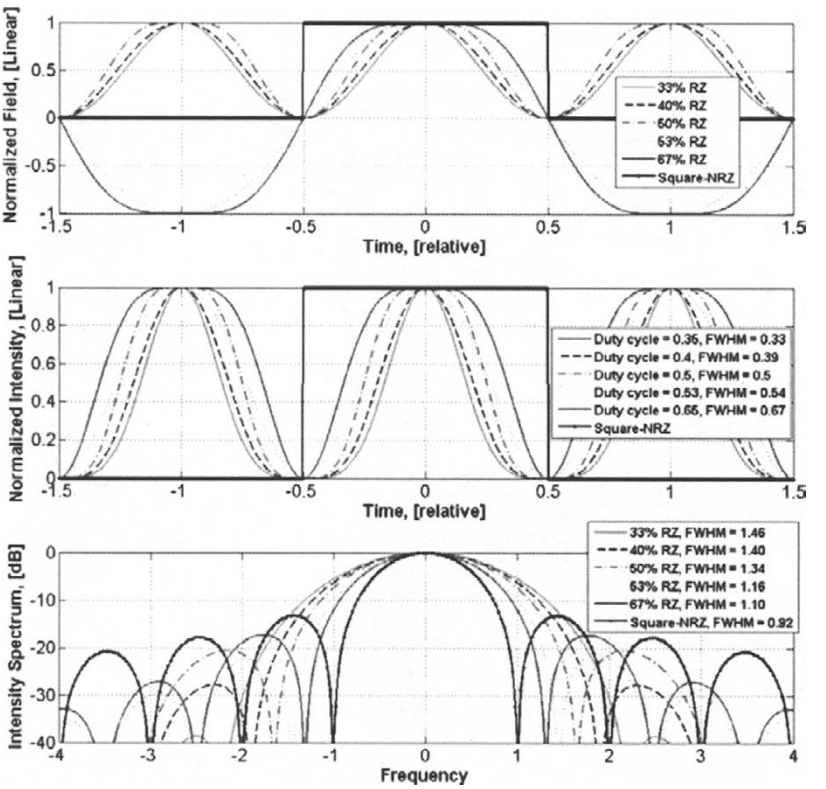

Fig. 29. Pulsed RZ waveform generation using periodically driven Mach-Zehnder modulator. (Top) Electric field; (middle) power, (bottom) power spectrum.

not needed for OOK but is needed to precode other modulation formats, such as DPSK or PPM.

3.5.3. High Power Optical Amplifier

Efficient high-power optical transmitters are necessary in optical communications scenarios such as broadband distribution networks where electrical power is increasingly becoming a valuable commodity. Efficiency also benefits large-scale WDM transmission where TX power is distributed over many channels (λs), and FSO links, where transmitter power is often a limiting design driver (see e.g., [2,21,339]). High power optical amplifier needs have historically been met by erbium-doped fiber amplifiers (EDFAs) operating near 1550nm [126,340–342]. When compared with RF amplifiers, EDFAs have many desirable characteristics including high gain (> 40 dB), large average output power (> 10 W), and ultra-wide bandwidth > 10 THz. However, as noted in Table 3 and discussed later in this section, for high-duty-cycle waveforms

Table 7. Pulse carving characteristics and trade space matrix highlighting drive frequency and drive amplitude (V_a) requirements, bias position, waveform duty cycle (DC_{pulse}), time-bandwidth-product, and sensitivities. *Adapted from Stevens in* [142].

#	Waveform Type	Time-Bandwidth Product			Waveform Characteristics			Drive Characteristics						
		3 dB $\Delta t_i * \Delta f_i$	10 dB $\Delta t_i * \Delta f_i$	20 dB $\Delta t_i * \Delta f_i$	FWHM	Duty Cycle	Carver Loss, [dB]	Drive Type	Drive Freq., [fRate]	Drive Amp. (V/Vπ)	Rel. Drive Power	Bias Point	Sensitivities Bias	Drive
1	NRZ Square	0.89	1.49	3.6	100%	100%	0	Sq.	na	0.5	8	Quad	Moderate	Moderate
2	RZ-Square (50%)	0.89	1.49	3.6	50%	50%	-3	Sq.	na	0.5	4	Quad	Moderate	Moderate
3	RZ-33% (Gaussian)	0.49	1.54	2.7	33%	35%	-4.8	Sin	0.5	1	16	Peak	High	High
4	RZ-66% (CSRZ)	0.73	1.62	2.9	67%	65%	-1.7	Sin	0.5	1	16	Null	High	High
5	RZ-53% (Raised Cosine)	0.63	1.62	2.4	54%	53%	-5.7	Sin	0.5	0.5	4	Null	High	Low
6	RZ-50%	0.66	1.62	4.0	50%	50%	-3	Sin	1	0.5	4	Quad	Moderate	Moderate
7	RZ-40% (Gaussian)	0.55	1.57	2.6	39%	40%	-7.1	Sin	1	0.25	1	Offset	Very High	Low

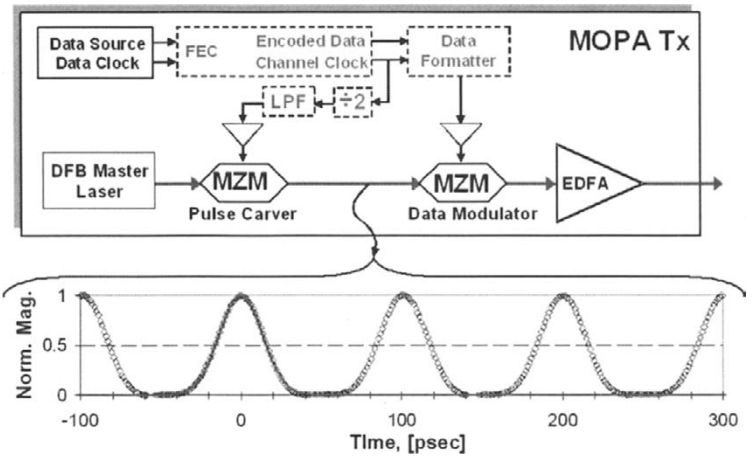

Fig. 30. (Top) A pulse-carving MOPA TX with optional FEC and Data Formatting elements. 33%-RZ pulse carving requires sinusoidal drive at $\frac{1}{2}$ the channel clock rate. (Bottom) Measured 10 Gbps 33%-RZ waveforms nearly indistinguishable from a superimposed 35-ps full-width-half-max (FWHM) Gaussian fit centered at $t = 0$.

optical amplifiers are typically less power efficient than their RF counterparts, but for low-duty-cycle waveforms the efficiencies are more comparable.

The ability to efficiently transmit a variety of signaling waveforms at high average and peak output power levels in a single spatial and polarization mode is of particular importance to free space applications. Single spatial mode operation is nec-

essary for efficient power delivery to a far-field FSO target. In fiber-optic networks, a single-polarization TX simply reduces the amount of unnecessary (orthogonally polarized) amplified spontaneous emission (ASE) noise entering the network. In FSO applications, single-polarization transmitters can improve TX-RX isolation and allow for simple polarization diplexing of TX/RX signals within an FSO terminal [46], without the need for active polarization tracking. Furthermore, single-polarization receivers can offer improved receiver sensitivity [20,41,77] since orthogonally polarized amplified spontaneous emission (ASE) noise can be eliminated at both RX and TX.

The ability to maintain transmission efficiency over a wide range of duty cycles, which is facilitated by high-gain and average-power limited properties of optical amplifiers [11,343–346], allows for aggressive pulse shaping at the transmitter. This can improve receiver sensitivity and provide flexible multi-rate capabilities with simplified receiver design options [11,12,15], a subject discussed below and further in section 5.

3.5.3.1. Average Power Limited (APL) Properties

EDFAs are average-power limited (APL) amplifiers, meaning the amplifier gain and average output power are fixed for a given average input power, independent of the shape or duty cycle of the incoming signal. This holds whenever the power-off time of the incoming signal is much less than upper state life time of the gain-medium [172]. For EDFAs, which have a slow $\sim$1 ms time constant, this is true for practical optical communications rates above $\sim$1 Mbps. Detailed experimental analysis and simulations of amplifier transients and average power limited amplifier dynamics are given in [126,340,347].

For APL amplifiers, the peak to average power ratio varies inversely with the duty cycle - as it decreases, the peak power grows while average power is maintained (see Figs. 35 and 36). This is in sharp contrast with RF amplifiers, which are generally peak-power limited (PPL), meaning there is a maximum (peak) voltage or output power they can deliver. In order to maximize the average power transmitted, which is important for power-starved communication links, a PPL TX must operate with nearly a 100% duty-cycle—a constraint that does not apply to APL optical transmitters.

3.5.3.2. Amplifier Gain, Saturation, and Noise

The functional dependence of amplified signal output power (P_{out}) and gain G as a function of average signal input power (P_{in}) is given by

$$P_{out} = P_{in}G(P_{in}) = P_{in}\left(1 + \frac{g_o}{1 + g_o\,(P_{in}/P_{sat})}\right) \underset{P_{in}g_o \gg P_{sat}}{\Rightarrow} P_{in} + P_{sat}, \tag{71}$$

where g_o is the small signal gain at the signal wavelength, and P_{sat} is the average output power when the amplifier is driven deep into saturation[7]. Note that the amplifier gain can have a strong wavelength dependence [126, 340], but for this analysis, the gain is assumed to be relatively constant over the narrow-band surrounding the signal. The dependence of amplifier gain, average output power, and noise figure on average input power are illustrated in Fig. 31.

[7] Note, that we refer to P_{sat} as the maximum useful amplified output power, which is different from the term P_{sat}^{out}, which is conventionally defined as the output power for which the EDFA gain has dropped by 3 dB from the small signal gain G_o [126].

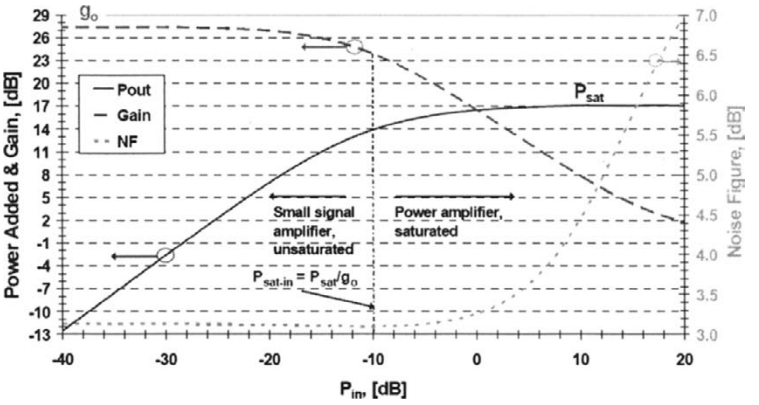

Fig. 31. Typical EDFA average power added *(blue, solid line)* and gain *(red, dashed line)* both on the left-hand axis, and noise figure *(green, dotted line)* on the right-hand axis versus average input power ($P_{\rm in}$). For this example, g_o = 27 dB and $P_{\rm sat}$ = 17 dBm, yielding $P_{\rm sat-in}$ = –10 dBm.

The 3-dB gain compression point occurs when $P_{\rm in} = P_{\rm sat}/g_o$, which is referred to as the saturated input power ($P_{\rm sat-in}$). To efficiently extract maximum output power, power amplifiers are typically run with $P_{\rm in} \gg P_{\rm sat-int}$. In this regime, the gain $G(P_{\rm in})$ is significantly compressed and the amplifier operates in a 'power added' mode, contributing most of Psat to the total output power. For $P_{\rm in} > P_{\rm sat-in}$ + 10dB, over 90% of the available power is extracted corresponding to an efficiency penalty of ~0.5 dB. This penalty drops to < 0.1 dB for $P_{\rm in} > P_{\rm sat-in}$ + 15dB.

Note that as the input power exceeds $P_{\rm sat-in}$, and the amplifier gain is reduced, the noise figure increases as a result of incomplete population inversion in the amplifying medium [126]. However this generally is of little consequence since the SNR at the amplifier input is typically large enough such that even a several-dB SNR degradation is not sufficient to impact communications performance. This holds as long as

$$GN_{\rm sp}\eta_{\rm ch} \ll 1, \tag{72}$$

and

$$\mathrm{SNR_{TX}} \cong \frac{N_{\rm sig-in}}{2N_{\rm sp}} > N_{Rx-\rm min} \gg 1, \tag{73}$$

where $\eta_{\rm ch}$ is the net channel loss, G is gain, $\mathrm{SNR_{TX}}$ is the transmitter output SNR[8], $N_{\rm sig-in}$ is the input signal PPB, $N_{Rx-\rm min}$ is the minimum required RX SNR[9], and $N_{\rm sp}$ is the spontaneous emission factor, equivalent to the number of noise-photons-per-mode at the input of the amplifier. For high-gain and a large signal input,

[8] This definition of $\mathrm{SNR_{TX}}$ assumes that $N_{\rm sig-in}$ is large enough that out-of-band ASE × ASE noise terms can be neglected. While this will be accurate for narrow-band or matched RX filtering, it will not be accurate for unfiltered-broad-band RXs.

[9] Note that for shot-noise-limited direct-detected signals, SNR = PPB so SNR and PPB can be used interchangeably. This is not the case for optically amplified signals.

$$N_{sp} = \frac{NF}{2}, \tag{74}$$

where NF is the linear noise figure. For a fully inverted amplifier *NF* approaches the quantum limit of 2 (3 dB) [126], corresponding to $N_{sp} = 1$. When the condition of Eq. (72) is satisfied, the received TX ASE noise is small relative to the shot noise of the signal and the minimum ASE noise added by an optically preamplified RX. If Eq. (72) is not satisfied, communication performance then becomes dominated by the received TX ASE [348], which limits SNR_{TX}. However, in this case, the conditions of Eq. (73) are generally easy to obtain, and as long as the $SNR_{TX} > N_{RX-min}$, the impact on communication performance is negligible.

Consider, for example, a TX amplifier operating at 10 Gbps with $P_{in} = -10$ dBm, 27 dB gain, 10 dB noise figure, and $P_{out} = 17$ dBm. The shot-noise-limited input SNR during the 100 psec bit period is ~49 dB and the corresponding $SNR_{TX} = N_{sig}/(2N_{sp})$ = 39 dB. Recall that the quantum limit receiver sensitivity (at 10^{-9} BER) for an uncoded optically preamplified OOK RX is ~40 PPB (16 dB SNR). Thus, in the regime where the SNR_{TX} dominates, this link would have 23 dB margin. The large SNR_{TX} indicates that the noise added by the amplifier is still small relative to the signal, corresponding to ~2500 ASE PPB out of 3.9×10^7 PPB transmitted in the single-spatial-temporal-polarization mode of the signal. Subsequently passing both the signal and ASE photons through a 60-dB attenuating channel results in a –43 dBm received signal that is nearly shot-noise limited, comprised of 38.9 signal PPB and 0.003 ASE PPB, with an SNR of 15.9 dB. For an optically preamplified RX, as long as the received ASE PPB $\ll N_{sp}$ of the RX, the TX ASE has a negligible impact on communication performance. A more detailed analysis including the impact of broad-band ASE on TX performance is given later in this section.

While we have shown above that the noise figure for a power amplifier is not a driving design concern, it is worth noting that with careful design, power amplifiers can deliver high gain, efficiency, and output power. By incorporating mid-stage isolation and out-of-band ASE filtering, multi-stage amplifiers have been designed with > 50 dB gain and near quantum-limited noise figures of ~3.1 dB, (see, e.g., [349,350]). This class of performance can be obtained from commercially available EDFAs, with small-signal-gain > 45 dB and NF < 3.5 dB readily available. When cascading additional stages, the net noise figure is given by [126]

$$NF_{net} = NF_1 + \frac{NF_2 - 1}{G_1} \underset{G_1 \gg NF_2 - 1}{\Longrightarrow} NF_1, \tag{75}$$

where NF_i and G_i represent the gain and noise figure of the ith amplifierstage. Clearly, with high-gain in the first amplifier, the net cascaded noise figure can be dominated by the (low) noise figure of the first. Since high-gain and low-NF can be achieved for relatively low (<~100mW) pump powers [350], reduced power efficiency in the first stage amplifier should have little impact on the overall efficiency for > 1 W high-power EDFAs.

3.5.3.3. Amplifier Efficiency

The net power amplifier electrical–to–optical conversion efficiency ($\eta_{E/O}$) is an important design consideration, especially for space-based transmitters since it generally consumes a significant portion of the overall power budget. For example, the design

target for the 5W Mars Lasercom YDFA transmitter power amplifier [1,2] transmitter YDFA power amplifier $\eta_{E/O}$ was ~15% [198], requiring > 33W of electrical power, more than 20% of the total power budget.

The main factors that contribute to $\eta_{E/O}$, include pump laser electrical-to-optical efficiency (η_{pump}), pump coupling efficiency ($\eta_{coupling}$), and pump-to-amplified-signal optical-to-optical conversion efficiency ($\eta_{O/O}$), with

$$\eta_{E/O} = \frac{P_{optical-out}}{P_{electrical}} = \eta_{pump}\eta_{coupling}\eta_{O/O}\eta_{overhead}. \quad (76)$$

Here, $\eta_{overhead}$ is included to account for any cooling or control that is not included in the other terms.

Pump laser efficiency includes the electrical power required to drive the pump as well as temperature and current control needed to reliably operate the pump at the proper wavelength. Improvements in pump laser efficiencies in the 0.9 μm absorption bands have occurred in several areas, including significant advancements in the reduction of heating/cooling power required to keep the pump wavelength within the absorption band of the gain medium. In single-mode pump lasers, FBG stabilized designs have been used to efficiently lock the laser wavelength near the absorption peak over an extended temperature range [257–259,351,352], with η_{pump} >~40% and > 200 mW coupled into single-mode fiber for individual single-mode sources. Single-mode coupling techniques often incorporate polarization and/or wavelength multiplexing to combine pump and signal. To increase single-mode pump power levels, both polarization and dense WDM of stabilized pump-lasers can be used to efficiently combine multiple sources into a single-mode [353]. These techniques can scale multi-stage single-mode EDFAs to Watt-class power levels [354]. In high-power cladding-pumped amplifier designs [75], ER:Yb codoped gain fiber is often used to broaden the absorption band, which can extend from 850 to 1100 nm [355–357]. This provides greater flexibility in selection of pump wavelengths, and allows for efficient absorption of uncooled pump wavelengths as they drift over an extended temperature range. Codoping also permits high erbium doping concentrations in fused silica fibers with without quenching induced degradation in gain or efficiency [358].

Cladding-pumped amplifier designs permit efficient coupling of many multi-Watt multimode pump lasers into a double-clad gain fiber, which consists of a large multimode outer-diameter waveguide with high numerical aperture (NA), and a smaller doped-core single-mode waveguide (required for FSO applications) with lower-NA [359]. Pump power coupled into the low-loss outer waveguide is eventually absorbed by the gain-media within the inner single-mode core. The ability to accept output from multimode pump lasers in the large-NA outer waveguide, significantly increases pump coupling efficiency and available pump power levels, enabling the use of efficient high-power (multi-Watt) sources with η_{pump} =~50% [360–362] and a variety of low-loss pump-coupling and combining strategies [75,349,363–372].

Optical-to-optical conversion or power conversion efficiency [126], defined as the ratio

$$\eta_{O/O} = \frac{P_{out} - P_{in}}{P_{in}^{Pump}} \leq \frac{\lambda_{pump}}{\lambda_{sig}} \quad (77)$$

is limited by the quantum-optical conversion efficiency in which a single pump-photon at λ_{pump} is converted to a single signal-photon at λ_{signal}. For 1.55 μm EDFAs with

0.98 μm pumping, $\eta_{O/O} \leq 63\%$, whereas for 1.06 μm YDFAs with 0.98 μm pumping, $\eta_{O/O} \leq 90\%$. Optical-to-optical conversion efficiency is further reduced by other losses in the amplifier such as incomplete pump absorption, insertion loss of filters, isolators and splices, excited state absorption, scattering, and other parasitic loss mechanisms [373].

The state-of-the-art high-efficiency high-power amplifier demonstrations are based cladding-pumped designs and include a high-reliability single-polarization EYDFA at 1550 nm with output power > 10W and $\eta_{E/O} = \sim 13\%$ [199]. With the combined use of PM components and internal polarizers, a 30-dB polarization extinction ratio (PER) was achieved. At 1064 nm, a high-efficiency YDFA design based on high-reliability PM components but without polarizing elements demonstrated output power > 8W, $\eta_{E/O} = \sim 21\%$, and ~13 dB PER [204]. Efficient laboratory-grade YDFAs with $\eta_{O/O}$ approaching 80% [374] and $\eta_{E/O}$ up to 40% [200] have been reported. We note that Nd-doped amplifiers have also been considered for use in space-based applications, however reported efficiencies are lower and they are less tolerant to the effects of radiation [228].

In section 1.1, we introduced net transmitter efficiency (η_{TX}), which represents the energy required to generate TX photons. In absolute terms, this is limited by $\eta_{E/O}$ and TX wavelength as summarized in Table 8 for the amplifiers mentioned above. Note that while 1μm amplifiers generally have better $\eta_{E/O}$ in terms of power efficiency due to a smaller quantum defect, this advantage is reduced by a comparable amount when TX efficiency η_{TX} is normalized in terms of energy per photon as shown below. This is a direct consequence of Eq. (4) with photon-energy being inversely proportional to wavelength.

Table 8. Minimum TX photon-generation efficiency in units of Joules/photon for demonstrated high-efficiency power amplifiers. Note, 1 attoJoule (aJ) = 10^{-18}J.

λ, [μm]	$\eta_{E/O}$	$\eta_{TX} \geq \frac{h\nu}{\eta_{E/O}} = \frac{hc}{\lambda\eta_{E/O}}$, [aJ/photon]
1.55	13%	1.0
1.06	21%	0.9
1.06	40%	0.5

Another important efficiency metric is the amplifier wall-plug efficiency, which includes conversion and conditioning ($\eta_{E/E}$) required to adapt the available power source from the "wall", (e.g., 120 V_{ac} for terrestrial applications or 28 V_{dc} for space-based applications) to voltage levels suitable for driving the amplifier hardware, primarily the pumps, which typically require a ~3 V_{dc} supply to drive lasers with bias voltage < 2.5 V:

$$\eta_{wall} = \eta_{E/E}\eta_{E/O}. \tag{78}$$

Typical values for $\eta_{E/E}$ are between ~70% and 90% depending on the voltage conversion levels, a factor that can influence the amplifier electrical design. In [204], for example, the pump lasers for each stage are wired in series to maximize electrical power conversion efficiency, yielding a YDFA with $\eta_{E/E} = \sim 85\%$, and $\eta_{wall} = \sim 19\%$.

3.5.3.4. Polarization-Maintaining (PM) Fiber Amplifier Designs

As noted at the beginning of section 3.5.3, optical amplifiers that can maintain the polarization of the optical signal are desirable for free-space applications since they provide additional capabilities including polarization diplexing of TX and RX signals and improved communication performance since orthogonally polarized amplifier and background noise can be eliminated in the receiver. They are also necessary for transmitting polarization modulated signals and expand the options for implementing multi-access FSO terminals that incorporate both wavelength and polarization multiplexing [48].

The conventional method of maintaining a single-polarization through a fiber amplifier uses passive PM components and gain media. However, it is challenging to achieve good polarization extinction ratio (PER) with this approach due to polarization cross-coupling of multiple cascaded components with limited PER. Amplifiers using this design typically can achieve ~12–17 dB PER as in [198,204]. To maintain good PER, polarizing elements, such as single-polarization isolators, can be introduced to the PM optical path to remove the orthogonal polarization seepage before it becomes excessive. As shown in [199], this approach is consistent with achieving good polarization extinction (PER = ~30 dB) without degrading electrical-to-optical conversion efficiency. However, this approach precludes the use of polarization modulation.

Active polarization control [375–377] can be used to compensate for polarization fluctuations in a non-PM amplifier at the expense of additional complexity and increased size, weight, and power. Alternatively, passive compensation can be achieved through a double-pass amplifier design incorporating a mid-stage Faraday rotator mirror [353,354,378]. This approach can compensate for both inherent and time varying birefringence to maintain either single or dual-polarization states with good PER unlike the passive designs based entirely on cascaded PM components noted above.

The basic amplifier configuration is shown in Fig. 32. A single-mode PM optical signal enters the amplifier through the input port of the PM I/O coupling element, which could be a polarization beam splitter (PBS) in a single-polarization design or a PM circulator for dual-polarization applications. Unlike conventional PM designs, the input and output ports of the I/O coupler are the only ones that must be polarization maintaining. This greatly simplifies the amplifier design since all other elements can be non-PM. The signal makes a first pass through the gain media and filter, and is then reflected by the Faraday rotator mirror (FRM) which reflects the amplified-filtered signal and rotates the polarization orthogonal to that of the input. After the second pass, the twice-amplified signal polarization is orthogonal to that of the PM input, and is directed towards the amplifier PM output. The PER performance for the entire amplifier is primarily a function of the PM I/O coupler PER and the 90° rotation of the FRM, which can exceed 30 dB with commercially available components. Pump coupling to the gain media can be achieved through a variety of single or multi-mode, WDM, side- or end-coupled elements mentioned in the Amplifier Efficiency Section above and related references.

A key feature of the double-pass design is that it re-uses the same gain medium, giving it twice the comparable small-signal gain of the equivalent single-pass design, but with fewer components in the critical path. However, with the double-pass design, the forward gain is equal to the backward gain and pump power that is not converted during the forward pass can be extracted during the backward pass. When operating

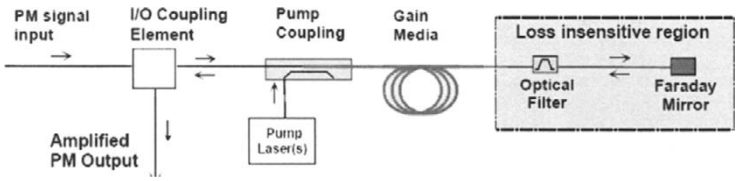

Fig. 32. Schematic for double-pass polarization-maintaining optical amplifier.

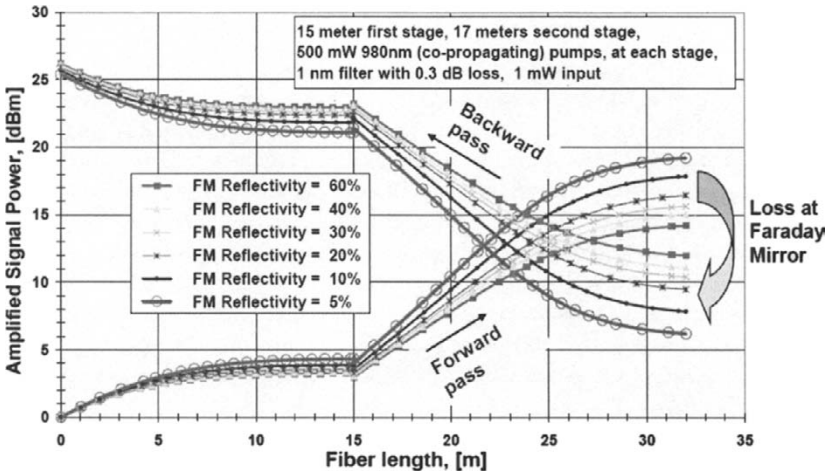

Fig. 33. Simulation of amplified signal power as a function of length and Faraday mirror reflectivity in a 2-stage double-pass EDFA with forward-propagating pumps. For FRM losses between 2 and 13 dB, simulated results show $<\sim$0.5 dB loss in output power, consistent with experimental measurements [354].

in saturation, the average gain adjusts over the length of the double pass EDFA until the amplified signal extracts all the available converted pump power. As a result, the double pass design is less sensitive to the distribution of pump power, in contrast to single pass designs, where the pump power of the final stage is critical. Furthermore, while excess loss near the amplifier output directly reduces the output power by 1 dB per dB loss, additional attenuation in the loss-insensitive region of the double–pass has little effect on net output power, as long as the amplifier continues to operate in saturation [354] as shown in Fig. 33.

Consequently, advantageous but lossy elements such as optical filters, additional pump-coupling elements, WDMs, etc., can be inserted into the design in the loss insensitive region with little power penalty at the output [379]. The optical filtering, for example, can perform double-pass pulse-shaping and remove out-of-band ASE that competes with the signal for gain, enabling the amplifier to saturate at lower

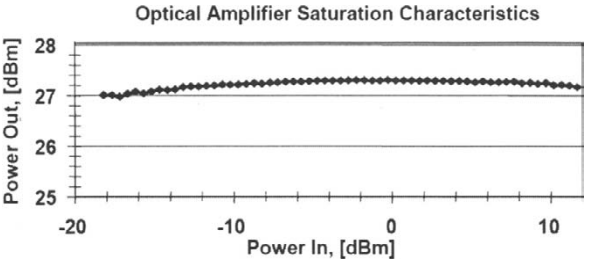

Fig. 34. Measured output saturation characteristics for a high-gain two-stage double-pass ~0.5W EDFA with mid-stage narrow-band optical filter [354].

input power levels. The filter also makes the amplifier more stable by increasing the threshold of lasing at the ASE peak, thus reducing the risk of potentially damaging Q-switched pulses. This is illustrated in Fig. 34, for a high-gain double-pass EDFA with mid-stage narrow-band optical filter. Without any internal isolation, the output power is stable to better than 0.5 dB over a 30-dB dynamic range of input power and 45-dB gain. In addition to stable PM performance, this amplifier design has demonstrated good power efficiency, with optical-to-optical conversion efficiency of ~45% at 1.55 μm [354]. Such characteristics combined with radiation tolerance of ~0.1 dB/krad [380], are attractive for use in space-based lasercom systems [21], especially those with variable-duty-cycle variable-rate capabilities discussed further in section 3.5.5

3.5.4. High-Efficiency Semiconductor Optical Amplifiers

While power-amplifier needs historically have been met by rare-earth-doped fiber amplifiers, alternative semiconductor-based optical amplifier technologies show promise at Watt-class power levels [197,381]. Efficiency, single-polarization, and extened wavelength range are some performance advantages that semiconductor optical amplifiers (SOAs) have over fiber amplifiers. More importantly, SOAs have the potential for improved size, weight, and power which, along with to manufacturability and integration into more comprehensive subsystems, can significantly reduce cost. Since SOAs are electrically pumped, the quantum-defect and other losses associated with optical-optical conversion are absent, so in principle, $\eta_{E/O}$ could be greater than $>$ 25%. Slab-coupled optical waveguide amplifiers (SCOWAs) are of particular interest since they have demonstrated Watt-class (chip) output powers with large mode size compatible with efficient coupling to single-mode fiber [197].

In comparison with EDFAs, the dynamics in SOAs, like semiconductor lasers discussed in section 3.1, are more complex and faster by over six orders of magnitude. The slow millisecond upper-state lifetime in erbium yields attractive kHz-class high-pass characteristics that are well suited for high-speed optical communications, enabling EDFAs to deliver a constant average power limited (APL) output when driven by high-frequency time-varying input signals above ~10 kHz [126]. For signals with frequency content below the cut-off frequency, the average amplifier gain and output power track the input signal. Output power and efficiency are reduced for low-frequency, low-duty

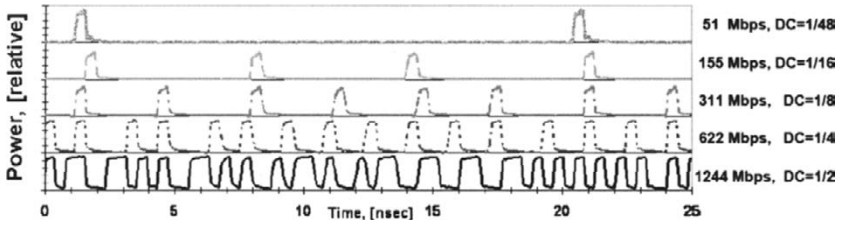

Fig. 35. Measured peak-power-limited (PPL) variable-duty-cycle 2-PPM waveforms at the input to a high-gain average-power-limited EDFA [11].

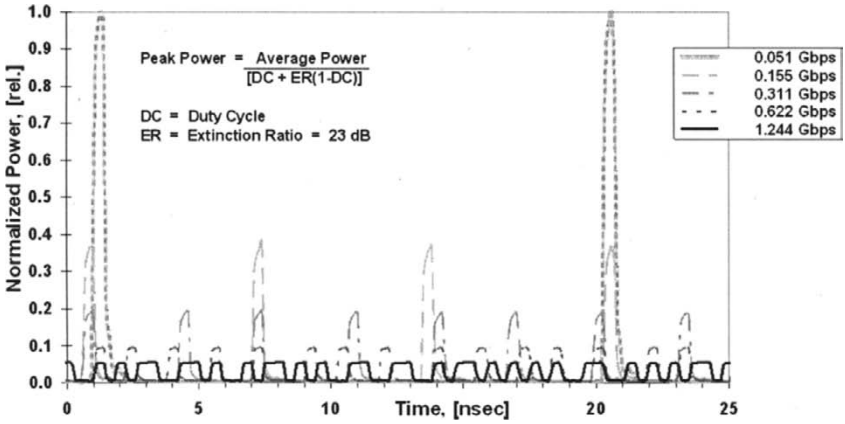

Fig. 36. Measured variable-duty-cycle 2-PPM waveforms at the output of an average-power-limited high-gain EDFA [11]. Reprinted with permission of IEEE. (©1999 IEEE.)

cycle waveforms, i.e., the amplifier acts peak-power-limited in this low frequency regime. Since SOAs have a nanosecond-class upper-state lifetime, the high-pass corner frequency is shifted up towards ~1 GHz, comparable to the Gbit/sec data rates of interest. Owing to these high-pass characteristics, maximum TX power-efficiency is attained whenever the transmitted waveforms have little (power off) spectral content below ~1 GHz, or equivalently, the power-off time is short relative to the upper-state lifetime [172]. For this class of amplifier, power efficiency is optimized for modulation formats that have high ~100% duty-cycles, such as DPSK and FSK, or formats with constrained power-off time such as binary-PPM at rates >~5 Gbps or RZ-DPSK/FSK at rates >~10 Gbps. Outside of these efficiency considerations, communication experiments using an SOA-based MOPA TX have achieved near-quantum-limited receiver sensitivities for binary-PPM, OOK, and DPSK modulation formats, showing that SOA-based transients have little impact on RX sensitivity [172].

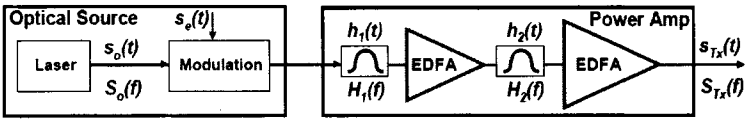

Fig. 37. An average-power-limited MOPA TX. Net optical filtering can comprise multiple pulse-shaping and mid-stage ASE rejection filters, i.e., $h_{\text{net}}(t) = h_1(t) * h_2(t)$, or equivalently, $H_{\text{net}}(f) = H_1(f) \cdot H_2(f)$.

3.5.5. Arbitrary Waveforms and Variable-Duty-Cycle Signaling

The characteristics of an average-power-limited high-gain saturated-EDFA described above provide a flexible and powerful platform for waveform optimization. Once a power amplifier is driven far into saturation, the output power added by the amplifier becomes insensitive to the average input power, making it a stable source of average power. Higher amplifier gain is beneficial since it widens the range of input power levels that can extract the maximum saturated output power. This makes the TX less sensitive to insertion loss changes in the preceding elements that can arise due to modulation or degradation [354], and allows the use of arbitrary waveforms over a wide range of duty-cycles without sacrificing transmitter power efficiency [10].

For the constant average output power delivered by a saturated EDFA, the peak output power is described by

$$P_{\text{peak}} = \frac{\bar{P}}{\text{DC}_{\text{eff}}} \quad \underset{go P_{\text{in}} \gg P_{\text{sat}}}{\Longrightarrow} \quad \frac{P_{\text{sat}}}{\text{DC}_{\text{eff}}} \tag{79}$$

and grows as the duty cycle is reduced. Here we have introduced the term, $\text{DC}_{\text{eff}} = \text{DC}_{\text{mod}}\,\text{DC}_{\text{pulse}}$ to identify the combined influence of both modulation and pulse shape on the effective duty cycle. The impact of variable duty cycle input waveforms (Fig. 35) on the output of a saturated high-gain EDFA is shown in Fig. 36.

Given these basic properties, an average-power-limited MOPA TX can be used to efficiently deliver high-power high-fidelity waveforms of arbitrary type [10], within limitations described below. For instance, a narrow-band electrical waveform $s_e(t)$ can simply be imparted on the CW laser source $s_o(t)$ in Fig. 37 and subsequently amplified without distortion as long as the bandwidth of the net filter $H_{\text{net}}(f)$ is sufficiently wide.

To generate high-fidelity optical waveforms that exceed the available electrical bandwidth, pulse carving techniques described in section 3.5.2 can be used. In this case, the electrical drive waveform could perform additional shaping or serve as a lower-frequency windowing function to select which pulses are transmitted. Additional pulse-shaping can also be performed in the optical domain through subsequent optical filtering, a process that can efficiently generate shaped signaling-waveforms with THz of spectral content. For example $s_o(t)$, could be a windowed short-pulse laser source. The TX output waveform $s_{\text{TX}}(t)$ becomes

$$s_{\text{TX}}(t) = [s_e(t)s_o(t)] * h_{\text{net}}(t) \quad \overset{\text{FT}}{\longleftrightarrow} \quad S_{\text{TX}}(f) = [S_e(f) * S_o(f)]\, H_{\text{net}}(f). \tag{80}$$

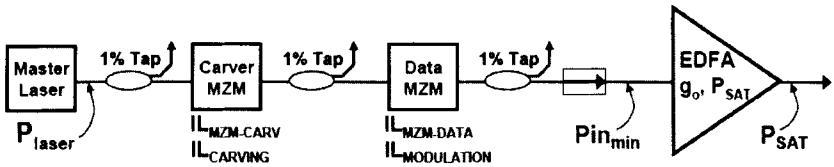

Fig. 38. Variable-duty-cycle pulse-carved MOPA-TX.

For sufficiently short optical pulses, s_o(t) looks like a delta function $\delta(t)$, and $s_{\mathrm{TX}}(t) \rightarrow h_{\mathrm{net}}(t)$. These and other wide-band pulse-shaping techniques (see, e.g., [382]), could, in principle, be incorporated into an APL TX with little impact on overall TX power efficiency.

When using a MOPA configuration with a wide range of variable-duty-cycle waveforms such as those shown in Figs. 35 and 36, the final power amplifier stage needs to run deeply saturated in order to efficiently deliver maximum average power. Efficiency is ultimately limited by the power of the master laser, mid-stage optical filtering and losses, and amplifier gain and noise figure. The impact on transmitter design is illustrated in the representative TX power budget given in Table 9 for the MOPA-TX shown in Fig. 38.

Table 9. Variable-duty-cycle, pulse-carved MOPA-TX power budget.

	Low Duty Cycle	High Duty Cycle
Master Laser Power (P_{laser})	15.0 dBm	15.0 dBm
99:1 PM tap	–0.2 dB	–0.2 dB
Static carver loss ($IL_{MZM-CARV}$)	–3.5 dB	–3.5 dB
Pulse-carving loss	–3.0 dB	–3.0 dB
99:1 PM tap	–0.2 dB	–0.2 dB
Static data mod. loss($IL_{MZM-DATA}$)	–3.5 dB	–3.5 dB
(VDC) Modulation loss	–13.0 dB	–3.0 dB
Isolator	–0.6 dB	–0.6 dB
99:1 PM tap	–0.2 dB	–0.2 dB
Other loss	–0.8 dB	-0.8 dB
Σ = Minimum power delivered to Power Amp PA (Pin_{min})	–10.0 dBm	0.0 dBm
Amplifier small-signal gain (g_o)	50.0 dB	50.0 dB
Efficient power extraction for Psat < Pinmin + go –10 dB	30.0 dBm	40.0 dBm

In this example, an amplifier with a small signal gain of 50 dBm can provide a 10-dB range in duty cycle, and deliver up to 1W (30 dBm) of average power with less than $\frac{1}{2}$ dB loss in efficiency. In order to maintain maximum output power and extend the range of duty cycles, additional gain stages along with inter-stage filtering may be required as discussed in the following Sections. With proper design, a dynamic range of operation in excess of 20 dB can be achieved [354].

3.5.5.1. *Low Duty Cycle Limitations*

As shown in the previous section, careful TX design is necessary to maintain TX efficiency over a wide range of duty-cycles. Several other factors can limit the useful range of duty cycles of a MOPA TX. These include a) limited modulation extinction, b) buildup of ASE, and c) nonlinear impairments.

3.5.5.2. *A) Limited TX Modulation Extinction*

Imperfect extinction can reduce the effective transmitted signal power for low-duty-cycle waveforms (see also section 3.5.2). As seen in Eq. (67), the peak power is a function of the average power, effective duty cycle and extinction ratio. For the case of an EDFA operating deep in saturation, Eq. (67) becomes [314]

$$P_{\text{peak}} = \frac{P_{\text{sat}}}{\text{DC}_{\text{eff}} + \text{ER}(1 - \text{DC}_{\text{eff}})} \quad \underset{\text{ER} \ll \text{DC}}{\Longrightarrow} \quad \frac{P_{\text{sat}}}{\text{DC}_{\text{eff}}}. \tag{81}$$

As the duty cycle becomes low, the average power seeping through the modulator due to imperfect extinction can become significant. For example, for a 1% duty cycle signal and a modulator with a –20 dB ER, the net signal power out of the modulator during the 1% transmission will be about the same as the seepage during the remaining 99%. The subsequent average power limited amplifier will output equal power in both signal and seepage, effectively reducing the transmitted signal power by ~3 dB. The extinction *power robbing* penalty is given by

$$\eta_{\text{TxER}} = \frac{\text{DC}_{\text{eff}}}{\text{DC}_{\text{eff}} + ER(1 - \text{DC}_{\text{eff}})} \quad \underset{\text{ER} \ll \text{DC}_{\text{eff}}}{\Longrightarrow} \quad 1. \tag{82}$$

In order to extract maximum amplified signal power from a saturated EDFA the modulation extinction must be much less than the duty cycle. For less than 0.1 dB "power robbing" penalty due to accumulated signal seepage during the (1-DC_{eff}) *off* portion of the waveform, the ER target should be 15 dB less than the duty cycle, i.e., ER $\leq \text{DC}_{\text{eff}}$ –15 dB. Thus, for 1024-PPM with an 0.1% duty cycle (DC_{eff} = –30dB), an ER better than –45 dB is required. A plot of ER measurements and calculated fit (from Eqs. and associated TX power penalty for a modulator with about –52 dB extinction is shown in Fig. 39. Using this modulator with 1024-PPM waveforms would result in negligible <~0.05 dB TX power penalty.

3.5.5.3. *B) Transmitter ASE*

Transmitter ASE buildup can degrade communication performance in two ways: by limiting the transmitted SNR (SNR_{TX}), and by reducing the transmitter efficiency and transmitted-signal output power. The first relates to the ratio of signal photons to ASE photons within the signal-mode and is independent of TX filtering, whereas the second relates to the ratio of output signal to total ASE power ($\text{TXPowerRatio}_{\text{sig/ASE}}$), and has a strong dependence on optical filtering.

As discussed earlier in section 3.5.3, the conditions of Eq. (73) can be met by simply providing sufficient input signal to the power amplifier. This results in sufficient SNR_{TX}, so that the TX ASE has little impact on communication performance. This

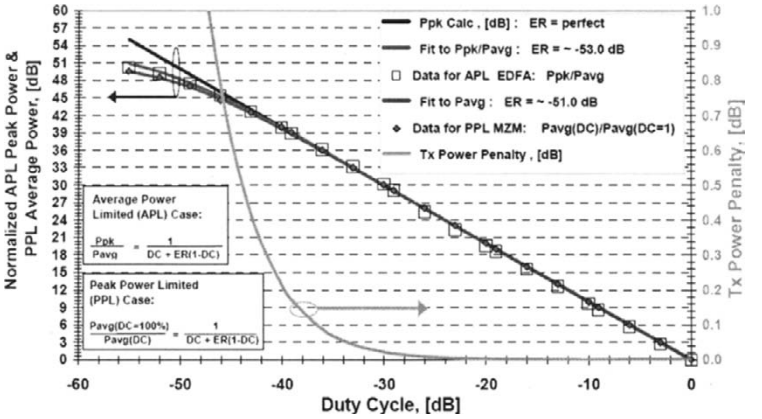

Fig. 39. (Left axis) measurements of modulator extinction using variable duty-cycle techniques described in section 3.5.2. Right axis) TX power penalty [15].

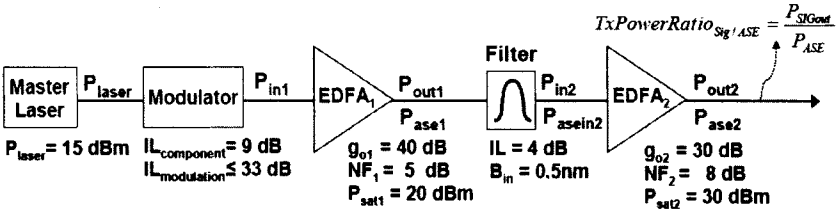

Fig. 40. MOPA transmitter configuration used for modeling the ASE buildup described by Eqs. (83)–(88).

also holds for a cascade of amplifiers, since the net noise figure (and N_{sp}) for the cascade is dominated by the first stage.

However, high-gain multi-stage power amplifiers, can generate significant amounts of broad-band ASE which can reduce the TX power efficiency. With proper design of both the TX power budget and mid-stage optical filtering the $\mathrm{TXPowerRatio}_{\mathrm{sig/ASE}}$ can be optimized. To avoid ASE power robbing, a $\mathrm{TXPowerRatio}_{\mathrm{sig/ASE}} > 20$ dB is desired, meaning more than 99% of the output power is the signal and less than 1% of the TX power is ASE. An example MOPA TX shown in Fig. 40 with a wide operational range of input powers is modeled using Eqs. (83)–(88) [126,142].

$$\mathrm{TxPowerRatio}_{\mathrm{sig/ASE}} = \frac{P_{\mathrm{SIGout}}}{P_{\mathrm{ASE}}}, \tag{83}$$

$$P_{\mathrm{SIGout}} = G\frac{P_{\mathrm{laser}}}{\mathrm{IL}_{\mathrm{component}}\mathrm{IL}_{\mathrm{modulation}}} = GP_{\mathrm{SIGin}}, \tag{84}$$

$$P_{\mathrm{in}} = P_{\mathrm{SIGin}} + P_{\mathrm{ASEin}}, \tag{85}$$

$$P_{\mathrm{ASE}} = (G-1)(N_{\mathrm{sp}}mBh\nu) + GP_{\mathrm{ASEin}} \cdot \min(B/B_{\mathrm{in}}, 1), \tag{86}$$

$$N_{\mathrm{sp}} = \frac{\mathrm{NF}}{2}\left(\frac{G}{G-1}\right) \underset{G\gg 1}{\approx} \frac{\mathrm{NF}}{2}, \tag{87}$$

$$G(P_{\mathrm{in}}, P_{\mathrm{sat}}) = 1 + \left(\frac{g_o}{1 + P_{\mathrm{in}}g_o/P_{\mathrm{sat}}}\right). \tag{88}$$

Here, B is the optical filter bandwidth and m is the number of polarization modes. These equations can be iteratively applied to solve for the cascaded amplifier output signal to ASE power ratio, which depends directly on the signal input power, and varies with the modulation duty cycle. For the first amplifier stage, $P_{\mathrm{ASEin}} = 0$ in Eq. (85). The amplified signal P_{SIGout} and ASE power P_{ASE} from the first amplifier are then used as inputs to the second amplifier stage. Variable-duty-cycle M-ary PPM waveforms are simulated for the binary case ($M = 2$) through 1024-PPM with 50%-RZ pulse carving. The corresponding modulation insertion loss, $\mathrm{IL}_{\mathrm{modulation}} = 1/\mathrm{DC} = 2M$ varies from 6 to 33 dB (assuming perfect ER). Representative elements contributing to the component insertion loss ($\mathrm{IL}_{\mathrm{component}}$) are given in Table 9.

Simulation results for the two-amplifier cascade with a narrow $\frac{1}{2}$ nm (62 GHz) mid-stage filter are shown in Fig. 41. Over the 27-dB range of input powers, the average output power is stable to ~0.5 dB. For M = 1024, with 10 bits of information carried per PPM symbol, the duty-cycle and input power are the lowest, but under these conditions, the APL amplifier generates the highest peak power of 62.5 dBm (~1.8 kW). In this case, the minimum $\mathrm{SNR}_{\mathrm{TX}}$ is ~27 dB and has more than 99% of TX output power in the signal with $\mathrm{TXPowerRatio}_{\mathrm{sig/ASE}}$ >22 dB.

3.5.5.4. *C) Nonlinear Impairments*

Optical nonlinearities are another factor that can impact low duty cycle transmission through a saturated average-power-limited transmitter. Fast nonlinear effects such as self-phase modulation (SPM), four-wave mixing (FWM), and Stimulated Raman Scattering (SRS) tend to shift usable signal power out of band, an effect that reduces transmitter efficiency and makes an average power limited amplifier appear peak power limited. Nonlinear effects occur when the peak power exceeds a threshold

$$P_{\mathrm{th}} \propto \frac{A_{\mathrm{eff}}}{g_{\mathrm{NL}}L_{\mathrm{eff}}}, \tag{89}$$

in which A_{eff} is the effective area, G_{NL} is the nonlinear gain coefficient (a material property), and L_{eff} is the effective propagation length [110,111]. Standard steps to increase the nonlinear threshold include using larger core fiber (which reduces the power density), minimizing amplifier lengths [383], and distributing amplified signal energy in time to lower the effective peak power through the amplifier. A summary of high power amplifier design options and tradeoffs is given in Table 10.

Practically, P_{th} can be defined as the peak output power when greater than ~1% of the average amplifier output is contained in the nonlinear induced spectrum. Typically,

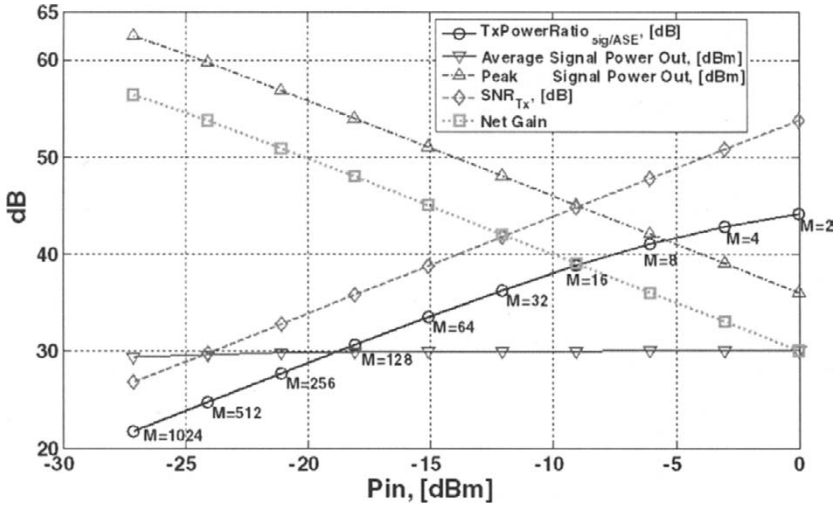

Fig. 41. Simulated amplifier signal to ASE power ratio ($\mathrm{TXPowerRatio_{sig/ASE}}$ in circles), average signal output power (down-pointing triangles), peak signal output power (up-pointing triangles), TX SNR (diamonds), and net amplifier gain (squares) as a function of input power.

P_{th} is about 250W to 1kW in commercially available EDFAs [21,198,199], although promising research-grade EDFAs have generated 100 kW-class peak power with little or no nonlinear effects [224]. Once beyond P_{th}, the nonlinear effects rapidly dominate. For the MOPA TX modeled above, the lowest duty cycle generated a peak power of $\sim$1.8 kW, which can lead to prohibitive nonlinear impairments in conventional power amplifiers. Such effects are illustrated in Fig. 42.

Note that the signal at $\sim$1557 nm is $>$ 33 dB larger than the amplifier ASE which peaks at $\sim$1567 nm for this amplifier. Therefore the net ASE power is less than 1% of the net transmitted power and can be neglected. As the peak power of the amplifier is increased (by lowering the duty cycle of the input), nonlinearities appear. The combined effects of dispersion and SPM can lead to *modulation instability* [111], which can generate spectral sidebands around the signal. These are often the first noticeable nonlinear effect. SPM on its own can broaden the amplified signal spectrum, although this is not as apparent when viewing the broad band optical spectrum. As the peak power continues to increase, the nonlinearly-induced side bands grow and take a larger percentage of the amplifier output power. For this amplifier, SRS tends to dominate at higher peak powers, shifting the optical spectrum to the longer wavelengths. As the peak power is increased further the SRS-generated spectral components can extend beyond 100 nm, stealing a significant portion of the net amplifier output power.

Another nonlinear effect is stimulated Brillouin scattering (SBS) which is a slow nonlinearity that scatters light in the backward direction. This attenuates the forward propagating signal, reducing the TX efficiency and can lead to catastrophic damage in the final amplifier stage due to SBS induced Q-switching. In standard single-mode fiber with an effective area of 50 $\mu\mathrm{m}^2$, an estimate of the SBS power-length threshold

Table 10. Design options for stable high-peak-power single-mode (spatial and temporal) wave guide amplifiers.

#	Option	Benefit	Limitation	Drawback
1	Larger core fiber	~2 – 10 x	Multimode operation	• Poor fiber coupling • Reduced NA • Coupling loss • Sensitive to bend loss
2	Minimize fiber lengths through higher doping concentration	~2 – 4 x	Maximum doping concentrations in fused silica	• Dopants may lead to enhanced radiation sensitivity for space-based applications • Reduced power efficiency
3	Coiled multimode [224, 384]	~100 x	Efficiency of fundamental mode	• Induced polarization dependence • Reduced power efficiency • Reliability of coiled fiber • Research grade only
4	Self-imaging waveguide [385]	~100 x	Technical, doping levels	• Coupling efficiency and stability • Thermal and modal stability • Research grade only
5	Post amplified chirped pulse compression	~2 – 4 x	Maximum chirp and compensation	• Reduced power efficiency • Potential for waveform distortion
6	WDM distribution [22]	~100 x	• Complexity and cost (SWAP) • Available optical bandwidth • FWM efficiency reduction	• Increased complexity, cost, and SWAP over single channel • FWM nonlinearities may lead to data-dependent power efficiency reduction, which can lead to an error floor without FEC

is ~20 W m within the ~50 MHz Brillouin linewidth. However, in contrast with the ultra-fast SPM and SRS nonlinearities, SBS has a narrow gain bandwidth ($\Delta\nu_b$ <~50 MHz), and therefore, can be mitigated by broadening the signal spectrum. This can be achieved with the use of short duration signaling waveforms or inducing additional phase modulation [110,111]. For example, by using short 100 ps pulsed waveforms with ~10 GHz class bandwidth, this threshold can be increased by a factor of 200, to ~4 kW m. In addition to the nonlinear mitigation techniques highlighted in Table 10, SBS can be suppressed through temperature gradients in the fiber [374]. As a result of the temperature dependent Brillouin frequency shift, temperature segmentation of the high-power-handling fiber can be used to disrupt the SBS phase matching, yielding up to 7 dB suppression [386].

The use of WDM (Fig. 43) to reduce peak power by distributing the amplified signal energy over many wavelengths is particularly attractive for use in communication systems employing strong FEC. This approach directly reduces slow SBS effects by lowering the peak power within the SBS bandwidth. However, fast SPM, FWM, and SRS nonlinearities have many THz of bandwidth, so the benefits of this approach occur only when the WDM signals do not overlap in time for relatively short, ~10 m amplifier lengths. Fortunately, as the duty cycles get lower and peak power impairments grow, the probability of pulse overlap is reduced. Nonlinear impairments that occur due to

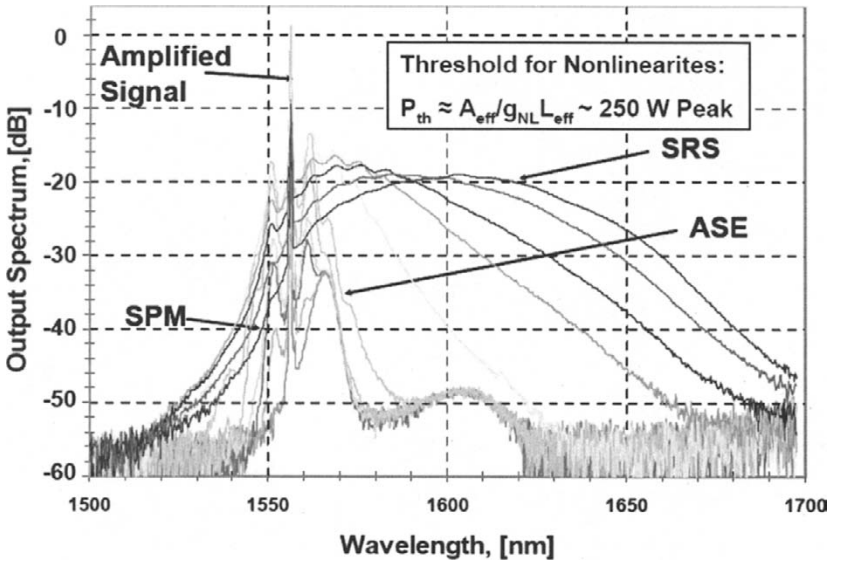

Fig. 42. Nonlinearly-induced spectrum for several peak output powers in an Er:Yb doped cladding pump amplifier. The bottom trace shows the amplified signal spectrum from a 4-W EDFA without any nonlinear effects. Fiber nonlinearities can generate new spectral components which shift usable signal power out of band, effectively making an average-power-limited amplifier look peak-power-limited [21].

sporadic pulse overlap can cause a pattern-dependent performance degradation. But as long as these events occur infrequently enough, they can be compensated for by FEC.

Consider, for example, a 10-W MOPA-TX with $P_{\rm th} = \sim 1$ kW using square 1024-PPM waveforms, and a receiver employing FEC with an error-free cutoff at a 10^{-3} error rate. Single-channel peak powers would be ~ 10 kW. By distributing the TX over 32 wavelengths, the peak-power per channel is reduced to 320 W. But the aggregate peak power can be higher due to multi-channel pulse overlap. Assuming equal probability for each PPM symbol and time-alignment between the independent channels, an upper-bound for the probability distribution of peak aggregate power is shown in Fig. 44 for 8, 16, 32, and 64 WDM channels.

For the 32-channel configuration, the overlap of 3-pulses yields a peak power of 960kW, below $P_{\rm th}$. The overlap of 4-pulses yields a peak power of 1.28 kW, above $P_{\rm th}$, but with a probability $< 3 \times 10^{-5}$, well below the FEC error cutoff. Therefore, the WDM signal distribution over 32 channels effectively suppresses broadband nonlinear impairments by about a factor of ten. This corresponds to the ratio of the number of WDM channels, w, to the effective number of pulses that overlap with a probability greater than the FEC threshold rate, $\kappa_{\rm eff}$, which is 3 in the example above. The effective peak power then becomes

$$P_{\rm pk}^{\rm eff} = \left(\frac{\kappa_{\rm eff}}{w}\right) \frac{\bar{P}\cdot}{DC_{\rm eff}}. \tag{90}$$

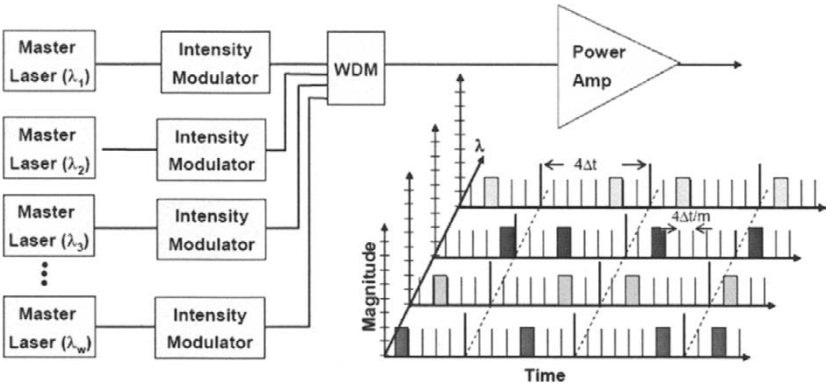

Fig. 43. M-PPM/WDM waveforms illustrating the WDM method of diminishing peak signal power by distributing it over many wavelengths Relative to a single channel TX of same duty cycle, average power, and symbol time Δt, a w-channel WDM transmitter reduces the peak power and bandwidth of each channel by a factor of w [22]

This benefit could be furthered by intentionally staggering the time alignment of the WDM channels to reduce κ_{eff}.

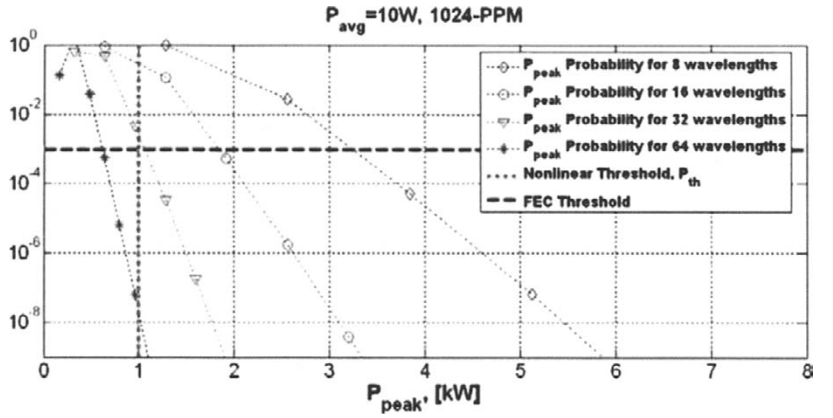

Fig. 44. Peak power probability distribution due to pulse overlap in a 10-W average power 1024-PPM multi-channel WDM MOPA TX. The pulses are assumed to be synchronized, so that the overlap, when it occurs is complete. Note that the resulting peak powers occur at discrete levels, depending on the integer number of pulses that overlap. Also shown are representative thresholds for the onset of nonlinear effects (vertical dotted line) and FEC cutoff (horizontal dashed line) [22,479] that break the chart into 4-quadrants. BER performance will be degraded for curves with points contained within the upper-right quadrant.

The use of WDM has additional advantages. First, it increases the average input to the TX power amp, which reduces the amplifier gain and output ASE, and improves the output signal-power to ASE ratio. It is also a means of overcoming electronic bandwidth and performance limitations, enabling scaleable data-rates that can leverage the available THz optical spectrum.

4. Receiver Technologies

Along with photon and power efficiency, important receiver metrics include reliability, especially in the space environment, and performance in the presence of background noise and atmospheric channel effects. In this section we will present the relative performance of photon-counting, coherent-homodyne, and preamplified receivers. Systems based on these technologies show the most promise for next generation solutions for ultra-long distance communication.

For a quantum-limited optical receiver, the SNR of received optical signals is ultimately limited by the number of photons/bit, which is independent of the shape the waveform. This leads to flexibility in the receiver to accept waveforms of arbitrary shape. The average-power-limited properties of optical power amplifiers discussed in section 3 allow similar freedom in waveform generation. This combination enables the use of aggressive pulse shaping to efficiently match the TX signal waveform to realizable RX filters. Furthermore, there is abundant optical spectrum available which eliminates channel bandwidth limitations and enables excess spectrum to be traded for improved sensitivity through modulation and coding.

Note that there is an important distinction between the quantum-limited SNR defined in Eq. (32) and the optical SNR (OSNR), which is a commonly used metric for accessing communication performance in fiber-based WDM systems. As discussed in section 2.3.5, the quantum-limited SNR is an absolute measure of SNR relative to quantum-noise ($h\nu$), equivalent to the incident number of photons/bit (for direct-detection receivers) regardless of signal shape. This is not necessarily the case for relative measurements of OSNR, which are often determined by measuring the signal and out-of-band noise power within a specified bandwidth, typically 0.1 nm. The signal power estimated using this technique can vary with pulse-shape, which can lead to dB-class waveform-dependent OSNR errors without proper calibration. Moreover, since the noise power can be much larger than the quantum noise, OSNR measurements of this type are generally a poor measure of absolute receiver sensitivity—the relevant metric for most free-space applications.

4.1. Direct Detection–PIN

The most common receiver for high-speed optical communications is the PIN-photodiode-based detector[10] shown in Fig. 45. PIN detectors can be extremely wide-band, with DC to 50+ GHz response commercially available. While PIN-based receivers are relatively simple, they are the least sensitive and require careful front-end electronic design to achieve good high-rate performance [20,39,387].

[10] The PIN or p-i-n photodiode is a semiconductor-based detector structure with an intrinsic (i) region in between n- and p-doped regions. Relative to p-n photodiodes, PIN detectors have a thicker depletion region,

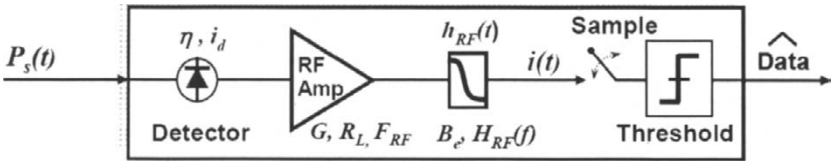

Fig. 45. Schematic of PIN-based direct-detection receiver with input waveform $s(t)$, electrical amplification with load resistance R_L, gain G and noise figure F_{RF}, postdetction filtering with impulse response $h_{\mathrm{RF}}(t)$ and effective electrical bandwidth B_e [see Eq. (39)], prior to sample and thresholding circuitry.

In section 2.3.5, we introduced the subject of shot-noise in the ideal detection process [(see Eqs. (32) and (35)–(40)]. In practice other noise sources such as dark current i_d and thermal noise contribute to the SNR, with

$$\sigma_{\mathrm{th}}^2 = (4k_BT/R_L)F_{\mathrm{RF}}B_e \quad [\mathrm{amps}^2], \tag{91}$$

$$\sigma_{\mathrm{sh}}^2 = 2q(i_s + i_d)B_e, \quad [\mathrm{amps}^2], \tag{92}$$

where σ_{sh}^2 is the shot noise resulting from signal and dark current, and σ_{th}^2 is the thermal noise generated in the load resister R_L [216] scaled by the amplifier noise figure F_{RF} [20, 111]. Incorporating these noise sources into the direct-detection SNR expression in Eq. (40) we obtain

$$\mathrm{SNR}_{\mathrm{DD}} = \frac{\langle i_s \rangle^2}{\sigma_{\mathrm{sh}}^2 + \sigma_{\mathrm{th}}^2} = \frac{\left(R_{\mathrm{A/W}}P_s\right)^2}{2q(R_{\mathrm{A/W}}P_s + i_d)B_e + (4k_BT/R_L)F_{\mathrm{RF}}B_e}, \tag{93}$$

where P_s is the incident signal power, and $i_s = R_{\mathrm{A/W}}P_s$ is the signal photocurrent. The detector responsivity $R_{\mathrm{A/W}} = \eta q/hv = 1$ mA/mW at 1.55 μm, for detection efficiency $\eta = \sim 0.8$, causing a $\sim$1 dB reduction in detected power. When $\sigma_{\mathrm{sh}}^2 \gg \sigma_{\mathrm{th}}^2$, Eq. (93) converges to the quantum-limited SNR in Eq. (40), as expected.

Amplifier noise is often given in terms of thermal noise current density i_{th} [pA/Hz$^{1/2}$], which incorporates both thermal noise and amplifier excess noise. This results in a current noise variance $\sigma_{\mathrm{th}}^2 = i_{\mathrm{th}}^2 B$ [amps^2], and corresponds to an effective resistance $R_{\mathrm{eff}} = 4k_BT/i_{\mathrm{th}}^2$. While thermal noise is a white noise source, RF amplifiers can add frequency dependent $1/f$ noise, which further degrades the SNR at frequencies below $\sim$100 MHz [20]. Relative to the dominant thermal noise, the few nanoamp dark current typical of detectors at 1.55 μm can be neglected in Eq. (93).

To relate the signal and noise terms to OOK communication performance, we introduce the Q-factor, which can be expressed as

$$Q = \frac{i_1 - i_0}{\sigma_1 + \sigma_0} = \frac{R_{\mathrm{A/W}}P_s\,(1 - \mathrm{ER})}{\sqrt{2q(R_{\mathrm{A/W}}P_s(1 + \mathrm{ER}) + i_d)B_e} + 2\sqrt{(4k_BT/R_L)F_{\mathrm{RF}}B_e}}, \tag{94}$$

which improves detection efficiency and reduces capacitance, resulting in wider bandwidth—making them well suited for communications applications.

where $i_{1,0}$ and $\sigma_{1,0}$ are mean signal photocurrent and noise terms for the '1' and '0' symbols, respectively, and ER $= i_0/i_1$ is the modulation extinction ratio (see section 3.5.2), ideally equal to 0. With optimized thresholding, the bit-error-rate (BER) can be estimated by the Q-function given in Eqs. (8) and (9), with the Q-factor above as the argument. A 10^{-9} BER is achieved for $Q = 6$.

To reduce the impact of thermal noise, the load resistance can be increased using transimpedance amplifiers (TIAs). However, due to residual capacitance this limits the bandwidth of the system to about $(2\pi \mathrm{RC})^{-1}$ [20]. Commercial 1-kΩ TIAs are available with B_e = 7 GHz suitable for 10 Gbps communications. Typical thermal noise current for this class of devices is $i_{\mathrm{th}} = \sim 7$ [pA/Hz$^{1/2}$], which corresponds to R_{eff} = 320 Ω, or equivalently $F_{\mathrm{RF}} = \sim 5$ dB. For these parameters, the 10^{-9} BER can be achieved with –21dBm power incident on the detector, which corresponds to ~6200 PPB.

Another means of improving the performance of direct-detection RXs limited by thermal noise is to use low-duty-cycle return-to-zero (RZ) impulsive coding. As noted by Personick [39] in 1973, and more recently, demonstrated by Boivin et al. [343], such techniques can lead to several dB enhancement of RX sensitivity. Discussion of the transmitter considerations of using such waveforms is given in section 3.5.5, and we elaborate on the use of this class of waveforms in section 5.1 for preamplified receivers. For further details on optimizing the direct-detection RX, we refer the reader to thorough analysis by Winzer and Calmar [345].

We note that while PIN-based RX performance is far from ideal, it provides a basis for understanding the benefits of techniques used to achieve near quantum-limited RX sensitivities discussed in the following sections.

4.2. *Direct Detection Avalanche-Photodiode (APD)*

APDs can improve performance over PIN detectors by providing internal gain within the detection process, which multiplies the photocurrent by an average factor of M. However as with any amplification process it is not noiseless. The resulting direct-detection SNR expression becomes [20,121,236]

$$\mathrm{SNR_{DD}} = \frac{i_{\mathrm{avg}}^2}{\sigma_i^2 + \sigma_{\mathrm{th}}^2} = \frac{\left(R_{\mathrm{A/W}} P\right)^2}{2qF_{\mathrm{APD}}(i_{\mathrm{avg}} + i_d)B_e + (4k_B T/R_L)F_{\mathrm{RF}} B_e/M^2}, \tag{95}$$

where F_{APD} is the excess noise factor associated with variations in M. The thermal noise term is reduced by M^2 relative to the PIN detector, whereas the shot-noise term is increased by F_{APD}, which generally grows with M. Typical values of M range from ~3 to 100, corresponding to F_{APD} values of 2 to 10, although these values are vary considerably depending on wavelength, data rate, and technology. At rates of 10 Gbps, $M = \sim 3$ to 10, and $F_{\mathrm{APD}} = \sim 4$, providing about a 10-dB benefit over PIN-receivers, with 10^{-9} BER achieved for –29 dBm or ~1000 PPB receiver sensitivity (see, e.g., [388,389]). At lower rates—less than 1 Gbps, APDs have demonstrated performance in the 100 to 200 PPB regime [390–392]. However, PIN-based RXs offers superior bandwidth and dynamic range of operation, and are less temperamental, offering robust performance over a wide range of environmental conditions.

4.3. Direct Detection–Photon Counting

Qualitatively, photon-counting detectors can be viewed as an extension of APD-type detectors with infinite gain in which, a digital output signal is generated for each detected photon. Due to the binary nature of the detection output, noise in the detection process appears in the form of dark counts or varying detection efficiency, and the detector is limited to counting at most one photon per reset time. As a result, the detector is blinded after a detection event, missing all incident photons until reset, an effect which is referred to as blocking loss [34,35]. Detector arrays can be used to extend the dynamic range of detected signal to multiple counts per-interval and mitigate blocking loss, although this comes at the expense of increased dark count rate.

Photon-counting receiver architectures have been proposed [1,26,43,169,170,393] and realized at Mbit/s [44] and ~Gbit/s [33,34] data rates with the best demonstrated coded RX sensitivities near 1 photon/bit (PPB), with potential for improvement to multiple-bits/photon sensitivities and greatly simplified processing due to the digital nature of the counting process.

However, these photon-counting RXs are presently limited to power-starved links with little or no background noise and <~Gbit/sec rates due to dark-count and reset-time constraints, which preclude their use with the sun in the field of view. Rates are also limited by the need of near-Shannon-limited-capacity coding [42,394] needed to avoid performance degradation due to dark counts, blocking losses, and background noise. These powerful FEC codes place additional burden on the RX electronics in terms of SWAP and bandwidth constraints[45]. Also, the suitability of the key detector technologies, Geiger-mode avalanche photodidode (GM-APD) arrays [32] and superconducting single photon counting detectors SSPDs [222] has not yet been established in the space environment. Si-based GM-APDs, for example, have shown sensitivity to radiation [395], and SSPDs require cooling to cryogenic temperatures, requiring a significant overhead in SWAP.

For ground-based receivers, however, where reliability and receiver SWAP are not a driving limitation, these technologies offer significant potential. Unlike coherent and preamplified RXs, these photon-counting detectors can receive multiple spatial modes and can efficiently collect signals distorted by the atmospheric channel without the need for wavefront correction. Furthermore, the net detection area can be efficiently scaled in distributed telescope arrays without the need to build large and costly telescopes [396].

The scalable-multimode-detection capability of photon-counting RXs comes with the expense of increased sensitivity to background noise, which is enhanced by the broad, several-hundred-nanometer spectral response of the detectors. However, the background can be mitigated with the use of single-polarization narrow-band low-loss high-rejection spectral filtering. Such filtering can be implemented using a cascade of loss-loss volume-Bragg-grating [397] and etalon filters with ~0.5 –1 dB insertion loss and noise-equivalent bandwidth of 0.01 to 0.1 nm over a spectral range exceeding 500 nm .[398]. Thus, many of the key elements needed for high-performance photon-counting receivers have been reduced to practice [44]. As the detector technologies mature, they may become the technology of choice for future ground and space-based receiver solutions.

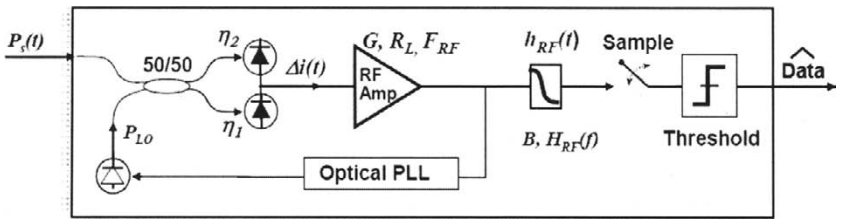

Fig. 46. Schematic of balanced coherent homodyne PSK receiver.

4.4. Coherent Homodyne Receivers

Coherent receivers are another means of boosting the shot noise relative to the thermal noise though coherent gain in the detection process. Homodyne detection of binary-PSK provides among the best theoretical RX sensitivity and is spectrally efficient. Coherent mode-matching requirements combined with matched electrical filtering also provide superior rejection of background noise over multi-mode receivers, which could enable, for example, improve communication performance with the sun in the field of view as noted in section 2.3.7. Information is carried in the phase $\phi_m(t)$ of the optical carrier and demodulated using a balanced receiver shown in Fig. 46.

The signal is received in one port of a 50/50 coupler and a local oscillator (LO) laser of the same frequency is injected into the other input port. The signal and LO mix at the two balanced square-law detectors, and generate a difference photocurrent that is given by [20,156,236]

$$\Delta i(t) = \left((\eta_1 - \eta_2) \left(\frac{P_{\rm LO}}{2} + \frac{P_s}{2} \right) + 2\eta_{\rm avg} \sqrt{P_s P_{\rm LO}} \cos\left(2\pi \Delta f t + \Delta\phi + \phi_m(t)\right) \right) \frac{q}{h\nu}$$

$$\xrightarrow[\substack{\eta_1=\eta_2=\eta \\ f_s=f_{\rm LO}}]{} \quad \frac{2\eta_{\rm avg}}{h\nu} \sqrt{P_s P_{\rm LO}} \cos\left(\Delta\phi_m(t)\right) \quad \text{[amps]}, \tag{96}$$

where $\eta_{\rm avg} = (\eta_1 + \eta_2)/2$ is the average detection (ideally equal to one), Δf and $\Delta\phi$ are the frequency and phase differences between LO and signal, that are set to zero with feedback from an optical phase-locked loop [153,156,166, 99], and $\phi_m(t)$ contains the (0 or π) phase modulation. The resulting SNR is given by [20, 156, 236]

$$\begin{aligned} {\rm SNR}_{\rm PSK} &= \frac{i_{\rm avg}^2}{\sigma_{\rm sh}^2 + \sigma_{\rm th}^2 + \sigma_{\rm LO}^2} \\ &= \frac{4R_{\rm avg}^2 P_s P_{\rm LO}}{2q(R_{\rm avg} P_{\rm LO})B + \sigma_{\rm th}^2 + (\eta_1 - \eta_2)\, P_{\rm LO}({\rm RIN})B}, \end{aligned} \tag{97}$$

where the shot noise term is due to the LO power and $R_{\rm avg} = \eta_{\rm avg} q/h\nu$. The local oscillator noise term $\sigma_{\rm LO}^2$ is the due to excess relative intensity noise (RIN) in the LO, which vanishes when the two detectors have the same detection efficiency [400,401]. In this case, the shot noise power can become the dominant noise source by increasing $P_{\rm LO}$. In the limit when $\sigma_{\rm sh}^2 \gg \sigma_{\rm th}^2$:

$$\mathrm{SNR_{PSK}} = 2\frac{\eta_{\mathrm{avg}} q P_s}{h\nu B} = 4\mathrm{SNR_{DD}}, \tag{98}$$

four times the SNR of ideal direct-detection. Even in the shot-noise limit, the SNR is proportional to the detection efficiency η_{avg}, meaning any detection losses, including spatial or polarization mode-mismatch, directly impact RX sensitivity.

However, in practice the high-sensitivity potential of optical PSK has not yet been realized, in part due to challenging component and laser linewidth requirements, the need for high-detection efficiencies, signal-LO polarization mismatch, and difficulties associated with phase-locking the local-oscillator [156,399]. In the Gbit/s regime the best reported uncoded PSK performance is ~35 PPB at ~6 Gbit/s and ~80 PPB at ~8 Gbps [158], providing little performance benefit over optically preamplified DPSK [24,25,133], which is WDM scalable and easier to implement (see Differential Phase Shift Keying (DPSK) in section 5.2). At lower rates < 1 Gbps, PSK performance is somewhat better, with uncoded RX sensitivities of 16 and 20 PPB at 4 and 565 Mbps, respectively [157,195].

Some of the reduction in PSK sensitivity at high data rates can be understood through the expression for SNR degradation in Eqs. (99) and (100). To the extent that the shot noise does not overwhelm all other sources of noise in the receiver, the SNR is degraded by

$$\Delta\gamma = 10\log_{10}\left(1 + \frac{\sigma_{\mathrm{th}}^2}{\sigma_{\mathrm{sh}}^2}\right) = 10\log_{10}\left(1 + \frac{i_{\mathrm{eq}}}{i_{\mathrm{avg}}}\right), \tag{99}$$

$$i_{\mathrm{eq}} = \frac{2k_B T}{qR_L} \quad [\mathrm{amps}], \tag{100}$$

where i_{eq} is the equivalent photocurrent needed to make $\sigma_{\mathrm{sh}}^2 = \sigma_{\mathrm{th}}^2$. For $\mathrm{R}_L = 50\Omega$ at 290K (room temperature), i_{eq} = 1 mA which corresponds to ~1 mW.

In order for shot noise to dominate thermal noise, large photocurrent or load resistance is required. For a maximum photocurrent of ~1 mA and $R_L = 50\Omega$ the shot noise and thermal noise are equal and the SNR is halved. This penalty can be reduced by boosting R_L, at the expensive of limiting the bandwidth due to residual capacitance in the TIA. Furthermore, as noted in the Direct detection—PIN section, the effective resistance in wide band TIAs is often limited by excess noise to ~300 Ω, which for a ~1 mA current reduces the RX sensitivity by > 1/ 2 dB.

Thus, the design of the front-end receiver electronics in coherent receivers remain critical [402]. At high data rates, achieving near-quantum-limited performance with coherent-homodyne PSK receivers is challenged by a combination of detection-efficiency, photocurrent, and transimpedance-gain limitations, whereas at lower data rates, laser-linewidth, RIN, and $1/f$ noise impose additional constraints [20]. In the following sections, we discuss the use of low-noise high-gain wide-bandwidth preamplification as a means of overcoming thermal noise and bandwidth limitations in the detection process, and reducing the impact of the front-end design on receiver performance.

4.5. Optically Preamplified Direct Detection

Preamplified RXs can directly leverage the field-tested heritage of telecom-type 1.55 μm technologies that are compatible with operation in the space environment and

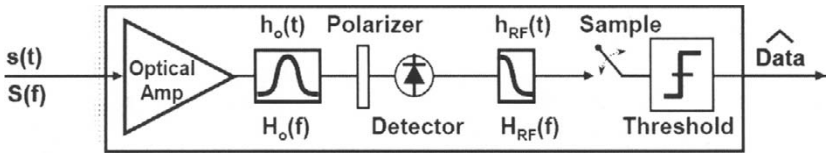

Fig. 47. Schematic of an optically preamplified receiver with input signal $s(t)$, optical and RF postdetction filters $h_o(t)$ and $h_{\mathrm{RF}}(t)$, respectively, optional polarizer, and sample and thresholding circuitry.

have demonstrated the best sensitivities at high data-rates (>∼Gbit/s) of 25–30 PPB for uncoded DPSK and 7–10 PPB with coding [24,25,133]. With the use of M-ary orthogonal modulation formats, RX sensitivities can approach the 1–2 PPB regime albeit with substantial bandwidth expansion [15,22]. In this case, the use of hybrid modulation formats including frequency, position, and polarization modulation along with WDM rate scaling can be used to access the many THz available in EDFAs at 1.55 μm and/or YDFAs at 1.06 μm, and overcome electronic bandwidth limitations. We address these modulation possibilities further in section 5.3.

In sections 3.5.3 and 3.5.5, we introduced some of the high-level characteristics of EDFA performance from the transmitter perspective. Here we provide additional detail on the impact of amplifier noise on SNR and receiver sensitivity. The noise processes in EDFAs and impact on receiver performance has been discussed extensively in the literature e.g., [20,36–38,76,77,126,336,340,403–406]. The basic optically preamplified receiver setup is shown in Fig. 47.

The signal field $s(t)$ with power $P_s(t) = |s(t)|^2$ is amplified by a factor of G which adds $\mathrm{GN_{sp}}$ noise photons per mode with noise power spectral density $N_{\mathrm{ASE}} = mh\nu GN_{\mathrm{sp}}$ [W/Hz]. Here, m is the number of polarization modes, and N_{sp} is the spontaneous emission factor of the amplifier (NF = $2N_{\mathrm{sp}}$). Out-of-band amplifier noise (ASE) is removed by optical filter $H_o(f)$, with field impulse response $h_o(t)$. The mean detected signal current is given by

$$i_{\mathrm{avg}}(t) = R_{\mathrm{A/W}} G\,|y(t)|^2 \underset{B_o \gg B_s}{\approx} R_{\mathrm{A/W}} G P_s(t), \tag{101}$$

where B_o and B_s are the noise equivalent bandwidths of the filter $H_o(f)$ and signal $S(f)$ spectra respectively, and

$$y(t) = s(t) * h_o(t) = \int_0^t s(t-\tau) h_o(\tau) d\tau \tag{102}$$

is the filtered signal field incident on the detector. Due to the square-law detection process, like-polarized signal and noise components mix, generating S × ASE and ASE × ASE noise terms in addition to shot-noise σ^2_{sh} and thermal noise σ^2_{th}. After the postdetection filter noise-terms are given by [344,345]

$$\sigma^2_{\mathrm{ASE}\times\mathrm{ASE}} = \int_{-\infty}^{\infty} d\tau_1 h_{\mathrm{RF}}(t-\tau_1) \int_{-\infty}^{\infty} d\tau_2 h_{\mathrm{RF}}(t-\tau_2) 2N^2_{\mathrm{ASE}} \left|R_o(\tau_1-\tau_2)\right|^2, \quad (103)$$

$$\sigma^2_{S\times\mathrm{ASE}}(t) = \mathrm{Re}\left\{ \int_{-\infty}^{\infty} d\tau_1 h_{\mathrm{RF}}(t-\tau_1) \times \int_{-\infty}^{\infty} d\tau_{21} h_{\mathrm{RF}}(t-\tau_2) 2N_{\mathrm{ASE}} y^*(\tau_1) R_o(\tau_1-\tau_2)\, y(\tau_2) \right\}, \quad (104)$$

$$\sigma^2_{\mathrm{sh}} = 2q(R_{\mathrm{A/W}} G P_s + mGN_{\mathrm{sp}} B_o + i_d) B_e, \quad (105)$$

$$\sigma^2_{\mathrm{th}} = (4k_B T/R_L) F_{\mathrm{RF}} B_e, \quad (106)$$

where $R_o(t) = h_o(t) * h_o(t)$ is the filter autocorrelation, $h_{\mathrm{RF}}(t)$ is the RF (electrical) filter impulse response, and B_e is the noise equivalent bandwidth of RF filter given in Eq. (39). For square optical filter $H_o(f)$ and $P_s(t)$ constant, Eqs. (103) and (104) reduce to [20, 37, 126]

$$\sigma^2_{S\times\mathrm{ASE}} \approx 4R^2_{\mathrm{A/W}} G P_s N_{\mathrm{ASE}} B_o = 4q^2 N_{\mathrm{sp}} \eta^2 G^2 \frac{P_s}{h\nu} B_o, \quad (107)$$

$$\sigma^2_{\mathrm{ASE}\times\mathrm{ASE}} \approx mR^2_{\mathrm{A/W}} N^2_{\mathrm{ASE}} B_e (2B_o - B_e) \approx m \left(N_{\mathrm{sp}} \eta q G B_o\right)^2, \quad (108)$$

and the expression for SNR becomes

$$\mathrm{SNR}_{\mathrm{Preamp}} = \frac{\left(P_s R_{\mathrm{A/W}} G\right)^2}{\sigma^2_{\mathrm{sh}} + \sigma^2_{\mathrm{th}} + \sigma^2_{S\times\mathrm{ASE}} + \sigma^2_{\mathrm{ASE}\times\mathrm{ASE}}} = \frac{\left(P_s \frac{\eta q}{h\nu}\right)^2}{\frac{\sigma^2_{\mathrm{sh}}}{G^2} + \frac{\sigma^2_{\mathrm{th}}}{G^2} + m\left(N_{\mathrm{sp}} \eta q B_o\right)^2 + 4q^2 N_{\mathrm{sp}} \eta^2 \frac{P_s}{h\nu} \frac{B_e}{B_o}}, \quad (109)$$

where we have assumed $B_o = \sim B_e$, a subject discussed further in section 5.1.2.

For large gain, optical bandwidth, and bit rate (e.g., $G > \sim$40 dB, $B_0 > 1$ GHz, and $R_b >$ 1Gbps), the σ^2_{sh} and σ^2_{th} terms are overwhelmed by the $\sigma^2_{S\times\mathrm{ASE}}$ and $\sigma^2_{\mathrm{ASE}\times\mathrm{ASE}}$ terms. For $m = 1$ and N_{sp}= 1, when

$$\frac{P_s}{h\nu} = \frac{B_o}{4}, \quad (110)$$

$\sigma^2_{S\times\mathrm{ASE}}$ and $\sigma^2_{\mathrm{ASE}\times\mathrm{ASE}}$ terms become equal [20]. Normalizing Eq. (110) by the bit rate this condition becomes

$$\frac{P_s}{h\nu R_b} = \mathrm{PPB} = \frac{B_o}{4R_b} \approx \frac{1}{4}. \quad (111)$$

For these filtering conditions ($B_o \approx B_e \approx R_b$), this implies that whenever the number of photons/bit $\gg$ 1/4, $\sigma^2_{S\times\mathrm{ASE}} \gg \sigma^2_{\mathrm{ASE}\times\mathrm{ASE}}$. In this case, Eq. (109) becomes

$$\mathrm{SNR}_{\mathrm{Preamp}} = \frac{\left(P_s R_{\mathrm{A/W}} G\right)^2}{\sigma^2_{S\times\mathrm{ASE}}} = \frac{P_s}{4h\nu B_e} = \frac{\mathrm{SNR}_{\mathrm{DD}}}{2}, \quad (112)$$

and we approach $\frac{1}{2}$ shot-noise limited direct-detection performance as expected due to the 3-dB noise figure of the optical amplifier. Note the performance in this limit

is not impacted by thermal noise or detection efficiency. For high-sensitivity applications, G $>\sim$40 dB is often necessary depending on the data rate and amplifier design, sometimes requiring more than two gain-stages and photocurrent $> \sim 1$ mA to overcome all other sources of noise. This makes high-current-capable high-speed 50 Ω photodetectors attractive [407,408]. Wideband transimpedance amplifiers can reduce this power requirement somewhat, but scaling the EDFA output power to the necessary levels is relatively straightforward and it is often challenging to obtain the combination of bandwidth, waveform fidelity, and dynamic-range of operation of the filtered EDFA-PIN photodetector combination with the addition of RF amplifiers. The saturating characteristics of the EDFA combined with adjustable pump power in the final gain stage can be useful for performing automatic gain control when operating over a wide range of power-levels or data rates.

The addition of a polarizer eliminates half the ASE (and other orthogonally polarized background [47,223]), leading to theoretical sensitivity improvements, which are typically about 0.5 dB in practice [41]. This requires some form of polarization control in the TX, RX, or both. Unlike coherent RXs, for preamplified RXs this is an option, and we note that control of polarization can increase sensitivity and extend modulation options as discussed in section 5.3.

Like coherent receivers, single-polarization optically preamplified receivers when implemented with matched optical filtering provide true-single-mode background rejection (see section 2.3.7), and therefore can perform well with the sun in the field of view (as long as coupling and tracking elements continue to function). In fact, since preamplified RX SNR is already degraded by ASE noise, the change in SNR due to solar background is less than that for coherent receivers.

The combination of low-noise, high-gain and bandwidth available in preamplified RXs relaxes many of the downstream component requirements in the receiver. Since EDFA gain and power in the preamplifier are inexpensive, they are a cost-effective means of achieving near quantum-limited receiver sensitivity over a wide range of data rates and modulation formats. Furthermore, rare-earth-doped EDFA and YDFA technologies have been shown to be robust in the space environment [198,204,380,409], making it the present technology of choice for future space-based applications. Methods of optimizing preamplified RX performance are discussed in the next section.

5. Performance and Implementation Considerations

For average-power-limited optical transmitters operating over the free-space channel, without dispersion or nonlinear impairments, the signaling waveform can be chosen arbitrarily without sacrificing transmitted power (subject to constraints discussed in section 3.5.5). This enables the selection of robust waveforms that are well suited for optimum communications performance and facilitates all-optical matching of the transmitter to the receiver [10]. With an abundance of available optical spectrum, waveforms can be chosen to provide nearly matched performance at multiple rates, diminished ISI, with little or no power penalty at the transmitter end. This approach is a paradigm shift from conventional techniques based on peak-power and bandwidth-limited RF designs, where there is always a significant trade between the choice of waveforms, filtering, and the power transmitted.

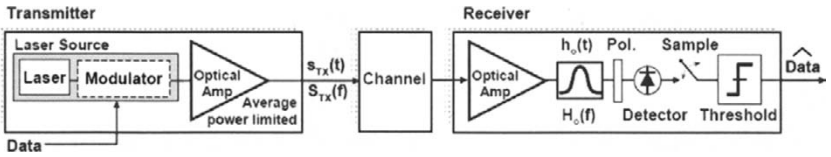

Fig. 48. Schematic of an average-power-limited MOPA TX with output field waveform $s_{\mathrm{TX}}(t)$ separated from a preamplified RX by an attenuating channel. A band-pass optical filter is followed by a polarizer, square-law detector, and postdetection sampling. The electrical response of the receiver is assumed to be relatively wideband, so that RF filtering is not explicitly included.

In the remainder of this section, we will combine well known concepts of matched filtering with the use of pulse shaping in the transmitter and optical filtering in the receiver to achieve robust high-sensitivity performance in optically preamplified receivers.

5.1. Waveform and Filtering Considerations

For high-rate and high-sensitivity applications, the MOPA TX and optically preamplified RX setup shown in Fig. 48 have demonstrated the best performance. It is well known that matched optical filtering yields the best performance for a signal corrupted by AWGN noise [156,410]. The SNR relative to the optimal matched filter condition is given by [18,120,411]

$$\Delta\gamma = \max_{t} \left\{ \frac{\left| \int_0^t s_{\mathrm{TX}}(\tau) h_o(t-\tau) d\tau \right|^2}{\int_{-\infty}^{\infty} |s_{\mathrm{TX}}(\tau)|^2 d\tau \int_{-\infty}^{\infty} |h_o(\tau)|^2 d\tau} \right\} \leq 1, \tag{113}$$

where $s_{\mathrm{TX}}(t)$ is the optical signal (field) waveform and $h_o(t)$ is the optical receiver filter (field) impulse response. The resulting SNR ($\Delta\gamma$) is maximized whenever

$$s(t) = h(-t) \quad \overset{\mathrm{FT}}{\longleftrightarrow} \quad S(f) = H^*(f). \tag{114}$$

The ratio in Eq. (113) represents the filtered signal waveform (power incident on the detector) as a function of time, normalized by the product of signal and filter waveform energies. The best SNR is achieved by sampling this waveform at its maximum.

The matching condition does not specify the waveform; rather it specifies the optimum relationship between the signal $s_{\mathrm{TX}}(t)$ and filter $h_o(t)$, that occurs when the filter impulse response is the time-reverse of the signal waveform. For waveforms that are symmetric in time, i.e., $s(t) = s(-t)$, the matching conditions reduce to

$$s_{\mathrm{TX}}(t) = h_o(t) \quad \overset{\mathrm{FT}}{\longleftrightarrow} \quad S_{\mathrm{TX}}(f) = H_o(f), \tag{115}$$

meaning the signal and filter impulse response have the same shape in both the time and frequency domains.

Early efforts towards optimizing preamplified RX sensitivity for high-rate optical systems focused on matching square non-return-to-zero (NRZ) signal waveforms[410,412] or optimizing performance with available Fabry–Perot (FP) optical filters .[128,404,413,414]. The NRZ waveform is particularly difficult to match as we show later in this section, and is prone to inter-symbol interference (ISI) penalties since the NRZ waveform energy is uniformly distributed between the symbol boundaries. This is especially problematic when received with the asymmetric exponentially decaying response of the FP filter, which requires a large optical bandwidth, $B_o = 3.7R_b$ and tight postdetection filtering in order to avoid significant ISI penalties [413]. The optimized FP bandwidth in this case is more than seven times larger than the best FP filter without ISI (see Table 11).

Matched optical filtering is desirable since it minimizes ASE or other out-of-band background optical noise, such as black-body radiation (see section 2.3.7) or inter-channel-interference (ICI) from adjacent WDM wavelengths, prior to conversion to the electrical domain. In this regard, all-optical matched filtering is desirable, from the standpoint of achieving optimum sensitivity [36,156] and a secondary benefit of improved spectral efficiency, since it enables tighter channel spacing [13].

The use of pulse-shaping in average-power-limited optical transmitters [10] improves RX sensitivity for two primary reasons. First it can reduce ISI penalties and second, it can facilitate the matching of the transmit waveform to realizable optical filters. This has led to high-sensitivity demonstrations (~2 dB from theory) of multi-rate variable-duty-cycle PPM [11,12], and RZ-OOK and RZ-DPSK [129] using FP optical filters.

Fortunately, there are many good waveforms that are easily generated (see section 3.5) and a wide selection of available filters such as single and multi-pass Fabry-Perot and dielectric filters, arrayed-waveguide (AWG), diffraction [415], and fiber Bragg (FBG) grating filters [133,416], and integrated waveguide filters [417]. Many of these can be customized to achieve a desired transfer function [418].

For the TX and RX in Fig. 48, the optimum signal-to-filter pulse-width-ratio β, defined as the ratio of signal FWHM to filter-impulse-response FWHM power waveforms, is calculated for a variety of waveform and filter type combinations summarized in the Matching Matrix in Table 11. For each waveform, the time-bandwidth product $(\Delta t_I \Delta f_I)$ is given for 3, 10, and 20 dB signal power levels. The SNR loss $(\Delta\gamma)$ is given in dB for the optimized β, without post-detection filtering. Note that ISI effects are assumed to be negligible, which is valid if these pulsed waveforms are of sufficiently low duty-cycle. No electrical filtering is included in this optimization, implying that the receiving electronics is relatively wide-band relative to the optical filter.

Also listed is the $\frac{1}{2}$ dB β-margin, which is the percent change from the optimum β that can be tolerated with less than $\frac{1}{2}$ dB reduction in SNR. This is an important measure of the SNR or matching robustness for the signal-filter pair and the sensitivity to deviations from the optimum. In this regard, the matched square waveform is a poor performer, a subject discussed further in section 5.1.2.

The example below illustrates how to use the matching matrix in Table 11.

Determine the optimum RX filter bandwidth for a 10-Gbps data stream formed by RZ-33% pulse carver.

From its name and as shown in Fig. 29, the FWHM of the RZ-33% is 33% of the period. For 10 Gbps, this would correspond to a 33-ps FWHM. Using a

Table 11. Matching matrix of 14 signaling waveform types (power pulse shapes) and a selection of four receiver filters. The SNR loss, $\Delta\gamma$ is calculated for the optimum $\beta \equiv \tau_o/\tau_s$, defined as the ratio of signal$_{\mathrm{FWHM}}$ to filter-impulse-response$_{\mathrm{FWHM}}$ (power) waveforms. Also listed for each filter type is the $\frac{1}{2}$ dB β margin, which is the percent deviation in β with $< \frac{1}{2}$ dB SNR change.

Time Domain Signal Power, $s_i(t)$ / Filter type: $h_i(t)$, Power Impulse Response				Square $h_i(t) = \mathrm{rect}(t/\tau)$			FP $h_i(t) = \exp(-2t/\tau)$			FP^2 $h_i(t) = (t)^2\exp(-2t/\tau)$			Gaussian $h_i(t) = \exp(-t^2/\sigma^2)$		
Waveform Type	$\Delta t_i\Delta f_i$ 3dB	10dB	20dB	$\Delta\gamma$ [dB]	Optim. β	1/2 dB Margin %	$\Delta\gamma$ [dB]	Optim. β	1/2 dB Margin %	$\Delta\gamma$ [dB]	Optim. β	1/2 dB Margin %	$\Delta\gamma$ [dB]	Optim. β	1/2 dB Margin %
Gaussian, $\exp(-t^2/\sigma^2)$	0.44	1.47	2.9	0.5	0.60	50	1	2.3	95	0.3	1.0	70	0.0	1	65
RZ-33% (~Gaussian)	0.49	1.54	2.7	0.5	0.60	55	1	2.2	100	0.3	1.1	70	0.0	1.1	60
RZ-40% (~Gaussian)	0.55	1.57	2.6	0.4	0.70	45	1	2.7	80	0.3	1.1	70	0.0	1.1	65
RZ-50%	0.66	1.62	4.0	0.3	0.80	35	1	2.9	90	0.3	1.3	70	0.1	1.4	50
RZ-53% (Raised Cos)	0.63	1.62	2.4	0.3	0.70	45	1	2.5	110	0.3	1.2	75	0.1	1.3	50
RZ-66⅔ (CSRZ)	0.73	1.62	2.9	0.2	0.80	40	1	3.1	85	0.3	1.5	55	0.2	1.3	66
$\mathrm{Sech}^2(t/\tau)$ (Soliton)	0.31	1.34	3.6	0.7	0.60	50	1	2	100	0.3	0.9	75	0.0	0.9	60
Gaussian^2 $\exp(-t^2/s^2)^2$	0.68	1.58	3.4	0.3	0.80	35	1	2.9	90	0.3	1.5	55	0.1	1.4	50
Gaussian^2 $\exp(-t^2/s^2)^4$	0.80	1.56	4.0	0.1	0.90	25	0.9	3.5	70	0.4	1.7	50	0.2	1.7	45
Square $\mathrm{rect}(t/\tau)$	0.89	1.49	3.6	0	1	10	0.9	3.5	80	0.6	1.8	45	0.5	1.7	50
FP^4 $(t^3/6)^2\exp(-2t/\tau)$	0.40	1.51	2.7	0.5	0.59	50	1.5	2.5	90	0.7	1.0	80	0.1	1	65
FP^3 $(t^2/2)^2\exp(-2t/\tau)$	0.39	1.51	1.5	0.5	0.25	50	1.6	2.4	100	0.8	1.0	80	0.2	1	70
FP^2 $(t)^2\exp(-2t/\tau)$	0.35	1.51	4.6	0.6	8.33	50	1.8	2.2	120	1.0	1.0	80	0.3	1	70
FP $\exp(-2t/\tau)$	0.11	1.11	7.3	0.9	0.01	80	2.7	1	130	1.8	0.4	105	1.0	0.4	105

matched Gaussian filter, the optimum filter impulse response ($\beta = 1.1$) has a FWHM of ~30 ps. From the time-bandwidth product, this corresponds to a 14.7 GHz filter, which provides nearly optimum SNR performance (~0 dB SNR loss) and can accommodate up to a ~60% bandwidth mismatch with only 0.5 dB added penalty.

The relaxed tolerances in this example can be used to assist in manufacturing yields and reduce component cost. The flexibility in filter bandwidth permits, for example, widening the filter to mitigate ISI or narrowing the filter to diminish ICI with little or no SNR penalty.

5.1.1. Symmetric Filtering

Pulse-shaping at the transmitter can be exploited to implement near optimum communications waveforms with non-ideal components (modulators, drivers, and receiver filters). Consider the TX in Fig. 37 with a wide-band optical source generating short (impulse-like) pulses in time followed by a high-gain APL amplifier with optical filtering. Passive optical filtering can be used to perform TX pulse shaping such that $S_{\mathrm{TX}}(f) \approx H_{\mathrm{net}}(f)$. A *symmetrically filtered* RX has the same net optical filtering,

$H_{\text{net}}(f)$, and if the filter time-response is also symmetric, match filtered performance can be achieved. For filters with an asymmetric response, such as the Fabry-Perot, with multi-pass or cascaded filtering, the response can be made progressively more symmetric (and Gaussian-like). In this manner, near optimum communications performance can achieved by cascading readily available filters which would otherwise yield sub-optimal performance when used individually [10]. Mathematically, this is equivalent to convolving a function with itself, which qualitatively tends to spread a function making it more symmetric.

The performance benefits of using symmetric TX and RX filtering for cascaded asymmetrical filters can be observed for the case of the commonly used Fabry–Perot filter (FP^n) listed in Table 11. Without additional filtering, a first-order FP incurs a 2.7-dB SNR loss. For the second order (FP^2), which can be implemented by a double-pass through a single FP, the SNR falls about 1 dB from optimum. A three-pass configuration yields a mere ~0.6 dB deviation, and as expected, departure from the optimum continues to diminish as additional iterative passes are made, and the time domain signal becomes increasingly symmetric. Note that along with increased symmetry, the time and frequency domain characteristics of FP^n start to resemble those of a Gaussian, the subject of the next section.

5.1.2. Gaussian Waveforms and Matched Optical Filtering

Combining *symmetric filtering* with the use of matched Gaussian-like waveforms [14], nearly optimal performance can be achieved with relaxed filter tolerances [13,133]. Gaussian waveforms are relatively easy to generate (see Pulsed Waveform Generation in section 3.5.2) and Gaussian filters can be realized with filter technologies such as diffraction gratings [13,415], AWGs [419,420], apodized FBGs [133,421], and cascaded filters discussed in the previous section. The Gaussian probability distribution function is known as a minimum-uncertainty-packet in quantum-mechanics, providing the minimum variance in two conjugate variables (e.g., position and momentum, or arrival time and energy of a particle). As a signaling waveform, Gaussian waveforms have a narrow time-bandwidth product, $\Delta f_I \Delta t_I = 0.44$ (at the 3-dB power point), making them well suited for both TDM and WDM communications. The Gaussian function is part of a class of functions known as "Self-characteristic functions" [422], which have a Fourier transform of the same form, i.e., a Gaussian time-domain waveform also has a Gaussian spectrum. Another well known optical waveform which shares this property is the soliton, which is Gaussian-like and also has a narrow time-bandwidth product (see Table 11). The soliton waveform is considered for use in ultra-high-speed fiber-optic links since the waveform maintains its shape due to a balance of dispersion and nonlinearities [111,236,423,424]. In this regard, fiber-based communications using solitons is similar to communication over the dispersionless free-space channel.

5.1.2.1. Relaxed Filter Tolerances

In contrast with *self-characteristic minimum-uncertainty waveforms*, the square-NRZ signaling waveform, which is completely contained in the time-domain, has a frequency domain spectrum with infinite extent, making it a poor choice for use in dense WDM systems. Furthermore, as noted earlier, the square waveform is susceptible to inter-symbol interference (ISI) penalties and requires tight filter tolerances to avoid

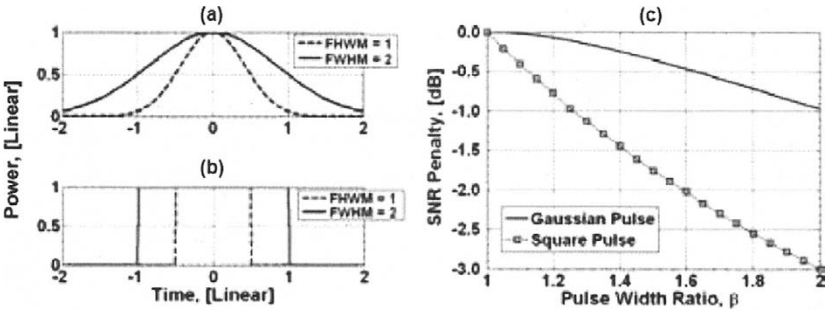

Fig. 49. Signal $s_i(t) = |s(t)|^2$ in solid line and filter impulse response $h_i(t) = |h_f(t)|^2$ in dashed line for Gaussian and square waveforms in (a) and (b) above. The pulse width ratio β is defined as the signal FWHM to filter-impulse-response FWHM. For the waveforms in (a) and (b), β =2. (c) Shows the reduction in SNR as a function of β for matched Gaussian and square filters.

SNR penalties as illustrated for the case of Gaussian and square matched filters in Fig. 49.

In Fig. 49(a), a wider Gaussian signal waveform (solid) and filter impulse response (dashed) are shown. The full-width-half-max pulse width ratio for the signal and filter response is defined as β, where the matched filter occurs for $\beta = 1$. Similarly, a wide square-signal-waveform and filter-response are shown in Fig. 49(b). For both waveform types illustrated, $\beta = 2$. Excluding ISI effects, the SNR penalty ($\Delta\gamma$) is calculated using Eq. (113) and plotted for Gaussian and Square waveform types in Fig. 49(c). While both Gaussian and square waveforms have no penalty for the matched condition (β = 0), the square degrades much more quickly from waveform-filter mismatch. For a 60% mismatch (β = 1.6), the Gaussian incurs ~0.5 dB, whereas the square waveform degrades by ~2 dB. For SNR loss $< \frac{1}{2}$ dB the square filter bandwidth must be within 10% of the signal bandwidth, effectively six $\times$ more or sensitive to mismatch than the Gaussian at the $\frac{1}{2}$ dB point. For β = 2, the square waveform SNR degrades by 2 dB more than the Gaussian, illustrating that the Gaussian waveform is more robust and easier to match than the square.

In an attempt to capture both SNR magnitude and its matching tolerance for a particular waveform combination in a single term, we introduce $\Delta\gamma_{\text{eff}}$, defined as the average SNR for $\beta_{\text{optimum}} < \beta < 1.6$, i.e.,

$$\Delta\gamma_{\text{eff}} = \frac{\int_{\beta_{\text{optimum}}}^{1.6\beta_{\text{optimum}}} \Delta\gamma\,(\beta)\,d\beta}{0.6\beta_{\text{optimum}}}. \tag{116}$$

$\Delta\gamma$ is listed in Table 12 and displayed in Fig. 50 for several signaling waveforms and filter types, sorted by $\Delta\gamma_{\text{eff}}$, and shows Gaussian-like properties and better effective SNR.

Table 12. Effective Matching-matrix. Effective SNR loss, $\Delta\gamma_{\text{eff}}$ resulting from the overlap of several signaling waveform types (power pulse shapes) with a selection of RX optical filters, sorted by $\Delta\gamma_{\text{eff}}$ from Eq. (116). ISI effects are neglected.

Signal	Receiver Filter, $h_i(t)$							
Waveform, $s_i(t)$	Gauss	FP^4	FP^3	$Gaus^{(2)}$	$FP^{(2)}$	$Gaus^{(4)}$	Square	FP
Gaussian	0.2	0.3	0.3	0.3	0.4	0.5	0.8	1.1
RZ-33%	0.2	0.4	0.4	0.2	0.5	0.4	0.7	1.1
RZ-40%	0.2	0.4	0.4	0.4	0.5	0.4	0.7	1.1
Soliton	0.2	0.4	0.4	0.4	0.5	0.5	0.8	1
RZ-50%	0.3	0.4	0.4	0.4	0.5	0.5	0.7	1.1
RZ-53%	0.3	0.4	0.4	0.2	0.5	0.4	0.6	1.1
RZ-66%	0.3	0.6	0.6	0.4	0.6	0.5	0.6	1.1
$SuperGauss^{(2)}$	0.3	0.4	0.4	0.3	0.5	0.5	0.7	1
$FP^{(4)}$	0.3	0.7	0.7	0.4	0.8	0.5	0.8	1.6
$FP^{(3)}$	0.3	0.7	0.7	0.4	0.9	0.6	0.8	1.7
$FP^{(2)}$	0.4	0.9	0.9	0.5	1.1	0.6	0.7	1.8
$SuperGauss^{(4)}$	0.5	0.5	0.5	0.4	0.7	0.5	0.7	1.2
Square	0.7	0.7	0.7	0.7	0.9	1.2	1	1
FP	1.0	1.6	1.6	1.0	1.9	1.0	1	2.7

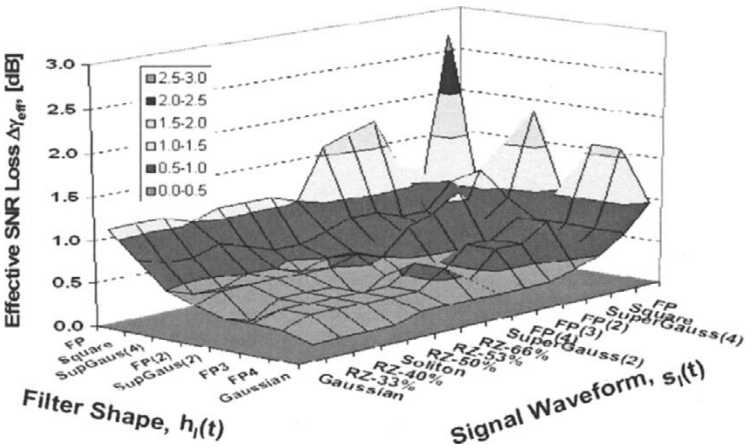

Fig. 50. Effective SNR loss for a variety of signal and filter shapes sorted $\Delta\gamma_{\text{eff}}$. The more symmetric, Gaussian-like waveforms yield better SNR performance, whereas the sharp-edged square and asymmetric FP filters incur the biggest losses.

5.1.2.2. Reduced Sensitivity to Timing Jitter

The SNR analysis in section 5.1 assumes that the received waveform is sampled at its maximum. However, deviations from the optimum sample point due to noise in the clock-recovery processes [236,419,425] or other sources of timing-jitter [426] reduce

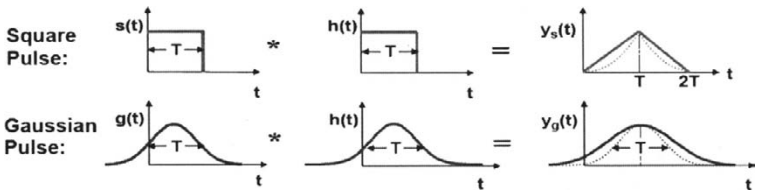

Fig. 51. Convolution of signal and matched filter field-impulse-response $h(t)$ for square (top) and Gaussian waveforms (bottom) of the same pulse-width. The filtered signal field $y(t)$ is the solid line and signal power (e.g., photocurrent after square law detection) is in the dotted line [13].

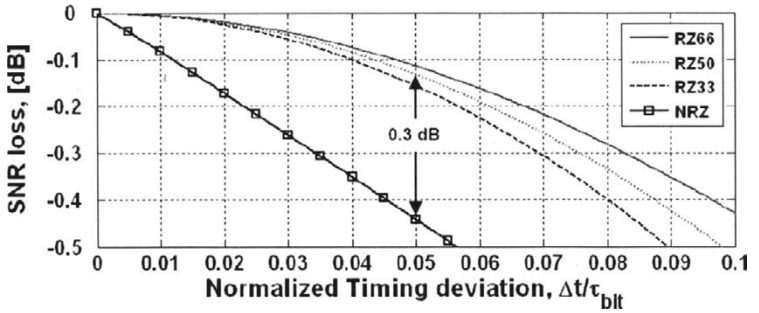

Fig. 52. SNR sensitivity to timing jitter for matched Gaussian-like and square-NRZ waveforms (excluding ISI) [13].

the SNR at the thresholding circuitry which degrades RX performance. Such effects are dependent on waveform shape as shown in Figs. 51 and 52, where, square $s(t)$ and Gaussian $g(t)$ field waveforms are received by their respective matched filters $h(t)$. The output from the matched optical filter $y(t) = s(t) * h(t)$, with detected photocurrent $i(t) = \eta|y(t)|^2$, indicated by the dotted-lines in Fig. 51.

The convolution of the square waveform and its matched filter yields the triangular waveform, which is subsequently narrowed by the square-law detection processes. The best SNR is achieved by sampling photocurrent at the peak. In this case, the peak is a relatively narrow target, which tends to magnify the any SNR penalties due to fluctuations in the sample time.

For the Gaussian waveform, the matched-filtered output is broadened 41% by the convolution process, but the waveform remains Gaussian. After square-law detection, the received photocurrent still has a Gaussian shape, but the pulse width is reduced by $\sqrt{2}$, so that it has the same pulse width and shape as the incident signal field. Note that the peak sampling point for the Gaussian is a much broader target than that of the square. The resulting SNR degradation ($\Delta\gamma$) as a function of time deviation from the optimum sampling point is shown in Fig. 52.

The sensitivity of matched-Gaussian-like waveforms to timing errors and sampling duration is significantly better than that of matched-square waveforms as shown above. This can reduce the impact of timing-errors from a variety of sources (e.g., Gordon-Haus timing-jitter [426]), and relax tolerances for sampling speed, accuracy, and stability of clock-recovery and detection hardware. This is especially important for M-ary PPM and high-rate communications which are more sensitive to the effects of timing jitter. For example, at 40 Gbps the timing precision required for less than 0.1 dB penalty is ~1 ps for 33% RZ waveforms. Despite being three-times wider, the square-NRZ waveform is over three-times more sensitive than 33% RZ to timing jitter, requiring $\Delta t <$ ~300 fs for < 0.1 dB penalty. For only $\Delta t =$ ~1 ps SNR is reduced by ~0.35 dB, excluding additional ISI penalties.

5.1.2.3. Combined Optical and Postdetection Filtering

For systems where electronic bandwidth is a limitation, both optical and RF postdetection filtering can be adjusted for better overall RX performance. Practically, obtaining RF bandwidths wide relative to the data rate is not always an option, but SNR loss ($\Delta\gamma$) can be avoided to a large extent, by increasing the optical filter bandwidth accordingly. As noted earlier, a similar trade between optical and RF bandwidths can be used to compensate when suitable narrow (matched) optical filtering is unavailable [345,346,404].

The SNR penalty as a function of optical and electrical bandwidths [344,345,404–406,427,428] has been evaluated for a variety of waveforms and filter shapes, often numerically and for the case of optical filters with bandwidths wide relative to the signal spectrum. Below, we evaluate Gaussian-like signal-waveforms and Gaussian-optical- and postdetection-RX filters for which the impact of deviations from the matched condition on SNR can be estimated analytically [429].

The SNR trade space for optical- and RF- filter time-response pulse widths (τ_o and $\tau_{\rm RF}$) relative to the optical signal pulse width (τ_s) is shown in Fig. 53. We use the signal-pulsewidth for normalization rather than the bit-duration ($\tau_{\rm bit}$) since matching is independent of data rate. The bit period, for instance, can be adjusted to vary the data rate or lengthened to reduce the effects of ISI if needed.

As expected, for wide RF filtering ($\tau_{\rm RF}/\tau_s \ll 1$), optimum performance is achieved for the matched condition, when $\beta = \tau_o/\tau_s = 1$, but extends over a large sweetspot surrounding the dashed *centerline* ($\tau_{\rm RF} \approx 3(\tau_s - \tau_o)$). As noted earlier, the Gaussian waveform relaxes the optical filter tolerances needed for nearly-matched performance, i.e., <~0.1 to 0.2 dB filtering penalty. Similar benefits are seen for Gaussian electrical filters.

If the $\tau_s/\tau_{\rm bit}$ ratio is sufficiently short, ISI penalties can be made negligibly small, and the analysis in Fig. 52 is broadly applicable. Otherwise, uncorrected ISI penalties start to degrade performance for longer τ_o and $\tau_{\rm RF}$ (upper right quadrant), compressing the SNR contours towards shorter pulse widths (lower left quadrant) as $\tau_s/\tau_{\rm bit}$ increases. Staying to the lower-left of the *centerline,* avoids ISI penalties as shown for the displayed RZ33, RZ40, and RZ50 data points. The SNR-optimized pulsewidth coordinates for Gaussian filter and RZ signals shown in Fig. 53 are linked to the data rate and bit duration is in Table 13.

For all three waveform types, optical and electrical bandwidths can be chosen for near-quantum-limited performance well within the 0.1-dB SNR sweetspot in Fig. 53,

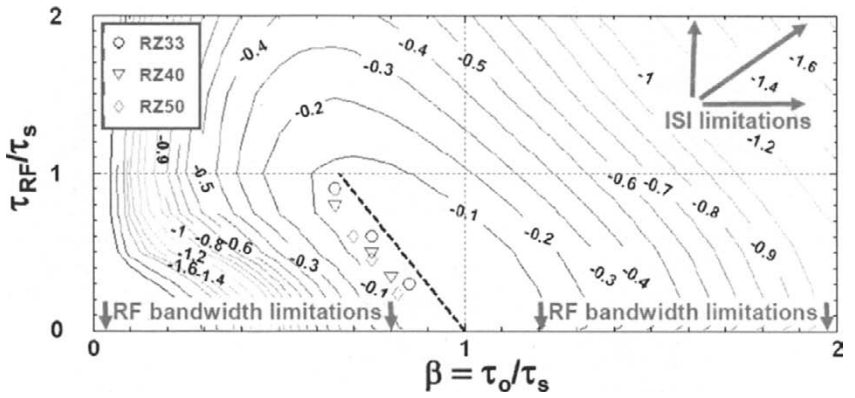

Fig. 53. Estimated SNR impact ($\Delta\gamma$) on a preamplified receiver with combined optical and RF Gaussian filtering and low photon/bit Gaussian signals. Contours represent lines of constant SNR (in dB) as a function of both RF and optical filter-response-pulse-widths relative to the signal power pulse width τ_s. ISI effects are not included in this calculation since they are dependent on both waveform shape and duty-cycle. However, ISI can be neglected for small τ_o and $\tau_{\rm RF}$ (the lower-right quadrant of the filter space) and for low-duty-cycle waveforms, i.e., $\tau_s \ll \tau_{\rm bit}$. Detailed parameters for RZ33, RZ40, and RZ50 points are given in Table 13. Simulations based on SNR analysis by J. Shapiro [429].

Table 13. Relative pulse width and bandwidth for data points shown in the optimized SNR region of Fig. 53. The bit duration $\tau_b = 1/R = 1$ for all entries. Optical parameters are in terms of FWHM intensity.

	Optical Signal			Optical Filter				RF Filter			
Signal Type	τ_s/τ_{bit}	$\tau_s\Delta f_s$	BW $\Delta f_s/R$	τ_o/τ_{bit}	$\tau_o/\Delta t_s$	$\tau_o\Delta f_o$	BW τ_o/R	τ_{RF}/τ_{bit}	$\tau_{RF}/\Delta t_s$	$\tau_{RF}\Delta f_{RF}$	BW $\Delta f_c/R$
RZ33	0.33	0.49	1.5	0.21	0.65	0.44	2.1	0.30	0.90	0.22	0.7
RZ33	0.33	0.49	1.5	0.25	0.75	0.44	1.8	0.20	0.60	0.22	1.1
RZ33	0.33	0.49	1.5	0.28	0.85	0.44	1.6	0.10	0.30	0.22	2.2
RZ40	0.4	0.55	1.4	0.26	0.65	0.44	1.7	0.32	0.80	0.22	0.7
RZ40	0.4	0.55	1.4	0.30	0.75	0.44	1.5	0.20	0.50	0.22	1.1
RZ40	0.4	0.55	1.4	0.32	0.80	0.44	1.4	0.14	0.35	0.22	1.6
RZ50	0.5	0.66	1.3	0.35	0.70	0.44	1.3	0.30	0.60	0.22	0.7
RZ50	0.5	0.66	1.3	0.38	0.75	0.44	1.2	0.23	0.45	0.22	1.0
RZ50	0.5	0.66	1.3	0.41	0.82	0.44	1.1	0.12	0.24	0.22	1.8

with *realizable* optical filter bandwidths $\sim$1 to 2 times the data rate (R) and RF filter bandwidths 0.7 to 2.2 R. When limited RF bandwidth drives the design, the optical filter can be chosen to reduce the RF bandwidth to $< 0.7R$ with little or no SNR penalty. The breadth of matching tolerance is also noticeable. For an optical filter bandwidth of about $1.3R$, nearly optimal performance can be achieved for all three waveforms with RF bandwidth between R and $2R$.

We note that with nearly matched optical filters, a single-polarization preamplified RX achieves true single-mode spatio-temporal filtering, which maximizes rejection to background noise, but also modifies the ASE noise statistics [122–125]. While accurate analysis of single-mode Bose-Einstein and noncentral-negative-binomial distributions for '0' and '1' ASE statistics, respectively, may influence theoretical predictions of optimum threshold and receiver sensitivity, they are unlikely to impact the results above. Near-quantum-limited demonstrations using this class of Gaussian waveforms and filters for OOK [13] and DPSK [133] modulation lend additional support to the analysis above.

5.1.3. Optimized Multi-Rate Transceivers

In many free-space applications, the flexibility to operate over a wide range of data rates is desirable since it provides a straightforward means of adjusting the transmitted signal-to-noise ratio, providing increased margin as needed. This can be used to accommodate varying link losses, due to changes in link distance or atmospheric channel effects, or compensate for performance degradation and extend the useful lifetime of the system. Especially in space-based systems, such capabilities should not incur increased complexity, SWAP, or reduction in RX sensitivity.

For systems that employ APL amplifiers (see section 3.5.3), multi-rate communications with nearly matched filtering can be efficiently implemented[11,15]. As discussed in the sections 5.1.1 and 5.1.2, the transmitter pulse shape can be adjusted so that it is well matched to the receiver without sacrificing transmitted energy-per-bit. This can be extended to multiple bit-rates simply by lowering the duty-cycle or average repetition rate [10–12,15], causing the peak output power to increase while the average saturated output power remains constant (see Figs. 35 and 36). Lowering the bit-rate in this manner while maintaining the same pulse shape and width (i.e., reducing the duty cycle), increasing the transmitted energy-per-bit thereby improving the error rate while maintaining optimum performance.

This *variable-duty-cycle* multi-rate approach has been demonstrated for binary-PPM at 51 to 1244 Mbps [11,12] with performance ~2 dB from quantum-limited theory at all rates. Subsequent M-PPM demonstrations at 2.5 Gslots/s [15] similarly yielded near-quantum-limited multi-rate performance but with improved sensitivities (see Fig. 61), spanning a range exceeding 20 dB with only a 12-dB change in data rate. Such features are particularly useful for providing bandwidth on demand or fall-back modes for communications over a noisy or uncertain channel since SNR can be improved by simply lowering the duty cycle (bit-rate) without additional penalties or hardware. It is particularly well suited for free space laser communications since it allows for graceful degradation without significant cost or complexity. Effects that can limit the range of practical duty cycles are discussed in section 3.5.5.

Variable duty cycle techniques can also be used to simplify multi-rate DPSK receivers [10,134] discussed in the next section. With a reconfigurable DI (see section 5.2.4) that can adjust the delay to accommodate the bit rate, a single filter design can be used to achieve nearly-quantum-limited receiver sensitivity at all rates. Alternatively, for harmonically related data rates, a fixed DI sized to the lowest rate can be used [134] along with appropriate differential precoding. In this case, the same DI can be used to simultaneously demodulate multiple-rate WDM-DPSK signals (see section 5.2.3), providing both rate-flexibility and WDM scalability [136].

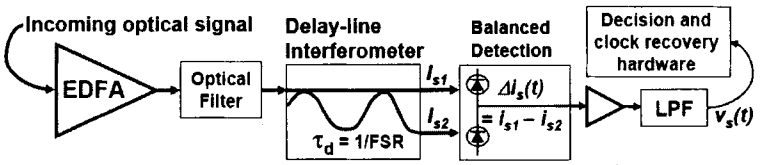

Fig. 54. Typical optically preamplified DPSK receiver.

5.2. *Differential Phase Shift Keying (DPSK)*

Optical differential-phase-shift-keying (DPSK) modulation was introduced in section 2.2.1 as a means of improving sensitivity over commonly used OOK. DPSK theoretically can offer among the best combined spectral and photon efficiency without requiring a coherent local-oscillator-based receiver. This has generated considerable attention by both the FSO community and the telecom industry, and led to the most sensitive high-rate demonstrations [24,25,41,128–131,133,172]. However the sensitivity benefits of DPSK come at the cost of increased complexity over OOK, requiring a phase modulator and differential precoding in the TX, and an optical delay-line interferometer (DI) and balanced detection in the RX as shown Fig. 54. The remaining DPSK RX elements including subsequent electrical amplification and filtering are similar to OOK RXs.

In practice, the complexities associated with DPSK make it challenging to achieve the potential 3-dB sensitivity advantage over OOK. The most significant performance penalties result from residual chirp in the transmitter waveforms [132,142] discussed section 3.5.2, and alignment of DI and the signal wavelength [144,146,430], discussed in the section 5.2.2. Smaller degradations in DPSK performance arise from non-ideal interferometer delay [135,146,31], extinction ratio, and detector imbalance in amplitude and timing [132,145]. The reader is directed to an excellent tutorial on long-haul fiber-based DPSK systems by Gnauck and Winzer in [132] and other references in this section for further details and analysis of DPSK performance.

Despite these possible degradations, DPSK receiver sensitivities closely approaching quantum-limited theory can be achieved [133]. However, it is important to realize that while implementation penalties may individually be considered negligible, the combined impact of several of these effects could be prohibitive. Unless the improvement in RX sensitivity can be realized with long-term reliability, DPSK provides little value for free-space applications, in contrast with long-haul fiber-based DPSK applications, which benefit from the reduction of nonlinear impairments that result from lower peak power.

In the DPSK receiver, the DI enables a comparison of the optical phase by splitting the optical signal field and recombining the two polarization-aligned components with a relative time-delay τ_d. At the output coupler, the two overlapping field components interfere constructively or destructively depending on the relative phase of the differentially encoded bits, with the resulting output power proportional to the product of the two fields, being directed to the first or second output port. For complete interference, the incident fields need to have the same amplitude, and a delay that is a positive integer multiple n of the bit-period τ_{bit} [134,135], i.e.,

$$\tau_d \equiv \frac{1}{\mathrm{FSR}} = n\tau_{\mathrm{bit}}, \tag{117}$$

where FSR is the DI free spectral range. Since the data rate $R_b = 1/\tau_{\mathrm{bit}}$, it is ideally equal to an integer multiple of the FSR, resulting in a delay-error $\Delta\tau = |\tau_d - \tau_{\mathrm{bit}}| = 0$. The associated delay-error or rate-to-FSR mismatch penalty is limited to less ~0.3 dB for $\Delta\tau < 0.05\tau_{\mathrm{bit}}$[146,431]. However, for larger errors, the SNR degradation is waveform and filter dependent [135]. For receivers optimized for 33%-RZ waveforms, 10% and 14% delay-errors lead to ~0.5 dB and ~1 dB SNR penalties, respectively. While manufacturers typically specify a ~1% tolerance for the DI delay accuracy, in practice, larger delay-errors can result from channel-rate changes in deployed systems to accommodate different FEC overhead [132] or to simplify WDM-DPSK receiver implementation while maintaining compliance with existing wavelength and rate standards [149,151,432,433].

For stability, size, and performance reasons, τ_d is typically chosen to equal only one bit period. This relaxes signal coherence requirements [264], minimizes frequency-alignment penalties, and simplifies TX precoding, which can be implemented with an OR gate to logically combine DATA and CLOCK inputs to drive a T-flip-flop [140,434–436], causing the transmitted phase to change whenever the DATA is a '1'. However, for multi-rate and multi-channel DPSK applications discussed later, it can be desirable to use a multiple-bit delay to accommodate simplified implementations that provide rate-flexibility and scalability with penalty-free performance that is compatible with existing channel-rate and channel-spacing standards [135, 136].

The DI outputs are received with balanced detection, which generates a signal $\Delta i(t)$ that is proportional to the power difference between the two output arms of the DI. This can be implemented by directly subtracting the photocurrent output from discrete [128] or integrated balanced photodetectors [25,408,437], or using subsequent differential electronics to generate the difference signal [25,130,159], all of which are commercially available with bandwidths exceeding 40 GHz. Balanced detection provides an implementation benefit over single detector RXs since the resulting photocurrent deviation between "0" and "1" symbols is twice that of single-detector receivers, making it easier to directly overcome the noise threshold in the subsequent decision circuitry without additional RF amplifiers.

5.2.1. DPSK Wavelength Alignment Considerations

Of the additional RX elements needed for DPSK, the delay-line interferometer often imposes the most demanding requirements. For good performance the DI is preferably polarization insensitive and the two arms must be stable to a small fraction of a wavelength. This requires careful, thermo-mechanical packaging and/or active stabilization [432,438–440], adding to DI size, weight, power, and cost. The DI is most commonly implemented with an asymmetric Mach–Zehnder design (see section 3.5.2 for detailed description), although Michelson[11] [432,441,442] and Sagnac-interferometer-based

[11] Albert Abraham Michelson, 1852–1931, invented and built what has become known as the Michelson-interferometer, used in accurate measurements of length and the speed of light. Conducted the Michelson-Morley experiment (1887) with E. W. Morley, which attempted to detect the expected difference in the speed of light caused by the motion of the earth. Michelson was awarded the Nobel Prize in physics in 1907.

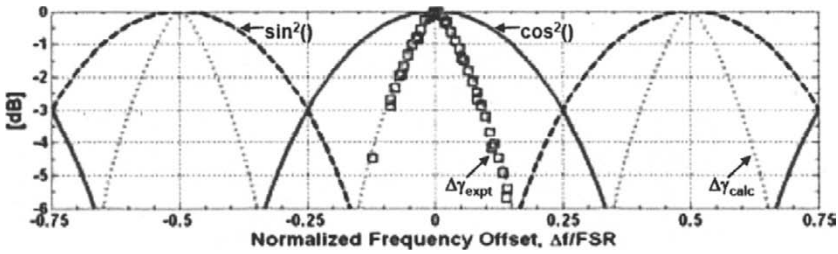

Fig. 55. Periodic transfer function (fringes) of a DI: $\sin^2()$ and $\cos^2()$ outputs; and calculated ($\Delta\gamma_{\mathrm{calc}}$) and measured ($\Delta\gamma_{\mathrm{expt}}$) SNR penalties at 10^{-9} BER as a function of carrier frequency offset Δf, normalized by the DI FSR (assuming polarity correction) [443].

designs [440] with an equivalent transfer function [see Eqs. (57)–(60)] may be used as well (see section 5.2.4 on Reconfigurable DPSK Demodulators below).

In contrast to the Mach–Zehnder interferometer-based modulators discussed in section 3.5.2, where a short sub-picosecond static time delay is desirable, the relatively long delay of at least one bit-period needed for DPSK demodulation causes an asymmetry that makes stabilization more difficult. Small changes in DI temperature, for example, even if uniform, generally lead to a phase difference between the arms that shift the spectral alignment of the interferometer, resulting in significant SNR degradation.

The ideal intensity transfer functions of the two interferometer output arms are periodic and complementary, given by

$$\begin{aligned} I_1 &= |E_1|^2 = \cos^2\left(\pi \tfrac{\Delta f}{\mathrm{FSR}} + \tfrac{\Delta\phi}{2}\right), \\ I_2 &= |E_2|^2 = \sin^2\left(\pi \tfrac{\Delta f}{\mathrm{FSR}} + \tfrac{\Delta\phi}{2}\right), \end{aligned} \tag{118}$$

where $\Delta\phi$ is a measure of the relative optical phase between the internal interferometer arms and is typically controlled to maximize the signal interference in one or both of the output arms. When the bias $\Delta\phi = 0$, the Δf term represents the frequency deviation from optimum alignment of the incoming signal to the interferometer. The SNR degradation associated with Δf (frequency offset error) forms periodic SNR fringes at even multiples of FSR/2 as shown in Fig. 55. The received signal is reduced by an amount proportional to the difference of signal intensities at the output arms. The received signal is maximum for $\Delta f = 0$ and goes to zero as Δf approaches odd multiples of FSR/4, when the outputs of the two arms are equal. Beyond this point, the received data are inverted, an effect that can be compensated with polarity correction, until the next maximum is reached which occur an even multiple FSR/2.

The net DPSK wavelength offset SNR penalty includes both signal reduction and increased noise that is numerically analyzed in [132,144,430,431]. A simplified estimate of the offset penalty can be obtained in closed-form following the approach in [116,120,404]. Using the Marcum Q-function defined as

$$Q_{\text{Marcum}}(a,b) = \int_b^\infty x \exp\left[-\tfrac{1}{2}\left(x^2+a^2\right)\right] I_0(ax)\,dx, \tag{119}$$

where I_0 is the modified Bessel function of the first kind of zero order, the BER and SNR estimate (γ_{calc}) are given by [135]

$$\text{BER}_{\text{calc}} \cong 0.5 \left[\begin{array}{l} 1 - Q_{\text{Marcum}}\left(\sqrt{2\gamma_{\text{th}}}\cos(\frac{\pi\Delta f}{\text{FSR}}), \sqrt{2\gamma_{\text{th}}}\sin(\frac{\pi\Delta f}{\text{FSR}})\right) \\ +Q_{\text{Marcum}}\left(\sqrt{2\gamma_{\text{th}}}\sin(\frac{\pi\Delta f}{\text{FSR}}), \sqrt{2\gamma_{\text{th}}}\cos(\frac{\pi\Delta f}{\text{FSR}})\right) \end{array}\right], \tag{120}$$

$$\gamma_{\text{calc}} \cong -\ln(2\text{BER}_{\text{calc}}), \tag{121}$$

$$\Delta\gamma \cong 10\log_{10}\left(\frac{\gamma_{\text{calc}}}{\gamma_{\text{th}}}\right), \tag{122}$$

where γ_{th} is the ideal SNR (or PPB) at the input to the preamplified RX (without frequency offset) and $\Delta\gamma$ is the effective SNR penalty in dB. This straightforward estimate for the offset SNR penalty provides excellent agreement with the measured data at 40 Gbit/s shown in Fig. 55 and in [135] at 2.5 Gbit/s, and is consistent with measurements and calcuations in [144,146,431]. For $|\Delta f/\text{FSR}| <\sim 4\%$, $\Delta\gamma$ is less than $\frac{1}{2}$ dB at the 10^{-3} BER, which is an error-free threshold point for commonly used FEC [24,25,41,115,444]. Note that for a fixed frequency offset, this alignment penalty is reduced as the FSR gets larger, an effect that makes it more challenging to avoid penalties at lower data rates. For 40 Gbit/s DPSK channels received with a 40-GHz FSR interferometer, wavelength alignment ($|\Delta f|$) needs to be within ± 1.6 GHz in order to limit $\Delta\gamma < \frac{1}{2}$ dB. At 2.5 Gbit/s, the $\frac{1}{2}$ dB wavelength tolerance is reduced to ± 100 MHz. But this can be achieved with commercial sources, as noted in section 3.3. With appropriate temperature and wavelength control, laser DFB laser wavelength can be stable for extended periods with less than 15 MHz standard deviation, consistent with 2.5 Gbit/s DPSK communication performance with < 0.1 dB SNR deviation [135].

5.2.2. Interferometer Stabilization

Given the significant SNR penalties for wavelength offset errors, the need for stable signal and DI wavelength alignment is clear. Passive athermal DI designs have been constructed to align to the 50 GHz ITU grid with Δf less than ± 0.8 GHz [432,433] over a 0–70C° temperature range. Assuming an otherwise perfectly aligned incoming signal wavelength, this would lead to only $\sim$0.1 dB temperature induced penalty at 40 Gbit/s. However, at 10 Gbit/s or lower data rates, even this level of stability would lead to prohibitive SNR penalties. Moreover, the TX signal wavelengths are not necessarily stable in free-space applications, an effect that discourages the use of passively-stabilized DIs. For example, space-based links between Geosynchronous and Low-Earth orbits (GEO-LEO) can experience Doppler shifts up to $\sim$9 GHz (for 1.55 μm signal wavelengths), that would preclude the use of an athermal interferometer without some form of TX signal compensation [135] for Doppler or other long-term wavelength shifts.

For single channel RXs, the preferred means of wavelength-offset compensation is local tracking at the RX for reasons of simplicity, speed, and stability of control. This

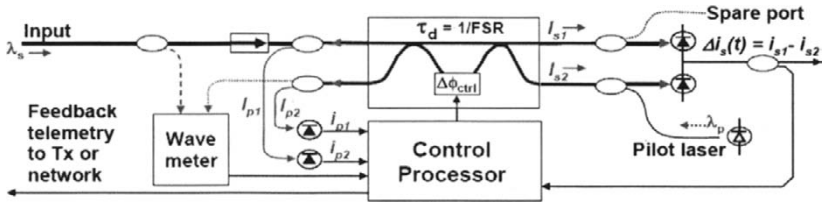

Fig. 56. Example setup for a pilot-stabilized DPSK receiver.

is typically implemented using synchronous phase-locking techniques that introduce a small dither on Δi_s in order to determine the sign of the phase error, and maximizing the peak baseband (RF) signal power accordingly [399]. The dither may be applied to one of the DI arms [438] or TX signal wavelength [439,445,446] [$\Delta\phi$ and Δf, respectively in Eq. (118)]. The amplitude of the dither can be reduced to sufficiently low levels so that active control can be achieved with little or no RX sensitivity penalty [133].

An alternative approach to interferometer stabilization makes use of pilot tones to stabilize the DI [135], which can provide dither-free open-loop DI control without an RX signal, and the flexibility to tune the DI to optimize performance when an RX signal is present [267,268]. Such capabilities are particularly useful during the spatial acquisition phase in a free-space link. With absolute DI wavelength control, for instance, the DI can be tuned to the proper wavelength in advance of the RX signal, thereby expediting the acquisition process and eliminating the need to re-align the DI after dropouts or fades. This also removes the polarity ambiguity, in which the sign of the data is unknown when using the standard phase-locking techniques.

An example of a pilot-based stabilization setup is shown in Fig. 56. The pilot signal, which could be generated by a low-power DFB laser, is injected into the DI through an optical tap in the reverse direction. As discussed in section 3.3 and earlier in this section, the pilot wavelength λ_p can be calibrated via temperature and current settings with a (short term) stability $<\sim$30 MHz [135], or through other methods, such as a feedback from a built in temperature controlled etalon [231] or an external wavelength reference such as a wavemeter, with sub-GHz long-term stability.

The pilot tone outputs from the DI (I_{p1} and I_{p2}) can be detected by low-speed photodetectors and the resulting photocurrents are processed to measure the normalized Δi_{pilot} or *contrast ratio* given by

$$D = \frac{I_{p1} - I_{p2}}{I_{p1} + I_{p2}} = \frac{\cos^2(\theta) - \sin^2(\theta)}{\cos^2(\theta) + \sin^2(\theta)} = \cos(2\theta). \tag{123}$$

Here $\theta = \pi\Delta f_p$ /FSR + $\Delta\phi_{\text{ctrl}}$ +$\Delta\phi_{\text{error}}$ is the net phase argument, Δf_p is the relative pilot carrier frequency, which is either known or measured, $\Delta\phi_{\text{ctrl}}$ is an interferometer phase control term, and $\Delta\phi_{\text{error}}$ is a random interferometer phase term, which can be constant or have time and temperature dependencies that need to be compensated for. Fig. 57 shows a plot of D and normalized I_{p1} and I_{p2} as a function of the Δf.

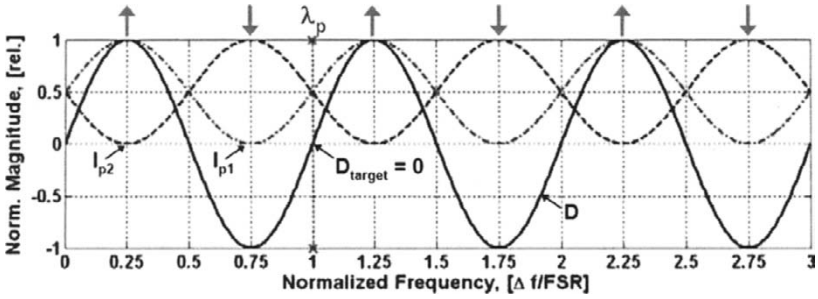

Fig. 57. The *contrast ratio* D and normalized pilot outputs I_{p1} and I_{p2} as a function of Δf normalized by the DI FSR. Arrows above the I_{p1} and I_{p2} fringe peaks indicate the location and polarity of signal wavelengths that the DI can accept without penalty when the DI is locked to the pilot wavelength at λ_p at $\Delta f/\mathrm{FSR} = 1$.

The contrast ratio ranges from +1 to −1 and has a period equal to the DI FSR. Thus, with the pilot capabilities shown in Fig. 56, the FSR and other important DI parameters such as extinction ratio can be measured by sweeping the pilot carrier frequency with fixed phase terms $\Delta\phi_{\mathrm{ctrl}}$ and $\Delta\phi_{\mathrm{error}}$, a capability that would also be useful for performing automated diagnostics in the field. Such capabilities could be enhanced with the use of multiple pilot tones (distinguishable by dither frequency and or wavelength), in which one pilot is used for stabilization, and the other for characterization.

By choosing a target contrast ratio, e.g., $D_{\mathrm{target}} = 0$, $\Delta\phi_{\mathrm{ctrl}}$ can be adjusted to make the error between the measured and target contrast equal to zero (i.e., $D_{\mathrm{error}} = D_{\mathrm{measured}} - -D_{\mathrm{target}}$) using standard feedback control techniques. This locks the DI to the pilot wavelength so that it is aligned to accept signal wavelengths at

$$\lambda_s(m) = \lambda_p \pm (2m+1)\frac{\mathrm{FSR}}{4}, \tag{124}$$

where m is an integer and polarity correction is needed to invert the data when m is odd. This provides flexibility in placement of the pilot wavelength. For instance, it could be placed outside of the communication band to conserve spectrum and prevent potential in-band interference. While the pilot tone in the example above can be used as a CW single wavelength source, dithers in either wavelength and/or amplitude can be introduced to allow synchronous control/detection methods.

In practice, a pilot-stabilized DPSK RX can be used in the following manner. Prior to acquisition, the pilot tone can be used to align the interferometer to the anticipated RX wavelength. This eliminates the need for scanning the interferometer to search for an incoming wavelength as long as the anticipated and received wavelength are relatively close, e.g., correct to within about ±10% of an FSR. Once the signal is received, with incoming power above a predefined threshold $\mathrm{P_{min}}$, the interferometer control can switch to tracking the signal using standard approaches. Therefore, the control system only needs to track on the signal, if at all, when the signal is relatively strong, which reduces the dynamic range of operation required for signal tracking.

While the signal is strong, any misalignment between the pilot wavelength needed for correct interferometer alignment to the signal can be eliminated by having the pilot tone align to the interferometer. In this manner, a locally resident pilot tone can effectively track an incoming signal that can be slowly drifting due to poor control, aging, or Doppler shifts in moving platforms. Should the signal drop out, the interferometer control can switch back to the well aligned pilot control, which can remain stably aligned to the correct wavelength until the incoming signal exceeds P_{min}. This provides seamless interferometer performance during fades, and reduces any interferometer induced acquisition delay [268].

5.2.3. Multi-Wavelength DPSK Receiver Options

For high-rate 100+ channel WDM-DPSK systems (e.g., [138–140,167,447]), the size, weight, power, and costs associated with reliably maintaining a stable delay-line interferometer for each channel can be substantial. Miyamoto and coauthors [149,151] demonstrated concurrent PSK to ASK conversion of 43 Gbit/s WDM-DPSK channels to WDM-duobinary channels on the 100 GHz ITU grid using a 50-GHz free-spectral-range (FSR) DI. While well suited for applications where spectral efficiency is required, this simplified DPSK RX incurs sensitivity penalties of 3 dB due to single-ended DPSK reception and another ~0.5 dB due to the ~14% mismatch between the 50-GHz DI FSR and the 42.8 GHz data rate when used with 66% RZ waveforms. As noted earlier, the mismatch penalty is waveform dependent; with ~14% delay error, the penalty increases to ~1 dB for 33% RZ waveforms further reducing the sensitivity benefit of DPSK.

Simplified multi-channel 'DPSK' receivers have also been implemented with periodic narrow band optical filtering and similar duobinary signals over dispersive channels [148,150,416,448]. While dispersion tolerant, these single-ended demodulators also incur sensitivity penalties in excess of 3 dB when compared to balanced DPSK receivers.

However, multi-channel WDM-DPSK reception can be achieved using a single DI with near-quantum-limited performance and be compatible with existing standards without waveform-dependent penalties [135].

By leveraging the DI's periodic transfer function shown in Fig. 55, and constraining the received wavelength spacing ($\Delta\nu_{ch}$), multiple WDM-DPSK channels can be simultaneously demodulated using a single interferometer. Unlike single-channel DPSK receivers in which the DI can track the incoming signal, in the multi-channel configuration, independent channels must have the same wavelength periodicity as the DI in order to avoid significant SNR penalties. For WDM-PDSK signals coming from the same TX, this periodicity can be configured locally at the TX. In this case, the RX DI can also track locally on any of the received signals in order to align to all of the incoming WDM channels. However, local tracking at the RX is precluded for multi-access applications, where independent TXs send WDM-DPSK signals to a common RX. In this case, proper wavelength alignment can be achieved with either absolute λ-control at the TX and RX, or with (slow) feedback from the RX via network-level maintenance and control of the TXs. Transmitter-centric control could also be used to compensate for aperiodicities that can occur in the DI [449]. As noted in the previous section, absolute λ-control of the DI can be achieved via stable thermal design [432] or with pilot tone stabilization, which could be a locally-resident calibrated laser. Another

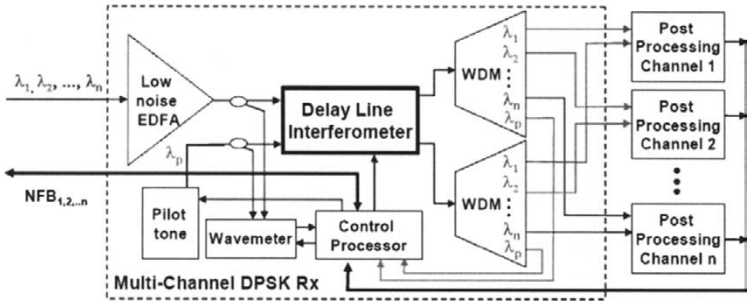

Fig. 58. A Multi-channel DPSK RX with feedback and feedforward alignment capabilities that can include a pilot tone (λ_p) or master-channel, wavemeter, channel power and bit-error rate (BER), and interactive communication with the network (NFB) [266].

option is to use a master-reference channel that the DI, and all other signal and pilot λs can align to with feedback [268], providing the capability for sub-GHz (perhaps sub 100 MHz) wavelength alignment capability across the network.

WDM-DPSK channel separation can be achieved via optical demultiplexing after the DI [149,151,266,450,451] as shown in Fig. 58. Since balanced detection is needed to achieve high-sensitivity, this WDM-DPSK RX requires one extra WDM filter, but the WDM cost is small relative to the potential cost of tens of interferometers and associated stabilization hardware.

In order to avoid SNR degradation when using a multi-channel DPSK receiver, three conditions must be satisfied. First, the channel rate (R) must be nearly equal to an integer multiple n of the FSR to satisfy Eq. (117) and minimize delay-error. Second, $\Delta\nu_{\text{ch}}$ must be within a small frequency offset (Δf) from an integer multiple m, of FSR/2 (with polarity correction), i.e.,

$$\Delta\nu_{\text{ch}} = m\frac{\text{FSR}}{2} \pm \Delta f = m\frac{R}{2n} \pm \Delta f. \tag{125}$$

The third condition requires that transmitted channels each be aligned to target SNR fringe peaks so that $\Delta f \to 0$.

For wavelengths on the ITU grid (e.g., 100 GHz channel separation), standard SONET rates of 2.5, 10, and 40 Gbps for instance, are compatible with these conditions since the channel rates (or half-channel rates) are integer submultiples ($1/m$) of the ITU channel spacing.

However, when commonly used 7%-overhead G.709 compliant FEC is used with standard SONET rates, bringing a 10-Gbps SONET data rate to a 10.7-Gbps coded channel rate, it is impossible for all of the ITU grid-based WDM channels to align with the periodicity of the interferometer and satisfy the conditions in Eq. (125) above. In this case, SNR penalties can be avoided by either: a) adjusting the channel spacing to be a multiple of half the channel rate, abandoning the ITU grid if necessary, or b) adjusting $R/2$ to be an even factor of the channel spacing, abandoning, for example, SONET or G.709 standards if necessary.

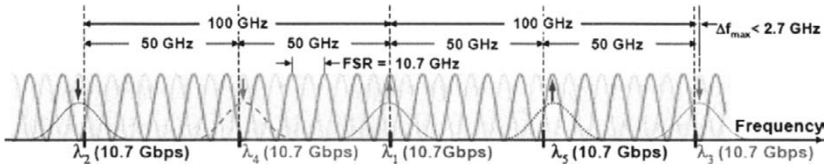

Fig. 59. WDM-DPSK channel spacing for 10.7 Gbps rate signals aligned near the 50/100 GHz ITU grid and to a 10.7-GHz FSR delay-line interferometer. Arrows centered on each wavelength indicate location and polarity of the received data.

If conforming with existing standards is the priority, Eq. (125) may not be satisfied exactly, but the associated performance penalties and deviation from the standards can be constrained to acceptable levels. For example, 10.7 Gbit/s channels on the 100-GHz ITU grid can be demodulated without performance penalty by a 10.7-GHz FSR DI, which can accept optical center frequencies every ~5.3 GHz with polarity correction. While most of the DI fringes will not align exactly to the 100-GHz ITU grid, none will misalign by more than 5.3/2 or ~2.7 GHz (FSR/4), with the average deviation of only ~1.4 GHz (FSR/8) as shown in Fig. 59. This deviation can be further reduced by a factor of n by demodulating with an n-bit DI, albeit with tighter wavelength alignment requirements as shown in Fig. 55 and bounded in Eq. (125) [266].

It is important to note that there are additional cost and performance benefits associated with the increase in alignment requirements needed for multi-channel WDM-DSPK RXs. For instance, spectral efficiency and RX sensitivity could benefit from reduced wavelength uncertainty throughout the network, which in turn, may allow reduced filter bandwidth margins (needed to accommodate wavelength uncertainties) and improved performance. Moreover, as noted in section 3.3, the additional cost of providing infrequent feedback to optimize wavelength alignment and communication performance of relatively stable tunable devices can be smaller than the expense of developing fieldable hardware with 20+ year stability.

Expanding on the example above, with proper differential precoding, the same 10.7-GHz DI could also be used to simultaneously demodulate 43 Gbit/s channels with negligible delay error. Thus, for near-harmonically related data rates, a single interferometer can be used to simultaneously demodulate multiple-rate WDM-DPSK signals [136]. To further diminish deviation from the ITU grid and to provide additional rate/alignment flexibility, a 2.68 GHz DI could be used to simultaneously demodulate 2.5, 2.67, 10.7, 40, 42.7, and 43.02 Gbps SONET and G.709-compliant WDM-DPSK signals within 700MHz of the ITU grid and with less than 7% delay-error.

For high-channel count WDM-DPSK links where spectral efficiency is more important, tight channel spacing is desirable but often comes with a decrease in RX sensitivity due to inter-channel interference resulting from limited WDM channel isolation. For single polarization RXs, this cross-talk penalty can be reduced by polarization multiplexing odd and even channels [452]. Another method of suppressing cross-talk can be seen in Fig. 55, for WDM channels separated by exactly an odd multiple of FSR/4. For this spacing, the signal intensities on the DI output arms are equal regardless of the data, and the resulting signal photocurrent $\Delta i(t)$ goes to zero. This property could be

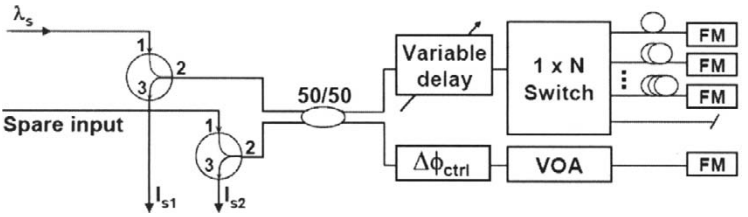

Fig. 60. A reconfigurable polarization-independent delay-line interferometer, based on a double-pass Michelson interferometer design using Faraday-rotator mirrors (FMs) to compensate for residual polarization rotation in the arms of the interferometer. Variable-delays and switching elements can be included to adjust the delay or FSR, and variable-optical-attenuators (VOAs) can adjust the relative power in the two arms to optimize the DI-extinction [267,268].

used to benefit dense WDM systems, by staggering the channel spacing so that delay-line interferometer improves rejection and reduces potential cross talk penalties. This is especially helpful for adjacent channels where WDM rejection is the poorest. For the multi-channel receivers described above, this could be implemented by sending odd and even WDM-DPSK channels to two separate WDM-DPSK RXs, staggered by FSR/4. Moreover, when n-bit DIs are used for demodulation (yielding FSR $= R_b/n$), the channel spacing can be adjusted by integer submultiples of the data rate, providing n-times finer wavelength adjustment for optimizing the trade between photon and spectral efficiency of the system.

5.2.4. Reconfigurable DPSK Demodulators

The ability to simultaneously demodulate many WDM-DPSK signals with a single DI, becomes even more useful if the DI can be reconfigured to optimize performance or accommodate other data rates. For example, a DPSK receiver could be adjusted to accept different (non-harmonically related) rates or FEC upgrades without delay-error penalties. Even in single-channel DPSK RX designs, it may be preferable to have one reconfigurable DI and associated control that can operate at several rates, rather than a fixed DI for each rate.

A polarization independent extension of the double-pass amplifier design [354] discussed in section 3.5.3 is a Michelson-based interferometer that incorporates Faraday rotator mirrors in both arms of the interferometer as shown in Fig. 60.

This geometry compensates for residual polarization rotation over a broad-range of wavelengths, making it well suited for WDM-DPSK applications, and the lack of polarization dependence enables useful non-polarization-maintaining elements to be incorporated into the arms of the interferometer without introducing polarization dependent losses (PDL) or degradation in DI performance. For example, a standard single-mode variable-delay-line with $>\sim$200 ps delay could be used to continuously tune a reconfigurable DI to accept DPSK signals at any rate greater than $\sim$2.5 Gbit/s, and provides a built-in means of adjusting the FSR to compensate for rate-FSR mismatch. The tuning and phase-control range in this case benefits by a factor of two from the double-pass geometry. Alternatively, $1 \times N$ switching elements can be used

to vary the DI-delay by discrete steps to extend the DI tuning range further. When used in combination with a variable-delay, the continuous tuning provides additional rate flexibility and relaxes path-length tolerances.

Other elements, such as a variable-optical-attenuator (VOA) can be used to compensate for relative changes in insertion loss between the two paths, which, in combination with pilot-based characterization, can be used to measure and optimize DI-extinction ratio. By including the ability to terminate the reflection from the arms of the interferometer, either by adjusting the VOA or switching to an angle-terminated port, the splitting ratio of the 50/50 coupler and the output intensities I_{s1} and I_{s2} and corresponding photocurrents can be measured and balanced.

Pilot tones can be injected at the spare input port in this geometry to stabilize and characterize the DI (see Fig. 58 and section 5.2.2. This, in combination with variable-delay adjustment enables autocalibration and *in-situ* feedback and optimization capabilities. For example, the DI-delay can be adjusted to minimize received BER, and pilot-based stabilization/characterization can provide independent measure of the DI-FSR (channel-rate) and the incoming signal wavelength. This information can be used to track/manage wavelengths and relative Doppler shifts throughout the network.

5.3. Hybrid Modulation Formats

In order to optimize overall system design, performance, and cost, we can consider hybrids of the orthogonal modulation formats described in section 2.2.1, which can be used to access the many THz of available optical spectrum. Selection of f-FSK frequencies, p-PPM positions, and L-polarization states distributed over w-WDM channels can be used to overcome practical limitations such as electrical bandwidth, nonlinear impairments, and available channel bandwidth as highlighted in Eqs. (126)–(129). The number of bits/symbol in such a multi-dimensional hybrid format is given by

$$k = \log_2(pfL) = \log_2(M_{\text{eff}}), \tag{126}$$

where M_{eff} is the effective number of orthogonal symbols in the constellation. In order to maintain orthogonality, the maximum number of polarization states $L_{\max} = 2$. In the Shannon-sense, the bandwidth expansion factor (as illustrated in Fig. 1) is given by

$$F = \frac{1}{r} = \frac{\log_2(pfL)}{pfL\,(1+\eta_{\text{FEC}})} = \frac{k}{M_{\text{eff}}\,(1+\eta_{FEC})} \quad \left[\frac{\text{bit/s}}{\text{Hz}}\right]^{-1}, \tag{127}$$

which can be used to improve RX sensitivity and photon efficiency. Here r is spectral efficiency, and the $(1+\eta_{\text{FEC}})$ term accounts for additional FEC overhead such that the channel rate, R_b $(1+\eta_{\text{FEC}})$. For a given data bit rate R_b, the combination of the number of wavelengths and symbol constellation size can be used to reduce the required electrical bandwidth per channel:

$$B_E = \frac{R_b\,(1+\eta_{\text{FEC}})\,p}{wk}, \tag{128}$$

which benefits from the use of orthogonal bases (polarization and frequency) and independent WDM channels. The net optical bandwidth required is

$$B_O = \frac{2R_b\,(1+\eta_{\mathrm{FEC}})\,pf}{k}, \tag{129}$$

where the factor of 2 is a conservative estimate for the minimum wavelength spacing. The corresponding effective peak TX power is given by

$$P_{\mathrm{pk}}^{\mathrm{eff}} = \left(\frac{\kappa_{\mathrm{eff}}}{w}\right)\frac{\bar{P}p}{\mathrm{DC}_{\mathrm{pulse}}}, \tag{130}$$

where κ_{eff} is the effective number of overlapping symbols defined Eq. (90) in section 3.5.5A.

From these equations, the impact of adjusting the hybrid-modulation parameters (p, f, L, and w) can readily evaluated, to optimize the lasercom system. For example, given a maximum electronic bandwidth limitation $B_E^{\max}$, the maximum achievable data rate can be determined from Eq. (128),

$$R_b^{\max} = \frac{B_E^{\max} wk}{(1+\eta_{\mathrm{FEC}})\,p} = \frac{Swk}{(1+\eta_{\mathrm{FEC}})\,p}, \tag{131}$$

where S is the bandwidth-limited p-PPM slot rate. From Eq. (131) it is easy to see that $R_b^{\max}$ can be increased directly through the number of WDM channels or by increasing the net bits per symbol k, by expanding the constellation size with supplementary frequency or polarization bases. The former linearly increases $R_b^{\max}$ while maintaining the same spectral efficiency and sensitivity per channel, whereas the latter can be used to augment $R_b^{\max}$ while improving RX sensitivity [see Eqs. (126) and (17)–(20)] at the expense of spectral efficiency.

5.4. Demonstrated Communication Performance

Throughout the paper, we have discussed methods of optimizing receiver sensitivity through use of various TX and RX designs, modulation and coding. An extension of Alexander's compilation of representative high-sensitivity lasercom demonstrations is given in Table 14 and Fig. 61 [20]. Receiver sensitivity at 10^{-9} BER is listed as a function of data-rate for various modulation formats, waveforms, and RX designs. These demonstrations bridge the gap between theory and what can be achieved given realistic design and technology constraints, and support many of the conclusions and design guidelines presented here. As laser communication technologies and TX/RX designs have matured, data rates have increased and sensitivities have improved, moving towards the lower-right quadrant of the Fig. 61, with the current state-of-the-art rapidly approaching the fundamental quantum and Shannon limits of communication performance.

As we can see in Fig. 61, at high rates, optically preamplified receivers have demonstrated the best sensitivities, despite inferior theoretical sensitivities relative to coherent-homodyne and photon-counting RXs. This is largely due to the nearly ideal characteristics of wideband high-gain average-power-limited optical amplifiers discussed throughout this paper that enable the preamplified RX structure to leverage the strengths and mitigate the deficiencies in essential RX electronics. As a result, preamplified systems can often leverage ongoing developments in wideband telecom optical and high-speed electronic technologies, proving a cost-effective means of advancing the state-of-the-art. When combined with the maturity and sophistication

Table 14. List of high-sensitivity optical receiver demonstrations shown in Fig. 61.

#	Rate, [Mbit/s]	Sensitivity, [avg. PPB]	Modulation/ Waveform	RX	Coding, O/H	Ref.
1	65*	1	32-PPM	Phot. Cnt. SSPD	SCPPM Turbo, 100%	[34]
2	14	1	64-PPM	Phot. Cnt. GM-APD	SCPPM Turbo, 100%	[44]
3	781	2	32-PPM	SSPD Phot. Cnt.	SCPPM Turbo, 100%	[34]
4	73	4	256-PPM	Opt. Preamp	RS255/239, 7%	[15]
5	2	5	PSK	Homodyne	Conv. Cd.	[157]
6	10000	7	DSPK-RZ	Opt. Preamp	Turbo Block, 25%	[24]
7	781	8	32-PPM	Phot. Cnt. SSPD	SCPPM Turbo, 100%	[33]
8	40000	8.7	DSPK-RZ	Opt. Preamp	E-RS255/239, 7%	[25]
9	78	9	256-PPM	Opt. Preamp	no	[15]
10	136	10	128-PPM	Opt. Preamp	no	[15]
11	10000	11	DSPK-RZ	Opt. Preamp	E-RS255/239, 7%	[41]
12	233	10	64-PPM	Opt. Preamp	no	[15]
13	389	12	32-PPM	Opt. Preamp	no	[15]
14	4	16	PSK	Homodyne	no	[157]
15	622	16	16-PPM	Opt. Preamp	no	[15]
16	10000	16	OOK-RZ	Opt. Preamp	E-RS255/239, 7%	[41]
17	565	20	PSK	Homodyne	no	[195]
18	781	20	32-PPM	Phot. Cnt. SSPD	SCPPM Turbo, 100%	[33]
19	933	20	8-PPM	Opt. Preamp	no	[15]
20	140	25	PSK	Homodyne	no	[453]
21	2500	25	DPSK-RZ	Opt. Preamp	no	[133]
22	10000	30	DSPK-RZ	Opt. Preamp	no	[129]
23	1244	31	4-PPM	Opt. Preamp	no	[15]
24	5600	35	PSK	Homodyne	no	[158]
25	10000	36	DSPK	Opt. Preamp	no	[129]
26	400	36	PSK	Homodyne	no	[155]
27	110	37	4-FSK	Heterodyne	no	[160]
28	1000	37	OOK	Opt. Preamp	4/5 Conv. Cd., 25%	[454]
29	10000	38	DSPK	Opt. Preamp	no	[128]
30	42700	38	DPSK	Opt. Preamp	no	[159]
31	5000	43	OOK-RZ	Opt. Preamp	no	[13]
32	1250	45	OOK-RZ	Opt. Preamp	no	[455]
33	400	45	DPSK	Heterodyne	no	[456]
34	12500	45	DSPK-RZ	Opt. Preamp	no	[24]
35	42700	45	DSPK-RZ	Opt. Preamp	no	[130]
36	1250	46	FSK-RZ	Opt. Preamp	no	[455]
37	1000	46	PSK	Homodyne	no	[164]
38	10000	57	OOK-RZ	Opt. Preamp	no	[406]
39	10000	60	OOK-RZ	Opt. Preamp	no	[129]
40	1244	61	2-PPM	Opt. Preamp	no	[15]
41	3000	62	DPSK	Opt. Preamp	no	[438]

*Note that #1 is the #3 32-PPM demonstration at 10 Gslots/s with a 12× repeat code. This lowers photon flux and reduces blocking losses by 3 dB, and lowers the data rate to 65 Mbps. It also emulates the performance of a 12-detector array operating at 781 Mbps.

Table 14. (Continued) List of high-sensitivity optical receiver demonstrations shown in Fig. 61.

#	Rate, [Mbit/s]	Sensitivity, [avg. PPB]	Modulation/ Waveform	RX	Coding, O/H	Ref.
42	51	65	2-PPM	Opt. Preamp	no	[11,12]
43	155	65	2-PPM	Opt. Preamp	no	[11,12]
44	311	65	2-PPM	Opt. Preamp	no	[11,12]
45	622	65	2-PPM	Opt. Preamp	no	[11,12]
46	1244	65	2-PPM	Opt. Preamp	no	[11,12]
47	2500	66	CPFSK	Heterodyne	no	[194,457]
48	60	68	4-PPM	APD-FET	no	[391]
49	120	71	4-PPM	APD-FET	no	[391]
50	4000	72	PSK	Homodyne	no	[458]
51	200	74	FSK	Heterodyne	no	[179]
52	560	78	DPSK	Heterodyne	no	[459]
53	30	80	4-PPM	APD-FET	no	[391]
54	7800	81	PSK	Homodyne	no	[158]
55	10000	81	OOK	Opt. Preamp	no	[129]
56	140	84	FSK	Heterodyne	no	[460]
57	10000	88	Duobinary	Opt. Preamp	no	[152]
58	6000	89	CPFSK	Heterodyne	no	[461]
59	5000	93	PSK	Homodyne	no	[166]
60	10000	100	PSK	Homodyne	no	[462]
61	15	108	4-PPM	APD-FET	no	[391]
62	325	110	OOK	APD-trans-Z	no	[390]
63	10000	112	OOK	Opt. Preamp	no	[463]
64	565	116	DPSK	Heterodyne	no	[464]
65	3000	116	DPSK	Opt. Preamp	no	[465]
66	140	119	FSK	Heterodyne	no	[162]
67	5000	135	OOK	Opt. Preamp	no	[466]
68	2500	137	OOK	Opt. Preamp	no	[316]
69	10000	147	OOK	Opt. Preamp	no	[467]
70	622	152	OOK	Opt. Preamp	no	[468]
71	622	155	OOK	APD-HEMPT	no	[469]
72	1244	156	OOK	Opt. Preamp	no	[470]
73	4000	175	OOK	Heterodyne	no	[471]
74	4000	191	FSK	Heterodyne	no	[471]
75	10000	193	OOK	Opt. Preamp	no	[316]
76	4000	209	DPSK	Heterodyne	no	[471]
77	20000	270	OOK	Opt. Preamp	no	[472]
78	10000	297	PSK	Homodyne	no	[165]
79	2000	705	OOK	APD-FET	no	[473]
80	1000	1162	OOK	APD-FET	no	[474]
81	20000	1600	OOK	Opt. Preamp	no	[475]
82	10000	3000	OOK-RZ	APD-FET	no	[388]

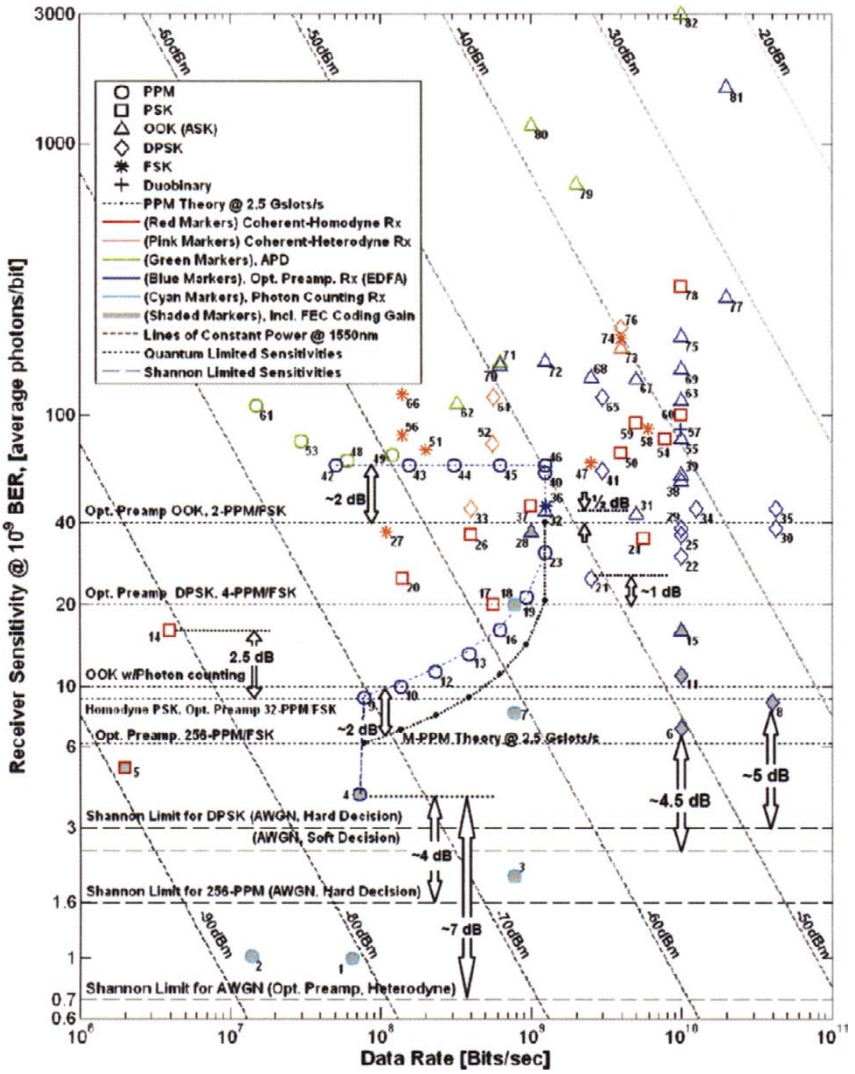

Fig. 61. Summary of high-sensitivity optical communication demonstrations showing reported sensitivities as a function of data rate. Modulation type is indicated by marker type, for instance PPM is represented by circles. Receiver type is indicated by color: Red indicates coherent (dark red = homodyne and pink = heterodyne), dark blue indicates an optically preamplified, and light-blue indicates a photon-counting RX. Coded demonstration results are shaded. Also shown are the quantum-limited sensitivities for the various modulation formats (uncoded), M-PPM theory for 2.5 Gslots/s, Shannon-limited sensitivities, and lines of constant power (dashed diagonal). See also Robinson et al. [214], 1.5 PPB sensitivity at 100 kbps. *Adapted from S. Alexander* [20].

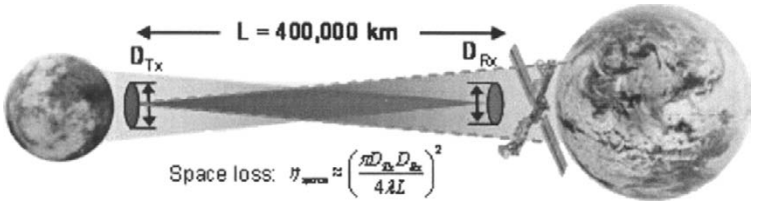

Fig. 62. Illustration of bidirectional Earth–Moon lasercom link [22].

of these technologies, performance is more robust and much closer to the theoretical limits over a wide range of data rates from the Mbit/s regime to tens of Gbit/s [13,15,24,25,41,130,159]. Furthermore, the data rate for high-speed preamplified receivers can be scaled using standard WDM techniques without additional performance penalty, providing a significant performance advantage over coherent- and photon-counting-based receiver designs.

Recent advancement in photon-counting detector technologies combined with powerful FEC has led to the most sensitive demonstrations in Fig. 61. These demonstrations include detector characteristics such as detection-efficiency and internal detector noise sources such as dark-counts, after-pulsing, and blocking loss (due to limited detector bandwidth). Note that these demonstrations do not include external background noise, which is an important consideration that can vary widely with channel conditions [108,109,476]. The multi-mode detection area of these detectors that is beneficial for mitigating channel turbulence and simplifying spatial acquisition, tracking, and photon-collection, combined with a broad spectral acceptance, make background noise a practical limitation in many photon-counting applications. Thus, for photon-counting receivers limited by background noise, optical filtering along with associated insertion losses must be included in the evaluation of RX performance. However after incorporating the additional ~0.5 to 1 dB losses for narrow-band optical filtering [398,477,478], photon-counting receivers sill show great promise for use in power-starved links, especially ground-based receivers, where atmospheric effects may be considerable and size, weight, power, and reliability are not necessarily critical design drivers.

5.5. Applications: to the Moon and Beyond

We conclude this paper with discussion of a long-haul application, which illustrates many of the benefits of FSO. Renewed interest in manned missions to the moon and beyond would require robust bidirectional high-rate links to support the human infrastructure, telemetry, science data, diagnostics, remote monitoring and control, and web-based connectivity. Here we present four notional lasercom link budgets for the ~400,000 km Earth–Moon link (Fig. 62), based on mature technologies that are readily available today and incorporate many of the concepts discussed earlier in the paper.

The budgets in Table 15 use the following communication parameters:

Modulation format M-PPM

Slot Rate: $S = 10$ Gslot/s
Coding gain: 5 dB
Waveform: 50% RZ
Wavelength: $\lambda = 1550$ nm
Aperture size: $D_{\mathrm{TX}} = D_{\mathrm{TX}} = 0.2$ m $\rightarrow \eta_{\mathrm{space}} = 86$ dB.

The budgets also include the following estimates of implementation losses:

Transmitter optics: $\eta_{\mathrm{TX}} = -3$ dB
Receiver optics: $\eta_{\mathrm{RX}} = -3$ dB
Pointing and tracking: $\eta_{\mathrm{PAT}} = -2$ dB
Receiver dB from theoretical: $\eta_{\mathrm{QL}} = -2$ dB.

Raybon and co-authors presented an impressive all optical 400 km regenerating optical loop experiment at 40 Gbit/s, with each loop consisting of four EDFA- and Raman-amplified 100 km spans [138,303]. They postulated that such technologies could be used to span a distance equivalent to the Earth– Moon link, but would require ~1000 regenerators to overcome the ~100,000 dB fiber loss. Long-haul FSO has clear benefits over such guided-wave links, since the net space-loss for 0.2 m TX and RX apertures is ~86 dB, a savings of over 99,000 dB. This advantage combined with more energy-efficient modulation and coding, and reduced data-rates enables the link to be closed with Watt-class transmitters.

Table 15. Lunar lasercom link budgets for various configurations of PPM constellation size (M), number of channels (w), and aperture diameter. Common to each of the four configurations is the slot rate $S = 10$ Gslot/s, coding overhead, wavelength ($\lambda = 1550$ nm), link distance, and assumptions for implementation penalties. These include losses in the TX ($\eta_{\mathrm{TXOpt}} = -3$ dB) and RX ($\eta_{\mathrm{RXOpt}} = -3$ dB) optics, pointing and tracking ($\eta_{\mathrm{PAT}} = -2$ dB) and RX deviation from theoretical performance ($\eta_{\mathrm{QL}} = -2$ dB). Adapted from [22].

Key Parameters for Earth ↔ Moon link	Units	#1	#2	#3	#4
Communication System Parameters:					
1 Constellation size (M)		1024	128	1024	256
2 Number of WDM channels (w)		1	1	8	120
3 Data Rate/channel, $R_{ch} = S \cdot \log_2(M)/[M \cdot (1+\eta_{FEC})]$	GBit/sec	0.065	0.365	0.065	0.208
Transmitter:					
4 Average Tx Power/channel (P_{Tx})	dBW	-3	-3	-12.0	-7.8
5 Peak Tx Power/channel = $P_{Tx} \cdot M/(w \cdot \mathrm{Pulse}_{DC})$	dBW	30	21	21	19
6 Net Tx Power = $w \cdot P_{Tx}$	dBW	-3	-3	-3	13
Receiver:					
7 Approx. Uncoded Rx sensitivity M-PPM, (PPB_{QL})	dB-PPB	6.0	7.6	6.0	7.0
8 Net Rx sensitivity @ Data Rate (S_{Rx})	dBW	-107.8	-98.7	-107.8	-101.7
9 Received Power/channel at EDFA input (P_{Rx})	dBW	-96.9	-96.9	-105.9	-101.7
Performance					
10 Implemented Receiver Sensitivity	dB-PPB	3.0	4.6	3.0	4.0
11 Net Bandwidth Required = $2 \cdot S \cdot w \cdot (1+\eta_{FEC})/125E9$	nm	0.24	0.24	1.92	28.8
12 Net Rate: Rnet = $R_{ch} \cdot w$	GBit/sec	0.065	0.365	0.521	25.0
13 Margin	dB	10.9	1.8	1.8	0.0

A representative TX and RX pair suitable for long-term use in space [21,198,380,409] that can achieve the performance in the budget above is a Master-Oscillator-Power Amplifier (MOPA) transmitter with an optically preamplified receiver [15]. Quasi-Gaussian 50%-RZ pulse-shaping in the transmitter is used to ensure a robust match between the TX-waveforms and the Gaussian optical filter in the RX and minimize

the impact of timing jitter [14], with demonstrated performance within 1 dB of the quantum limit [13,133]. Furthermore, as discussed in sections 3.5.5 and 5.1.3, fixing the pulse shape for all M enables flexible multi-rate capability with a single receiver optimized for all rates [11,12,15].

In Table 15, configuration #1 highlights a low-rate 65-Mbit/s link achieved with ~11 dB margin using a 0.5 W transmitter, 0.2m TX and RX apertures, and 1024-PPM. Of course, the margin could be traded to reduce aperture size or net output power. Alternatively, by simply changing the PPM alphabet size to M = 512, 256, or 128 as in configuration #2, the excess margin could be used to increase the data rate up to 365 Mbit/s with ~2 dB margin, providing the option for bandwidth-on-demand or fall-back modes of operations as needed.

Another option would be to include additional WDM channels with 0.2nm spacing as in configuration #3, which can provide up to 521 Mbit/s with ~2 dB margin. Relative to #2, the increase in net data rate is enabled by the 1.6 dB improvement in RX sensitivity due to the larger alphabet size. Although more hardware is required to support the additional WDM channels, #3 provides similar flexibility in net data throughput as #1 and #2 with additional redundancy. In addition, having multiple channels share a common power amplifier effectively reduces the peak TX power avoiding the nonlinear impairments that can limit M [21]. Such effects start to impact communication performance at 24 to 30 dBW peak levels as discussed in section 3.5.5C, and could necessitate a change of design parameters in #1. For example, hybrid-orthogonal constellations including polarization and frequency bases can be used to maintain M_{eff} and reduce the peak power.

By increasing average TX power to 13 dBW (20 W), and WDM channel count to 120 in configuration #4, a link with up to ~25 Gbit/s throughput can be achieved. This requires ~29nm of bandwidth, which easily falls within the 35-nm EDFA C-band, and corresponds to only 0.007 bit/s/Hz spectral efficiency. However, the resultant improvement in receiver sensitivity to 2.5 PPB enables a respectable distance-rate product of $\sim 10^{16}$km-bit/s—comparable to the best fiber-based demonstrations [93,138,139,141], without the need for ~1000 regenerators, emphasizing the difference between square- and exponentially-dependent channel loss. For #4, the overall link efficiency (using $\eta_{\text{E/O}}$ = 13% [199]) is

$$\eta_{\text{link}} = \frac{P_{\text{TX}}^{\text{net}}}{\eta_{\text{E/O}} R_{\text{net}}} = 6 \quad [\text{nJ/bit}] \tag{132}$$

for the 400,000 km lunar link.

We conclude that established technologies developed for the telecom industry can be leveraged to implement scalable photon-efficient optical communication capabilities today. These example lunar link budgets, based on an average-power-limited MOPA TX and a near-quantum-limited M-orthogonal optically-preamplified RX, show the potential for high-capacity long-haul free-space optical links at variety of data rates from the Mbit/s regime to tens of Gbit/s, rates that cannot be practically achieved using RF technologies. And, as photon-counting technologies mature, the sensitivity of optical receivers could potentially improve another 5–10 dB. These capabilities are likely to become an essential part of the space-based communications infrastructure, providing cost-effective support for deep-space exploration and future manned missions to the Moon, Mars, and beyond.

Acknowledgments

For most of the past decade, I've had the pleasure to work in the challenging and innovative atmosphere at MIT Lincoln Laboratory, perhaps best described by Don McClellan, the former head of the Communications Division who said, "If the laws of physics will permit it, we can build it."

Many thanks to Vincent Chan, Roy Bondurant, Kristin Rauschenbach, and Eric Swanson for providing me with the initial opportunity to work in this stimulating environment, where I have been able to contribute to the field of optical communications and bring many new ideas to reality, alongside an extremely talented group of present and former colleagues from the MIT community. These include Walid Atia, Richard Barron, David Bold, Don Boroson, Larry Candell, Steve Constantine, Jerry Chen, Eric Dauler, Bill Freking, Jeff Gottschalk, Matt Grein, Farhad Hakimi, Katie Hall, Scott Hamilton, Scott Henion, Paul Juodawlkis, Alan Kachelmyer, John Kaufmann, Andrew Kerman, Sumanth Kaushik, Bill Keicher, Mark Kuzenetzov, Farzana Khatri, Emily Kintzer, Sarah Klein, Jeff Livas, Jeff Mendenhall, John Moores, Bob Murphy, Dan Murphy, Ron Parenti, Wayne Phoel, Al Pillsbury, Jinendra Ranka, Jeff Shapiro, Neal Spellmeyer, Peter Schulz, Todd Ulmer, Simon Verghese, Matt Willis, Tim Yarnell, and many others in the community.

It has been a privilege to work closely with people of the caliber of John Carney, Bryan Robinson, Fred Walther, and especially Mark Stevens. As friends and colleagues with tremendous breadth and depth of experience with optics, communications, and making things happen, they have been a catalyst for many of the new ideas that are reflected in this paper. Along with other members of the Optical Communication Technology Group, they have contributed significantly to the content and initial demonstration of many of the concepts presented.

To my wife Rose and my family I owe the most gratitude. Without their continuing support and encouragement, this would not have been possible.

Symbols

α	Chirp parameter
$\Delta\gamma$	SNR penalty
κ_{eff}	Effective number of overlapping WDM pulses
λ	Wavelength $= c/\nu$, [m]
η_{atm}	Atmospheric loss
η_{ch}	Net channel loss = $\eta_{\text{TXOpt}}\eta_{\text{atm}}\eta_{\text{PAT}}g\eta_{\text{space}}\eta_{\text{RXOpt}}$
η_{link}	Overall link efficiency = $\eta_{\text{TX}}\eta_{\text{ch}}\eta_{\text{RX}}$TX-Joules/RX-bit, [J/bit]
η_{PAT}	Pointing and tracking losses
η_{RX}	Net Receiver efficiency= $\text{PPB}_{\text{QL}}G_{\text{code}}$[Photons/bit]
η_{RXOpt}	Receiving optics (telescope) losses
η_{space}	Space diffraction loss = $[\pi D_T D_R/(4\lambda L)]^2$
η_{TX}	Net Transmitter efficiency (E/O) [TX-Joules/Photon]
η_{TXER}	Transmitter ER penalty
η_{TXOpt}	Transmitting optics (telescope) losses
ν	Optical frequency = c/λ [Hz]
τ_{bit}	Bit or symbol duration [s]
τ_o	3 dB pulsewidth of optical filter impulse resp. [s]
τ_s	3 dB pulsewidth of signal (power) [s]
B	Bandwidth [Hz]
B_o	Optical bandwidth [Hz]
c	Speed of light in vacuum $c = \lambda\nu = 3.0 \times 10^8$ [m/s]
D_{TX}	Diameter of transmit aperture [m]
D_{RX}	Diameter of receive aperture [m]
DC_{eff}	Effective duty cyle $\text{DC}_{\text{eff}} = \text{DC}_{\text{mod}}\ \text{DC}_{\text{pulse}}$
DC_{mod}	Modulation duty cycle
DC_{pulse}	Pulse shape duty cycle
e	Electron charge 1.601×10^{-19} [C]
f_c	RF filter 3-dB bandwidth (cutoff frequency) [Hz]
f-FSK	f= # of FSK frequencies in a hybrid symbol
g_o	Optical amplifier small-signal gain
G	Gain
G_{code}	FEC coding gain
h	Planck's constant 6.626×10^{-34} [J/s]
k_B	Boltzman's constant 1.379×10^{-23} [W/°K-Hz]
k	number of bits-per M-ary symbol $k = \log_2(M)$
k_{eff}	Effective number of bits-per M-ary symbol
L-PolSK	L = # of PoSLK polarizations in a hybrid symbol
M	Symbol constellation size, as in M-ary PPM
$M =$	$2^k, k = \log_2(M)$ = # of bits/symbol
N_{avg}	Average photon count per interval [photons]
N_b	Background-noise photon count [photons]
$N_o/2$	Noise power spectral density [W/Hz]
$N_{\text{RX}-\text{min}}$	Minimum required RX SNR
N_{shot}	Shot noise power spectral density $= h\nu$ [W/Hz]
N_{sp}	Spontaneous emission factor [photons/mode]
N_{th}	Thermal noise power spectral density $= k_B T$ [W/Hz]

$P_{\text{in-sat}}$	Amplifier input saturation power $P_{\text{in-sat}} = P_{\text{sat}}/g_o$
P_{sat}	Amplifier saturated output power
P_{shot}	Shot noise power spectral density $= h\nu B$ [W]
P_{th}	Thermal noise power $= k_B T B$ [W]
PPB_{QL}	Uncoded quantum-limited RX sensitivity [photons/bit]
p-PPM	p = # of PPM positions in a hybrid symbol
r	Spectral efficiency [(bits/s)/Hz]
R_{ph}	Photon flux rate $P/(h\nu)$ [photons/s]
R_b	Bit rate, $R_b = 1/\tau_{\text{bit}}$[bits/s]
$R_{\text{A/W}}$	Detector responsivity, $R_{\text{A/W}} = \eta q/hv$ [mA/mW]
V_π	Switching voltage
w	Number of WDM channels
Z_o	Impedance Ω = [V/A]

Acronyms and Abbreviations

ADC	Analog-to-digital converter
APL	Average power limited
ARTEMIS	Advanced Relay Technology Mission Satellite
ASK	Amplitude shift keying, 2-ASK the same as OOK
AWGN	Additive white Gaussian noise
BER	Bit-error rate
CML	Chirp-managed laser
CW	Continuous wave
COTS	Commercial off-the-self
DAC	Digital-to-analog converter
DC	Duty cycle
dB	Decibel = 10*$\log_{10}$(Power/P_{ref})
dBm	10 $\log_{10}$(Power/1 mW)
dBW	10 $\log_{10}$(Power/1 W)
DI	Delay-line interferometer
DPSK	Differential phase shift keying
EDFA	Erbium-doped fiber amplifier
EYDFA	Erbium-Ytterbium (codped) fiber amplifier
EM	Electromagnetic
EMI	Electromagnetic interference
ER	Extinction ratio = $\text{Power}_{\text{off}}/\text{Power}_{\text{on}}$
FBG	Fiber Bragg grating
FEC	Forward error correction (coding)
FIT	Failure in time (#failures per billion hours of operation)
FM	Frequency modulation
FP	Fabry-Perot
FP^n	nth order Fabry-Perot
FSK	Frequency-shift keying
FSO	Free-space optical
FWHM	Full width half max
FWM	Four-wave mixing

Gbps	Gigabit per second
GEO	Geostationary earth orbit
GeoLITE	Geosynchronous Lightweight Technology Experiment
GOLD	Ground-to-Orbit Lasercom Demonstration
IM	Intensity modulation
IM-DD	Intensity-modulated direct-detection
ICI	Inter-channel-interference
ISI	Inter-symbol-interference
ITU	International Telecommunications Union
ITU-R	Radiocommunication Standard
ITU-T	Telecommunication Standard
ITU-grid	Standard 100 GHz WDM channel spacing
LEO	Low earth orbit
Mbps	Megabit per second
MLCD	Mars Laser Communication Demonstration
MZI	Mach-Zehnder interferometer
MZM	Mach-Zehnder Modulator
MTTF	Mean time to failure
NA	Numerical aperture, NA = $n\sin(\theta)$
NF	Noise Figure
OICETS	Optical Inter-orbit Communications Engineering Test Satellite
OOK	On-off keying (binary-ASK)
PAT	Pointing acquisition and tracking
PM	Polarization maintaining
PPB	Number of photons/bit
PPM	Pulse position modulation
PPL	Peak power limited
PRBS	Pseudo-random bit sequence
PSD	Power spectral density, [dBm/Hz]
P[$a|b$]	Probability of a given b
PER	Polarization extinction ratio
RF	Radio frequency, generic term for electrical
RX	Receiver
SCOWA	Slab-coupled optical waveguide amplifier
SCM	Subcarrier multiplexing
SBS	Stimulated Brillouin scattering
SILEX	Semiconductor Intersatellite Link Experiment
SPM	Self-phase modulation
SPOT-4	System Probatoire/Satellite Pour d'Observation de la Terra 4 satellite
SNR	Signal-to-noise-ratio
SRS	Stimulated Raman scattering
TDM	Time division multiplexing
TEC	Thermo-electric cooler
TIA	Transimpedance amplifier
TX	Transmitter
VDC	Variable duty cycle
VBG	Volume Bragg grating
WDM	Wavelength division multiplexing or multiplexer
YDFA	Ytterbium-doped fiber amplifier

References

1. B.L. Edwards, et. al., "Overview of the Mars laser communications demonstration project," in American Institute of Aeronautics and Astronautics, Space 2003 Conference & Exposition, 2003.
2. S.A. Townes, et. al., "The Mars laser communication demonstration," presented at IEEE Aerospace Conf., 2004.
3. E.A. Swanson and R.S. Bondurant, "Fiber-based free-space optical system," in US Pat. 5,062,150, 1991.
4. "Reliability assurance practices for optoelectronic devices in interoffice applications," Bellcore TR-NWT-000468 Issue 1, Dec. 1991.
5. "Generic reliability assurance requirements for optoelectronic devices used in telecommunications equipment," Telcordia GR-468-CORE no. 2, Dec. 2002.
6. "Generic requirements for fiber optic branching components," Bellcore GR-1209-CORE, Issue 1, Nov. 1994.
7. "Generic requirements for optical fiber amplifiers," GR-1312-CORE, Issue 2, Dec. 1996.
8. "Generic reliability assurance requirements for fiber optic branching components," GR-1221-CORE, Issue 1, Dec. 1994.
9. "Test methods and procedures for microelectronics," Military Standard MIL-STD-883C, Aug. 1983.
10. D.O. Caplan, M.L. Stevens, and D.M. Boroson, "Variable-rate communication system with optimal filtering," in US Pat. 6,694,104, 2004, (filed 1998).
11. D.O. Caplan, M.L. Stevens, D.M. Boroson, and J.E. Kaufmann, "A multi-rate optical communications architecture with high sensitivity," in LEOS, 1999.
12. M.L. Stevens, D.M. Boroson, and D.O. Caplan, "A novel variable-rate pulse-position modulation system with near quantum limited performance," in LEOS, 1999.
13. D.O. Caplan and W.A. Atia, "A quantum-limited optically-matched communication link," in Optical Fiber Conference (OFC), 2001.
14. D.O. Caplan and W.A. Atia, "Methods of achieving optimal communications performance," in US Pat. 7,181,097, 2007.
15. D.O. Caplan, B.S. Robinson, R.J. Murphy, and M.L. Stevens, "Demonstration of 2.5-Gslot/s optically-preamplified M-PPM with 4 photons/bit receiver sensitivity," in Optical Fiber Conference (OFC): Paper PDP23, 2005.
16. C.E. Shannon, "A mathematical theory of communication," Bell Syst. Technol. J. **27**, 379-423, 623-656, 1948.
17. S. Haykin, *Digital Communications* (John Wiley & Sons, Inc., 1988).
18. J.G. Proakis and M. Salehi, *Communication Systems Engineering* (Prentice-Hall, Inc., 1994).
19. Peebles, Peyton Z. Jr., *Digital Communications Systems* (Englewood Cliffs, NJ: Prentice-Hall, 1987).
20. S.B. Alexander, *Optical communication receiver design* (Bellingham, Washington, USA: SPIE Optical Engineering Press, 1997).
21. D.O. Caplan, "High-performance free-space laser communications and future trends," in Optical Amplifiers and Their Applications (OAA'05) Topical Meeting, Budapest, Hungary, 2005.

22. D.O. Caplan, B.S. Robinson, M.L. Stevens, D.M. Boroson, and S.A. Hamilton, "High-Rate Photon-Efficient Laser Communications with Near Single Photon/bit Receiver Sensitivities," in Optical Fiber Conference (OFC), 2006.

23. D.M. Boroson, "Optical Communications, A Compendium of Signal Formats, Receiver Architectures, Analysis Mathematics, and Performance Comparisons," 2005.

24. T. Mizuochi, et. al., "Forward error correction based on block turbo code with 3-bit soft decision for 10-Gb/s optical communication systems," IEEE Sel. Top. Quantum Electron. **10**, 376–386, 2004.

25. N.W. Spellmeyer, J.C. Gottschalk, D.O. Caplan, and M.L. Stevens, "High-sensitivity 40-Gb/s RZ-DPSK with forward error correction," IEEE Photon. Technol. Lett. **16**, 1579–1581 (2004).

26. J.R. Pierce, "Optical Channels: Practical Limits with Photon Counting," IEEE Trans. Commun. **COM-26**, 1819-1821, 1978.

27. Y. Yamamoto and H.A. Haus, "Preparation, measurement and information capacity of optical quantum states," Rev. Mod. Phys. **58**, 1001-1020, 1986.

28. H.A. Haus, "Limits on communication using photons," in MIT-EECS Colloquium Series, 1997.

29. G.N. Gol'tsman, O. Okunev, G. Chulkova, A.L.A. Semenov, K. Smirnov, B. Voronov, A. Dsardanov, C. Williams, and R. Sobolewski, "Picosecond superconducting single-photon optical detector," Appl. Phys. Lett. **79**, 705–707, 2001.

30. K.A. McIntosh, et. al., "InGaAsP/InP avalanche photodiodes for photon counting at 1.06 μm," Appl. Phys. Lett. **81** (2002).

31. J. Zhang, W. Slysz, A. Verevkin, O. Okunev, G. Chulkova, A. Korneev, A. Lipatov, G.N. Gol'tsman, and R. Sobolewski, "Response time characterization of NbN superconducting single-photon detectors," IEEE Trans. App. Supercond. **13**, 180–183, 2003.

32. K.A. McIntosh, et. al., "Arrays of III-V semiconductor Geiger-mode avalanche photodiodes," in LEOS, 2003.

33. B.S. Robinson, A.J. Kerman, E.A. Dauler, R.J. Barron, D.O. Caplan, M.L. Stevens, J.J. Carney, S.A. Hamilton, J.K.W. Yang, and K.K. Berggren, "781-Mbit/s Photon-Counting Optical Communications Using Superconducting NbN-Nanowire Detectors," Opt. Lett. **31**, 444– 446 (2006).

34. B.S. Robinson, A.J. Kerman, E.A. Dauler, R.J. Barron, D.O. Caplan, M.L. Stevens, J.J. Carney, S.A. Hamilton, J.K.W. Yang, and K.K. Berggren, "High-Data-Rate Photon-Counting Optical Communications Using a NbN Nanowire Superconducting Detector," in Conference on Lasers and Electro-Optics (CLEO), 2006.

35. E.A. Dauler, B.S. Robinson , A.J. Kerman, V. Anant, R.J. Barron, K. Berggren, D.O. Caplan, J.J. Carney, S.A. Hamilton, K.M. Rosfjord, M.L. Stevens, and J.K.W. Yang, "1.25-Gbit/s photon-counting optical communications using a twoelement superconducting nanowire single photon detector," in Proc. SPIE, (Advanced Photon Counting Techniques), 2006.

36. P.S. Henry, "Error-rate performance of optical amplifiers," in Optical Fiber Conference (OFC), 1989.

37. N.A. Olsson, "Lightwave Systems With Optical Amplifiers," J. Lightwave Technol. **7**, 1071–082 (1989).

38. P.A. Humblet and M. Azizoglu, "On bit error rate of lightwave systems with optical amplifiers," J. Lightwave Technol. **9** (1991).

39. S.D. Personick, "Receiver design for digital fiber optic communication systems, I & II," Bell Syst. Tech. J. **52**, 843-886, 1973.

40. S. Vanstone and P.C. v. Oorschot, *An introduction to Error Correcting Codes with Applications* (Kluwer Academic Publishers, 1989).

41. D.O. Caplan, J.C. Gottschalk, R.J. Murphy, N.W. Spellmeyer, M.L. Stevens, and A.M.D. Beling, "Performance of high-rate high-sensitivity optical communications with forward error correction coding," in Conference on Lasers and Electro-Optics (CLEO): Paper CPDD9, 2004.

42. B.E. Moision and J. Hamkins, "Coded modulation for the deep-space optical channel: serially concatenated pulse-position modulation," 42-161, 2005.

43. D.M. Boroson, C.C. Chen, and B.L. Edwards, "The Mars laser communication demonstration project: truly ultralong-haul optical transport," in Optical Fiber Conference (OFC), 2005.

44. P.I. Hopman, P.W. Boettcher, L.M. Candell, J.B. Glettler, R. Shoup, and G. Zogbi, "An End-to-End Demonstration of a Receiver Array Based Free-Space Photon Counting Communications Link," in SPIE, (Free-Space Laser Communications VI), vol. 6304, 2006.

45. R. Shoup, "Hardware implementation of a high-throughput 64-PPM serial concatenated turbo decoder," in SPIE, (Optical Information Systems IV), vol. 6311, 2006.

46. E.A. Swanson and R.S. Bondurant, "Using fiber optics to simplify free-space lasercom systems," in Proc. SPIE, (Free-Space Laser Communication Technologies II), **1218**, 70–82 (1990).

47. R.M. Gagliardi and S. Karp, *Optical Communication*, 2nd Ed. (New York,: John Wiley & Sons, Inc., 1995).

48. F. G. Walther, J.M. Roth, W.E. Keicher, A.E. DeCew, and "Wavelength division and polarization division multiple access free space optical terminal using a single aperture," in US Pat. Appl. 20040081466, 2004.

49. A.G. Bell and S. Tainter, "Photophone transmitter," in US Pat. 235,496, 1880.

50. A.G. Bell, "On the Production and Reproduction of Sound by Light," Am. J. Sci., 3rd Series, **XX**, 305–324 (1880).

51. A.G. Bell and S. Tainter, "Photophonic receiver," in US Pat. 241,909, 1881.

52. A.G. Bell, C.A. Bell, and S. Tainter, "Transmitting and recording sounds by radiant energy," in US Pat. 324,213, 1886.

53. D. Killinger, "Free space optics for laser communication through the air," in *Optics & Photonics News*, 2002.

54. Hertz, "Heinrich Rudolf Hertz discovered GHz radio waves in 1887," 1887.

55. A.G. Bell, "Improvement in Telegraphy," in US Pat. 174,465, 1876.

56. T.A. Edison, "Telephones or Speaking Telegraphs," in US Pat. 203,018, 1878.

57. G. Marconi, "A system of telegraphy using Hertzian waves," in British Pat. 12039, (filed June 2, 1896, demonstrated Sept. 2, 1896), 1896.

58. M. Loomis, "Improvement in Telegraphing," in US Pat. 129,971, 1872 (first US wireless telegraphy patent).

59. R.A. Fessenden, "Wireless Telegraphy," in US Pat. 706,737, 1902, (filed 1901).

60. A.L. Schawlow and C.H. Townes., "Infrared and Optical Masers," Phys. Rev.**112**, 1940–1949 (1958).

61. T.H. Maiman, "Stimulated optical radiation in ruby," Nature **187**, 493 (1960).

62. T.H. Maiman, "Ruby Laser Systems," in US Pat. 3,353,115, 1967, (filed 1963).

63. A. Javan, Bennett, W.R. Jr., and D.R. Herriott, "Population Inversion and Continuous Optical Maser Oscillation in a Gas Discharge Containing a He-Ne Mixture," Phys. Rev. Lett. **6**, 106–110, 1961.

64. "Research groups at GE, IBM, and Lincoln Laboratory at MIT demonstrated semiconductor lasers using gallium arsenide (GaAs) in 1962. (Courtesy W. Keicher)," 1962.

65. C.H. Gooch, *Gallium Arsenide Lasers* (New York: John Wiley & Sons, 1969).

66. C.J. Koester and E. Snitzer, "Amplification in a Fiber Laser," Appl. Opt. **3**, 1182–86 (1964).

67. E. Snitzer, "Means for producing and amplifying optical energy," in US Pat. 3,729,690, (filed 1969, 1961), 1973.

68. Z.I. Alferov, V.M. Andreev, D.Z. Garbuzov, Y.V. Zhilyaev, E.P. Morozov, E.L. Portnoi, and V.G. Trofim, "Investigation of the influence of the AlAs-GaAs heterostructure parameters on the laser threshold current and the realization of continuous emission at room temperature," Sov. Phys. Semicond. **4**, 1573–1575 (1971).

69. C.K. Kao and G.A. Hockham, "Dielectric-Fiber Surface Waveguides for Optical Frequencies," Proc. IEE **133**, 1151–58 (1966).

70. R.D. Maurer and P.C. Schultz, "Fused silica optical waveguide," in US Pat. 3,659,915, 1972, (filed 1970).

71. D.B. Keck and P.C. Schultz, "Method of producing optical waveguide fibers," in US Pat. 3,711,262, 1973, (filed 1970).

72. C.K. Kao and T.W. Davies, "Spectroscopic studies of ultra low loss optical glasses," J. Sci. Instrum. (1968).

73. F.P. Kapron, D.B. Keck, and R.D. Mauer, "Radiation losses in glass optical waveguides," Appl. Phys. Lett. **17**, (1970).

74. E. Snitzer, "Cylindrical dielectric waveguide modes," J. Opt. Soc. Am. (1961).

75. E. Snitzer, H. Po, R.P. Tumminelli, and F. Hakimi, "Optical fiber lasers and amplifiers," in US Pat. 4,815,079, (filed 1987), 1989.

76. R.J. Mears, L. Reekie, I.M. Jauncey, and D.N. Payne, "Low-noise erbim-doped fibre amplifier operating at 1.54 μm," Electron. Lett. **23**, 1026 (1987).

77. E. Desurvire, J.R. Simpson, and P.C. Becker, "High-gain erbium-doped traveling wave fiber amplifier," Opt. Lett. **12**, 888 (1987).

78. "TAT-8, the first trans-Atlantic fiber cable (2 $\times$ 280 Mb/s, 1.3 μm), was AT&T's 8th transatlantic telephone cable, in operation from 1988, initially carrying 40,000 telephone circuits between USA and France.."

79. "TAT-10, AT&T's 10th transatlantic telephone cable, in operation from 1992, initially carrying 2 $\times$ 565Mb/s between USA and Germany, using 1.5 μm technology."

80. Y. Arimoto, M. Toyoshima, M. Toyoda, T. Takahashi, M. Shikatani, and K. Araki, "Preliminary result on laser communication experiment using Engineering Test Satellite-VI (ETS-VI)," in Proc. SPIE 2381, 1995.

81. K.E. Wilson, J.R. Lesh, K. Araki, and Y. Arimoto, "Preliminary results of the Ground/Orbiter Lasercom Demonstration experiment between Table Mountain and the ETS-VI satellite," in Proc. SPIE (Free-Space Laser Communication Technologies VIII), 1996.

82. K.E. Wilson, et. al., "Results from Phase-1 and Phase-2 GOLD experiments," Feb. 15 1997.

83. K.E. Wilson and J.R. Lesh, "Overview of the Ground-to-Orbit Lasercom Demonstration (GOLD)," in Proc. SPIE (Free-Space Laser Communication Technologies IX), 1997.

84. "TAT-12/13 (1996) first used optical amplification (EDFA) and ring topology."

85. A.R. Chraplyvy, A.H. Gnauck, R.W. Tkach, J.L. Zyskind, J.W. Sulhoff, A.J. Lucero, Y. Sun, R.M. Jopson, F. Forghieri, R.M. Derosier, C. Wolf, and A.R. McCormick, "1-Tb/s transmission experiment," Photonics Technol. Lett. **8**, 1264–1266 (1996).

86. A.H. Gnauck, et. al., "One Terabit/s Transmission Experiment," presented at Optical Fiber Conference (OFC), 1996.

87. T. Morioka, et. al., "100 Gb/s × 10 Channel OTDM/WDM Transmission Using a Single Supercontinuum WDM Source," presented at Optical Fiber Conference (OFC), 1996.

88. H. Onaka, et. al., "1.1 Tb/s WDM Transmission over a 150 km 1.3 mm Zero-Dispersion Single-Mode Fiber," presented at Optical Fiber Conference (OFC), 1996.

89. KMI Corporation, Nashua, NH, USA.

90. S. Bigo, A. Bertaina, Y. Frignac, S. Borne, L. Lorcy, D. Hamoir, D. Bayart, J.-P. Hamaide, W. Idler, E. Lach, B. Franz, G. Veith, P. Sillard, L. Fleury, P. Guénot, and P. Nouchi, "5.12 Tbit/s (128 × 40 Gbit/s WDM) transmission over 3 × 100 km of TeraLight fiber," in Proc. Eur. Conf. Optical Communications (ECOC), paper PD1.2, Munich, Germany, 2000.

91. W. Idler, S. Bigo, Y. Frignac, B. Franz, and G. Veith, "Vestigial side-band demultiplexing for ultra-high capacity (0.64 bit/s/Hz) of 128 × 40 Gbit/s channels," in Optical Fiber Conference (OFC), 2001.

92. K. Fukuchi, T. Kasamatsu, M. Morie, R. Ohhira, T. Ito, K. Sekiya, D. Ogasahara, and T. Ono, "10,92 Tb/s (273 × 40 Gb/s) triple band/ultra dense WDM optical repeatered transmission experiment," presented at Optical Fiber Conference (OFC), 2001.

93. S. Bigo, Y. Frignac, G. Charlet, W. Idler, S. Borne, H. Gross, R. Dischler, W. Poehlmann, P. Tran, C. Simonneau, D. Bayart, G. Veith, A. Jourdan, and J.-P. Hamaide, "10.2 Tbit/s (256 × 42.7 Gbit/s PDM/WDM) transmission over 100 km TeraLight fiber with 1.28 bit/s/Hz spectral efficiency," in Optical Fiber Conference (OFC), paper PD25, 2001.

94. Y. Frignac, G. Charlet, W. Idler, R. Dischler, P. Tran, S. Lanne, S. Borne, C. Martinelli, G. Veith, A. Jourdan, J.-P. Hamaide, and S. Bigo, "Transmission of 256 wavelength-division and polarization-division multiplexed channels at 42.7 Gb/s (10.2 Tb/s capacity) over 3 × 100 km of TeraLight fiber," in Optical Fiber Conference (OFC), 2002.

95. "Press Release: NRO GeoLITE Satellite Successfully Launched". http://cartome.org/geolite .htm, 2001.

96. "Press Release: Delta Launches GeoLITE Satellite for U.S. NRO." http://www.spaceandtech.com/digest/flash2001/flash2001-038.shtml Andrews Space & Technology, 2001.

97. "Press Release: NRO Awarded the David Packard Excellence in Acquisition Award". http://www.nro.gov/PressReleases/prs_rel62.html, 2002.

98. T.T. Nielsen and G. Oppenhaeuser, "In-orbit test result of an operational optical intersatellite link between ARTEMIS and SPOT4, SILEX," in Proc. SPIE, (Free-Space Laser Communication Technologies XIV), 2002.

99. T.T. Nielsen, G. Oppenhaeuser, B. Laurent, and G. Planche, "In-orbit test results of the optical intersatellite link, SILEX. A milestone in satellite communication," in 53rd International Astronautical Congress, IAC-02-M.2.01, 2002.

100. H.P. Lutz, "Optical Communications in Space—Twenty Years of ESA Effort," in *ESA Bulletin (* http://esapub.esrin.esa.it/bulletin/bullet91/b91lutz.htm), **1**, 25–31 (1997).

101. B.I. Edelson, J.N. Pelton, C.W. Bostian, W.T. Brandon, V.W.S. Chan, E.P. Hager, N.R. Helm, R.D. Jennings, R.K. Kwan, C.E. Mahle, E. F. Miller, and L. Riley, "Satellite Communications Systems And Technology," in http://www.wtec.org/loyola/satcom/ ,Loyola College in Maryland, 1993.

102. M. Reyes, S. Chueca, A. Alonso, T. Viera, and Z. Sodnik, "Analysis of the preliminary optical links between ARTEMIS and the Optical Ground Station," in Proc. SPIE 4821, 2003.

103. A. Alonso, M. Reyes, and Z. Sodnik, "Performance of satellite-to-ground communications link between ARTEMIS and the Optical Ground Station," in Proc. SPIE 5572, 2004.

104. D.M. Boroson, C.C. Chen, and B.L. Edwards, "The Mars laser communications demonstration project: truly ultralong-haul optical transport," in Optical Fiber Conference (OFC), 2005.

105. M. Toyoshima, "Special Report: Trends of research and development of optical space communications technology," Space Japan Review 12 - 1, No. 44, 2005.

106. E. Hecht, *Optics, 2nd Ed.* (Addison Wesley, 1987).

107. A. Biswas, K.E. Wilson, S. Piazzolla, J.P. Wu, and W.H. Farr, "Deep-space optical communications link availability and data volume," in Proc. SPIE **5338**, 175 (2004).

108. F.I. Khatri, D.M. Boroson, D.V. Murphy, and J. Sharma, "Link analysis of Mars-Earth optical communications system," in Proc. SPIE **5338**, 143 (2004).

109. F.I. Khatri and A. Biswas, "Signal and Background Levels for the Mars Lasers Communications Demonstration (MLCD)," in IEEE LEOS Summer Topical Meetings, 2005.

110. R.W. Boyd, *Nonlinear Optics* (New York: Academic Press, Inc., 2003).

111. G.P. Agrawal, *Nonlinear Fiber Optics*, 2^{nd} ed. (New York: Academic Press, Inc., 1995).

112. W.E. Webb and J.T. Marino, Jr., "Threshold detection in an on-off binary communications channel with atmospheric scintillation," Appl. Opt. **14**, 1413–1417 (1975).

113. W.C. Brown, "Optimum Thresholds for Optical On-Off Keying Receivers Operating in the Turbulent Atmosphere," in Proc. SPIE, (Free-Space Laser Communication Technologies IX), vol. 2290, 254–261 (1997).

114. H. Haunstein, R. Schlenk, and K. Sticht, "Control of Combined Electrical Feed-Forward and Decision Feedback Equalization by Conditional Error Counts from FEC in the Presence of PMD," in Optical Fiber Conference (OFC), 2003.

115. D.M. Castagnozzi, "Digital signal processing and electronic equalization (EE) of ISI," in Optical Fiber Conference (OFC), 2004.

116. M. Schwartz, W.R. Bennett, and S. Stein, *Communication Systems and Techniques* (New York: IEEE Press, 1996).

117. S.D. Personick, P. Balaban, J. Bobsin, and P. Kumar, "A Detailed Comparison of Four Approaches to the Calculation of the Sensitivity of Optical Fiber System Receivers," IEEE Trans. Comm. **25**, 541–548 (1977).

118. R.G. Smith and S.D. Personick, *Semiconductor devices for optical communication* (New York: Springer-Verlag, 1982), vol. 39.

119. S.O. Rice, "Mathematical analysis of random noise," Bell Syst. Technol. J. **24**, 46–156 (1945).

120. S. Stein and J.J. Jones, *Modern communication principles* (New York: McGraw-Hill, 1967).

121. Saleh, B.E.A. and M.C. Teich, *Fundamentals of Photonics* (New York: Wiley, 1991).

122. T. Li and M.C. Teich, "Bit-Error Rate For A Lightwave Communication System Fibre Amplifier Incorporating An Erbium-doped Fibre Amplifier," Electron. Lett. **27**, 598–599 (1991).

123. T. Li and M.C. Teich, "Photon Point Process for Traveling-Wave Laser Amplifiers," IEEE J. Quantum Electron. **29**, 2568–2578 (1993).

124. W.S. Wong, H.A. Haus, L.A. Jiang, P.B. Hansen, and M. Margalit, "Photon statistics of amplified spontaneous emission noise in a 10-Gbitys optically preamplified direct-detection receiver," Opt. Lett. **23**, 1832-834 (1998).

125. W.S. Wong, J.D. Moores, J. Korn, and H.A. Haus, "Photon statistics of NRZ signals in high-bit-rate optically pre-amplified direct detection receiver," Optical Fiber Conference (OFC), 1999.

126. E. Desurvire, *Erbium-doped fiber amplifiers* (New York: John Wiley & Sons, 1994).

127. H.A. Haus, *Electromagnetic Noise and Quantum Optical Measurements* (Springer-Verlag, 2000).

128. J.C. Livas, "High sensitivity optically preamplified 10 Gb/s receivers," in Optical Fiber Conference (OFC), Paper PD4, 1996.

129. W.A. Atia and R.S. Bondurant, "Demonstration of return-to-zero signaling in both OOK and DPSK formats to improve receiver sensitivity in an optically preamplified receiver," in LEOS, 1999.

130. A.H. Gnauck, S. Chandrasekhar, J. Leuthold, and L. Stulz, "Demonstration of 42.7-Gb/s DPSK receiver with 45 photons/bit sensitivity," IEEE Photon. Technol. Lett. **15**, 99–101 (2003).

131. J.H. Sinsky, A. Adamiecki, A.H. Gnauck, C.A. Burrus, J. Leuthold, O. Wohlgemuth, and A. Umbach, "A 42.7-Gb/s Integrated Balanced Optical Front End with Record Sensitivity," in Optical Fiber Conference (OFC): Paper PD39-1, 2003.

132. A.H. Gnauck and P.J. Winzer, "Optical phase-shift-keyed transmission," J. Lightwave Technol. **23**, 115–130 (2005).

133. D.O. Caplan, M.L. Stevens, J.J. Carney, and R.J. Murphy, "Demonstration of Optical DPSK Communication with 25 Photons/Bit Sensitivity," in Conference on Lasers and Electro-Optics (CLEO), 2006.

134. J.R. Minch, D. J. Townsend, and D.R. Gervais, "Rate Adjustable NRZ-DPSK Modulation Scheme with a Fixed Interferometer," in IEEE LEOS, 2005.

135. D.O. Caplan, M.L. Stevens, and J.J. Carney, "A High-Sensitivity Multi-Channel Single-Interferometer DPSK Receiver," Opt. Express **14**, 10984–10989 (2006).

136. D.O. Caplan, M.L. Stevens, and J.J. Carney, "High-Sensitivity Demodulation of Multiple-Data-Rate WDM-DPSK Signals using a Single Interferometer," in Optical Fiber Conference (OFC), 2007.

137. K. Yonenaga and K. Hagimoto, "10-Git/s × four-channel WDM transmission experiment over 2400-km DSF using optical DPSK direct detection scheme," in Optical Fiber Conference (OFC), 1997.

138. A.H. Gnauck, G. Raybon, S. Chandrasekhar, J. Leuthold, C. Doerr, L. Stulz, A. Agarwal, S. Banerjee, D. Grosz, S. Hunsche, A. Kung, A. Marhelyuk, D. Maywar, M. Movassaghi, X. Liu, C. Xu, X. Wei, and D.M. Gill, "2.5 Tb/s (64 × 42.7 Gb/s) transmission over 40 × 100 km NZDSF using RZ-DPSK format and all-Raman-amplified spans," in Optical Fiber Conference (OFC), 2002.

139. J.-X. Cai, D.G. Foursa, C.R. Davidson, Y. Cai, G. Domagala, H. Li, L. Liu, W. Patterson, A. Pilipetskii, M. Nissov, and N. Bergano, "A DWDM Demonstration of 3.73 Tb/s over 11,000 km using 373 RZ-DPSK Channels at 10 Gb/s," in Optical Fiber Conference (OFC): Paper PD22-1, 2003.

140. C. Rasmussen, T. Fjelde, J. Bennike, F. Liu, S. Dey, B. Mikkelsen, P. Mamyshev, P. Serbe, P. van der Wagt, Y. Akasaka, D. Harris, D. Gapontsev, V. Ivshin, and P. Reeves-Hall, "DWDM

40G transmission over trans-Pacific distance (10 000 km) using CSRZ-DPSK, enhanced FEC and all-Raman amplified 100 km Ultrawave fiber spans," in Optical Fiber Conference (OFC): Paper PD18-1, 2003.

141. B. Zhu, L. E. Nelson, S. Stulz, A.H. Gnauck, C. Doerr, J. Leuthold, L. Gruner-Nielsen, M.O. Pedersen, J. Kim, R.L. Lingle, Jr., Y. Emori, Y. Ohki, N. Tsukiji, A. Oguri, and S. Namiki, "6.4 Tbit/s (160×42.7 Gb/s) transmission with 0.8 bit/s/Hz spectral efficiency over 32×100 km of fiber using CSRZ-DPSK format," in Optical Fiber Conference (OFC): Paper PD19, 2003.
142. M.L. Stevens, "Transmitter pulse issues," private communication, 2004.
143. R.A. Griffin, "Integrated DQPSK Transmitters," in Optical Fiber Conference (OFC), 2005.
144. H. Kim and P.J. Winzer, "Robustness to laser frequency offset in direct-detection DPSK and DQPSK systems," J. Lightwave Technol. **21**, 1887–1891 (2003).
145. G. Bosco and P. Poggiolini, "On the joint effect of receiver impairments on direct-detection DQPSK systems," J. Lightwave Technol. **24**, 1323–1333 (2006).
146. P.J. Winzer and H. Kim, "Degradations in balanced DPSK receivers," IEEE Photon. Technol. Lett. **15**, 1282–1284 (2003).
147. I. Morita and N. Yoshikane, "Merits of DQPSK for Ultrahigh Capacity Transmission," in LEOS, 2005.
148. A. Royset and D.R. Hjelme, "Novel dispersion tolerant optical duobinary transmitter using phase modulator and Bragg grating filter," in ECOC, 1998.
149. Y. Miyamoto, H. Masuda, A. Hirano, S. Kuwahara, Y. Kisaka, H. Kawakami, M. Tomizawa, Y. Tada, and S. Aozasa, "S-band WDM coherent transmission of 40 × 43-Gbit/s CS-RZ DPSK signals over 400 km DSF using hybrid GS-TDFAs/Raman amplifiers," Electron. Lett. **39**, 1569–1570 (2002).
150. D. Penninckx, H. Bissessur, P. Brindel, E. Gohin, and F. Bakhti, "Optical differential phase shift keying (DPSK) direct detection considered as a duobinary signal," in ECOC, 2001.
151. Y. Miyamoto, A. Hirano, S. Kuwahara, M. Tomizawa, and Y. Tada, "Novel modulation and detection for bandwidth-reduced RZ formats using duobinary-mode splitting in wideband PSK/ASK conversion," J. Lightwave Technol. **20**, 2067–2078 (2002).
152. L. Moller, C. Xie, R. Ryf, L. Xiang, and X. Wei, "10 Gb/s duobinary receiver with a record sensitivity of 88 photons per bit," presented at Optical Fiber Conference (OFC), 2004.
153. L.G. Kazovsky and D.A. Atlas., "PSK synchronous heterodyne and homodyne experiments using optical phase-locked loops," presented at Optical Fiber Conference (OFC), 1990.
154. L.G. Kazovsky and D.A. Atlas, "A 1320-nm Experimental Optical Phase-Locked Loop: Performance Investigation and PSK Homodyne Experiments at 140 Mb/s and 2 Gb/s," J. Lightwave Technol. **8**, 1414–1425 (1990).
155. F.T. Herzog, "An optical phase locked loop for coherent space communications," Swiss Federal Institute of Technology, 2006.
156. L.G. Kazovsky, S. Benedetto, and A. Willner, *Optical Fiber Communication Systems* (Norwood, MA: Artech House, Inc., 1996).
157. B. Wandernoth, "5 photon/bit low complexity 2 Mbit/s PSK transmission breadboard experiment with homodyne receiver applying synchronization bits and convolutional coding," Proc. Eur. Conf. Opt. Commun. (ECOC), **1**, 59–62 (1994).
158. R. Lange and B. Smutny, "Highly-Coherent Optical Terminal Design Status and outlook," in LEOS, 2005.

159. J.H. Sinsky, A. Adamiecki, A.H. Gnauck, C.A. Burrus, J. Leuthold, and O. Wohlgemuth, "RZ-DPSK Transmission Using a 42.7-Gb/s Integrated Balanced Optical Front End With Record Sensitivity," J. Lightwave Technol. **22**, (2004).

160. S.B. Alexander, R. Barry, D.M. Castagnozzi, V.W.S. Chan, D.M. Hodsdon, L.L. Jeromin, J.E. Kaufmann, D.M. Materna, R.J. Parr, M.L. Stevens, and D.W. White, "4-ary FSK coherent optical communication system," Electron. Lett. **26**, 1346–1348 (1990).

161. M.L. Stevens, D.M. Boroson, and J.E. Kaufmann, "A near-optimum discriminator demodulator for binary FSK with wide tone spacing," IEEE Microwave and Guided Wave Lett. **3**, 227–229 (1993).

162. R. Noe, et. al., "Optical FSK transmission with pattern independent 119 photoelectrons/bit receiver sensitivity with endless polarization control," Electron. Lett. **25**, 757–758 (1989).

163. B.S. Robinson "Semiconductor-based all-optical switching for optical time-division multiplexed networks," Thesis, MIT, 2003.

164. J.M. Kahn, "1 Gbit/s PSK homodyne transmission system using phase-locked semiconductor lasers," IEEE Photon. Technol. Lett. **1**, 340–342 (1989).

165. S. Norimatsu, K. Iwashita, and K. Noguchi, "10 Gbit/s optical PSK homodyne transmission experiments using external cavity DFB LDs," Electron. Lett. **26**, 648–649 (1990).

166. S. Norimatsu, K. Iwashita, and K. Sato, "PSK optical homodyne detection using external cavity laser diodes in Costas loop," IEEE Photon. Technol. Lett. **2**, 374–376 (1990).

167. B. Zhu, L. Leng, L. E. Nelson, L. Gruner-Nielsen, Y. Qian, J. Bromage, S. Stulz, S. Kado, Y. Emori, S. Namiki, P. Gaarde, A. Judy, B. Palsdottir, and R.L. Lingle, Jr., "3.2 Tb/s (80 × 42.7 Gb/s) transmission over 20 × 100km of nonzero dispersion fiber with simultaneous C + L-band dispersion compensation," in Optical Fiber Conference (OFC), 2002.

168. J.M. Ross, S. I. Green, and J. Brand, "Short-pulse optical communication experiments," Proc. IEEE **58**, (1970).

169. J.R. Lesh, J. Katz, H.H. Tan, and D. Zwillinger, "2.5 bit/detected photon demonstration program: description, analysis, and phase 1 results," Jet Propulsion Laboratory, Pasadena, CA 42-66, Dec. 1981.

170. J.R. Lesh, "Capacity Limit of the Noiseless, Energy-Efficient Optical PPM Channel," IEEE Trans. Comm., **31**, 546–548 (1983).

171. A.J. Phillips, R.A. Cryan, and J.M. Senior, "An optically preamplified intersatellite PPM receiver employing maximum likelihood detection," IEEE Photon. Technol. Lett. **8**, 691–693, 1996.

172. D.O. Caplan, P.W. Juodawlkis, J.J. Plant, and M.L. Stevens, "Performance of high-sensitivity OOK, PPM, and DPSK communications using high-power slab-coupled optical waveguide amplifier (SCOWA) based transmitters," in Optical Fiber Conference (OFC), 2006.

173. C. Chen and C.S. Gardner, "Performance of PLL Synchronized Optical PPM Communication Systems," IEEE Trans. Comm. **COM-34**, 988–994 (1986).

174. F. Nekoogar, *Ultra-Wideband Communications: Fundamentals and Applications* (Upper Saddle River: Prentice Hall, 2005).

175. M.L. Stevens, "Estimation of M-PPM Spectra for Pseudo-Random Bit Sequences." private communication, 2006.

176. B.S. Robinson, S.A. Hamilton, and E.P. Ippen, "Demultiplexing of 80 Gbit/s pulse-position modulated data with an ultrafast nonlinear interferometer," IEEE Photon. Technol. Lett. **14**, 2002.

177. R.S. Vodhanel, J.L. Gimlett, N.K. Cheung, and S. Tsuji, "FSK Heterodyne Transmission Experiments at 560 Mbit/s and 1 Gbit/s," J. Lightwave Technol. **LT-5**, 461–468 (1987).

178. A.R. Chraplyvy, R.W. Tkach, A.H. Gnauck, and R.M. Derosier, "8Gbit/s FSK modulation of DFB lasers with optical demodulation," Electron. Lett., **25**, 319–321 (1989).

179. B. Glance, et. al., "Densely spaced FDM optical coherent system with near quantum-limited sensitivity and computer controlled random access channel selection," in Optical Fiber Conference (OFC): Paper PD11, 1989.

180. M.L. Stevens, B. R. Hemenway, and S.B. Alexander, "Simultaneous TDM/FDM digital optical transmission with polarization-diversity heterodyne detection," Microwave Symposium Digest, **1**, 171–173 (1994).

181. R. Gross and R. Olshansky, "Multichannel Coherent FSK Experiments Using Subcarrier Multiplexing Techniques," J. Lightwave Technol. **8**, 406–415 (1990).

182. H. Gross, M. Schmidt, R. Olshansky, and V. Lanzisera, "Coherent Transmission of 60 FM-SCM Video Channels," Photonics Technol. Lett. **2**, 288–290 (1990).

183. S. Bendetto, R. Gaudino, and P. Poggiolini, "Direct detection of optical digital transmission based on polarization shift keying modulation," IEEE Sel. Areas Commun., **13**, 531–542 (1995).

184. E. Hu, K. Wong, M. Marhic, L.G. Kazovsky, K. Shimizu, and N. Nikuchi, "4-Level Direct-Detection Polarization Shift-Keying (DD-PolSK) System with Phase Modulators," in Optical Fiber Conference (OFC), 2003.

185. M.M. Matalgah and R.M. Radaydeh, "Hybrid Frequency-Polarization Shift-Keying Modulation for Optical Transmission," J. Lightwave Technol. **23**, 1152–1162 (2005).

186. M. Nazarathy and E. Simony, "Generalized Stokes Parameters-Shift Keying: A New Perspective on Optimal Detection Over Electrical and Optical Vector Incoherent Channels," IEEE Trans. Comm. **54**, 499–509 (2006).

187. M. Nazarathy and E. Simony, "Stokes Space Optimal Detection of Multidifferential Phase and Polarization Shift Keying Modulation," J. Lightwave Technol. **24**, 1978–1988 (2006).

188. R. Zhang and G.S. La Rue, "Clock and data recovery circuits with fast acquisition and low jitter," presented at IEEE Workshop on Microelectronics and Electron Devices, 2004.

189. N.W. Spellmeyer, "Communications performance of a multimode EDFA," IEEE Photon. Technol. Lett. **12**, 1337–1339 (2000).

190. R.H. Kingston, *Detection of Optical and Infrared Radiation* (New York: Springer-Verlag, 1978).

191. B. Glance, "Polarization independent coherent optical receiver," J. Lightwave Technol. **5**, 274–276 (1987).

192. B.S. Glance, K. Pollock, C.A. Burrus, B.L. Kasper, G. Einstein, and L.W. Stulz, "WDM coherent optical star network," J. Lightwave Technol. **6**, 67–72 (1988).

193. B.S. Glance and M. Kavehrad, "Polarization-insensitive frequency-shift-keying optical heterodyne receiver using discriminator demodulation," J. Lightwave Technol. **6**, 1386–1394 (1988).

194. N. Ohkawa, T. Sugie, and Y. Hayashi, "A highly sensitive balanced receiver for 2.5 Gb/s het-erodyne detection systems," IEEE Photon. Technol. Lett. **3**, 375–377 (1991).

195. B. Wandernoth, "20 photon/bit 565 Mbit/s PSK homodyne receiver using synchronization bits," Electron. Lett. **28**, (1992).

196. F.H. Raab, P. Asbeck, S. Cripps, P.B. Kenington, Z.B. Popovic, N. Pothecary, J.F. Sevic, and N.O. Sokal, "RF and Microwave Power Amplifier and Transmitter Technologies—Part 1," High Frequency Electronics, 22–36 (2003).

197. P.W. Juodawlkis, J.J. Plant, R.K. Huang, L.J. Missaggia, and J.P. Donnelly, "High-power 1.5-/spl mu/m InGaAsP-InP slab-coupled optical waveguide amplifier," IEEE Photon. Technol. Lett. **17**, (2005).

198. N.W. Spellmeyer, D.O. Caplan, and M.L. Stevens, "Design of a 5-Watt PPM transmitter for the Mars Laser Communications Demonstration," in LEOS, 2005.

199. P. Wysocki, T. Wood, A. Grant, D. Holcomb, K. Chang, M. Santo, L. Braun, and G. Johnson, "High Reliability 49 dB Gain, 13W PM Fiber Amplifier at 1550 nm with 30 dB PER and Record Efficiency," in Optical Fiber Conference (OFC), paper PDP17, 2006.

200. L. Goldberg, J.P. Koplow, and D.A.V. Kliner, "Highly efficient 4-W Yb-doped fiber amplifier pumped by a broad-stripe laser diode," Opt. Lett. **24**, 673–675 (1999).

201. A.N. Curren, J.A. Dayton, Jr., R.W. Palmer, K.J. Long, D.A. Force, C.E. Weeder, Z.A. Zachar, and W.L. Harvey, "The Cassini mission Ka-band TWT," in International Electron Devices Meeting, 1994.

202. D. Morabito, S. Butman, and S. Shambayati, "The Mars Global Surveyor Ka-Band Link Experiment (MGS/KaBLE-II)," in Telecommunications and Mission Operations Progress Report 42-137, Jet Propulsion Laboratory, 1999.

203. I. Haque, "Ka-Band Traveling Wave Tube Amplifier," in IND Technology and Sciency News, Jet Propulsion Laboratory, 2002, pp. 11–14: http://tmot.jpl.nasa.gov/Program_Overview_Information/IND_Program_News/Issue15.pdf.

204. N.W. Spellmeyer, D.O. Caplan, B.S. Robinson , D. Sandberg, M.L. Stevens, M.M. Willis, D.V. Gapontsev, N.S. Platonov, and A. Yusim, "A High-Efficiency Ytterbium-Doped Fiber Amplifier Designed for Interplanetary Laser Communications," in Optical Fiber Conference (OFC), 2007.

205. R. Loudon, *The Quantum Theory of Light* (New York: Oxford University Press, Inc., 2000).

206. C.W. Gardiner and P. Zoller, *Quantum Noise* (New York: Springer Verlag, 2000).

207. J.W. Goodman, *Statistical Optics* (New York: John Wiley & Sons, Inc., 2000).

208. A. Papoulis, *Probability, Random Variables, and Stochastic Processes* (New York: McGraw-Hill, Inc., 1984).

209. R. Sobolewski, et. al., "Ultrafast superconducting single-photon optical detectors and their applications," IEEE Trans. Appl Superconduct **13**, 1151–1157 (2003).

210. J.K.W. Yang, et. al., "Fabrication development for nanowire GHz-counting-rate single-photon detectors," IEEE Trans. Appl. Superconduct., 2005.

211. B.S. Robinson, "Private communication," 2005.

212. J.H. Shapiro, "Imaging and Optical Communication through Atmospheric Turbulence," in *Laser Beam Propagation in the Atmosphere*, J.W. Strohbehn, Ed. (Berlin: Springer-Verlag, 1978).

213. R.J. Barron, "Binary shaping for low-duty-cycle communications," in International Symposium on Information Theory (ISIT), 2004.

214. B.S. Robinson, D.O. Caplan, M.L. Stevens, R.J. Barron, E.A. Dauler, and S.A. Hamilton, "1.5-photons/bit Photon-Counting Optical Communications Using Geiger-Mode Avalanche Photodiodes," in IEEE LEOS Summer Topical Meetings, 2005.

215. J.B. Johnson, "Thermal agitation of electricity in conductors," Phys. Rev. **32**, 97–109 (1928).

216. H. Nyquist, "Thermal agitation of electric charge in conductors," Phys. Rev. **32**, 110–113 (1928).

217. B. M. Oliver, "Thermal and quantum noise," presented at Proc. IEEE, 1965.

218. A. Yariv, *Optical Electronics in Modern Communications, 5th Ed.* (New York: Oxford Un. Press, 1997).

219. S.G. Lambert and W.L. Casey, *Laser Communications in Space* (Boston: Artech House, 1995).

220. ITU-R Recommendation PI.372-6: Radio Noise, 1994.

221. K. P. Phillips, "An overview of propagation factors influencing the design of mobile satellite communication systems," Electron. & Commun. Eng. J., (1997).

222. K. Rosfjord, J. Yang, E. Dauler, A. Kerman, V. Anant, B. Voronov, G. Gol'tsman, and K. Berggren, "Nanowire single-photon detector with an integrated optical cavity and anti-reflection coating," Opt. Express, **14**, 527–534 (2006).

223. W.R. Leeb, "Degradation of signal to noise ratio in optical free space data links due to background illumination," Appl. Opt. **28**, 3443–3449 (1989).

224. F.D. Teodoro, J.P. Koplow, and S.W. Moore, "Diffraction limited, 300-kW peak power pulses from a coiled multimode fiber amplifier," Opt. Lett., (2002).

225. V.W.S. Chan, "Space coherent optical communication systems–An introduction," J. Lightwave Technol. **5**, 633–637 (1987).

226. S.B. Alexander, E.S. Kintzer, and J.C. Livas, "A Gbps, 1 Watt Free-space Coherent Optical Communication System," in LEOS, 1992.

227. A. Biswas, H. Hemmati, and J.R. Lesh, "High data-rate laser transmitters for free space laser communications," in Photonics West, 1999.

228. E. Rochat, R. Dändliker, K. Haroud, R.H. Czichy, U. Roth, D. Costantini, and R. Holzner, "Fiber Amplifiers for Coherent Space Communication," IEEE Sel. Top. Quantum Electron., **7**, 64–81 (2001).

229. R. Lange and B. Smutny, "BPSK Laser Communication Terminals to be verified in space," in Milcom, 2004, pp. 441–444.

230. R. Lange and B. Smutny, "Optical inter-satellite links based on homodyne BPSK modulation: Heritage, status and outlook," in Proc. SPIE, (Free-Space Laser Communication Technologies XVII), 2005.

231. T. Shinagawa, "Detailed investigation on reliability of wavelength-monitor-integrated fixed and tunable DFB laser diode modules," J. Lightwave Technol. **23**, 1126–1136 (2005).

232. T. Ikegami and Y. Suematsu, "Resonance-like characteristics of the direct modulation of a junction laser," presented at Proc. IEEE, 1967.

233. L.A. Coldren and S.W. Corzine, *Diode Lasers and Photonic Integrated Circuits* (John Wiley & Sons, Inc., 1995).

234. D.A. Ackerman, "Laser diodes for CATV," in IEEE LEOS, 1995.

235. M.R. Phillips, et. al., "112 channel split-band WDM lightwave CATV system," IEEE Photon. Technol. Lett. **4**, 790–792 (1992).

236. G.P. Agrawal, *Fiber-Optic Communication Systems* (New York: John Wiley & Sons, 1992).

237. J. Piprek and J.E. Bowers, "Analog modulation of semiconductor lasers," in *RF Photonic Technology in Optical Fiber Links*, W.S. C. Chang, Ed. (Cambridge Univ. Press, 2002).

238. R.S. Vodhanel, A. F. Elrefaie, M. Z. Iqbal, R. E. Wagner, J.L. Gimlett, and S. Tsuji, "Performance of directly modulated DFB lasers in 10-Gb/s ASK, FSK, and DPSK lightwave systems," J. Lightwave Technol. **8**, 1379–1386 (1990).

239. J. Zhang, N. Chi, P. V. Holm-Nielsen, C. Pueucheret, and P. Jeppesen, "An Optical FSK Transmitter Based on an Integrated DFB Laser–EA Modulator and Its Application in Optical Labeling," IEEE Photon. Technol. Lett. **15**, 984–986 (2003).

240. F. Koyama and K. Iga, "Frequency chirping in external modulators," J. Lightwave Technol. **6**, 87–93 (1988).

241. M. Kuznetsov, J. Stone, and L.W. Stulz, "Time- and frequency-resolved measurements of frequency-modulation and switching of a tunable semiconductor laser," Appl. Phys. Lett. **59**, 2492–2494 (1991).

242. M. Kuznetsov and D.O. Caplan, "Time-frequency analysis of optical communication signals and the effects of second and third order dispersion," in Conference on Lasers and Electro-Optics (CLEO), 2000.

243. R.A. Linke, "Modulation Induced Transient Chirping in Single Frequency Lasers," IEEE J. Quantum Electron. **QE-21**, 593–597 (1985).

244. P.A. Morton, G.E. Shtengel, L.D. Tzeng, R.D. Yadvish, T. Tanbun-Ek, and R.A. Logan, "38.5 km error free transmission at 10 Gbit/s in standard fibre using a low chirp, spectrally filtered, directly modulated 1.55 μm DFB laser," Electron. Lett. **33**, 310–311 (1997).

245. D.R. Hjelme and A. Royset, "RZ versus NRZ in space communication system using direct current modulated transmitter and optically pre-amplifed receiver with ultra-narrow optical filter," in LEOS, San Francisco, 1999.

246. M.M. Strasser, P.J. Winzer, M. Pfennigbauer, and W.R. Leeb, "Significance of Chirp-Parameter for Direct Detection Free-Space Laser Communication," in SPIE, 2001.

247. P. Corvini and T. Koch, "Computer simulation of high-bit-rate optical fiber transmission using single-frequency lasers," J. Lightwave Technol. **5**, 1591–1595 (1987).

248. D. Mahgerefteh, P.S. Cho, J. Goldhar, and H. I. Mandelberg, "Penalty-free propagation over 600 km of nondispersionshifted fiber at 2.5 Gb/s using a directly laser modulated transmitter," in Conference on Lasers and Electro-Optics (CLEO), 1999.

249. Y. Matsui, D. Mahgerefteh, X. Zheng, C. Liao, Z.F. Fan, K. McCallion, and P. Tayebati, "Chirp-Managed Directly Modulated Laser (CML)," Photon. Technol. Lett. **18**, 385–386 (2006).

250. S. Chandrasekbar, C.R. Doerr, L.L. Buhl, Y. Matsui, D. Mahgerefteh, X. Zheng, K. McCallion, Z. Fan, and P. Tayebati, "Repeaterless Transmission With Negative Penalty Over 285 km at 10 Gb/s Using a Chirp Managed Laser," Photon. Technol. Lett. **17**, 2454–2457 (2005).

251. S. Chandrasekbar, A.H. Gnauck, G. Raybon, L.L. Buhl, D. Mahgerefteh, X. Zheng, Y. Matsui, K. McCallion, Z. Fan, and P. Tayebati, "Chirp-Managed Laser and MLSE-RX Enables Transmission Over 1200 km at 1550 nm in a DWDM Environment in NZDSF at 10 Gb/s Without Any Optical Dispersion Compensation " Photonics Technol. Lett. **18**, 1560–1562 (2006).

252. M. Ito and T. Kimura, "Stationary and transient thermal properties of semiconductor laser diodes," IEEE J. Quantum Electron. **17**, 787–795 (1981).

253. H. Shalom, A. Zadok, M. Tur, P.J. Legg, W.D. Cornwell, and I. Andonovic, "On the Various Time Constants of Wavelength Changes of a DFB Laser Under Direct Modulation," IEEE J. Quantum Electron. **34**, 1816–1822 (1998).

254. A. Ma, J.C. Cartledge, and H.E. Lassen, "Performance implications of the thermal-induced frequency drift in fast wavelength switched systems with heterodyne detection," J. Lightwave Technol. **14**, 1090–1096 (1996).

255. D.O. Caplan, G.S. Kanter, and P. Kumar, "Characterization of dynamic optical nonlinearities by continuous time-resolved Z-Scan," Opt. Lett, **21**, 1342–1344 (1996).

256. A. A. Saavedra, R. Passy, and J.P. von der Weid, "Thermal drift in wavelength-switching DFB and DBR lasers," Electron. Lett. **33**, 780–781 (1997).

257. C.R. Giles, T. Erdogan, and V. Mizrahi, "Simultaneous wavelength-stabilization of 980-nm pump lasers," IEEE Photonics Technol. Lett. **6**, (1994).

258. S. Mohrdiek, T. Plisk, and C. Harder, "Coolerless operation of 980 nm pump modules," in Optical Fiber Conference (OFC), 2001.

259. J.-L. Archambault and S.G. Grubb, "Fiber Gratings in Lasers and Amplifiers," J. Lightwave Technol. **15**, 1378–1390 (1997).

260. B. R. Hemenway and M.L. Stevens, "Simultaneous TDM/FDM Using Rapidly-tunable Transmitters and Receivers For Multi-access Optical Networks," presented at IEEE/LEOS Integrated Optoelectronics Proceedings, 1994.

261. C.H. Henry, "Theory of the linewidth of semiconductor lasers," IEEE J. Quantum Electron. **QE-18**, 259–264 (1982).

262. K. Kojima, K. Kyuma, and T. Nakayama, "Analysis of the spectral linewidth of distributed feedback laser diodes," J. Lightwave Technol. **3**, 1048–1055 (1985).

263. H. Nakano, S. Sasaki, S. Tsuji, N. Chinone, and M. Maeda, "Comparison of optical reflection tolerance between conventional and ?/4-shifted DFB lasers in a 2.4 Gbit/s system," Electron. Lett. **4**, 1049–1051 (1988).

264. G. Jacobsen, "Performance of DPSK and CPFSK Systems with Significant Post-Detection Filtering," J. Lightwave Technol. **11**, (1993).

265. H. Nasu, T. Mukaihara, T. Takagi, M. Oike, T. Nomura, and A. Kasukawa, "25-GHz-spacing wavelength-monitor integrated DFB laser module for DWDM applications," Photon. Technol. Lett. **15**, 293–295 (2003).

266. D.O. Caplan, "Multi-channel DPSK Receiver," in US Pat. Appl. 11/022,344, 2004.

267. D.O. Caplan, "Polarization independent optical interferometers," in US Pat. Appl., 2004.

268. D.O. Caplan, "Reconfigurable Polarization Independent Interferometers and Methods of Stabilization," in US Pat. Appl. 11/318,255, 2005.

269. J.B. Abshire, et. al., "The Geoscience Laser Altimeter System (GLAS) for the ICESat mission," presented at Conference on Lasers and Electro-Optics (CLEO), 2000.

270. M. Albota, et. al. , "Three-dimensional imaging laser radars with Geiger-mode avalanche photodiode arrays," MIT Lincoln Lab. J. **13**, 351–370 (2002).

271. W.T. Roberts, "Cavity-dumped communication laser design," 42–152, Feb. 2003.

272. X. Sun, et. al., "Cloud and aerosol lidar channel design and performance of the Geoscience Laser Altimeter System on the ICESat mission," presented at Conference on Lasers and Electro-Optics (CLEO), 2004.

273. X. Sun, et. al., "Design and performance measurement of the mercury laser altimeter," in Conference on Lasers and Electro-Optics (CLEO), 2004.

274. M. Aoki, M. Suzuki, H. Sano, T. Kawano, T. Ido, T. Taniwatari, K. Uomi, and A. Takai, "InGaAs/InGaAsP MQW electroabsorption modulator integrated with a DFB laser fabricated by band-gap energy control selective area MOCVD," IEEE J. Quantum Electron. **29**, 2088–2096 (1993).

275. W.S.C. Chang, "Multiple quantum well electroabsorption modulators for RF photonic links," in *RF Photonic Technology in Optical Fiber Links*, W.S.C. Chang, Ed. (Cambridge Univ. Press, 2002).

276. G. Raybon, U. Koren, M.G. Young, B.I. Miller, M. Chien, T.H. Wood, and H. M. Presby, "Low chirp transmission at 5.0 Gbit/s using an integrated DBR laser-modulator transmitter," Electron. Lett. **30**, 1330–1331 (1994).

277. Y. Akage, K. Kawano, S. Oku, R. Iga, H. Okamoto, Y. Miyamoto, and H. Takeuchi, "Wide bandwidth of over 50 GHz travelling-wave electrode electroabsorption modulator integrated DFB lasers," Electron. Lett. **37**, 299–300 (2001).

278. A.H. Gnauck, S.K. Korotky, J.J. Veselka, J. Nagel, C.T. Kemmerer, W. J. Minford, and D. T. Moser, "Dispersion penalty reduction using an optical modulator with adjustable chirp," IEEE Photon. Technol. Lett. **3**, 916–918 (1991).

279. A.H. Gnauck, S.K. Korotky, and J.E. Zucker, "Tunable chirp, lightwave modulator for dispersion compensation," in US Pat. 5,303,079,. USA, 1992.

280. R.M. Jopson and A.H. Gnauck, "Dispersion compensation for optical fiber systems," IEEE Communi. Mag., **33**, 96–102 (1995).

281. L. Zehnder, "Ein neuer Interferenzrefractor," Z. Instrkde **11**, 275–285 (1891).

282. L. Mach, "Uber einer Interferenzrefractor," Z. Instrkde **12**, 89–93 (1892).

283. R.C. Alferness, "Waveguide Electrooptic Modulators,"IEEE Trans. Microwave Theory Technol., **82**, 1121–1137 (1982).

284. R.C. Alferness, "Corrections to "Waveguide Electrooptic Modulators"," IEEE Trans. Microwave Theory Technol. **83**, 315 (1983).

285. R.C. Alferness, L.L. Buhl, J.L. Jackel, S. P. Lyman, and V. Ramaswamy, " Fabrication method for $LiNbO_3$ and $LiTaO_3$ integrated optics devices," in U.S. Pat. 4,439,265, USA, 1984.

286. L. Thylen, "Integrated optics in LiNbO3: recent developments in devices for telecommunication," J. Lightwave Technol. **6**, 847– 861 (1988).

287. K. Noguchi, O. Mitomi, and H. Miyazawa, "Low-voltage and broadband Ti:$LiNbO_3$ modulators operating in the millimeter wavelength region," in Optical Fiber Conference (OFC), 1996.

288. K. Noguchi, O. Mitomi, and H. Miyazawa, "Millimeter-wave Ti:$LiNbO_3$ optical modulators," J. Lightwave Technol. **16**, 615–619 (1998).

289. G.E. Betts, "$LiNbO_3$ external modulators and their use in high performance analog links," in *RF Photonic Technology in Optical Fiber Links*, W.S. C. Chang, Ed. (Cambridge Univ. Press, 2002).

290. M.M. Howerton and W.K. Burns, "Broadband traveling wave modulators in $LiNbO_3$," in *RF Photonic Technology in Optical Fiber Links*, W.S. C. Chang, Ed. (Cambridge Univ. Press, 2002).

291. O. Leclerc, et. al., "40 Gbit/s polarization-independent, push-pull InP Mach-Zehnder modulator for all-optical regeneration," presented at Optical Fiber Conference (OFC), PD35, 1999.

292. O. Leclerc, B. Dany, D. Rouvillain, P. Brindel, E. Desurvire, C. Duchet, A. Shen, F. Devaux, E. Coquelin, M. Goix, S. Bouchoule, L. Fleury, and P. Nouchi, "Simultaneously regenerated 4×40 Gbit/s dense WDM transmission over 10000 km using single 40 GHz InP Mach-Zehnder modulator," Electron. Lett. **36**, 1574–1575 (2000).

293. B. Li, et. al. , "SiGe/Si Mach-Zehnder Interferometer Modulator based on the Plasma Dispersion Effect," Appl. Phys. Lett. **74**, (1999).

294. L. Liao, D. Samara-Rubio, M. Morse, A. Liu, and D. Hodge, "High speed silicon Mach-Zehnder modulator," Opt. Express, **13**, (2005).

295. G. L. Li and P.K.L. Yu, "Optical intensity modulators for digital and analog applications," J. Lightwave Technol. **21**, 2010–2030 (2003).

296. J.P. Sokoloff, P.R. Prucnal, I. Glesk, and M. Kane, "A terahertz optical asymmetric demultiplexer (TOAD)," IEEE Photon. Technol. Lett.**5**, (1993).

297. T. Durhuus, C. Joergensen, B. Mikkelsen, and K.E. Stubkjaer, "Penalty free all-optical wavelength conversion by SOA's in Mach–Zehnder configuration," in ECOC'93. Montreux, 1993.

298. B. Mikkelsen, et. al., "20 Gbit/s polarisation insensitive wavelength conversion in semiconductor optical amplifiers," in ECOC'93. Montreux, 1993.

299. N. Patel, et. al., "40-Gb/s demultiplexing using an ultrafast nonlinear interferometer (UNI)," IEEE Photon. Technol. Lett. **8**, 1695–1697 (1996).

300. N.S. Patel, K. L. Hall, and K.A. Rauschenbach, "Interferometric all optical switches for ultrafast signal processing," Appl. Opt. **37**, 2831–2842 (1998).

301. C. Janz, F. Poingt, F. Pommereau, W. Grieshaber, F. Gaborit, D. Leclerc, I. Guillemot, and M. Renaud, "All-active Dual Order Mode (DOMO) Mach-Zehnder wavelength converter for 10 Gb/s operation," Electron. Lett. **35**, 1862 (1999).

302. B.S. Robinson, S.A. Hamilton, and E.P. Ippen, "Demultiplexing of 80 Gbit/s pulse-position modulated data with an ultrafast nonlinear interferometer," IEEE Photon. Technol. Lett. **14**, 2002.

303. G. Raybon, Y. Su, J. Leuthold, R.-J. Essiambre, T. Her, C. Joergensen, P. Steinvurzel, and K. D. K. Feder, "40 Gbit/s pseudo-linear transmission over one million kilometers," in Optical Fiber Conference (OFC): Paper FD10-1, 2002.

304. J. Leuthold, G. Raybon, Y. Su, R. Essiambre, S. Cabot, J. Jaques, and M. Kauer, "40 Gbit/s transmission and cascaded all-optical wavelength conversion over 1000000 km," Electron. Lett. **38**, 890–892 (2002).

305. Y. Su, G. Raybon, R.-J. Essiambre, and T.-H. Her, "All-optical 2R regeneration of 40-Gb/s signal impaired by intrachannel four-wave mixing," Photonics Technol. Lett. **15**, 350–352 (2003).

306. J. Nayyer and H. Nagata, "Suppression of thermal drifts of high speed Ti:$LiNbO_3$ optical modulators," IEEE Photon. Technol. Lett. **6**, 952–955 (1994).

307. S.K. Korotky and J.J. Veselka, "An RC network analysis of long term Ti:LiNbO3 bias stability," J. Lightwave Technol. **14**, 2687–2697 (1996).

308. A. Waksberg and J. Wood, "An Automatic Optical Bias Control for Laser Modulators," Rev. Sci. Instrum., **43**, 1271–1273 (1972).

309. C.T. Mueller and J.G. Coffer, "Temperature-dependent bias drift in proton-exchanged lithium niobate Mach-Zehnder modulators," in Conference on Lasers and Electro-Optics (CLEO), 1999.

310. H. Nagata, "DC drift failure rate estimated on 10 Gb/s x-cut lithium niobate modulators," IEEE Photon. Technol. Lett. **12**, 1477–1479 (2000).

311. H. Nagata, N. Papasavvas, and D.R. Maack, "Bias stability of OC48 x-cut lithium-niobate optical modulators: four years of biased aging test results," Photon. Technol. Lett. **15**, 42–44 (2003).

312. H. Nagata, G. D. Feke, Y. Li, and W.R. Bosenberg, "DC drift of Z-cut $LiNbO_3$ modulators," IEEE Photon. Technol. Lett. **16**, 1655–1657 (2004).

313. H. Nagata, Y. Li, D.R. Maack, and W.R. Bosenberg, "Reliability Estimation From Zero-Failure $LiNbO_3$ Modulator Bias Drift Data," IEEE Photon. Technol. Lett. **16**, 1477–1479 (2004).

314. D.O. Caplan, "A technique for measuring and optimizing modulator extinction ratio," in Conference on Lasers and Electro-Optics (CLEO), 2000.

315. N. Kuwata, H. Nishimoto, T. Horimatsu, and T. Touge, "Automatic bias control circuit for Mach-Zehnder modulator," presented at Nat. Meet. Inst. Electon. Comm. Eng., Japan, 1990.

316. A.H. Gnauck and C.R. Giles, "2.5 and 10 Gb/s transmission experiments using a 137 photon/bit erbium-fiber preamplifier receiver," IEEE Photon. Technol. Lett. **4**, 80–82 (1992).

317. Q. Jiang and M. Kavehrad, "A Subcarrier-Multiplexed Coherent FSK System Using a Mach-Zehnder Modulator with Automatic Bias Control," IEEE Photon. Technol. Lett. **5**, 941–943 (1993).

318. H. Nagata, Y. Li, K. R. Voisine, and W.R. Bosenberg, "Reliability of Nonhermetic Bias-Free $LiNbO_3$ Modulators," IEEE Photon. Technol. Lett. **16**, (2004).

319. L. Fenghai, C.J. Rasmussen, and R.J.S. Pedersen, "Experimental verification of a new model describing the influence of incomplete signal extinction ratio on the sensitivity degradation due to multiple interferometric crosstalk," IEEE Photon. Technol. Lett. **11**, 137 (1999).

320. Z. Li, Y. He, B.F. Jorgensen, and R.J. Pedersen, "Extinction ratio effect for high-speed optical fiber transmissions," presented at Int. Conf. on Comm. Tech. Proc. (ICCT '98), 1998.

321. M. Pauer and P.J. Winzer, "Impact of Extinction Ratio on Return-to-Zero Coding Gain in Optical Noise Limited Receivers," IEEE Photon. Technol. Lett. **15**, 879 - 881 (2003).

322. H. Kim and A.H. Gnauck, "Chirp characteristics of dual-drive mach–zehnder modulator with a finite dc extinction ratio," IEEE Photonics Tech. Lett., **14**, (2002).

323. T. Kawanishi, T. Sakamoto, M. Tsuchiya, and M. Izutsu, "70 dB extinction-ratio $LiNbO_3$ optical intensity modulator for two-tone lightwave generation," in Optical Fiber Conference (OFC), 2006.

324. "Measuring extinction ratio of optical transmitters," Hewlett Packard App. Note, 1550-8, 1998.

325. P.O. Andersson and K. Akermark, "Accurate-optical extinction ratio measurement," IEEE Photon. Technol. Lett. **6**, 1356–1358 (1994).

326. C.R. Yang, W.-Y. Hwang, H. Park, H.H. Hong, and S.G. Han, "Off-level sampling method for bias stabilisation of electro-optic Mach-Zehnder modulator," Electron. Lett. **35**, 590–591 (1999).

327. R.C. Alferness, S.K. Korotky, and E. Marcatili, "Velocity-matching techniques for integrated optic traveling wave switch/modulators," IEEE J. Quantum Electron. **20**, 301–309 (1984).

328. R.C. Alferness, " Traveling wave, electrooptic devices with effective velocity matching " in US Pat. 4,448,479, 1984.

329. O. Mitomi, K. Noguchi, and H. Miyazawa, "Broadband and low driving-voltage $LiNbO_3$, optical modulators," IEE Proc. Optoelectron. **145**, 360–364 (1998).

330. R.C. Alferness, "Guided-wave devices for optical communication," IEEE J. Quantum Electron. **17**, 946–959 (1981).

331. N. Henmi, T. Saito, and T. Ishida, "N. Henmi, T. Saito, and T. Ishida, "Prechirp technique as a linear dispersion compensation for ultrahigh-speed long-span intensity modulation direct detection optical communication systems," J. Lightwave Technol. **12**, 1706–1719 (1994).

332. S.K. Kim, O. Mizuhara, Y.K. Park, L.A. Tzeng, Y.S. Kim, and J. Jeong, "Theoretical and experimental studies of 10 Gb/s transmission performance using 1.55 μm $LiNbO_3$ – based transmitters using adjustable extinction ratio and chirp," J. Lightwave Technol. **17**, 1320–1325 (1999).

333. J.J. Veselka, S.K. Korotky, P. V. Mamyshev, A.H. Gnauck, G. Raybon, and N. M. Froberg, "A Soliton Transmitter Using a CW Laser and an NRZ Driven Mach-Zehnder Modulator," IEEE Photon. Technol. Lett. **8**, 950–952 (1996).

334. N.M. Froberg, A.H. Gnauck, G. Raybon, and J.J. Veselka, "Method and Apparatus for Generating Data Encoded Pulses in Return-to-Zero Format," in US Pat. 5,625,722, 1997.

335. B. Zhu, L. Leng, A.H. Gnauck, M.O. Pedersen, D. Peckham, L.E. Nelson, S. Stulz, S. Kado, L. Gruner-Nielsen, R.L. Lingle, Jr., S. Knudsen, J. Leuthold, C. Doerr, S. Chandrasekhar, G. Baynham, P. Gaarde, Y. Emori, and S. Namiki, "Transmission of 3.2 Tb/s (80 $\times$ 42.7 Gb/s) over 5200 km of UltraWave^{TM} fiber with 100-km dispersion-managed spans using RZ-DPSK format," in ECOC: Paper PD4.2, 2002.

336. P.J. Winzer, "Optical transmitters, receivers, and noise," in *Wiley Encyclopedia of Telecommunications*, J.G. Proakis, Ed. (New York: Wiley, 2002), pp. 1824–1840.

337. M.L. Dennis, W. I. Kaechele, W.K. Burns, T. F. Carruthers, and I.N. Duling, "Photonic Serial–Parallel Conversion of High-Speed OTDM Data," IEEE Photon. Technol. Lett. **12**, 1561–1563 (2000).

338. R.C. Williamson, J.L. Wasserman, G.E. Betts, and J.C. Twichell, "Sinusoidal Drives for Optical Time Demultiplexers," IEEE Trans. Microwave Theory and Technol. **49**, 1945–1949 (2001).

339. V.W.S. Chan, "Optical satellite networks," J. Lightwave Technol. **21**, 2811–2827 (2003).

340. M.J.F. Digonnet, *Rare Earth Doped Fiber Lasers and Amplifiers* (New York: Marcel Dekker, 1993).

341. C.R. Giles and T. Li, "Optical amplifiers transform long-distance lightwave telecommunications," Proc. IEEE, **84**, 870–883 (1996).

342. J.-M.P. Delavaux and J.A. Nagel, "Multi-Stage Erbium-Doped Fiber Amplifier Designs," J. Lightwave Technol. **13**, 703–720 (1995).

343. L. Boivin, M.C. Nuss, J. Shah, D.A.B. Miller, and H.A. Haus, "Receiver sensitivity improvement by impulsive coding," Photon. Technol. Lett. **9**, 684–686 (1997).

344. L. Boivin and G.J. Pendock, "Receiver sensitivity for optically amplified RZ signals with arbitrary duty cycle," presented at Optic. Amplifiers and their Applications (OAA'99), 1999.

345. P.J. Winzer and A. Kalmar, "Sensitivity enhancement of optical receivers by impulsive coding," J. Lightwave Technol. **8**, 171–177 (1999).

346. W.R. Leeb, P.J. Winzer, and M. Pauer, "The potential of return-to-zero coding in optically amplified lasercom systems," in LEOS, 1999, pp. 224–225.

347. M. Pauer, P.J. Winzer, and W.R. Leeb, "Booster EDFAs in RZ-coded links: Are they average-power limited?," in Proc. SPIE, (Free-Space Laser Communication Technologies XIII), vol. 4272, 118–127, San Jose, USA, 2001.

348. P.J. Winzer, A. Kalmar, and W.R. Leeb, "Role of amplied spontaneous emission in optical free-space communication links with optical amplication - impact on isolation and data transmission; utilization for pointing, acquisition, and tracking," in Proc. SPIE (Free-Space Laser Communication Technologies XI), vol. 3615, 104–114, San Jose, CA, USA, 1999.

349. D.J. DiGiovanni and C.R. Giles, "Multistage optical amplifiers " in US Pat. 5115338, 1992.

350. R.I. Laming, M.N. Zervas, and D.N. Payne, "Erbium-Doped Fiber Amplifier with 54 dB Gain and 3.1 dB Noise Figure," IEEE Photon. Technol. Lett. **4**, 1345–1347 (1992).

351. T. Pliska, S. Mohrdiek, and C. Harder, "Power stabilisation of uncooled 980 nm pump laser modules from 10to 100°C," Electron. Lett. **37**, 33–34 (2001).

352. B. Schmidt, S. Pawlik, N. Matuschek, J. Muller, T. Pliska, J. Troger, N. Lichtenstein, A. Wittmann, S. Mohrdiek, B. Sverdlov, and C. Harder, "980 nm single mode modules yielding 700 mW fiber coupled pump power," in Optical Fiber Conference (OFC), 2002.

353. F. Hakimi, E.S. Kintzer, and R.S. Bondurant, "High-power single-polarization EDFA with wavelength mulitplexed pumps," in Conference on Lasers and Electro-Optics (CLEO), 1998.

354. D.O. Caplan and F. Hakimi, "A high-power high-gain single-polarization EDFA," in Conference on Lasers and Electro-Optics (CLEO), 2000.

355. C. Lester, A. Bjarklev, T. Rasmussen, and P. G. Dinesen, "Modeling of Yb^{3+}-Sensitized Er^{3+}-Doped Silica Waveguide Amplifiers," J. Lightwave Technol. **13**, 740–743 (1995).

356. Z. J. Chen, J.D. Minelly, and Y. Gu, "Compact low cost Er^{3+}/Yb^{3+} c o-doped fibre amplifiers pumped by 827 nm laser diode," Electron. Lett. **32**, 1812–1813 (1996).

357. M. Karasek, "Optimum Design of Er^{3+} –Yb^{3+} Codoped Fibers for Large-Signal High-Pump-Power Applications," IEEE J. Quantum Electron. **33**, 1699–1705 (1997).

358. J. Nilsson, P. Scheer, and B. Jaskorzynska, "Modeling and Optimization of Short Yb^{3+}-Sensitized Er^{3+}-Doped Fiber Amplifiers," Photon. Technol. Lett. **6**, 383–385 (1994).

359. A. Galvanauskas and B. Samson, "High Fiber," in SPIE's oemagazine, 2004, pp. 15–17.

360. I. Berishev, A. Komissarov, N. Moshegov, P. Trubenko, L. Wright, A. Berezin, S. Todorov, and A. Ovtchinnikov, "AlGaInAs/GaAs record high-power conversion efficiency and record high-brightness coolerless 915-nm multimode pumps," in SPIE, 2005.

361. V. Gapontsev, I. Berishev, G. Ellis, A. Komissarov, N. Moshegov, O. Raisky, P. Trubenko, V. Ackermann, E. Shcherbakov, J. Steineke, and A. Ovtchinnikov, "High-efficiency 970-nm multimode pumps " in SPIE, 2005.

362. V. Gapontsev, I. Berishev, G. Ellis, A. Komissarov, N. Moshegov, A. Ovtchinnikov, O. Raisky, P. Trubenko, V. Ackermann, and E. Shcherbakov, "9xx nm single emitter pumps for multi-kW systems," in SPIE, 2006.

363. D.J. Ripin and L. Goldberg, "High efficiency side-coupling of light into optical fibres using imbedded v-grooves," Electron. Lett. **31**, 2204–2205 (1995).

364. L. Goldberg, B. Cole, and E. Snitzer, "V-groove side-pumped 1.5 μm fibre amplifier," Electron. Lett. **33**, 2127–2129 (1997).

365. L. Goldberg and J. Koplow, "Compact, side-pumped 25 dBm Er/Yb co-doped double cladding fibre amplifier," Electron. Lett. **34**, 2027–2028 (1998).

366. D.J. DiGiovanni and A.M. Vengsarkar, "Article comprising a cladding-pumped optical fiber laser," in US Pat. 5,708,669, 1998.

367. D.J. DiGiovanni and A.J. Stentz, "Tapered fiber bundles for coupling light into and out of cladding-pumped fiber devices," in US Pat. 5,864,644, 1999.

368. V.P. Gapontsev and I. Samartsev, "Coupling arrangement between a multi-mode light source and an optical fiber through an intermediate optical fiber length," in US Pat. 5,999,673, 1999.

369. R.P. Espindola, I. Ryazansky, A.J. Stentz, K. L. Walker, and P.F. Wysocki, "Multi-stage optical fiber amplifier having high conversion efficiency," in US Pat. 6,104,733, 2000.

370. F. Hakimi and H. Hakimi, "New side coupling method for double-clad fiber amplifiers," in Conference on Lasers and Electro-Optics (CLEO), 2001.

371. L. Goldberg and M. Le Flohic, "Optical fiber amplifiers and lasers and optical pumping device therefor " in US Pat. 6,608,951, 2003.

372. A.B. Grudinin, D.N. Payne, W. Paul, L.J.A. Nilsson, M.N. Zervas, M. Ibsen, and M.K. Durkin, " Multi-fibre arrangements for high power fibre lasers and amplifiers " in US Pat. 6,826,335, 2004.

373. Y. Jeong, J. Sahu, D.B.S. Soh, C.A. Codemark, and J. Nilsson, "High-power, tunable, single-frequency, single-mode erbium:ytterbium codoped large core fiber master-oscillator power amplifier source," Opt. Lett. **30**, 2997 (2005).

374. Y. Jeong, J. Nilsson, J. Sahu, D.B.S. Soh, C. Alegria, P. Dupriez, C.A. Codemark, and D.N. Payne, "Single-frequency, single-mode, plane-polarized ytterbium-doped fiber master oscillator power amplifier source with 264 W of output power," Opt. Lett. **30**, 459–461 (2005).

375. N.G. Walker and G.R. Walker, "Polarization Control for Coherent Communications," J. Lightwave Technol. **8**, 438–458 (1990).

376. F. Heismann and M.S. Whalen, "Fast Automatic Polarization Control System," Photonics Technol. Lett. **4**, 503–505 (1992).

377. P. Oswald and C.K. Madsen, "Deterministic Analysis of Endless Tuning of Polarization Controllers," J. Lightwave Technol. **24**, 2932–2939 (2006).

378. Duling, I.N. III and R.D. Esman, "Single-polarisation fibre amplifier," Electron. Lett. **28**, 1126–1128 (1992).

379. D.O. Caplan, "Method and apparatus for stabilizing a high-gain, high-power single polarization EDFA," in US Pat. 6,831,779, 2004.

380. F. Hakimi, D.O. Caplan, H. Hakimi, and A.L. Tuffli, "Radiation effects on a two-stage double-pass single-polarization erbium fiber amplifier," in Conference on Lasers and Electro-Optics (CLEO), 2002.

381. K. Morito and S. Tanaka, "Record High Saturation Power (+22 dBm) and Low Noise Figure (5.7 dB) Polarization-Insensitive SOA Module," in Optical Amplifiers and Their Applications (OAA) Topical Meeting, paper TuC2, 2005.

382. Z. Jiang, D.E. Leaird, and A.M. Weiner, "Optical Arbitrary Waveform Generation and Characterization Using Spectral Line-by-Line Control," J. Lightwave Technol. **24**, 2487–2494 (2006).

383. J. Nilsson, Y. Jeong, C. Alegria, R. Selvas, J. Sahu, R. Williams, K. Furusawa, W. Clarkson, D. Hanna, D. Richardson, T. Monro, D. Payne, K. Yla-Jarkko, S. Alam, and A. Grudinin, "Beyond 1 kW with Fiber Lasers and Amplifiers," in Optical Fiber Conference (OFC), 2003.

384. J. Limpert, A. Liem, H. Zellmer, and A. Tuennermann, "Continuous wave ultrahigh brightness fiber laser systems," in IEEE Photonics West, 2003.

385. I.T. McKinnie, J.E. Koroshetz, W.S. Pelouch, D.D. Smith, J.R. Unternahrer, S.W. Henderson, and M. Wright, "Self-imaging waveguide Nd:YAG laser with 58% slope efficiency," in Conference on Lasers and Electro-Optics (CLEO), 2002.

386. M.D. Mermelstein, A.D. Yablon, and C. Headley, "Suppression of Stimulated Brillouin Scattering in an Er-Yb Fiber Amplifier Utilizing Temperature-Segmentation," in OAA, Paper TuD3, Budapest, Hungary, 2005.

387. R.G. Smith and S.D. Personick, "Receiver Design," in *Semiconductor Devices for Optical Communication*, H. Kressel, Ed. (New York: Springer-Verlag, 1980).

388. Y. Miyamoto, Y. Hagimoto, and T. Kagawa, "A 10 Gb/s high sensitivity optical receiver using an InGaAs-InAlAs superlattice APD at 1.3 μm/1.5 μm," IEEE Photon. Technol. Lett. **3**, 372–374 (1991).

389. T.Y. Yun, M.S. Park, J.H. Han, I. Watanabe, and K. Makita, "IO-Gigabit-per-Second High-Sensitivity and Wide-Dynamic-Range APD-HEMT Optical Receiver," Photonics Technol. Lett. **8**, 1232–1234 (1996).

390. T.V. Muoi, "Extremely sensitive direct detection receiver for laser communications," in Conference on Lasers and Electro-Optics (CLEO), 1987.

391. A. MacGregor and B. Dion, "39 Photons/bit direct detection receiver at 810 nm, BER=$1E^{-6}$, 60 Mb/s, QPPM," Proc. SPIE (Free-Space Laser Communication Technologies III), **1417**, (1991).

392. H. Matsuda, A. Miura, H. Irie, S. Tanaka, K. Ito, S. Fujisaki, T. Toyonaka, H. Takahashi, H. Chiba, S. Irikura, R. Takeyari, and T. Harada, "High-sensitivity and wide-dynamic-range 10 Gbit/s APD/preamplifier optical receiver module," Electron. Lett. **38**, 650–651 (2002).

393. J.R. Lesh, "Power Efficient Communications for Space Applications," in International Telemetering Conference, 1982.

394. B.E. Moision and J. Hamkins, "Deep-Space Optical Communications Downlink Budget: Modulation and Coding," JPL IPN Progress Report 42-154, 2003.

395. X. Sun, et. al., "Space-qualified silicon avalanche-photodiode single-photon-counting modules," J. Mod. Optics **51**, 1333–1350 (2004).

396. D.M. Boroson, R.S. Bondurant, and D.V. Murphy, "LDORA: A Novel Laser Communication Receiver Array Architecture," Proc. SPIE **5338**, 16–28 (2004).

397. O.M. Efimov, L.B. Glebov, L.N. Glebova, K.C. Richardson, and V.I. Smirnov, "High-Efficiency Bragg gratings in photothemorefractive glass," Appl. Opt. **38**, 619–627 (1999).

398. D.O. Caplan, "Spectral Filtering," in *Mars Laser Communication Demonstration (MLCD) Receiver Final Report* (MIT Lincoln Laboratory, 2005).

399. F. Herzog, K. Kudielka, D. Erni, and W. Bachtold, "Optical Phase Locking by Local Oscillator Phase Dithering," IEEE J. Quantum Electron. **42**, 973–985 (2006).

400. H.P. Yuen and V.W.S. Chan, "Noise in Homodyne and Heterodyne Detection," Opt. Lett. **8**, 177–179 (1983).

401. G.L. Abbas, V.W.S. Chan, and T.K. Yee, "A Dual-Detector Optical Heterodyne Receiver for Local Oscillator Noise Suppression," IEEE J. Lightwave Technol. **LT-3** (5), 1110–1122 (October 1985).

402. S.B. Alexander, "Design of Wide-Band Optical Heterodyne Balanced Mixer Receivers," J. Lightwave Technol. **LT-5**, 523–537 (1987).

403. L.G. Kazovsky and O.K. Tonguz, "Sensitivity of Direct-Detection Lightwave Receivers Using Optical Preamplifiers," Photon. Technol. Lett. **3**, 53–55 (1991).

404. S.R. Chinn, D.M. Boroson, and J.C. Livas, "Sensitivity of optically preamplified DPSK receivers with Fabry-Perot filters," J. Lightwave Technol. **14**, (1996).

405. P.J. Winzer, M. Pfennigbauer, M.M. Strasser, and W.R. Leeb, "Optimum filter bandwidths for optically preamplified NRZ receivers," J. Lightwave Technol. **19**, 1263–1273 (2001).

406. M. Pfennigbauer, M.M. Strasser, M. Pauer, and P.J. Winzer, "Dependence of Optically Preamplified Receiver Sensitivity on Optical and Electrical Filter Bandwidths—Measurement and Simulation," Photon. Technol. Lett. **14**, 831–833 (2002).

407. L.Y. Lin, M.C. Wu, and T. Itoh, "Figure of merit for high-power, high-speed photodetectors," in Optical Fiber Conference (OFC), 1997.

408. A.M.D. Beling, D. Schmidt, H.-G. Bach, G.G. Mekonnen, R. Ziegler, V. Eisner, M. Stollberg, G. Jacumeit, E. Gottwald, and J.-J. Weiske, "High power 1550 nm twin-photodetector modules with 45 GHz bandwidth based on InP," in Optical Fiber Conference (OFC), 2002.

409. T.S. Rose, D. Gunn, and G.C. Valley, "Gamma and proton radiation effects in erbium-doped fiber amplifiers: active and passive measurements," J. Lightwave Technol. **19**, 1918–1923 (2001).

410. P.A. Humblet, "Design of optical matched filters," in Globecom '91, 1991.

411. H.L. Van Trees, *Detection, estimation, and modulation theory, Part I* (New York: Wiley, 1968).

412. H. Geiger, M. Ibsen, and R.I. Laming, "Optimum receivers with fiber gratings," in Optical Fiber Conference (OFC), 1998.

413. S.R. Chinn, "Error-rate performance of optical amplifiers with Fabry-Perot filters," Electron. Lett. **31**, 756–757 (1995).

414. R.C. Steele and G.R. Walker, "High-sensitivity FSK signal detection with an erbium-doped fiber preamplifier and Fabry-Perot etalon demodulation," IEEE Photon. Technol. Lett. **2**, 753–755 (1990).

415. J.D. Berger, F. Ilkov, D. King, A. Tselikov, and D. Anthon, "Widely tunable, narrow optical bandpass Gaussian filter using a silicon microactuator," in Optical Fiber Conference (OFC), 2003.

416. A. D'Errico, R. Proietti, N. Calabretta, L. Giorgi, G. Contestabile, and E. Ciaramella, "WDM-DPSK Detection by Means of Frequency-Periodic Gaussian Narrow Filtering " in Optical Fiber Conference (OFC), 2006.

417. B.E. Little, et. al., "Very high-order microring resonator filters for WDM applications," IEEE Photon. Tech. Lett. **16**, 2263–2265 (2004).

418. C.K. Madsen and J.H. Zhao, *Optical filter design and analysis* (New York: John Wiley & Sons, Inc., 1999).

419. H. Takahashi, K. Oda, H. Toba, and Y. Inoue, "Transmission characteristics of arrayed-waveguide N × N wavelength multiplexer," J. Lightwave Technol. **13**, 447–455 (1995).

420. K. Takada, M. Abe, T. Shibata, and K. Okamoto, "A 25-GHz-Spaced 1080-Channel Tandem Multi/Demultiplexer Covering the S-, C-, and L-Bands Using an Arrayed-Waveguide Grating With Gaussian Passbands as a Primary Filter," Photon. Technol. Lett. **14**, 648–650 (2002).

421. I. Littler, M. Rochette, and B. Eggleton, "Adjustable bandwidth dispersionless bandpass FBG optical filter," Opt. Express **13**, 3397–3407 (2005).

422. A. Nosratinia, "Self-characteristic Distributions," J. Franklin Institute **36**, 1219–1224 (1999).

423. A. Hasegawa and F. Tappert, "Transmission of stationary nonlinear optical pulses in dispersive dielectric fibers. I. Anomalous dispersion," Appl. Phys. Lett. **23**, 142–144 (1973).

424. L.F. Mollenauer, "Ultra-long distance soliton transmission: putting fiber nonlinearity to work," in LEOS, 1993.

425. J. O'Reilly, J. da Rocha, and K. Schumacher, "Optical Fiber Direct Detection Receivers Optimally Tolerant to Jitter," IEEE Trans. Commun. **34**, 1141–1147 (1986).

426. J.P. Gordon and H.A. Haus, "Random walk of coherently amplified solitons in optical fiber transmission," Opt. Lett. **11**, 665–667 (1986).

427. G. Bosco, R. Gaudino, and P. Poggiolini, "An exact analysis of RZ versus NRZ sensitivity in ASE noise limited optical systems," in ECOC, 2001.

428. G. Bosco, A. Carena, V. Curri, R. Gaudino, and P. Poggiolini, "On the Use of NRZ, RZ, and CSRZ Modulation at 40 Gb/s With Narrow DWDM Channel Spacing," J. Lightwave Technol. **20**, 1694–1704 (2002).

429. J.H. Shapiro, "Signal-to-Noise Ratio Analysis for a Preamplified Direct-Detection Receiver with Pre- and Post-Detection Matched Filters," private communication, 2005.

430. G. Bosco and P. Poggiolini, "The Effect of Receiver Imperfections on the Performance of Direct-Detection Optical Systems using DPSK Modulation," in Optical Fiber Conference (OFC), 2003.

431. G. Bosco and P. Poggiolini, "The Impact of Receiver Imperfections on the Performance of Optical Direct-Detection DPSK," J. Lightwave Technol. **23**, 842–848 (2005).

432. J. Hsieh, A. Chiayu, V. Chien, X. Liu, A. Gnauck, and X. Wei, "Athermal Demodulator for 42.7-Gb/s DPSK Signals," in ECOC, 2005.

433. X. Liu, A.H. Gnauck, X. Wei, J. Hsieh, C. Ai, and V. Chien, "Athermal optical demodulator for OC-768 DPSK and RZ-DPSK signals," Photon. Technol. Lett. **17**, 2610–2612 (2005).

434. M.L. Stevens, "A High-speed DPSK encoder," private communication, 1998.

435. W. Kaiser, T. Wuth, M. Wichers, and W. Rosenkranz, " Reduced complexity optical duobinary 10-Gb/s transmitter setup resulting in an increased transmission distance," Photon. Technol. Lett. **13**, 884–886 (2001).

436. I. Kang, C. Xie, C. Dorrer, and A. Gnauck, "Implementations of alternate-polarization differential-phase-shift-keying transmission," Electron. Lett. **40**, 333–335 (2004).

437. C. Schramm, H.-G. Bach, A.M.D. Beling, G. Jacumeit, S. Ferber, R. Ludwig, R. Ziegler, G. G. Mekonnen, R. Kunkel, D. Schmidt, W. Schlaak, and G. Unterborsch, "High-bandwidth balanced photoreceiver suitable for 40-gb/s RZ-DPSK modulation formats," IEEE Sel. Topics Quantum Electron. **11**, 127–134 (2005).

438. E.A. Swanson, J.C. Livas, and R.S. Bondurant, "High sensitivity optically preamplified direct detection DPSK receiver with active delay-line stabilization," IEEE Photon. Technol. Lett. **6**, 263–265 (1994).

439. D.G. Heflinger , J.S. Bauch, and T. E. Humes, "Apparatus and method for tuning an optical interferometer," in US Pat. 6,396,605, 2002.

440. F. Séguin and F. Gonthier, "Tuneable All-Fiber® Delay-Line Interferometer for DPSK Demodulation," in Optical Fiber Conference (OFC), 2005.

441. D.O. Caplan, "Polarization Independent Interferometer designs," MIT Lincoln Laboratory, private correspondence, 1999.

442. D.A. Rockwell, D. H. Matsuoka, and C. L. Schulz, "Differential Phase Shift Keyed Demodulator System," in US Pat. 6,834,146 B2, 2004.

443. M.L. Stevens, S. Constantine, and D.O. Caplan, "Measured and calculated DPSK SNR change due to frequency offset error at 40 Gbit/s," private communication, 2006.

444. P.J. Winzer, F. Fidler, M.J. Matthews, L.E. Nelson, H.J. Thiele, J.H. Sinsky , S. Chandrasekbar, M. Winter, D.M. Castagnozzi, L.W. Stulz, and L.L. Buhl, "10-Gb/s Upgrade of Bidirectional CWDM Systems Using Electronic Equalization and FEC," J. Lightwave Technol. **23**, 203–210 (2005).

445. S.K. Nielsen, B.F. Skipper, and J.P. Vailladsen, "Universal AFC for use in optical DPSK systems," Electron. Lett. **29**, 1445–1446 (1993).

446. K. Kudielka and W. Klaus, "Optical homodyne PSK receiver: Phase synchronization by maximizing base-band signal power," in LEOS, 1999.

447. A.H. Gnauck, G. Raybon, S. Chandrasekhar, J. Leuthold, C. Doerr, L. Stulz, and E. Burrows, "25 × 40-Gb/s copolarized DPSK transmission over 12 × 100-km NZDF with 50-GHz channel spacing," IEEE Photon. Technol. Lett. **15**, 467–469 (2003).

448. H. Bissessur, G. Charlet, E. Gohin, C. Simonneau, L. Pierre, and W. Idler, "1.6 Tbit/s (40 × 40 Gbit/s) DPSK transmission over 3 × 100 km of TeraLight fibre with direct detection," Electron. Lett. **39**, 192–193 (2003).

449. T. Mizuno, M. Oguma, T. Kitoh, Y. Inoue, and T. Takahashi, "Mach–Zehnder Interferometer Exactly Aligned With ITU Grid Frequencies," Photon. Technol. Lett. **18**, 325–327 (2006).

450. T. Hoshida and H. Onaka, "Method and system for demultiplexing non-intensity modulated wavelength division multiplexed (WDM) signals," in U.S. Pat. 7,035,543, 2006 (filed 2001).

451. P.J. Winzer, "Optical Receiver for Wavelength-Division-Multiplexed Signals," in US Pat. Appl. 2004/0258423 A1, 2004.

452. B. Zhu, L. E. Nelson, S. Stultz, A.H. Gnauck, C. Doerr, J. Leuthold, L. Gruner-Nielsen, M.O. Pedersen, and R.L. Lingle, Jr., "High Spectral Density Long-Haul 40-Gb/s Transmission Using CSRZ-DPSK Format," J. Lightwave Technol. **22**, 208–214 (2004).

453. D.A. Atlas and L.G. Kazovsky, "An optical PSK homodyne transmission experiment using 1320 nm diode-pumped Nd:YAG lasers," IEEE Photon. Technol. Lett. **2**, 367–370 (1990).

454. D.M. Castagnozzi, J.C. Livas, E.A. Bucher, L.L. Jeromin, and J.W. Miller, "Performance of a 1 Gbit/s optically preamplified communication system with error correcting coding," Electron. Lett. **30**, 65–66 (1994).

455. D.O. Caplan, S. Constantine, and M.L. Stevens, "Near-quantum-limited OOK and binary-FSK receiver sensitivity using a Filtered Direct-Drive pulse-carved MOPA transmiter and an optically preamplified receiver at 1.25 Gbit/s," private communication, 2006.

456. R.A. Linke, et. al., "Coherent lightwave transmission over 150km fiber lengths at 400 Mbit/s and 1 Gbit/s data rates using phase modulation," Electron. Lett. **22**, 30–31 (1985).

457. T. Imai, T. N. Ohkawa, Y. Ichihashi, T. Sugie, and T. Ito, "Over 300 km CPFSK transmission experiment using 67 photon/bit sensitivity receiver at 2.5 Gbit/s," Electron. Lett. **26**, 357–358 (1990).

458. J.M. Kahn, A.H. Gnauck, J.J. Veselka, S.K. Korotky, and B.L. Kasper, "4-Gb/s PSK homodyne transmission system using phase-locked semiconductor lasers," IEEE Photon. Technol. Lett. **2**, 285–287 (1990).

459. T. Chikama, et. al., "Modulation and demodulation techniques in optical heterodyne PSK transmission systems," J. Lightwave Technol. **8**, 309–321 (1990).

460. I. Hardcastle, T. Large, F. Davis, and A. Hadjifotiou, "High performance 140 Mbit/s FSK coherent system," Electron. Lett. **26**, 1523–1525 (1990).

461. T. Naito, T. Chikama, and G. Ishikawa, "Optimum system parameters for multigigabit CPFSK optical heterodyne detection systems," J. Lightwave Technol. **12**, 1835–1841 (1994).

462. S. Norimatsu, H. Mawatari, Y. Yoshikuni, O. Ishida, and K. Iwashita, "10 Gbit/s optical BPSK homodyne detection experiment with solitary DFB laser diodes," Electron. Lett. **31**, 125–127 (1995).

463. R.I. Laming, A.H. Gnauck, C.R. Giles, M.N. Zervas, and D.N. Payne, "High-sensitivity two-stage erbium-doped fiber preamplifier at 10 Gb/s," IEEE Photon. Technol. Lett. **4**, 1348–1350 (1992).

464. E. Meissner, "116 photons/bit in a 565 Mbit/s optical DPSK heterodyne transmission experiment," Electron. Lett. **25**, 281–282 (1989).

465. T.J. Paul, E.A. Swanson, J.C. Livas, R.S. Bondurant, and R.J. Magliocco, "3 Gbit/s optically preamplified direct detection DPSK receiver with 116 photon/bit sensitivity," Electron. Lett. **29**, 614–615 (1993).

466. Y.K. Park, J.-M. P. Delavaux, Mizuhara, L.D. Tzend, T.V. Nguyen, M.L. Kao, P.D. Yeates, S.W. Granlund, and S.J., "5 Gbit/s Optical Preamplifier Receiver with 135 Photons/bit Usable Receiver Sensitivity," in Optical Fiber Conference (OFC), paper TuD4, 1993.

467. T. Saito, Y. Sunohara, K. Fukagai, S. Ishikawa, N. Henmi, S. Fujita, and Y. Aoki, "High Receiver Sensitivity at 10 Gb/s Using an Er-Doped Fiber Preamplifier Pumped with a 0.98 μm Laser Diode " IEEE Photon. Technol. Lett. **3**, 551–553 (1991).

468. P.P. Smyth, R. Wyatt, A. Fidler, P. Eardley, A. Sayles, and S. Craig-Ryan, "152 photons per bit detection at 622 Mbit/s to 2.5 Gbit/s using an erbium fibre preamplifier," Electron. Lett. **26**, 1604–1605 (1990).

469. L.D. Tzeng, R.E. Frahm, and W. Asous, "A high-performance optical receiver for 622 Mb/s direct-detection systems," Photon. Technol. Lett. **2**, 759–761 (1990).

470. K. Kannan, et. al., "High-sensitivity receiver optical preamplifiers," IEEE Photon. Technol. Lett. **4**, 272–275 (1992).

471. A.H. Gnauck, K.C. Reichmann, J.M. Kahn, S.K. Korotky, J.J. Veselka, and T.L. Koch, "4-Gb/s heterodyne transmission experiments using ASK, FSK and DPSK modulation," IEEE Photon. Technol. Lett. **2**, 908–910 (1990).

472. T. Kataoka, Y. Miyamoto, K. Hagimoto, and K. Noguchi, "20 Gbit/s long distance transmission using a 270 photon/bit optical preamplifier receiver," Electron. Lett. **30**, 716–716 (1994).

473. M. Shikada, et. al., "1.5 m high bit rate long span transmission experiments employing a high power DFB-DC-PBH laser diode," in *European Conference on Optical Communication* (Istituto Internazionale delle Communicazioni: Genva, 1985).

474. J.C. Campbell, et. al., "High performance avalanche photodiode with separate absorption grading and multiplication regions," Electron. Lett. **19**, 818–820 (1983).

475. K. Hagimoto, et. al., "Twenty-Gbit/s signal transmission using a simple high-sensitivity optical receiver," in Optical Fiber Conference (OFC), 1992, paper Tul3.

476. V. Vilnrotter, C.-W. Lau, M. Srinivasan, K. Andrews, and R. Mukai, "Optical Array Receiver for Communication Through Atmospheric Turbulence," J. Lightwave Technol. **23**, 1664–1675 (2005)..

477. D.O. Caplan and J.J. Carney, "Angstrom class narrow band filters at 1060–1080 nm," MIT Lincoln Laboratory, internal memorandum, 2003.

478. D.O. Caplan, "Spectral Filtering " in *Mars Laser Communication Demonstration (MLCD) Preliminary Design Review (PDR)* (MIT Lincoln Laboratory and NASA, 2005).

479. D.O. Caplan and B.S. Robinson, "WDM Mitigation of Nonlinear Impairments in Low-Duty-Cycle M-PPM Free-Space Optical Transmitters," submitted to OFC2008.